Petology and Geochemistry

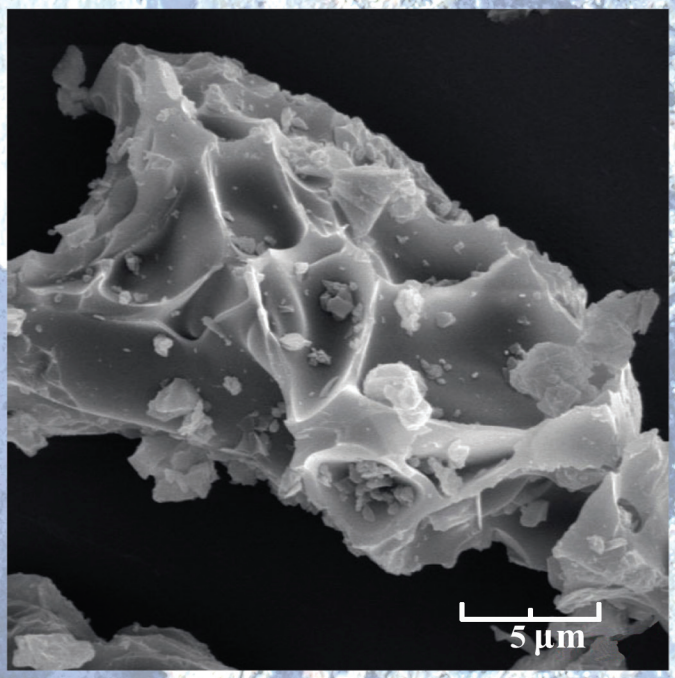

Oblique aerial photo, looking southeast, showing Augustine Volcano's 2006 lava dome and northeast lava flow at the end of the 2006 eruption's effusive phase. Alaska Volcano Observatory photo taken March 15, 2006, by Tim Plucinski.

The 2006 Eruption of Augustine Volcano, Alaska
Power, J.A., Coombs, M.L., and Freymueller, J.T., editors
U.S. Geological Survey Professional Paper 1769

Chapter 15

Petrology and Geochemistry of the 2006 Eruption of Augustine Volcano

By Jessica F. Larsen[1], Christopher J. Nye[2], Michelle L. Coombs[3], Mariah Tilman[1], Pavel Izbekov[1], and Cheryl Cameron[2]

Abstract

Deposits from the 2006 eruption of Augustine Volcano, Alaska, record a complex history of magma mixing before and during the eruption. The eruption produced five major lithologies: low-silica andesite scoria (LSAS; 56.5 to 58.7 weight percent SiO_2), mostly during the initial explosive phase; high-silica andesite pumice (HSA; 62.2 to 63.3 weight percent SiO_2), prevalent during the continuous phase; dense low-silica andesite (DLSA; 56.4 to 59.3 weight percent SiO_2), predominantly during the late effusive phase; and dense intermediate andesite (DIA) and banded clasts, present throughout the eruption but most abundant in the continuous phase. The DIA and banded clasts have compositions that fall between and partially overlap the ranges noted above. All rock types are phenocryst-rich (36 to 44 volume percent), containing plagioclase, orthopyroxene, augite, Fe-Ti oxides, olivine, and rare amphibole, apatite, and anhydrite. Glasses from tephra and flow-deposit clasts range from 66 to nearly 80 weight percent SiO_2 and represent highly evolved melt relative to the bulk rock compositions. Fe-Ti oxides recorded f_{O_2}~2 log units above the Ni-NiO buffer and temperatures of 904±47°C and 838±14°C from LSAS and HSA samples, respectively, with the intermediate lithologies falling in the middle of these ranges. The dense low-silica andesite and scoria (collectively LSA) are compositionally nearly identical, and trace-element patterns show that the HSA is not the result of shallow crustal fractionation of the LSA. The petrological and geochemical data indicate that two-component magma mixing between the LSA and HSA caused the compositional spread in eruptive products. The phenocryst population in the LSA suggests that it represents a hybrid formed from the HSA and an unerupted, basaltic "replenishing" magma. On the basis of petrological and geophysical observations reported here and elsewhere in this volume, the HSA was stored as a crystal-rich mush with its top at ~5-km depth. An influx of basalt remobilized and partially mixed with a portion of the mush, forming the hybrid LSA. The lower viscosity LSA ascended towards the surface as a dike, erupting during the explosive phase in mid-January 2006. In late January, a large explosion produced the first significant volumes of HSA, followed by several days of rapid HSA effusion during the eruption's continuous phase. After a three-week hiatus marked by elevated gas output, signifying an open system, degassed LSA erupted during the final, effusive phase. Consistency in eruptive styles and compositions suggests that the HSA magma body may have been similarly rejuvenated during the past several eruptions.

Introduction

Understanding the magmatic processes that drive eruptions is an integral component of volcano studies. Studying the deposits of recent, well-monitored eruptions allows us to place petrologic studies in a context that would be impossible for prehistoric or more poorly documented eruptions, thus yielding more insight into the link between what happens below the volcano's surface and what comes out of the vent. Augustine Volcano, located in Cook Inlet in south-central Alaska, is one of the most active volcanoes in the Aleutian arc, with eight confirmed explosive eruptions in the past 200 years (Waythomas and Waitt, 1998). Because of the frequency of eruptions and the unique hazards that Augustine presents, understanding the processes that trigger eruptive events there is an important role of the Alaska Volcano Observatory (AVO). The consistent

[1]Alaska Volcano Observatory, Geophysical Institute, 903 Koyukuk Drive, University of Alaska, Fairbanks, AK 99775.

[2]Alaska Volcano Observatory, Alaska Division of Geological and Geophysical Surveys, 3354 College Road, Fairbanks, AK 99709.

[3]Alaska Volcano Observatory, U.S. Geological Survey, 4200 University Drive, Anchorage, AK 99508.

pattern of eruptions, in terms of precursory activity and eruptive style, combined with the increased amount of independent datasets for the 2006 eruption, makes Augustine suitable for cross-disciplinary studies of volcanic processes that can be applied to less well monitored volcanoes. The frequency of eruptions at Augustine also presents an excellent opportunity to compare petrologic data from the three most recent eruptions in 1976, 1986, and 2006.

Petrologists have long recognized that many products of subduction-zone volcanoes show evidence of magma mixing, and recent studies of historical and ongoing eruptions show that mixing is often temporally linked to magma's arrival at the earth's surface (for example, Coombs and others, 2000; Costa and Chakraborty, 2004; Izbekov and others, 2002; Murphy and others, 2000; Nakamura, 1995; Pallister and others, 1996). Understanding the process of magma mixing as a potential eruption trigger is important in the case of Augustine Volcano's most recent eruptions. Magmas erupted at Augustine in the 30 years prior to the 2006 eruption show clear evidence of magma mixing in the form of mingling (banded clasts) and hybridization at both macro and micro scales (Johnston, 1978; Roman and others, 2005). Both the 1976 and 1986 eruptions are thought to have been triggered by the injection of basaltic magma into a more silica-rich andesite/dacite magma body. Their whole-rock compositions are similar and limited in range between 56 to 64 weight percent SiO_2. The 1976 deposits include olivine and hornblende phenocrysts that appear to have grown in a mafic magma that was not found in the erupted material (Johnston, 1978). After the 1986 eruption, a better understanding of magma storage and transport at Augustine emerged from the increased quantity of geophysical and petrological data (Harris, 1994; Power, 1988; Roman and others, 2005). Roman and others (2005) suggest a model of interconnected dikes to explain how Augustine commonly produces mixed magmas but maintains a relatively narrow compositional range (56–64 weight percent SiO_2) throughout 200 years of historical activity, while also maintaining compositional heterogeneity throughout individual eruptive cycles.

The 2006 eruption of Augustine Volcano followed a sequence of events similar to those in 1976 and 1986. A precursory phase began April 30, 2005, and both seismicity and inflation of the edifice slowly increased over the next 7 months (Jacobs and McNutt, this volume; Cervelli and others, 2006). By mid-December 2005, earthquakes were occurring at a rate of 15 per day at a depth close to sea level, along with intermittent steam explosions, the largest of which were observed on December 10, 12, and 15 (Power and others, 2006). On January 11, 2006, seismometers recorded two explosions at Augustine, marking the onset of the explosive phase of the eruption. The explosive phase was dominated by a series of 13 discrete Vulcanian blasts that produced pyroclastic flows and ash fall rich in low-silica andesite scoria (Coombs and others, this volume; Vallance and others, this volume; Wallace and others, this volume; fig. 1). On January 28, Augustine entered a continuous eruptive phase dominated by low-level, ash-rich plumes and multiple pyroclastic flows, likely the result of rapid effusion and collapse of lava at the summit (Coombs and others, this volume; Wallace and others, this volume). Deposits from this phase include crystal-rich high-silica andesite and lesser amounts of banded clasts, dense intermediate andesite, and dense low-silica andesite (Vallance and others, this volume). After a hiatus in eruptive activity that lasted from February 10 to March 3, the eruption entered an effusive phase dominated by dome growth and the extrusion of rubbly lava flows accompanied by small-volume block-and-ash flows (Coombs and others, this volume). The effusive deposits contained primarily dense low-silica andesite and dense intermediate andesite (Vallance and others, this volume). The 2006 eruptive sequence ended on March 16, 2006, with the cessation of drumbeat earthquakes that accompanied the dome growth (Power and Lalla, this volume).

In this paper we present an overview of the petrography, petrology, and geochemistry of the products from the 2006 Augustine eruption. Our results are tied to the dominant lithologies erupted during each of the explosive, continuous, and effusive eruptive phases. We show that the eruptive products are the result of hybridization of an unerupted replenishing mafic magma, not seen in the eruption products in its pure, unmixed form, and a shallowly residing high-silica andesite body that was reinvigorated just before eruption. The data presented in this chapter are used in conjunction with companion studies on melt inclusion preeruptive volatile contents (Webster and others, this volume), geodetic constraints (Cervelli and others, this volume), and reaction-rim growth on olivines (Tilman, 2008), among others, to develop a model for the locations of magma storage and the timescales of magma movement before and during the different phases of the 2006 eruption. This model provides one explanation for the conveyor-belt-like similarity and frequency of historic Augustine eruptions.

Geological Setting

Augustine Volcano lies in the eastern Aleutian arc, approximately 80 km above the Wadati-Benioff zone (Syracuse and Abers, 2006). Volcanism in the eastern arc is caused by northwestward subduction of the Pacific Plate beneath the North American Plate at a rate of roughly 55 mm/yr (Kienle and Swanson, 1983).

The wholly Quaternary volcano sits atop crust of the Peninsular Terrane, thought to have amalgamated with nearby terranes prior to Late Jurassic time and accreted to North America in the mid-Cretaceous (Detterman and Reed, 1980). The terrane comprises Mesozoic marine and nonmarine sedimentary rocks of the Jurassic Naknek Formation, which crop out on the south flank of Augustine from sea level to 400 m above mean sea level (amsl). It is overlain by a thin veneer of friable sandstone and conglomerate of the Cretaceous Kaguyak Formation (Waitt, this volume). Seismic velocity studies suggest that these rocks have been uplifted on the south shoulder by faulting, and that lower-velocity sediments underlie the volcano on other sectors from sea level to ~900

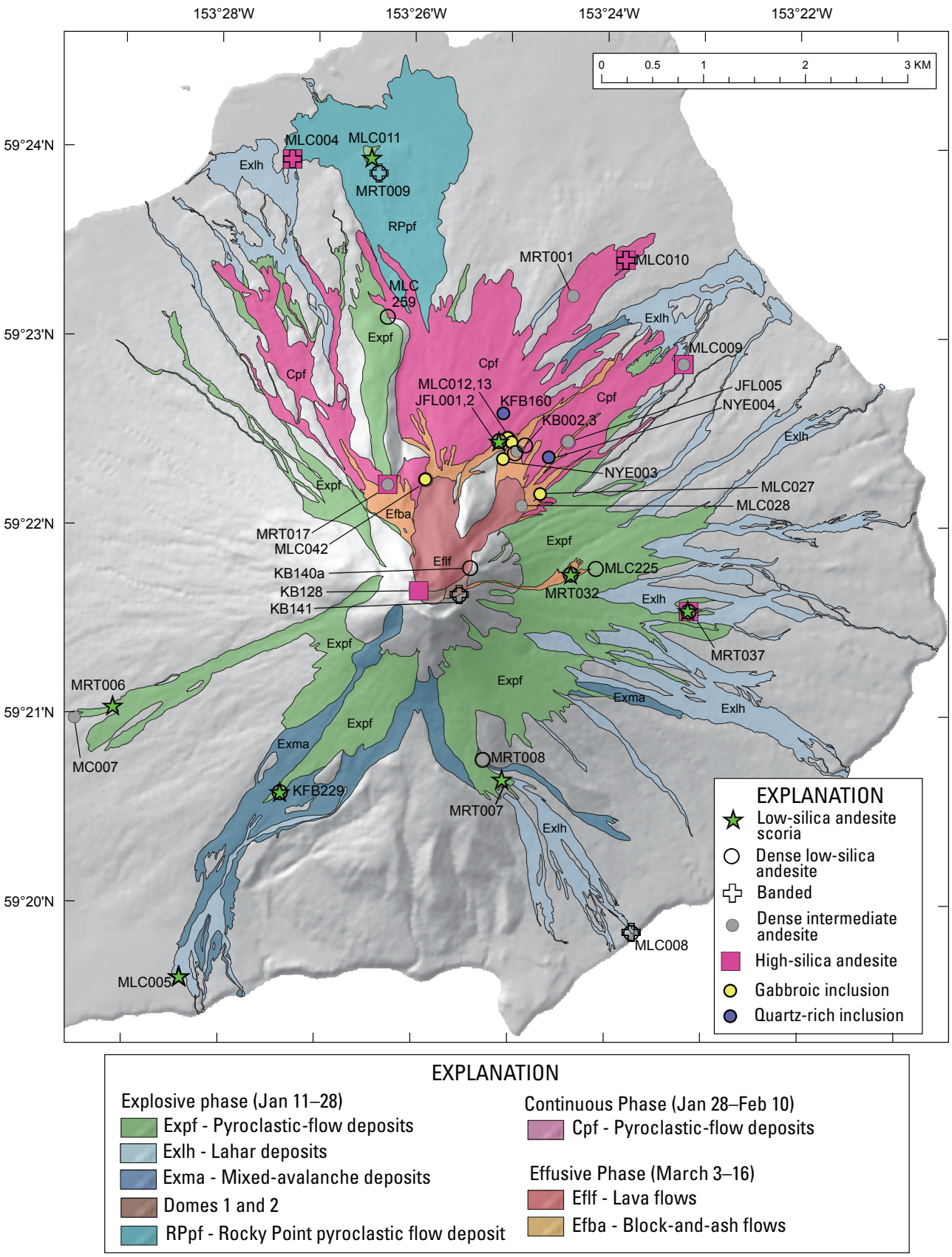

Figure 1. Map of Augustine Island showing deposits from the 2006 eruption and the location of samples used in this study. The 06AU- preface on sample locations is removed for clarity. Units simplified from Coombs and others (this volume).

m below mean sea level (bmsl) (Kienle and others, 1979). Beneath the summit, an intermediate-velocity region from sea level down to 900 m bmsl is interpreted as sedimentary strata that have been interlaced with volcanic dikes and sills (Kienle and others, 1979). High-velocity rocks everywhere underlie the volcano below 900 m bmsl, interpreted by Kienle and others as zeolitized Naknek Formation.

The oldest known products of Augustine Volcano are late Pleistocene in age (Johnston, 1978). They comprise poorly sorted bedded fragmental material, with clasts of olivine basalt as large as 20 cm in diameter, as well as radially fractured clasts of dense juvenile rhyolite. There is extensive palagonitization of the material and it appears to be the result of hyaloclastite eruption likely from a flank vent. The upper 20 cm is interlayered with the base of a rhyolitic tephra-fall deposit.

Records of early to middle Holocene Augustine eruptions are scarce and limited to the base of a few small tephra exposures on the south flank and some distal ashes with Augustine compositional affinities (Waitt, this volume). The late Holocene, prehistoric eruptive record is more complete, and shows that Augustine often erupted explosively, producing sometimes thick tephra falls, an apron of flowage deposits, and an edifice consisting of overlapping lava domes and short flows. In addition, repeated edifice failures and debris avalanches have marked the late Holocene record, with the most recent in 1883. Augustine has erupted historically in 1883, 1935, 1964, 1976, and 1986, each time producing andesitic through dacitic ash fall and pyroclastic flows.

Several lines of evidence have been used to argue that Augustine's subvolcanic plumbing system is immature and that it lacks a large, well-developed magma storage region, or "magma chamber." Recent eruptions have modest volumes (<0.5 km^3), thus involving small magma batches. Compositional heterogeneity is the norm and persisted throughout the 1986 eruption, suggesting that the eruption was not fed from a single magma storage region but instead by a system of small-volume dikes in the shallow subsurface, some of which contained residual magma from 1976 (Roman and others, 2005). Between eruptions, minimal edifice deformation and gas output have been observed (McGee and others, this volume; Power and others, 2006)

Despite the apparent absence of a large shallow magma body beneath Augustine, there are some indications of shallow-crustal magma storage and crystallization prior to previous eruptions. Seismicity prior to the 1976 eruption outlined a central, narrow plumbing system that reached from 8 km to the surface (Kienle and others, 1979). About half of Holocene eruptions produced magmas that contain hornblende, and Al-in-hornblende geobarometry from two Holocene fall units yields equilibrium pressures of 100 to 260 MPa, equivalent to depths between 3.5 and 9 km (Tappen and others, 2009). Melt inclusions in crystals within 1986 and prehistoric magmas contain wide ranges in both dissolved water and carbon dioxide, indicating crystallization at depths mostly between 8 km and several hundred meters bsl (Roman and others, 2005; Webster and others, this volume).

Sample Descriptions

Clasts within deposits of the 2006 eruption were initially separated into five major lithologic groups on the basis of hand-sample characteristics, primarily color and vesicularity (Vallance and others, this volume; fig. 2). Subsequent whole-rock analyses confirm the initial categories. The five lithologies are present in most deposits from the eruption, though in varying proportions. They are:

1. Low-silica andesite scoria (LSAS), almost exclusively erupted during the 2006 explosive phase, representing ~45 percent of the explosive-phase ejecta, with less than 3 percent appearing during the remainder of the eruption. LSAS clasts are moderately vesicular, with black to reddish-brown cores and olive-green to light-gray rinds.

2. High-silica andesite (HSA), most abundant in continuous-phase deposits but also present in explosive-phase ejecta. The most evolved whole-rock, matrix glass, and mineral compositions of 2006 ejecta belong to the HSA, which accounts for >5 to 30 percent of clasts within explosive-phase units, approximately 80 percent of continuous-phase deposits, and <10 percent of effusive phase deposits (Vallance and others, this volume). HSA mostly occurs as rounded, crystal-rich, slightly friable clasts that are light to dark gray, moderately vesicular, and often colored by oxidation.

3. Dense intermediate andesite (DIA), erupted during all eruptive phases but most prevalent in deposits of the continuous-phase. This lithology was originally identified in the field by its medium-grey color and makes up approximately 10 percent of explosive-phase ejecta and a third of continuous-phase ejecta (Vallance and others, this volume). We note, however, that some DIA clasts, especially in the explosive phase, may be accidental lithics of pre-2006 dome lavas. DIA is found as rounded to angular, medium to light gray, poorly to nonvesicular clasts, or as lava.

4. Dense low-silica andesite (DLSA), which composes the effusive-phase lava flows and is present throughout the eruption products in varying proportions as clasts in flow and fall deposits. DLSA makes up 8 to 25 percent of the deposits from the explosive and continuous phases and ~60 percent of effusive-phase deposits (Vallance and others, this volume). It is dark gray to black, poorly to nonvesicular, and commonly forms angular clasts, some of which have breadcrust rinds.

5. Banded clasts are any combination of the above colors and texture that show distinct to diffuse banding. They are found throughout the eruption but are most prevalent during the continuous phase.

In addition to these five major lithologies, crystal-rich, fine-grained gabbroic (FGGI) and quartz-rich inclusions were

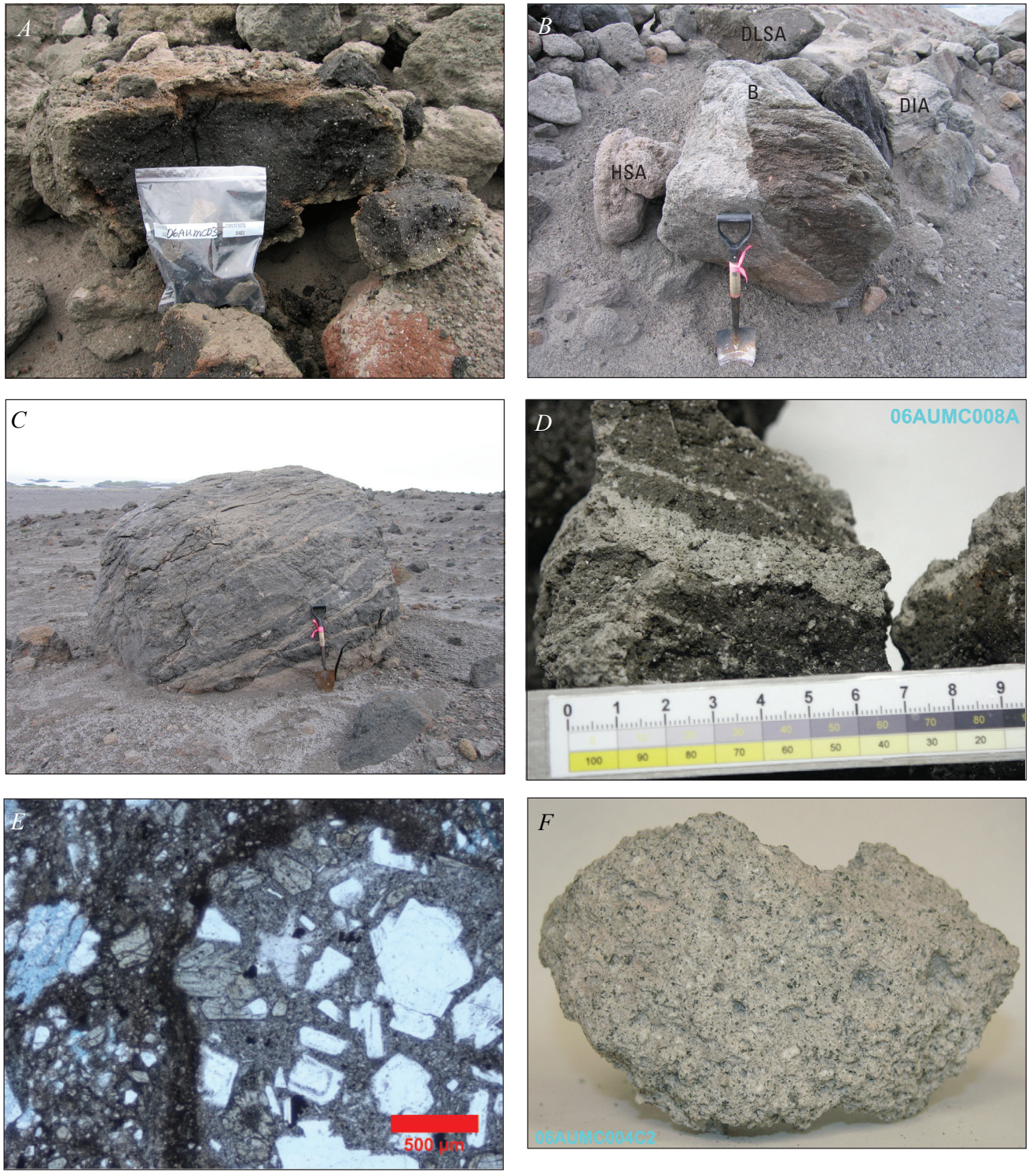

Figure 2. Photographs depicting typical occurrences and major lithologies of deposits from the 2006 Augustine eruption. *A,* Broken clast of low-silica andesite scoria with olive green rind and black interior, within an explosive-phase pyroclastic-flow deposit. Sample site 06AUMLC035. *B,* Continuous-phase pyroclastic-flow deposit containing high-silica andesite (HSA), dense intermediate andesite (DIA), dense low-silica andesite (DLSA), and banded (B) clasts. *C,* Large banded boulder found in Rocky Point pyroclastic-flow deposit from late in the explosive phase. *D,* Interior of banded clast 06AUMC008a, collected from an explosive-phase pyroclastic-flow deposit, showing distinct bands of high- and low-silica andesite. Scale is in centimeters. *E,* Transmitted-light photomicrograph showing crystal-rich and crystal-poor regions of sample 06AUMC007b from the January 13–14 low-silica andesite scoria. *F,* High-silica andesite sample 06AUMC004c2.

sampled from the continuous- and effusive-phase deposits (fig. 3). Fine-grained gabbroic inclusions are salt and pepper in color, nearly holocrystalline, and finely vesicular. They are almost exclusively found as inclusions within DLSA lavas of the effusive phase. Quartz-rich inclusions were found in continuous-phase deposits as light gray or salt-and-pepper bands or pods in larger andesite clasts.

Samples were collected by AVO scientists during the course of the eruption on January 12 and 24, February 8 and 20, and May 13 and after the eruption during August 2006. A geologic map of the 2006 deposits (Coombs and others, this volume) was used to determine sampling localities in order to collect samples from as many of the eruptive events as possible (fig. 1). For each eruptive unit, we collected samples of the multiple lithologies present in most deposits (table 1 and appendix 1). In addition to 2006 samples, we collected samples from a Pleistocene outcrop on the south flank of the island that contains coevally erupted hyaloclastite and pumice (Waitt, this volume), and some clasts from 1976 and 1986 pyroclastic flows for whole-rock analysis.

Analytical Methods

Major and trace element compositions of 70 samples from the 2006 eruption were determined at the Washington State University (WSU) Geoanalytical Laboratory using XRF and ICP-MS techniques (table 2 and appendix 3).[4] Samples were cleaned in deionized water, dried for several days at less than 100°C, partially crushed to pea-sized or smaller grains, and then sent to WSU for analysis. x-ray fluorescence and ICP-MS analyses were conducted following the methods outlined in Johnson and others (1999) and Knaack and others (1994), respectively. All intensity values were concatenated and reduced using a single calibration file to reduce interbatch analytical variations.

Petrographic analysis consisted of documentation of the groundmass and phenocryst types and textures and point-count analyses of thin sections. At least five thin sections for each of the five main lithologic types were counted for modal analyses. Point counts were conducted using an automated stage with a minimum of 1,000 points per slide, including void space. Normalized percentages were calculated after removing void counts.

Phenocryst, microlite, and groundmass-glass compositions were determined at the University of Alaska Fairbanks (UAF) Advanced Instrumentation Lab (AIL) using a Cameca SX-50 electron microprobe equipped with four wavelength-dispersive spectrometers and one energy-dispersive spectrometer. Phenocryst phases were analyzed for major elements using a 15-KeV, 10-nA focused beam and standard ZAF corrections. Glasses were analyzed using a 15-KeV,

[4]Note that tables 2 through 8 are at the back of this chapter.

Figure 3. Photographs depicting occurrences of fine-grained gabbroic and quartz-rich inclusions. *A,* Boulder of fine-grained, plagioclase-rich gabbro, itself containing inclusions of more mafic gabbro, found in effusive-phase block-and-ash-flow deposit. *B,* Close-up view of boulder in panel *A*. Bottom edge of meter stick is 2 cm across. *C,* Block shed from front of effusive-phase northeast lava flow, mainly comprising a single enormous fine-grained gabbroic inclusion, with a carapace of dense, low-silica andesite. Sampling site 06AUMLC027.

Table 1. Samples of Augustine Volcano 2006 eruptive products used in this study, sorted by eruptive unit and lithologic type.

[Unit names are defined by Coombs and others (this volume). On our figure 1, Expf, Expc, and Expct are lumped into Expf and Cpf and Cpfw are lumped into Cpf for simplicity. In addition, the appendix contains new major and trace element data for 2 samples from the 1883(?) lava flow; 3 samples from 1964 pyroclastic flows; 5 samples from 1976 pyroclastic flows; 11 samples from 1986 pyroclastic flows; 5 samples from early Holocene pumice fall and bombs; 8 juvenile clasts from the late Pleistocene basalt/basaltic andesite hyaloclastite; 3 dense juvenile rhyolite clasts from within the hyaloclastite; and 3 rhyolite pumice clasts from the fall unit directly overlying the hyaloclastite. The prefix "06AU" has been removed from all sample names for brevity. (#) indicates that the sample was analyzed for major and trace elements]

Deposit dates	Phase	Unit	Low-silica andesite scoria	Dense low-silica andesite	Banded	Dense intermediate andesite	High Silica Andesite	Inclusion
Jan 13–14 (E5–8)	Explosive	Expct, Expf	MRT037c#	MRT037b# MRT037f# MRT037a		MRT037e#		MRT037d# (low-K)
Jan 13–14 (E3–8)			MC005a# MC005c.p3# MC005c.p4# MC005c.p5# MC008b.p1# MC008b.p2# KFB229a# MRT007b#	MC008b.p3# KFB229b# MRT008a#	MC005c.p1# MC008a.f# MC008a.m# MC005c.p2	MC008b.l1# MRT008b#	MC005c.p2# (pumice)	
Jan 17 (E9)		Expf	MC007c#			MRT006#		
Jan 21		Exd1		KB141b#	KB141a			
Jan 22–28		Exd2					JWV059a# KFB128a#	
Jan 27 (E10)		Expc		MLC259e# MLC225#				
		RPpf	MRT009b# MC011a#		MC004c3m# MC004c3 MRT009c		MC004a MC004c1# MC004c2#	
Jan 28–Feb 4	Continuous	Cpf			MC010p2# MC010p3m# MC010p3	MC009l1# MRT001b#	MC009p1# MC009p2# MC010p1#	NYE004# (high-Si) KFB160# (high-Si)
		Cpfw				MRT017a#	MRT017b#	
March 3–16	Effusive	Eflf		KB140B# MLC042b# MLC057#		MLC028#		MLC042a# (gabbroic)
		Efba	JFL001e# MRT032c#	JFL001d# JFL001f# JFL002# JFL005b# KB003# MC012b# MRT032a# NYE001#		JFL001b# JFL005a# KB002A# KB002B# KB002C# MRT032b#		MC012a# (gabbroic) MC013a# (gabbroic) MC027a# (gabbroic) NYE003# (gabbroic)

10-nA, 10-micron-wide defocused beam and a routine to minimize Na loss. Comenditic glass standard KN-18 was routinely analyzed during glass analyses to monitor instrument drift.

Fe-Ti oxide grains were separated from crushed samples of the major lithologies using a magnet. Grain mounts of the separated oxides were polished and touching ilmenite-titanomagnetite pairs without obvious disequilibrium textures or exsolution lamellae were analyzed by microprobe. Analyses consisted of core to rim transects, in 3-micron increments across each grain, with anomalously high Si analyses removed because of possible interference with glass. The analyses showed no significant change in composition from core to rim, so the values for each oxide were averaged. The pairs were subjected to the Bacon and Hirschman (1988) equilibrium test, and those found to be in equilibrium were run through QUILF (Andersen and others, 1993) to determine the temperature and oxygen fugacity (f_{O_2}). As discussed below, the high f_{O_2} of the magmas is outside of the calibration for the QUILF algorithm (Evans and others, 2006; Lattard and others, 2005); thus temperatures presented herein have been adjusted downward by 30°C (Rutherford and Devine, 1996).

Results

Petrography

Eruptive products of the 2006 eruption are typical of andesite and dacite produced by convergent-margin volcanoes worldwide: they are porphyritic, variably vesicular, and have glassy to microlite-rich groundmasses. The 2006 magmas contained phenocrysts of, in order of decreasing abundance, plagioclase, augite, orthopyroxene, Fe-Ti oxides, olivine, and rare amphibole, apatite, anhydrite, quartz, and biotite. (fig. 4; table 2). Amphibole is rare within all major lithologies. Apatite and anhydrite are present in less than 0.6 volume percent in all lithologies, and apatite exists mainly as inclusions within plagioclase. Biotite, quartz, significant anhydrite, and abundant amphibole are present only within the FGGI minor lithology. Plagioclase is the most abundant mineral phase by far, averaging from 27 to 32 volume percent in the major lithologies.

All rock types are phenocryst-rich, with LSAS, DLSA, DIA, and banded samples ranging from 36 to 40 volume percent phenocrysts in terms of average values (table 2), though we note that individual samples may lie outside this range (appendix 2). Two fine-grained gabbroic inclusions have an average of 74 volume percent phenocrysts.

Of the five major lithologies, high-silica andesite samples are the richest in phenocrysts. From point-count analysis of seven HSA samples, we found an average of 45 volume percent crystals, with a standard deviation of 7 volume percent. Interestingly, three replicate point-count analyses of a single HSA thin section yielded results of 40 to 57 volume percent, an unexpectedly high range (appendix 2). (Replicate analyses of LSAS and DLSA samples yielded ranges within a few volume percent.) In addition, we noted that hand specimens of HSA appeared particularly crystal-rich. To further assess HSA phenocryst content, we use a mass balance approach. If we perform a linear least squares, mass balance regression of the phenocryst compositions determined by electron microprobe (see section on Phase Descriptions and Compositions below), using their modal percentages from the point counts against the whole rock compositions to derive the volume percent of glass in the groundmass, we find that the point-count modes yield significant mismatches in Si, Mg, Fe, and Ca. In contrast, when glass content is reduced from 55 to 46 volume percent and other phenocrysts are increased proportionally, we obtain a better fit in the mass balance calculation. We suggest that the disparity between the point-count and mass balance methods for the high-silica andesite is a result of assigning groundmass glass to points where the glass may account for less than the total thickness of the thin section. Thus the actual crystallinity of the high-silica andesite magma is likely closer to 55 volume percent.

All lithologies are variably vesicular, even those described as relatively dense, and range from 16 to 45 volume percent porosity. Average vesicularities for the major lithologies are 37.3 volume percent for HSA, 38.7 volume percent for banded, 33.6 volume percent for LSAS, 22.1 volume percent for DIA, and 19.8 volume percent for DLSA (fig. 5, table 2). Void spaces are commonly irregularly shaped and variably sized, from sub-mm size to more than 10 mm.

Both DLSA and LSAS have dark gray to brown groundmasses, dominated by abundant microlites and containing very little residual glass (<1 volume percent by point counts; figs. 5, 6*A*, *B*). In contrast, HSA pumice clasts have groundmass composed almost wholly of clear, microlite-free glass that often forms finely stretched filaments (fig. 6*C*). These filaments and bubble voids are often stretched or aligned in one orientation. Based on normalized point-count totals, the HSA contains an average of 51.7 volume percent glass and 1.4 volume percent microlite-rich groundmass (fig. 5). The DIA and banded clasts contain a mix of both groundmass textures, averaging 10.6 and 37.8 volume percent glass and 51.5 and 37.8 volume percent microlite-rich groundmass in the DIA and banded clasts respectively.

The major lithologies, especially LSAS, all show some glomerophenocrystic plagioclase, pyroxene, olivine, or symplectite olivine. The FGGI minor lithology contains notable pervasive skeletal plagioclase crystals, with a more equigranular texture than that observed in the major lithologies. Quartz-rich inclusions are marked by polycrystalline plagioclase and quartz masses as large as several mm in diameter, surrounded by a microlitic groundmass of quartz, plagioclase, orthopyroxene, and glass. Patches of granophyric texture are present. Graphic textures in plagioclase, hornblende, orthopyroxene, and clinopyroxene are occasionally present in samples from the major lithologies.

Diffuse to sharp banding representing various stages of magma-mingling and hybridization is evident in Augustine deposits at all scales, from large boulders to micro-scale textures seen in thin section (fig. 2*B* to 2*E*). Heterogeneity is

also observed from deposits from each phase of the eruption, in variations in glass color (tan to colorless), phenocryst abundances (appendix 2), and disequilibrium textures.

Whole-Rock Compositions

Systematic differences in whole-rock composition among the products of the 2006 eruption mirror the macroscopic differences first identified among lithologies in the field. Lavas and pyroclasts from the 2006 eruption range from 56.5 to 63.2 weight percent SiO_2, fully spanning the andesite range and extending slightly into both the basaltic-andesite and dacite fields (fig. 7; table 3). For simplicity we refer to them all as andesite. The samples range from 0.7 to 1.1 weight percent K_2O and straddle the low-K to medium-K boundary, which is low by comparison with other Aleutian arc lavas, but not with convergent margin lavas worldwide (Gill, 1981). Analyzed LSAS samples range from 56.5 to 58.7 weight percent SiO_2 and DLSA from 56.4 to 59.3 weight percent SiO_2. HSA samples span 62.2 to 63.3 weight percent SiO_2, though all but one sample cluster near 62.2 weight percent. DIA and banded samples fall between and partially overlap these ranges. Fine-grained gabbroic inclusions (FGGI) range from 54.5 to 57 weight percent SiO_2 and fall along a lower K_2O trend in comparison to other 2006 samples. A single sample, initially identified as HSA in the field, falls along this low-K trend as well and is termed "low-K HSA" (fig. 7). Two quartz-rich inclusions have 73 and 76.3 weight percent SiO_2 and 2.2 to 3.0 weight percent K_2O, which is much higher than other Augustine samples.

Major- and trace-element abundances in 2006 samples plot along linear trends on silica variation diagrams, except for inclusions and the low-K HSA sample (figs. 8, 9). For example, the R-squared value of a linear fit to the K_2O versus SiO_2 plot shown in fig. 7 is 0.99. Slight deviations from the linear trend exist at the mafic end in MgO and especially Cr. In Cr, the linear array appears to split from the most mafic LSAS towards increasing silica. Cr values for the majority of LSAS and about half of DLSA fall 10 to 20 ppm below the dominant array defined by HSA, DIA, banded, and some DLSA (fig. 9). At the silicic end, HSA samples have, for certain trace elements (for example, La and Nd), a larger and extend over a range that appears to fall outside the tight linear array formed by the rest of the 2006 rocks (fig. 9). Interestingly, the deviations appear to correlate with time

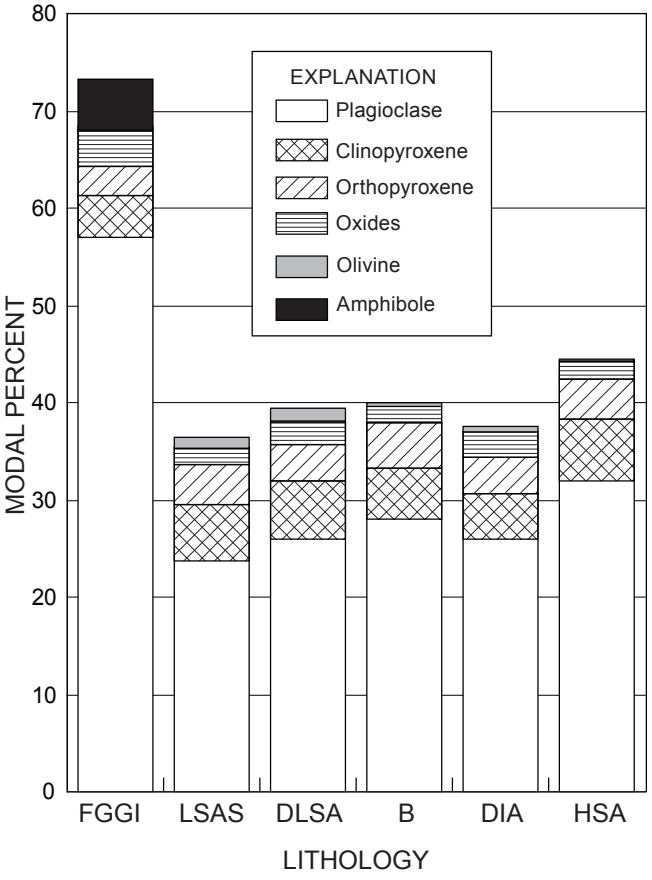

Figure 4. Modal percents of major and minor phenocryst phases in Augustine 2006 eruption deposits. HSA is high-silica andesite, DIA is dense intermediate andesite, B is banded, DLSA is dense low-silica andesite, LSAS is low-silica andesite scoria, and FGGI is fine-grained gabbroic inclusions. Modal percents are averages from point counts of at least 1,000 points per slide, normalized after removing void space counts. Groundmass percentages make up the balance to 100 percent. Oxides include all opaque minerals.

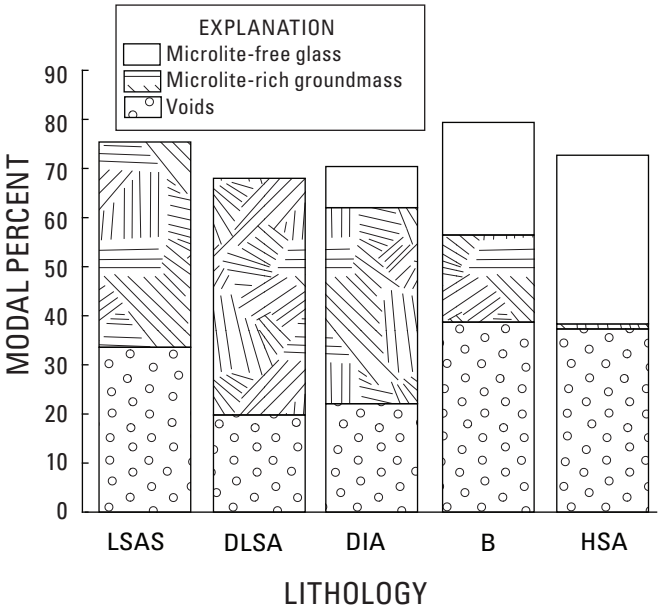

Figure 5. Average modal percentages of groundmass textures and void space (that is, vesicularity) for the five major lithologies from the Augustine 2006 eruption. Abbreviations as in figure 4.

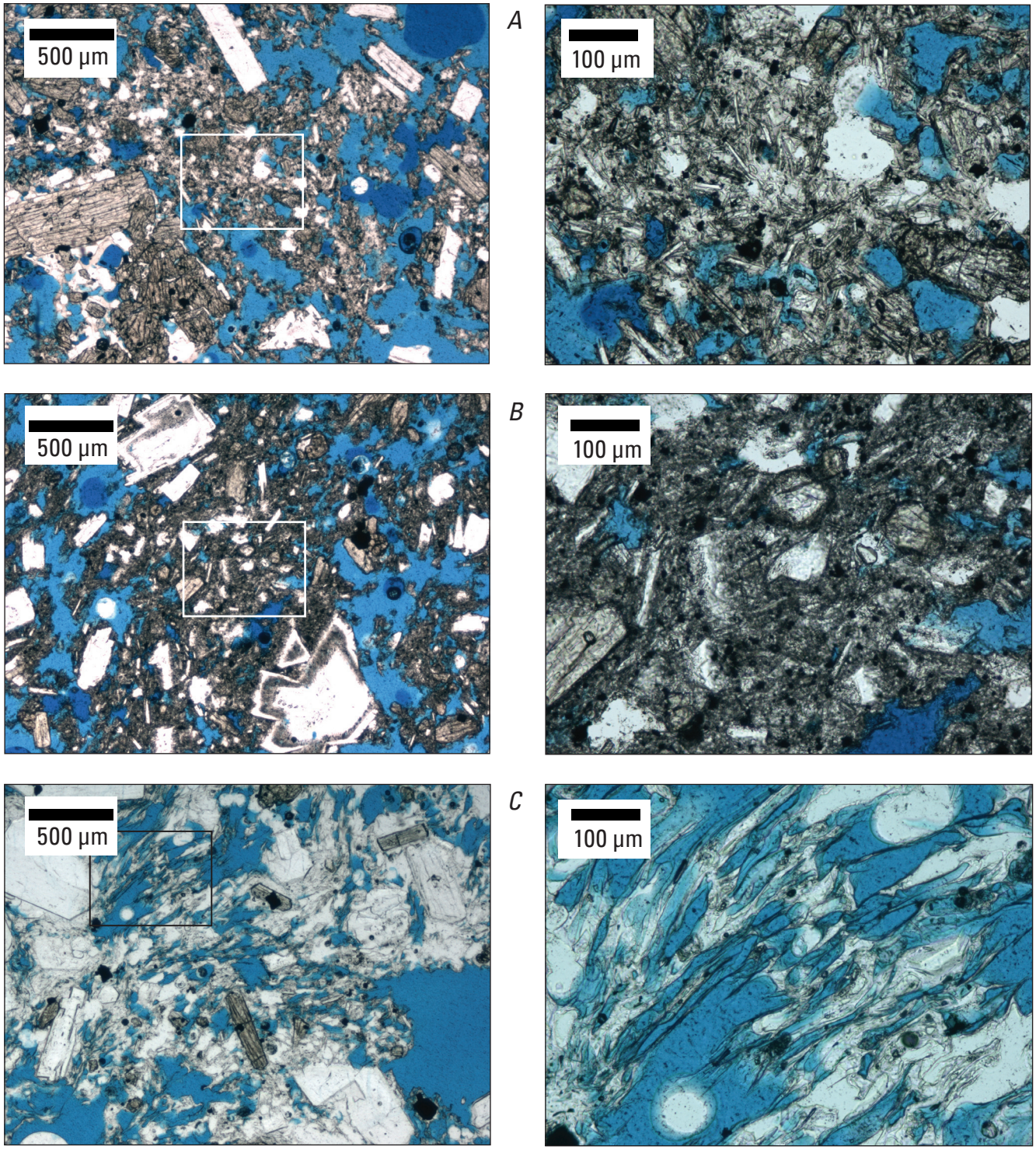

Figure 6. Transmitted-light photomicrographs showing groundmass textures of major Augustine 2006 lithologies. All samples have been impregnated with blue epoxy. Boxes in left-hand panels indicate regions that are enlarged in right-hand panels. *A,* Microlite-rich groundmass from sample 06AUMRT007b (low-silica andesite scoria) erupted during the explosive phase. *B,* Microlite-rich groundmass from sample 06AUMRT001b (dense low-silica andesite) erupted during the continuous phase. *C,* Nearly microlite-free clear glass from sample 06AUMC009p1 (high-silica andesite) erupted during the continuous phase.

of eruption: all explosive-phase low-silica andesites fall along the low-Cr trend, and all low-Nd high-silica andesites were erupted during the explosive phase.

To emphasize small trace-element differences within the 2006 ejecta suite, we have normalized their compositions to an average LSAS composition (fig. 10). This normalization scheme is preferred here because we focus on the changes across the 2006 eruption products only, rather than a broader comparison between different volcanic systems or across different tectonic settings. Normalization to the most primitive magma erupted allows us to look in greater detail at the relationships of the 2006 products to one another within the single eruption sequence. Trace element values for DLSA and LSAS samples are very similar (fig. 10*A, B*). HSA samples show elevated concentrations of large ion lithophiles (LILE), the U, Th, Pb group, and HFSE (Zr, Hf, Nb, Ta) and lower concentrations of compatible trace metals relative to the LSA samples. HREE (Eu through Lu) concentrations in the HSA are similar to those of LSAS and DLSA samples, whereas LREE (La through Sm) show a progressively greater enrichment with decreasing atomic number (fig. 10*C*). DIA and banded trace-element concentrations span a range bracketed by HSA and LSA (fig. 10*D*). Lower silica gabbroic inclusions show marginally higher concentrations of MREE and lower concentrations of LILE, HFSE, and Th, U, and Pb compared with LSA and HSA samples (fig. 10*E*). Gabbroic inclusions are also unusual in their lower concentrations of transition metals, despite their lower SiO_2 content. Two silicic inclusions are off the predominant range, and have very high concentrations of MREE, HREE, and some (but not all) of the LILE.

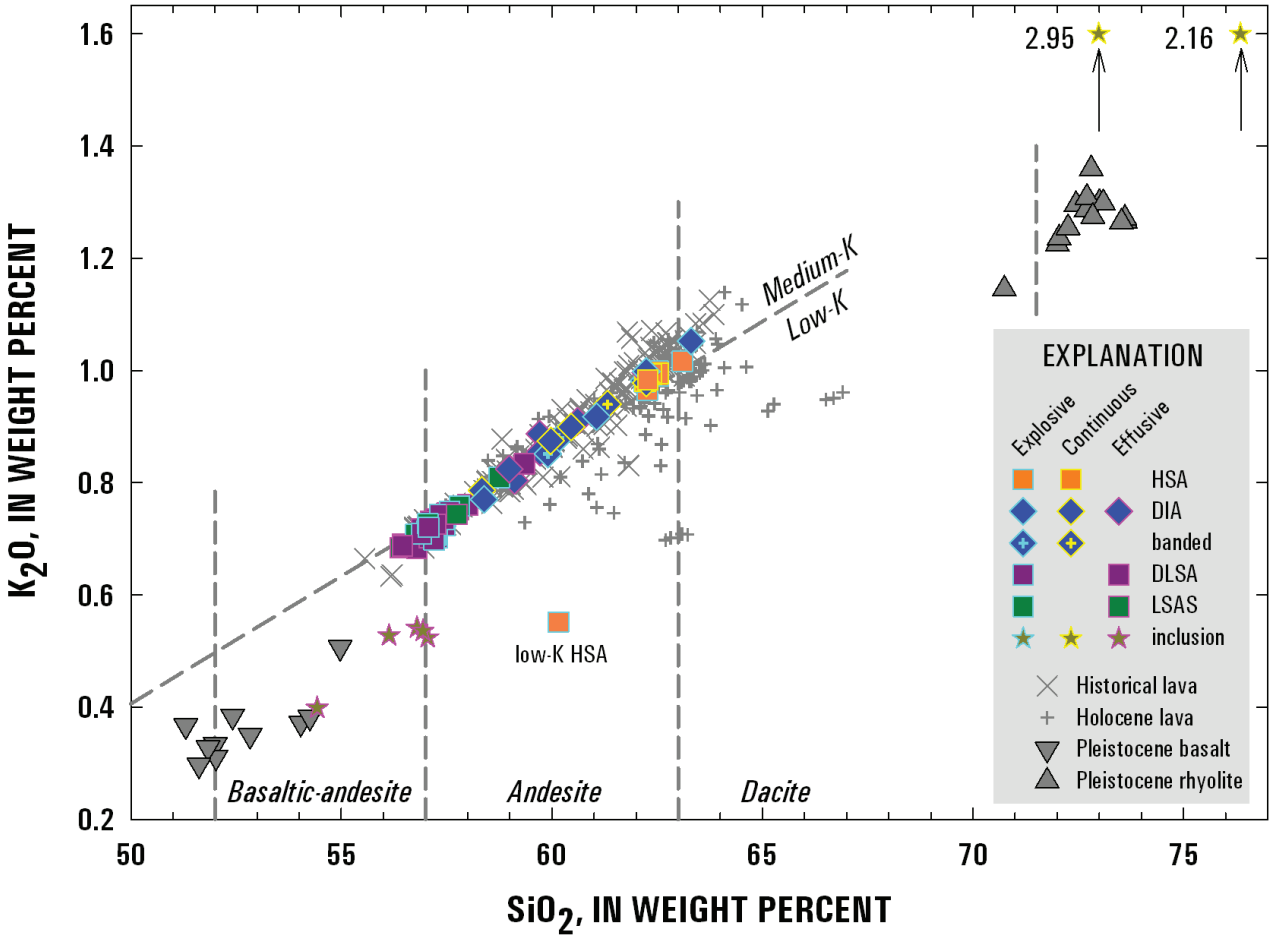

Figure 7. K_2O-silica variation diagram of Augustine whole-rock samples from Pleistocene to present. All 2006 data, and some of the pre-2006 historical, Holocene, Pleistocene basaltic rock, and Pleistocene rhyolite data are from this study; additional data are from Roman and others (2005), Daley (1986), Johnson and others (1996), C. Gardner (unpublished), C. Nye and J. Begét (unpublished), and K. Wallace (unpublished). Diagonal line shows boundary between low-K and medium-K andesites of Gill (1981). Vertical compositional boundaries from LeMaitre (1991).

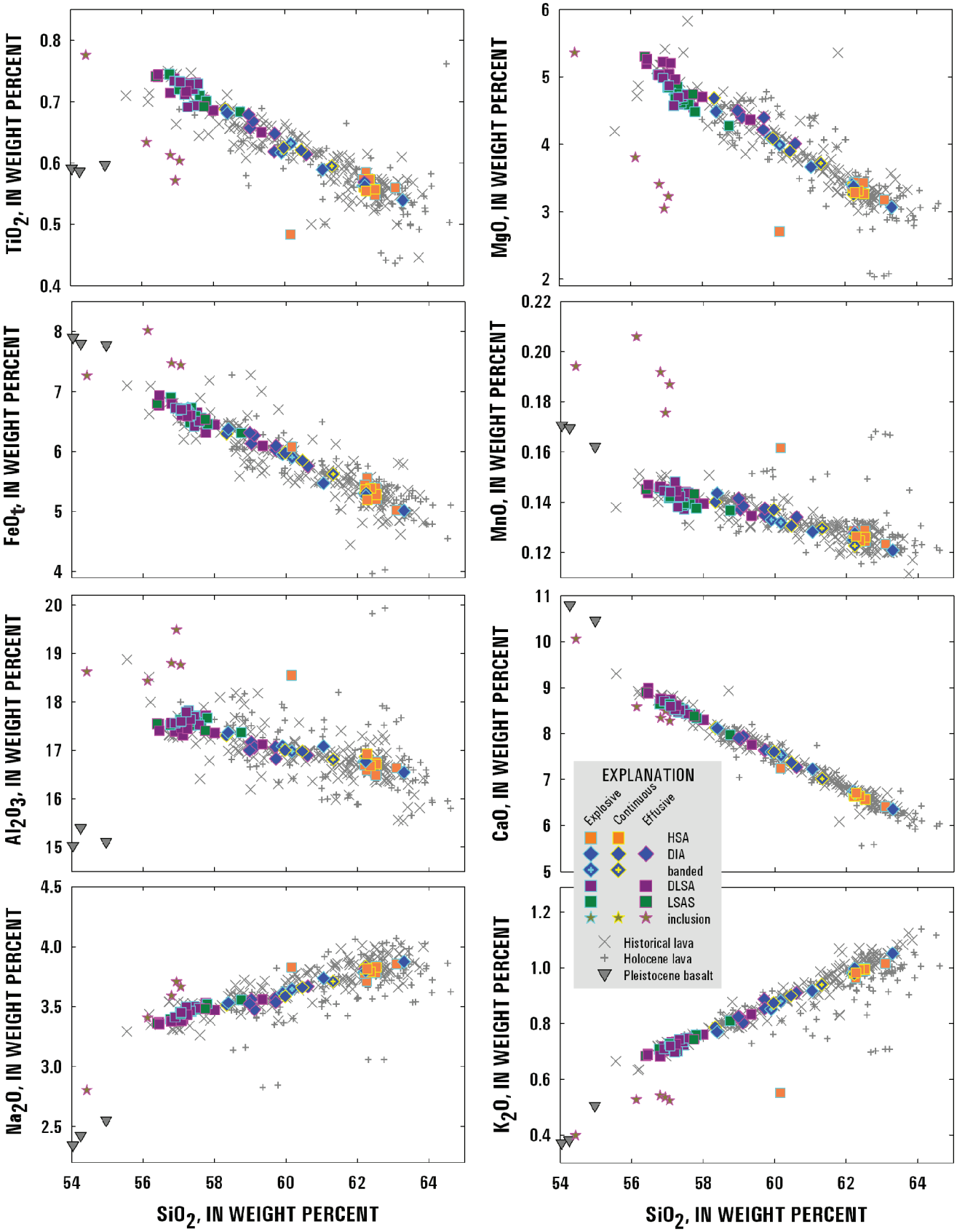

Figure 8. Major-element silica variation diagrams for Augustine 2006 samples (excluding quartz-rich inclusions). Data sources for pre-2006 samples are the same as for figure 7. FeO_t is total iron analyzed as FeO.

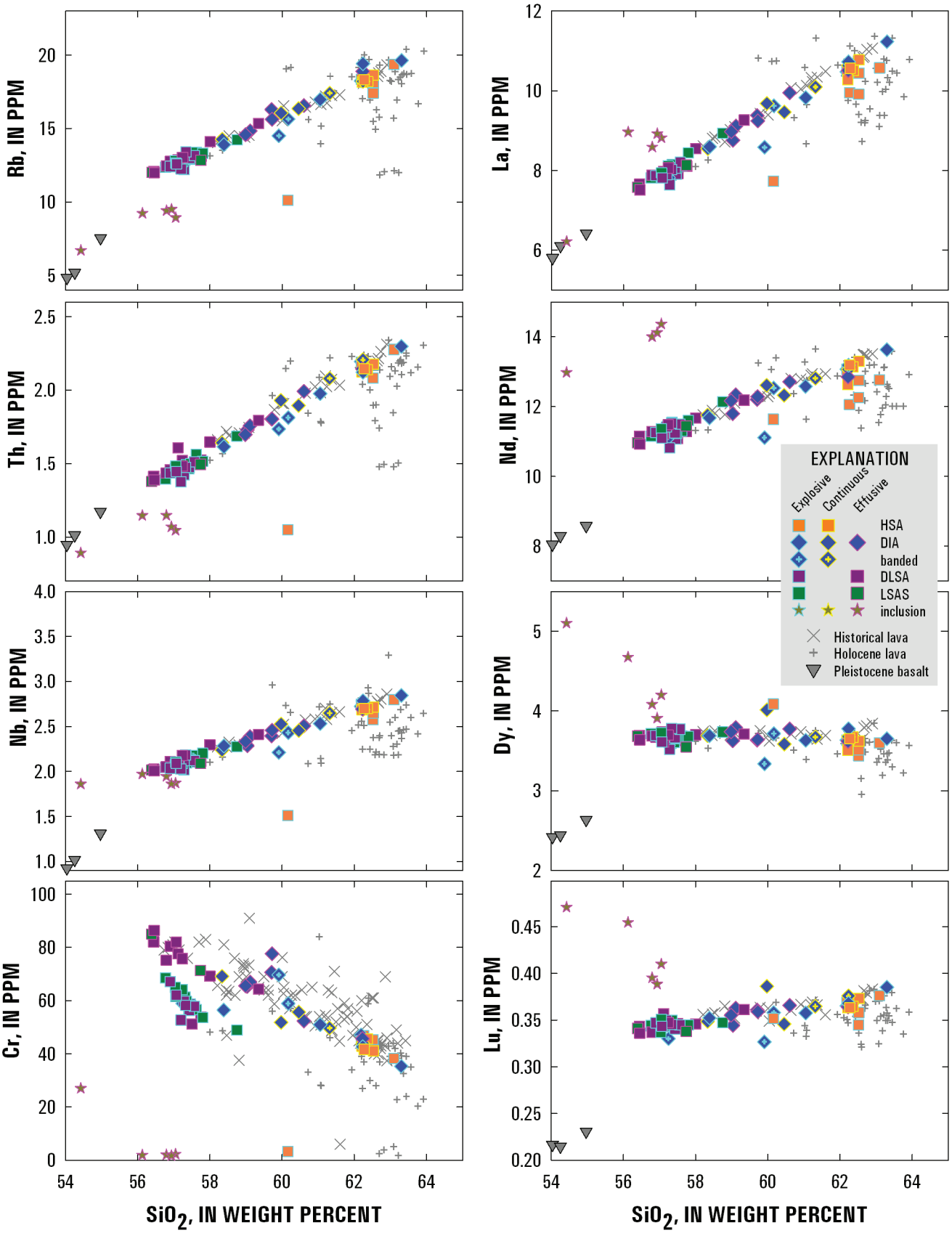

Figure 9. Trace-element silica variation diagrams for 2006 samples (excluding quartz-rich inclusions). Data sources for pre-2006 samples are the same as for figure 7.

Compositional Trends, Pleistocene to Present

The overwhelming majority of all analyzed samples from Augustine span 56 to 64 weight percent SiO_2, similar to the range of compositions produced in 2006 (fig. 7). Eruption products from 2006 yield trends on major and trace-element variation diagrams that broadly overlap those shown by products of Holocene and especially historical eruptions of the volcano, though 2006 samples are less dispersed about the linear trend than those erupted before 2006 (figs. 7 to 9).

In comparison with the 2006 eruptive products, other samples from historical eruptions are similar (figs. 7 to 9), yet tend to be slightly elevated in K_2O and Na_2O, especially at the high-silica end. Late Holocene (prehistoric) samples have compositions that are broadly similar to historical lavas, yet they extend to significantly lower middle and heavy REE abundances (fig. 10*F*).

The only known Augustine products to fall outside the basaltic-andesite-to-dacite spectrum are from the only Pleistocene outcrop on the island, which exposes rhyolitic pumice (71 to 74 weight percent SiO_2) and basaltic hyaloclastite (51 to 55 weight percent SiO_2), apparently erupted coevally (Plank and others, 2006; Waitt, this volume). Both mafic and silicic samples from this deposit fall along a lower K_2O trend than those from Holocene Augustine eruptions (fig. 7). Compared to typical Augustine products, the Pleistocene basalts have lower concentrations of all REE, LILE, and HFSE (fig. 10*F*). The rhyolites are higher in LILE, LREE, U, Th, and Pb, but their concentrations of MREE and HREE are dramatically lower than the andesites and are about as low as seen in the coerupted basalts.

Phase Descriptions and Compositions

Here we present an overview of the main phases found within rocks from the 2006 eruption. Phase compositions are illustrated in plots, and representative analyses are given in tables 3 to 6. The complete datasets for olivine, oxides, and pyroxenes are given in Tilman (2008). The full glass and plagioclase datasets are presented in electronic supplementary appendix 3 and 4, respectively.

Groundmass Glass

We analyzed matrix (groundmass) glass from most lithologies found within pyroclastic and lava flow deposits, as well as in tephra samples from January 13, 14 and 17 and the 1986 eruption (table 4; fig. 11). The high concentrations of plagioclase, pyroxene, and oxide microlites in the groundmasses, especially of the more mafic samples, made glass analysis difficult. During probe sessions, we identified glass pools within microlite-rich samples using a combination of backscattered electron images (BSE) and reflected light, but the results of some analyses indicate that the beam was at least partially on crystal(s) in addition to glass. Clearly anomalous analyses were deleted from the dataset presented here, though some analytical scatter is still likely the result of the electron beam hitting other phases. In contrast to the microlite-rich low-silica andesites, the groundmass of more silicic lithologies, comprising glass in the HSA pumice and lighter bands in banded clasts, is relatively microlite-poor, making it easier to find clean glass to analyze. This contrast resulted in an overrepresentation of silicic samples within our groundmass-glass dataset.

The entire glass dataset spans a range of SiO_2 contents from 66 to nearly 80 weight percent; matrix glasses from tephra and flow-deposit clasts span a similar range (fig. 11). All groundmass glass analyses represent melt that has evolved significantly away from the bulk rock compositions, reflecting the relatively crystal-rich nature of the 2006 eruption products. Within this range, however, the groundmass glass compositions show more than one simple trend, as a function of lithology and timing of deposition.

On an SiO_2-K_2O variation diagram, low-silica andesite scoria glasses from the explosive phase form a linear but discontinuous trend that includes dacitic (66 to 73 weight percent SiO_2) and rhyolitic (76 to 78 weight percent SiO_2) compositions (fig. 11). These glasses show a trend of steadily increasing K_2O with SiO_2, from ~1.5 to 3.0 weight percent K_2O between 66 and 78 weight percent SiO_2. Although "normal" groundmass glass within the low-silica andesite clasts shows a gap between 74 and 76.6 weight percent SiO_2, glass pools from within a plagioclase-rich clot in the LSAS span this range and fall along the same trend as other LSAS glasses. Dense low-silica andesite clasts have glass compositions similar to the low-silica end of the LSAS range.

Glasses from HSA clasts and the lighter portions of banded clasts all form a tight cluster on variation diagrams, with most of these glasses ranging from 74 to 77 weight percent SiO_2. Interestingly, these glasses have 1.5 to 2.6 weight percent K_2O, and fall slightly below the trend found in the low-silica andesite groundmass glass analyses (fig. 11). For other oxides, higher silica clasts generally fall along the same trend as the lower silica lithologies (not shown). The compositions of this group of samples do not vary with eruptive phase (table 4).

The few glass analyses from dense intermediate andesite clasts either fall into the low-silica end of the LSAS trend or in the HSA-dominated cluster.

The single low-K HSA clast contains rhyolitic glass with correspondingly low K_2O, from 1.1 to 1.6 weight percent (fig. 11). This sample also has the most silica-rich glasses analyzed, ranging from 76.7 to 79.7 weight percent. These glasses are not obviously different from other 2006 glasses in the abundances of other oxides. Groundmass glass from two fine-grained gabbroic inclusions trend toward these low values of K_2O, and partially overlap with HSA glasses (fig. 11).

Glass analyses from a distal tephra sample collected from an early explosion on January 13, 2006, follow the same trend as LSAS clasts. Lapilli clast samples from proximal tephras emplaced on January 13 through 17 were sorted according to lithologies assigned to flow samples (Wallace and others, this volume); glasses from these clasts fall along the same compositional trends as those from flow-deposit clasts (appendix 4).

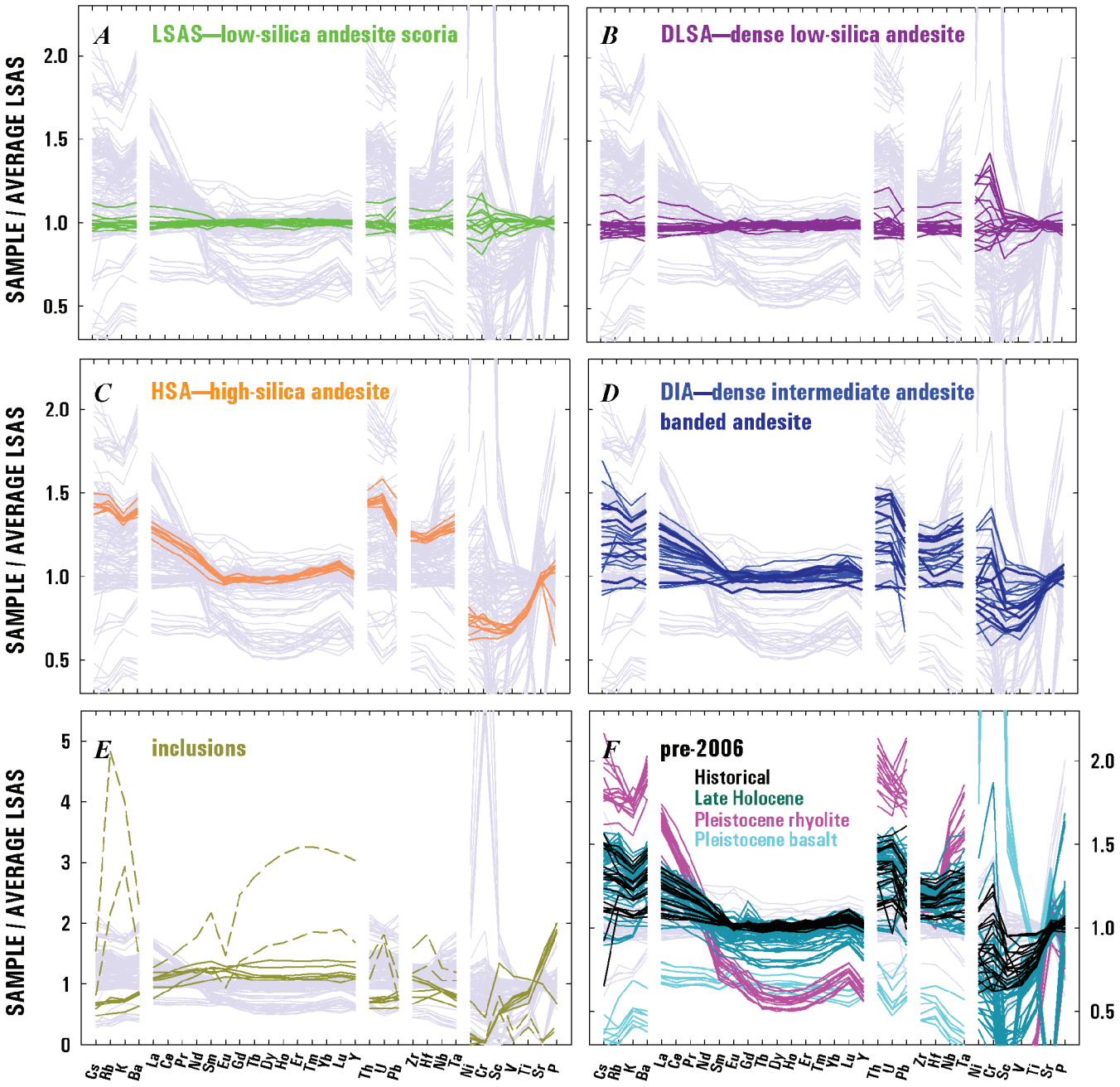

Figure 10. Incompatible-element variation diagrams showing trace-element abundances for 2006 and pre-2006 Augustine samples, normalized to the average composition of 2006 low-silica andesite scoria. Thin gray lines show the entire suite of measurements, and the colored lines in each panel show data highlighted for individual lithologies and ages. *A*, Low-silica andesite scoria. *B*, Dense low-silica andesite. *C*, High-silica andesite. *D*, Dense intermediate andesite and banded. *E*, Fine-grained gabbroic inclusions and low-K high-silica andesite (solid lines), and quartz-rich inclusions (dashed lines). *F*, Pre-2006 Augustine samples. Data are from this study, C. Nye and J. Begét (unpublished), and K. Wallace (unpublished).

Plagioclase

Plagioclase is the dominant mineral phase in the major lithologies with 24 to 32 volume percent phenocrysts and as much as 47 volume percent microlites in the groundmass (fig. 4; table 2). Phenocrysts are generally euhedral and tabular and range from 0.2 to 8.0 mm in size. In contrast, fine-grained gabbroic inclusions contain as much as 64 volume percent plagioclase. The FGGI phenocrysts have coarsely sieved interiors, showing extensive dissolution.

Five distinctive types of plagioclase phenocrysts are recognized in the major lithologies of the 2006 Augustine eruption on the basis of texture and composition. Type 1 plagioclases are texturally homogeneous, oscillatory zoned, have subtle compositional variations (fig. 12*A*), and are almost exclusively found within high-silica andesite pumices. They are optically clear with rare subtle dissolution surfaces, and contain almost no glass and mineral inclusions. Electron probe microanalysis (EPMA) profiles show fine oscillations superimposed on a weakly reverse compositional trend from An_{48} in the cores to An_{54} at the rims (fig. 12*A*). Type 2 plagioclases are oscillatory-zoned, with as much as 20 mole percent anorthite compositional variations across the zones (fig. 12*B*). Despite textural similarity to Type 1, Type 2 phenocrysts are characterized by larger chemical variations. Their EPMA profiles show abrupt jumps in An content corresponding to calcic zones at major dissolution surfaces. Each jump shows the same asymmetrical rim-ward pattern: an An_{48-54} plateau truncated by a dissolution surface, a sudden increase in An content as much as 80 mole percent, and a gradual return to the An_{48-54} plateau. Isolated glass inclusions and acicular microlites of ortho- and clinopyroxene are also abundant near dissolution surfaces. Large phenocrysts usually contain 2-3 major dissolution surfaces and associated jumps in An content. Type 2 plagioclases are present in all lithologies, although they are more common in high-silica andesite as compared to more mafic products of the 2006 eruption. Type 3 plagioclases are sub- to anhedral and are made up of oscillatory-zoned cores, surrounded by An_{70-90} rims with a distinctive texture formed by a network of profuse, interconnected inclusions of glass and microlites, commonly referred to as resorption rims, sieved texture, or "dusty zones" (Browne and others, 2006; Nakamura and Shimikata, 1998; Tsuchiyama, 1985). Type 3 cores are typically similar to those of Types 1 and 2, though larger Type 3 crystals may have more calcic cores. The resorption rims have the same principle characteristics as the calcic zones in Type 2 plagioclases, but they have higher An content (as much as 90 mole percent), more inclusions and are greater in width (fig. 12*C*). The proportions of glass and mineral inclusions in the resorption rims decrease conspicuously toward the boundary with the groundmass. Interestingly, glass inclusions

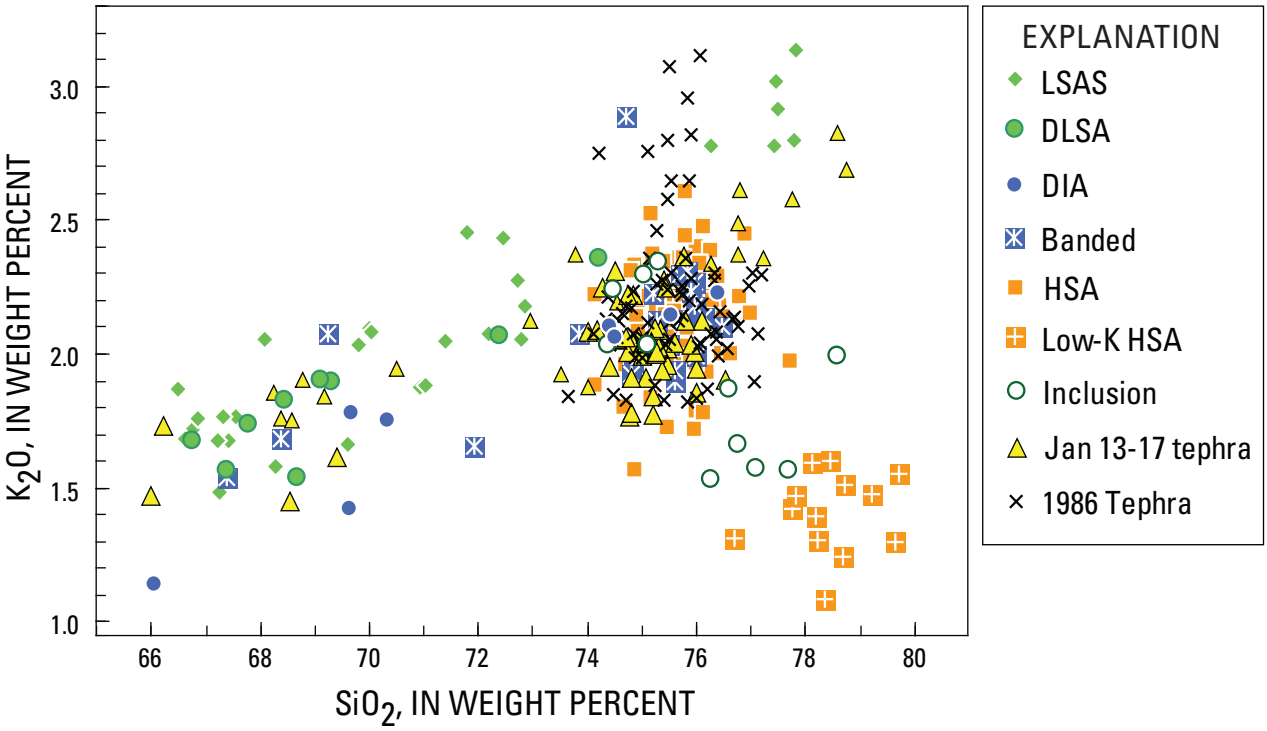

Figure 11. Groundmass-glass analyses from the Augustine 2006 lithologies, compared with select analyses from 2006 tephra fall deposits from the January 13–14 and January 17 explosions. Also plotted for comparison are analyses from 1986 tephras (P. Izbekov, unpublished data).

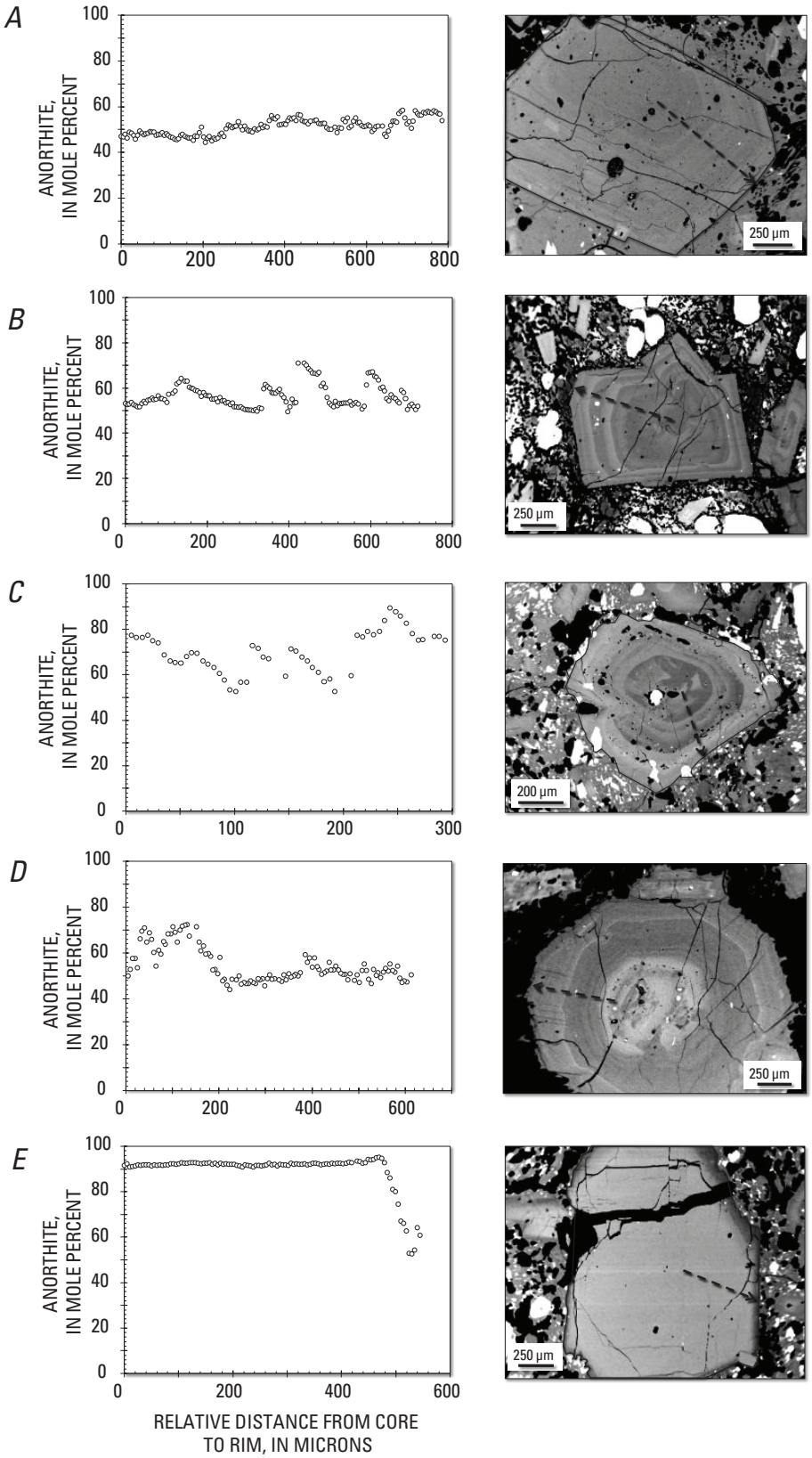

Figure 12. Back-scattered electron (BSE) images and corresponding profiles showing anorthite content of five major plagioclase phenocryst types identified in 2006 eruption deposits.

in the resorption rims are often vesicular. Type 3 plagioclases are present in all lithologies, although in high-silica andesite the resorption rim is surrounded by an oscillatory-zoned rim 10-150 microns wide, whereas in low-silica andesites the resorption rim contacts groundmass, with An_{65-75} composition at the contact. Type 4 plagioclases are compositionally and texturally heterogeneous, with calcic cores surrounded by oscillatory-zoned rims (fig. 12*D*). The cores commonly contain inclusions of glass and microlites, as well as patches of An_{48-54} plagioclase. The composition of cores reaches An_{90} and overlaps with the composition of resorption rims in Type 3 plagioclases. Type 4 plagioclase crystals have oscillatory rims that overlap in composition with Type 1 phenocrysts. Type 4 plagioclases are found predominantly in high-silica andesite. Type 5 plagioclase phenocrysts consist of euhedral, compositionally and texturally homogeneous An_{92-94} cores surrounded by oscillatory-zoned rims (fig. 12*E*). Type 5 plagioclases are rare, but found in all lithologies. Widths of the outermost oscillatory-zoned rims in high-silica andesites often exceed 150 to 200 micron, whereas in low-silica andesites they are significantly narrower (20–30 microns).

All major lithologies are characterized by similar ranges of phenocryst compositions of An_{45-90}, with a primary mode at ~An_{54} (fig. 13). The second mode at >90 mole percent in compositions of DLSA phenocrysts is due to the large number of Type 5 plagioclase analyses (fig. 13*D*). Plagioclase microlites have the same composition as the outermost rims of phenocrysts in all lithologies. Composition of microlites in HSA and DIA are nearly the same (An_{50-54} and An_{50-55}, respectively) and overlap with the composition of the Type 1 phenocrysts. Compositions of microlites in LSAS and DLSA are An_{57-73} and An_{64-77}, respectively, which both overlap considerably with the composition of calcic zones in Type 2 plagioclases, as well as of resorption rims in Type 3 plagioclases. Textural and compositional characteristics of plagioclases from products of the 2006 eruption are the same as those in products of 1964, 1976, and 1986 eruptions. For example, Type 2 oscillatory-zoned plagioclases from all four eruptions show impressive similarity of their EPMA profiles characterized by the "plateau" composition at An_{48-54} (fig. 14).

Pyroxenes

Although both are present in all lithologies, clinopyroxene (average 5.6 volume percent) is slightly more abundant than orthopyroxene (4.7 volume percent on average; fig. 4, table 2). Pyroxene phenocrysts are generally unzoned, although orthopyroxene is often rimmed with clinopyroxene, which is particularly common in LSA lithologies. Orthopyroxene phenocrysts from all lithologies have an average composition of $Wo_2En_{65}Fs_{32}$ (fig. 15, table 5). High-Ca pyroxene phenocrysts are predominantly augite to diopside, with an average composition $Wo_{44}En_{41}Fs_{14}$. Pyroxene phenocrysts are typically tabular and less than 1 mm in length, but some phenocrysts as large as 5 mm were observed, especially in low-silica andesites.

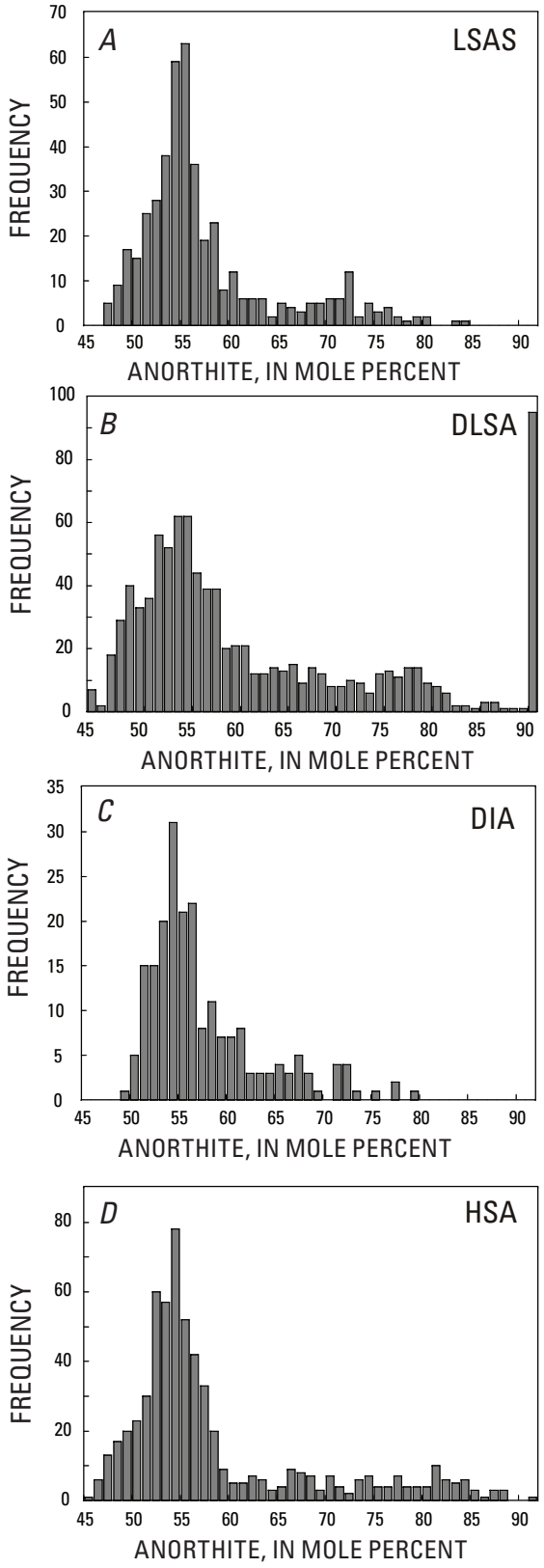

Figure 13. Histograms showing frequency versus anorthite content for spot analyses on plagioclase phenocrysts from the four major lithologies in 2006 eruption deposits. Abbreviations as in figure 4.

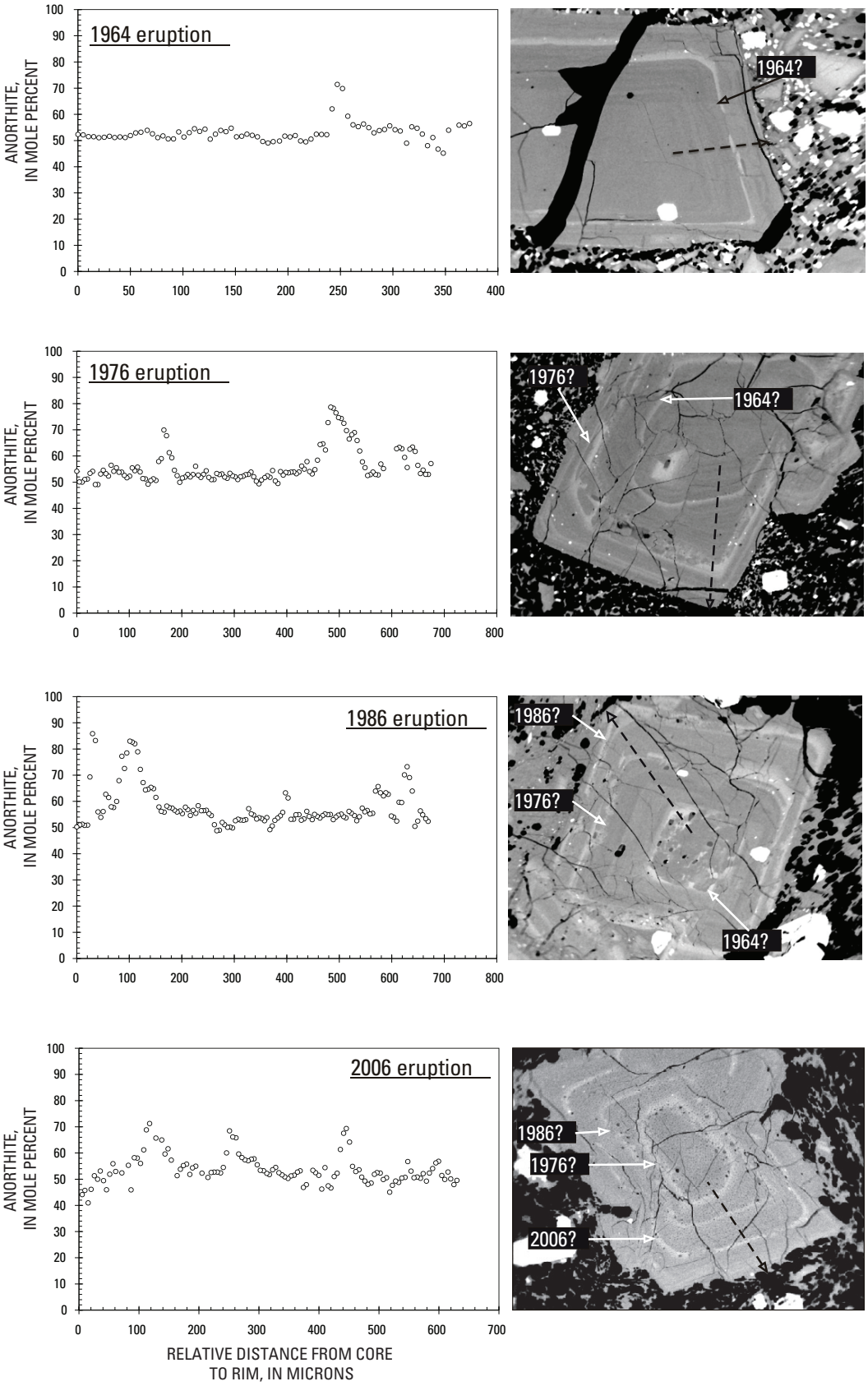

Figure 14. Back-scattered electron (BSE) images and anorthite-content profiles for representative plagioclase phenocrysts from the last four Augustine eruptions.

Orthopyroxene and clinopyroxene are both present in the 2006 deposits as microlites in the groundmass, and orthopyroxene is found in reaction rims on olivine. The compositions of the groundmass and rim pyroxenes are the same as the phenocrysts (fig. 15). Mg numbers range from 0.67 to 0.74 for orthopyroxene and 0.73 to 0.85 for clinopyroxene.

Fe-Ti Oxides and Geothermometry

All lithologies contain Fe-Ti oxides both in the groundmass and as inclusions in phenocrysts and reaction rims. Chromite is also present as inclusions in olivine phenocrysts. Fe-Ti oxides in the groundmass are commonly euhedral, less than 30 microns in width, and the pairs analyzed for this study are unzoned; often ilmenite and magnetite are present as touching pairs (fig. 16). Oxides present as inclusions in other minerals are almost always anhedral and are as large as 1 mm. DLSA clasts contain predominantly titanomagnetite, which often exhibits ilmenite exsolution lamellae. Ilmenite phenocrysts are rare in this lithology. The other lithologies also contain predominantly titanomagnetite, yet have more abundant ilmenite than DLSA.

Touching pairs in grain mounts used for geothermometry were groundmass grains as opposed to anhedral grains found as mineral inclusions. The f_{O_2} recorded by oxide pairs in 2006 Augustine magmas is approximately 2 log units above the Ni-NiO buffer (NNO), roughly equivalent to the rhenium-rhenium oxide (RRO) buffer (fig. 17). In investigating Mount Pinatubo magma, Rutherford and Devine (1996) experimentally confirmed that the QUILF algorithm overestimates temperatures by 30±5°C in magma with f_{O_2} near RRO

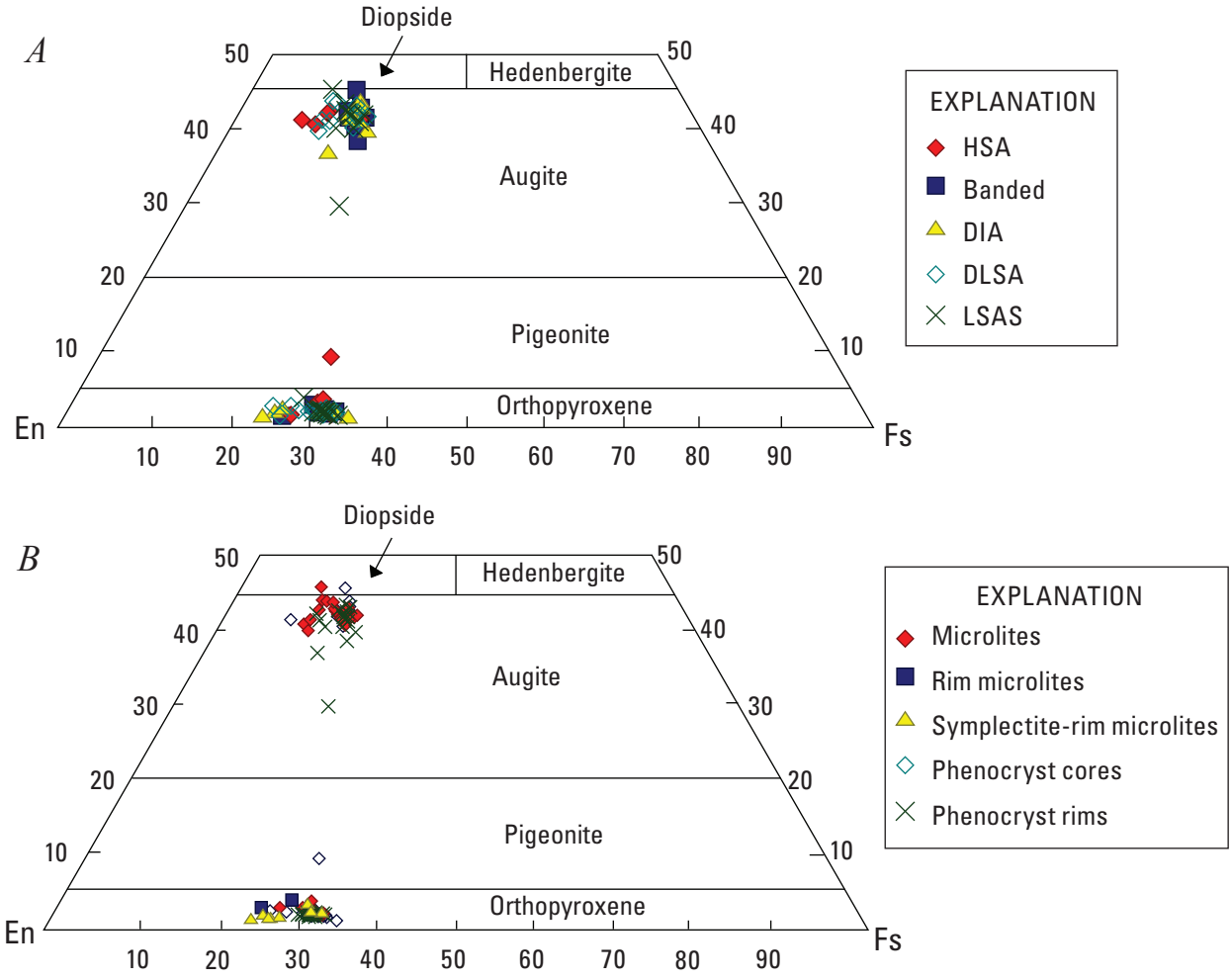

Figure 15. Classification diagram for pyroxene phenocrysts and microlites from the 2006 Augustine eruption. The apices of the ternary diagram represent 100 mol % of each pyroxene component as follows: En-enstatite, Fs-ferrosilite, and the top apex (not shown) represents wollastonite (Wo). Symbols represent single point analyses from rim and core of individual phenocrysts. Abbreviation of lithologic types as in figure 4: *A*, Pyroxenes sorted by lithology. *B*, Pyroxenes sorted by type. Rim pyroxene indicates pyroxenes found in the pyroxene-rimmed olivines. Symplectite pyroxene indicates pyroxenes found either in a symplectic olivine reaction rim or a symplectic pseudomorph.

because this is outside the limits of the calibration of Andersen and others (1993). Calculating the temperatures using other geothermometer algorithms (for example, Ghiorso and Evans, 2008), regardless of the method used to estimate the mol fractions of ulvospinel and ilmenite (for example, Stormer, 1983), all result in overestimations of the temperature, relative to the findings of Rutherford and Devine (1996). Thus, the temperature estimates included here have been decreased by 30°C from the original QUILF estimate.

Results using the QUILF algorithm (Andersen and others, 1993) indicate that LSAS was erupted at temperatures from 825 to 968°C (average of 904°C, one standard deviation of 47°C, n = 12) and HSA from 811 to 868°C (average of 838°C, one standard deviation of 14°C, n = 20; table 6 and fig. 17). Oxide pairs from banded and DIA clasts yield temperatures from 819 to 840°C and 829 to 853°C, respectively. A single oxide pair from a dense low-silica andesite sample yielded a temperature of 920°C. Oxide temperatures are consistent within each lithology type, but the HSA, banded, and DIA show a narrower range of temperatures, which are generally lower than those estimated for the low-silica andesites.

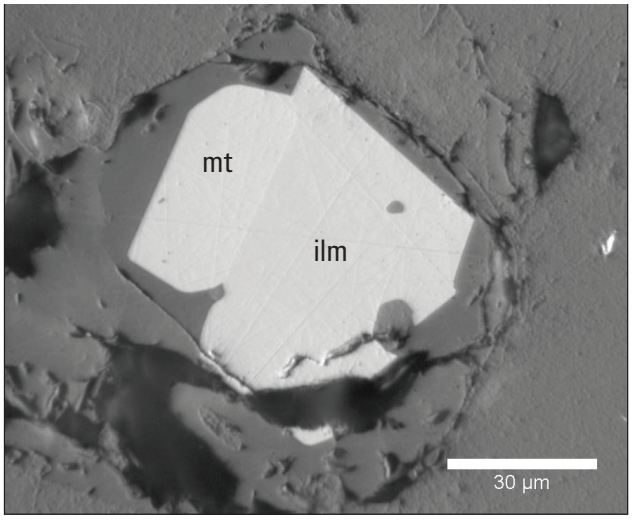

Figure 16. Back-scattered electron image of touching magnetite-ilmenite pair separated from groundmass of high-silica andesite sample 06AUMLC004c1.

Olivine

Olivine phenocrysts are present in all lithologies but are most abundant in the low-silica andesites, with 1.3 volume percent in DLSA and 1.0 volume percent in LSAS samples (fig. 4; table 2).

There are four main textural variations in the olivine phenocrysts. Type 1 are sub–to euhedral phenocrysts with no reaction rims (fig. 18*A*). They have core compositions that average 84 mole percent forsterite component (Fo_{84}) and are unzoned except for 5-10 micron, Fe-enriched (Fo_{73}) rims (table 7).

Type 2 olivines are sub- to anhedral phenocrysts that are resorbed and usually have thin (< 50 microns) reaction rims composed of orthopyroxene microlites (fig. 18*B*). Type 2 olivines are generally unzoned and have an average composition of Fo_{84}.

Type 3 olivines are subhedral with rims that consist of two concentric zones (fig. 18*C*). Inner rims can be as much as 500 microns thick, but average ~100 microns, and consist of fine-grained intergrowths of orthopyroxene and magnetite, commonly called a symplectite. This portion of the rim appears opaque in transmitted light, but the intergrowth texture is clearly visible in BSE images and x-ray maps. Outer rims are 50 microns thick, on average, and consist of orthopyroxene microlites. Some symplectite pseudomorphs after olivine are also present, and these are surrounded by orthopyroxene rims (fig. 18*D*). Orthopyroxenes in all rims have an average composition of $Wo_2En_{70}Fs_{28}$ (table 5), similar to the compositions of the phenocrysts and microlites. The titanomagnetite in the symplectite rims has approximately the same FeO, Al_2O_3, MnO, and MgO content and generally less TiO_2 and more Cr_2O_3 than in the titanomagnetite phenocrysts (table 6). Large (>600 micron) Type 3 olivines are normally zoned, with core compositions of ~Fo_{84} and rim compositions of ~Fo_{74}. Smaller Type 3 olivine crystals (<300 micron) are unzoned and have compositions that average Fo_{74}. Although HSA samples have the lowest percentages of olivine, those that are present are mostly Type 3.

Type 4 olivines are characterized by hopper and swallowtail habits (fig. 18*E* and 18*F*). They are often rimmed by thin jackets of orthopyroxene and occasionally by symplectite. Type 4 olivines are generally unzoned and have an average composition of Fo_{84}. They are most common in DLSA.

Amphibole

Amphibole is rare in all major lithologies and is unevenly distributed among different samples, with several grains in some thin sections and none in others, even within a single lithology. Rare amphibole phenocrysts in the low-silica and intermediate andesites have average lengths of 350 microns, are anhedral, and are typically surrounded by fine-grained reaction rims 40 to 100 microns thick (fig. 19*A*), composed of plagioclase, orthopyroxene, and oxides. In addition, pseudomorphs of amphibole, with the same mineralogy and texture as the reaction rims, are found in these lithologies, suggesting that amphiboles were once more abundant. Amphibole phenocrysts found in HSA clasts are sub- to euhedral, rarely surrounded by reaction rims, and larger than those in the more mafic rocks, with average lengths of ~600 microns (fig. 19*B*). Fine-grained gabbroic inclusions contain the highest modal abundances of amphibole, ranging to 10 volume percent. Amphiboles in this lithology are 0.6 to 2 mm in size, subhedral to anhedral, with plentiful reentrants and melt or plagioclase inclusions (fig. 19*C*). Analysis of a handful of grains from all lithologies yields compositions that straddle divisions between edenite, pargasite, hornblende, and tschermakite (table 8).

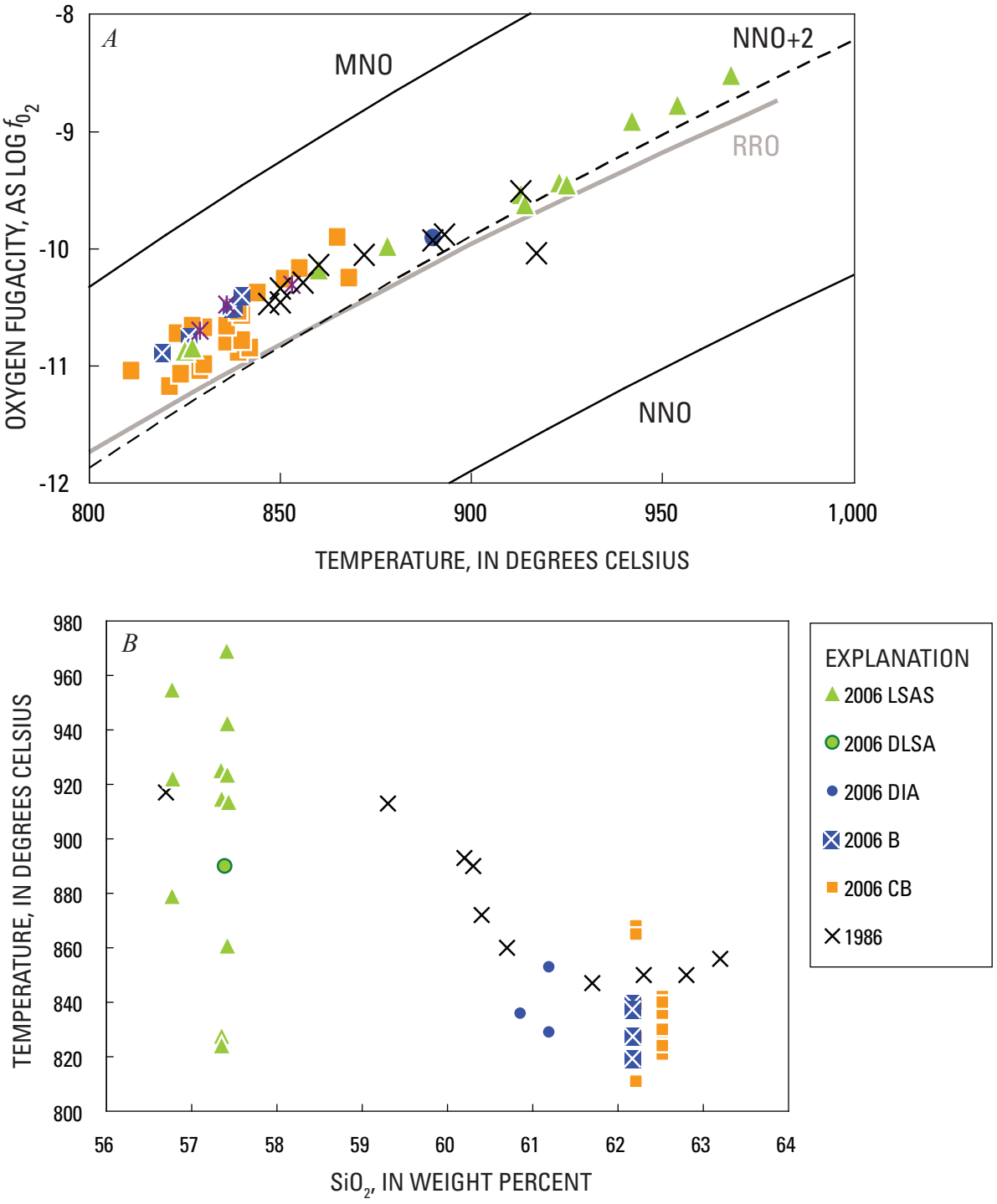

Figure 17. Temperature-composition relations of Augustine magmas and eruption products. *A*, Temperature and f_{O_2} for Augustine magmas as estimated from Fe-Ti oxide pairs. Rhenium-rhenium oxide (RRO) buffer was calculated using Pownceby and O'Neill's (1994) equation calibrated from 850-1250 K. *B*, Whole-rock SiO_2 content versus temperature. Abbreviations as in figure 4. 1986 data are taken from Roman and others (2005) and are averages of sample sets representing various rock types erupted during the explosive phase of the 1986 eruption. Temperature and oxygen fugacity for 2006 and 1986 samples calculated using QUILF (Andersen and others, 1993), with temperatures subsequently decreased by 30°C to account for overestimation at high oxygen fugacity (Rutherford and Devine, 1996).

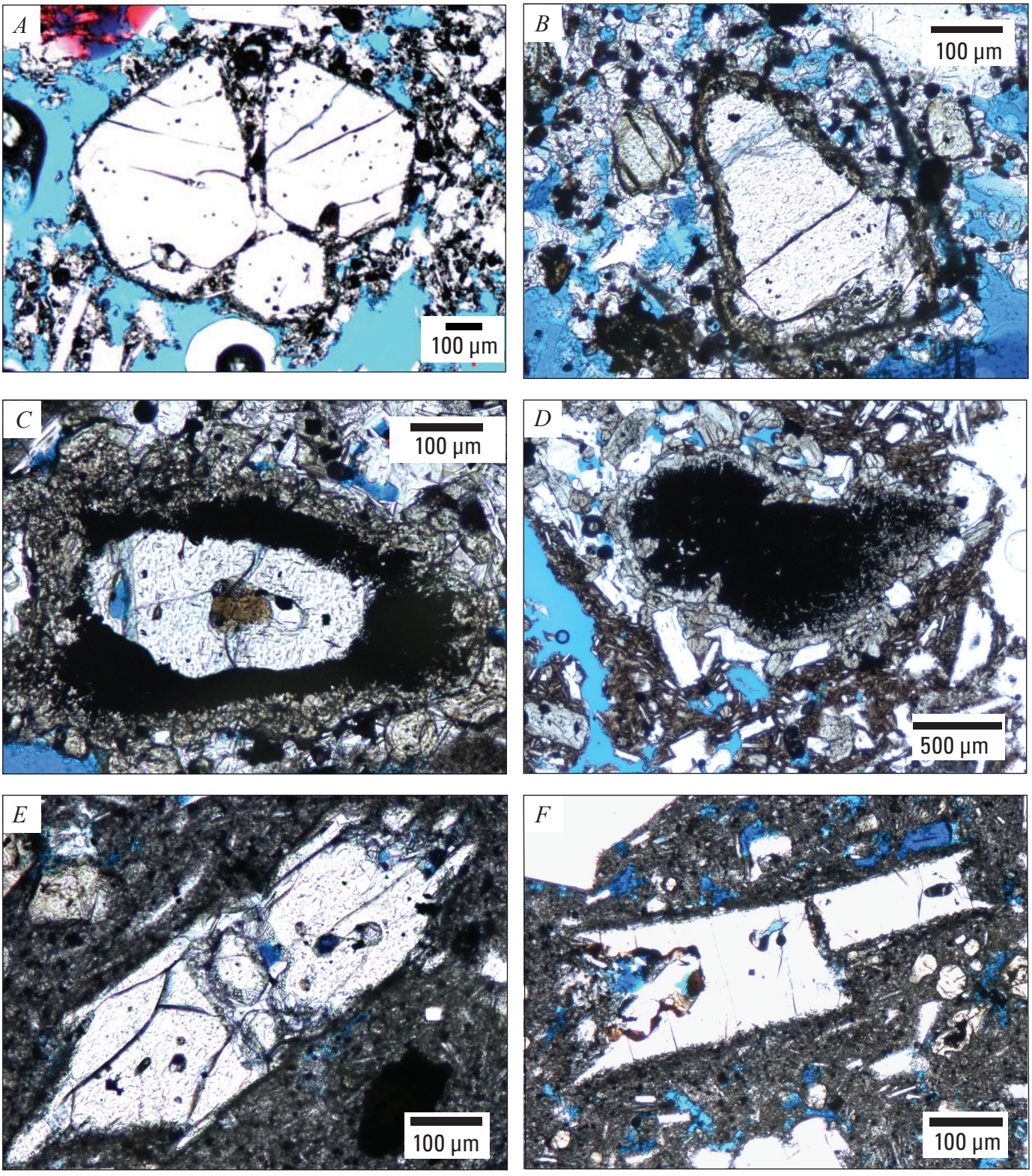

Figure 18. Olivine textures found in Augustine 2006 eruption deposits. All images are transmitted-light photomicrographs. *A*, Euhedral, unrimmed olivine from sample 06AUMC008a. *B*, Anhedral, pyroxene-rimmed olivine from sample 06AUKB002a. *C*, Symplectite-rimmed olivine from sample 06AUKB003. *D,* Symplectite olivine pseudomorph from sample 06AUMC008b.p3. *E*, Hopper olivine from sample 06AUKB003. *F,* Hopper olivine from sample 06AUMC005c.p3.

Accessory Minerals

Apatite is present throughout all lithologies, with the LSAand HSA containing greater modal abundances and the fine-grained gabbroic inclusions notably less (appendix 1). It consists of fine, needle-shaped crystals that are slightly green in plane polarized light. Crystals range in size from 6 to 200 microns and are most commonly found within larger plagioclase and clinopyroxene crystals, although some samples show fine apatite needles within the groundmass as well. Apatite inclusions are present in plagioclase with all textures, including "clean," melt-inclusion-rich, and coarsely sieved. Apatite needles in plagioclase, although not possessing a discernible orientation, preferentially occupy one or more oscillating zones within the plagioclase.

Anhydrite is a rare accessory mineral in these samples and is only found in a handful of thin sections and only within the banded, low-silica andesite scoria and fine-grained gabbroic intrusive lithologies. It is more abundant in the fine-grained gabbroic inclusions, but is still rare, with each thin section having only a couple of anhydrite crystals. Anhydrite was not found in samples collected after May 2006, but this is probably because of the extreme scarcity of anhydrite crystals and not a result of a change in crystal distribution. Primary

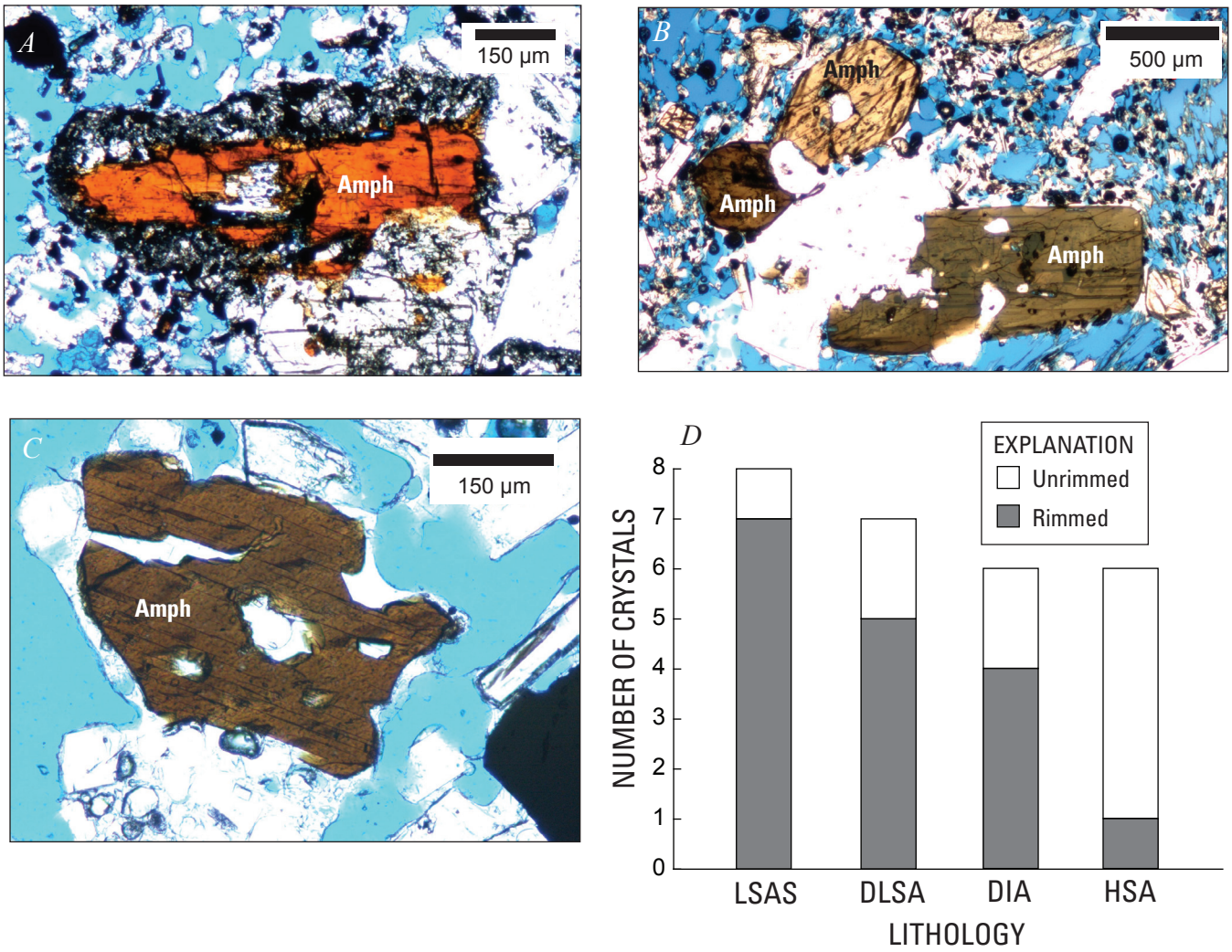

Figure 19. Transmitted-light photomicrographs and histogram of amphibole phenocrysts found in Augustine 2006 eruption deposits. *A*, Fine-grained reaction rim around amphibole phenocryst in DIA sample 06AUKB002a, collected from effusive-phase block-and-ash-flow deposit. *B*, Cluster of unrimmed, euhedral amphiboles from high-silica andesite sample 06AUMC004c, collected from Rocky Point pyroclastic-flow deposit. *C*, Resorbed phenocryst from gabbroic-inclusion sample 06AUMC013a, collected from effusive-phase block-and-ash-flow deposit. *D*, Histogram showing occurrence of rimmed and unrimmed amphibole in samples from the major lithologies of the 2006 eruption. Abbreviations are as in figure 4.

anhydrite crystals range from 200 to 600 microns long, are subrounded, and have a thin, dark-colored, fine-grained rim.

Discussion

Source and Origin of Erupted Magmas

The dominant geochemical signature of the 2006 Augustine magmas lies in the linear array of major oxides and trace elements, which is consistent with two-component magma mixing (figs. 7 to 10). The trends observed in the 2006 deposits mirror closely those observed from the historical Augustine eruptions and a significant proportion of Holocene magmas as well. The simplest explanation is that two-component mixing between the low-silica and high-silica andesites before and during the 2006 eruption creates the tight linear array in major and trace elements. However, complexities in petrogenesis of the LSA and HSA endmembers exist, and these will be discussed below.

High-Silica Andesite—Reinvigorated Resident of Shallow-Crustal Body

Several lines of evidence help place constraints on HSA storage conditions. Fe-Ti oxide geothermometry indicates that the high-silica andesite was stored at 838±14°C before eruption. Petrological results, including melt inclusion analyses (Webster and others, this volume), indicate that the HSA was stored at a depth of approximately 4 to 6 km below the surface. The presence of amphibole phenocrysts indicates that the magma resided at a depth equivalent to water pressures above amphibole stability. While the stability of amphibole has not been experimentally determined for this particular composition, we can look to other experimental studies on similar whole-rock compositions for comparison. Phase equilibrium experiments showed that amphibole was stable in the andesite (63.4 weight percent SiO_2) erupted in 1989–90 from Redoubt Volcano at pressures above 100 MPa from 850 to 875°C (Browne and Gardner, 2006). This is equivalent to depths equal to or greater than 3 to 4 km. The maximum dissolved water concentration measured in melt inclusions within high-silica andesite pyroxenes was 4 weight percent (with CO_2 below detection), equivalent to a pressure of 100 MPa (Webster and others, this volume).

Geophysical signals associated with the 2006 eruption are consistent with petrologic findings. Approximately 20 earthquakes, which occurred after the eruption in 2006 ended, were located beneath the summit at a depth of 4 km (Power and Lalla, this volume). One explanation for these post eruption events is that they occurred in response to pressure reduction after magma withdrawal and eruption from this depth. The majority of the high-silica andesite was erupted during the continuous phase, temporally coincident with a marked deflationary signal seen in the geodetic data. This signal has been modeled as being the result of a pressure decrease of a cylindrical body whose top is approximately 5 km below the surface (Cervelli and others, this volume).

It is likely that the HSA resided in this shallow-level reservoir for decades prior to eruption. The composition and phase assemblage of the 2006 high-silica andesite closely resemble those of the silicic end member of the 1976 and 1986 eruptions. For example, equilibrium plagioclase compositions in the host magma remained the same throughout the four most recent eruptions (1964, 1976, 1986, and 2006). This indicates relatively constant melt composition, temperature, and water pressure in the shallow-level host reservoir since at least 1964. For example, Type 2 oscillatory-zoned plagioclases from all four eruptions show impressive similarity of their EPMA profiles characterized by the "plateau" composition at $An_{48\text{-}54}$ (fig. 14). Increasing numbers of high-An "spikes" with each subsequent eruption suggest that some individual crystals may record multiple recharge events linked to these eruptions. Despite evidence for repeated recharge and magma mixing during each of these eruptions, the host magma has not changed significantly in composition. Also, the HSA phenocryst assemblage (table 2) shows less evidence of reaction and disequilibrium than the mixed, intermediate, and low-silica andesites. For example, fewer than than 10 percent of HSA plagioclases show visible resorption. This implies that if the shallow reservoir persists as a convecting liquid + crystal magma, then its volume must be large relative to newly arriving magma. On the other hand, if it persists as a largely solid crystal mush, then it is possible that during each eruption newly arrived magma "carves off" and mixes with only a portion of the mush.

Although the majority of chemical variations within the 2006 sample suite reflect two-component mixing, there is some deviation from the mixing trend for some trace elements, particularly the LREE. The 2006 HSA samples that diverge most from the mixing trend were erupted during the explosive phase and have LREE compositions similar to prehistoric Holocene lavas. They also diverge in composition from the pre-2006 historical lavas, which are similar to the majority of the 2006 lavas. If this difference is not simply an artifact of a limited dataset, then some of the HSA may be remobilized from a portion of the subvolcanic system, which is at least hundreds of years old. If material this old was erupted, we expect that it represents remobilized crystal mush and did not originate from a persistent liquid + crystal magma. This model is the best that fits both petrological and geophysical data available at this time.

Although the model for the HSA as derived from a crystal mush at 4 to 6 km fits the petrology and geophysical observations, the origins of the crystal mush itself are less well understood. It is tempting to assume that it is derived primarily by fractional crystallization of low-silica andesite remaining in the crust from previous eruptions. However, the trace-element data (fig. 9) argue against this in three ways. First, concentrations of REE heavier than Eu are the same as in the 2006 low-silica

andesite. Crystallization at ~100 MPa in these andesites is dominated by plagioclase, and because REE are incompatible, plagioclase crystallization should result in increased REE concentrations in the melt. At other Aleutian volcanoes, crystallization through the andesite and dacite range produces such increases (for example, Finney and others, 2008; Jicha and Singer, 2006). Second, concentrations of other incompatible elements, such as LILE, HFSE, and HPE only increase by 30–50 percent , which is less than half of the increase in other Aleutian andesite systems. Third, Cr and Ni concentrations, although lower than in the LSA, are still much higher than almost all other Aleutian andesites (Nye and others, 2008) and too high to reflect extensive fractional crystallization. The crystals are expected to be relatively depleted in incompatible elements and enriched in compatible elements compared to their host liquids, and a mixture of mush-plus-liquid could have a bulk composition similar to these andesites. Other petrogenetic paths can be imagined, such as production of HSA much deeper, where the pyroxene/plagioclase ratio of precipitating crystals is much higher, but these are less plausible.

Low-Silica Andesite Scoria and Dense Low-Silica Andesite—Similar Heterogeneous Hybrid Magmas

The two low-silica andesites are very similar in terms of bulk-rock composition, mineralogy, and mineral texture, and for most elements form a tight geochemical group that anchors the mafic end of the mixing array that is the dominant geochemical feature of 2006 lavas. LSAS and DLSA both contain reacted crystals, and plagioclase shows the largest degrees of disequilibrium, with roughly 30 percent of plagioclase phenocrysts in the LSA having sieved textures typical of Type 3 plagioclases described above. Elsewhere in 2006 ejecta, these plagioclase phenocrysts are in apparent textural equilibrium only in the HSA samples. Equilibrium plagioclase in the low-silica andesites have An-rich cores and less calcic rims. The composition of microlites and outermost rims of phenocrysts varies from An_{57} to An_{77}, correlating with the large variability of matrix glass compositions (fig. 11). Most likely this is due to rapid crystallization in response to two simultaneous syneruptive processes: (1) decompression (degassing) crystallization and (2) assimilation of the colder host magma.

An important feature of the LSAS erupted in 2006 is the presence of chromite-bearing Fo_{84} olivine and An_{92-94} plagioclase crystals. In combination with the strongly reacted plagioclase, those phases likely represent xenocrysts. Thus, the LSAS and DLSA are interpreted to be hybrid magmas, with strongly reacted plagioclase crystals representing xenocrysts derived from the LSA and with chromite-bearing olivine crystals and anorthite derived from a more mafic cryptic magma.

The range in temperatures recorded by Fe-Ti oxide microlites in the low-silica andesite scoria is consistent with a mixing origin for this magma. Temperatures range from 825°C, the temperature for the high-silica andesite body, to as high as ~970°C. Because small, unzoned groundmass crystals recorded these temperatures, we interpret the large temperature range to reflect postmixing conditions in the hybrid low-silica andesite magma. These grains either grew during or after mixing, or else they were small enough to undergo diffusive reequilibration. The highest temperature of 970°C may approach that of the injected, unerupted mafic end member.

The most significant, although still small, compositional differences between the dense and scoriaceous low-silica andesites are in Cr, Ni, and to a lesser extent Mg. The majority of LSAS samples, and about half of the DLSA samples have Cr concentrations of 50 to 70 ppm and fall below the dominant mixing array (fig. 9). The low-silica andesite, which anchors the mafic end of the mixing array, is dominantly DLSA and has 75 to 86 ppm Cr. The fact that many low-silica andesite samples fall below the mixing array, yet contain the signature reacted, An-poor, plagioclase crystals we infer to have been acquired during mixing, suggests that these low-Cr low-silica andesites acquired their low-Cr signatures after mixing. Point-count data are neither sufficiently precise nor numerous enough to rigorously constrain this model. However, they provide qualitative support, because the samples with the lowest whole-rock Cr have the lowest modal proportion of mafic phenocrysts and the highest Cr samples have the highest proportion. If the LSA was vertically heterogeneous as it tunneled through the HSA body (for example, Bergantz and Breidenthal, 2001), the top portion could have been relatively gas-rich and crystal-poor relative to the base, because of in-place phase segregation. The first-erupted, gas-rich and relatively crystal-poor LSA would thus have lower Cr, while the lower portion remained to further mix and degas in the HSA body and retained a higher proportion of its phenocrysts during segregation as the LSA dike tunneled through the HSA body.

Unerupted, Mafic End Member

If the low-silica andesites are hybrids, then it is axiomatic that a more mafic magma was present but did not erupt. Influxes of unerupted high-alumina basalt were also invoked to explain the spectrum of magmas erupted during the 1976 and 1986 eruptions, through mixing with a dacite to form the hybrid, low-silica andesites that were the most mafic composition erupted in both cases (Johnston, 1978; Roman and others, 2005). The most mafic magma erupted in 2006 closely resembles the low-silica andesites erupted in 1976 and 1986. We concur with the previous studies and suggest that similar processes were operating in 2006. However, no good candidates for the pure mafic mixing end member exist in the geologic record at Augustine. The only known basalt on Augustine, which erupted in the late Pleistocene, has major and trace element abundances that fall far off the mixing trend of the 2006 ejecta (figs. 7 to 10). Thus, there is no natural analog at Augustine for the replenishing basalt to use in models to constrain the proportion that hybridized to form the LSA. Projection of the 2006 trend to lower silica contents indicates overlap between potential end members and analyzed Aleutian magmas between ~49 and ~53 weight percent silica (not

shown in our plots). We suggest that the mafic end member falls within this compositional range, and could perhaps be further constrained by systematic compositional analysis of plagioclase populations within the LSA.

Evidence from other eruptions also shows that the erupted mafic end member must itself be the hybrid result of mixing, such as Lassen 1915 (Clynne, 1999), Miyakejima 1983 (Kuritani and others, 2003), and Hokkaido-Komagatake 1929 (Takeuchi and Nakamura, 2001). Also, in 1996 at Karymsky Volcano in Kamchatka, basalt and andesite erupted simultaneously from two vents. The andesite contained calcic plagioclase that derived from the basalt, but no other signs of mixing, indicating that hybridization was complete and occurred within two months (Izbekov and others, 2002). A similar process at Augustine could have yielded andesite that shows little beyond xenocrysts to reveal its hybridized origin. Hildreth (2007) notes that in the Cascades basaltic lavas are rare, or unknown, at the major polygenetic centers, although common at surrounding monogenetic centers. He infers this basic observation to require that there are efficient filters, perhaps in the form of mush columns, beneath polygenetic volcanoes such as Augustine. In summary, mafic replenishing magmas that do not erupt in their pure form, without hybridization, seem to be the rule, rather than the exception.

Dense Intermediate Andesite and Banded Clasts—Products of Syneruptive Mixing

Compositions and mineral assemblages of DIA are intermediate between HSA and LSA, and discrete domains in banded clasts comprise both end members. The DIA resulted from relatively complete hybridization of the LSA and HSA, whereas banded clasts preserve macroscopic heterogeneity. Because the DIA is most prevalent in the continuous phase, it is likely that mixing was initiated just before the onset of the 2006 eruption and that during the interval between January 17 and 28 mixing between the HSA and LSA was ongoing. Presumably the mixed magma was nearly exhausted during the continuous phase because LSA was the dominant product of the effusive phase.

Fine-Grained Gabbroic and Quartz-Rich Inclusions—Chamber Rind and Frozen Interstitial Liquids?

The fine-grained gabbroic inclusions and low-K HSA samples are both low in incompatible elements (figs. 9, 10), suggesting that they are crystal residua. However, low Cr, Ni, and MgO, high Al_2O_3, and mineral modes from the point-count data all show that the inclusions are plagioclase dominated, suggesting that if they are crystal residua, they formed under conditions where plagioclase crystallization was favored over clinopyroxene. The dominance of plagioclase, coupled with the presence of amphibole, suggests crystallization at mid-crustal depths. The highly evolved, low-K matrix glasses in these lithologies indicate that perhaps any matrix melt that evolved during crystallization was stripped away and that they subsequently remelted to form the evolved, low-K glasses (fig. 11). Perhaps they represent cumulate material that was remelted/mobilized during heating and magma mixing accompanying replenishment. This agrees with Harris (1994), who recognized that magma plumbing beneath Augustine Volcano in 1986 was perhaps more complex than previous workers thought, suggesting the mixing of three distinct magmas: residual 1976 magma, newly injected mafic magma, and partially crystallized chamber ‘rind’ material.

Quartz-rich inclusions have mineralogy and trace-element abundances (fig. 10) radically different from the gabbroic inclusions and must have a different origin. They may be hypabyssal plutonic rocks entrained in and partially melted by young Augustine magmas. Subsequently, the new melt fraction crystallized upon cooling and/or transport to the surface, resulting in the vesicular, fine grained groundmass aggregate of quartz, feldspar, orthopyroxene, and glass. It is unknown from where in the subsurface plumbing system these inclusions were entrained, but their relative abundance in deposits of the continuous phase indicate that they had to have come from depths less than or equal to the high-silica andesite magma body. Differential movement between partial melts and relict crystals likely accounts for drastic alterations in bulk composition from that of the parent magma.

Magma Mixing Processes and Timing

Constraints from Plagioclase Phenocrysts

As discussed in the sections above, there is evidence that two-stage mixing took place before the 2006 eruption, creating the hybrid LSA (mixing event 1) and DIA (mixing event 2) magmas. One way to track magma mixing is through the abundant disequilibrium phenocryst textures observed in the 2006 samples. Perhaps the most complex array of disequilibrium textures is found in the plagioclase phenocrysts (table 9). Just before the mixing events, HSA magma contained Types 1, 2, and 4 plagioclase phenocrysts. Type 1 phenocrysts had uniform compositions of $An_{40\text{-}50}$ and had grown entirely in the HSA with no evidence for disequilibrium. Type 2 plagioclases were similar, but more anorthitic spikes and associated resorption zones recorded previous rapid disequilibrium events. Type 4 phenocrysts had more calcic cores with thick overgrowths that suggested that they had been inherited from some previous, more mafic magma. The basaltic end member contained anorthitic, Type 5 plagioclase.

During mixing event 1, efficient mixing between the HSA and basalt formed the hybrid LSA. The new LSA thus contained crystals from both parents—Type 5 from the basalt

Table 9. Sources and mixing paths for plagioclase and olivine types from Augustine 2006 eruptive products.

Magma	Initial source	Just before mixing	Mixing event 1 (HSA+Basalt =LSA)	Mixing event 2 (HSA+LSA =DIA)	Erupted
Other mafic magma	4 3				Did not erupt
HSA	1 2	4 3 1 2	4 3 1 2 3	4 3 1 2 3	4 3 1 2 3
DIA & Banded	Did not exist	Did not exist	Did not exist	3	3
LSA	Did not exist	Did not exist	3 1 2 5 4	3 1 2 5 4	3 1 2 5 4
Unerupted basalt	1 5	1 5	1 5	1 5	Did not erupt

Plagioclase
Type 1: Clean, relatively unzoned, An_{40-50}
Type 2: Clean, An_{40-50} with spikes to An_{75}
Type 3: An_{40-50} cores with dusty zones and An_{80} spikes
Type 4: An_{70} cores with unzoned An_{40-50} rims
Type 5: An_{92-94} cores and thin more sodic rims

Olivine
Type 1: No reaction rim, narrow zoning profile
Type 2: Thin px reaction rim
Type 3: Thick symplectite rim
Type 4: Hopper and swallowtail

and mostly Type 1 from the HSA. These Type 1 crystals, and Types 2 and 4 to a lesser extent, underwent heating and chemical disequilibrium in their new host, leading to dissolution (sieved) zones around the relatively sodic cores. These became Type 3 plagioclase. Some Type 3 plagioclase likely mixed directly back into the HSA during this time period.

During mixing event 2, high-silica andesite and low-silica andesite mixed to form DIA and banded lithologies. This likely occurred predominantly between the end of the explosive phase (January 17) and the beginning of the continuous phase (January 28). The newly formed intermediate andesite incorporated mostly Type 3 plagioclase from the LSA and Type 1 plagioclase from the HSA, the latter of which likely underwent resorption in the somewhat hotter intermediate magma, creating additional Type 3 plagioclase. During this time, some Type 3 plagioclase mixed back into the HSA, as evidenced by some Type 3 crystals with sodic overgrowths that were found in HSA samples.

The clean, sodic rims on Type 3 plagioclase can be used to estimate timing between mixing events and eruption. Rims range in thickness from 10 to 150 microns. Recent estimates of rim growth rates on anorthite seed crystals in rhyodacitic melt range from 3×10^{-10} cm/s to 60×10^{-10} cm/s (Larsen, 2005). These rates yield times of 2 to 40 days for a 10 micron rim and 30 to 560 days for a 150 micron rim. This time range likely encompasses both mixing events described above.

Olivine Reaction Rims and Magma Mixing Time Scales

Another clue about the timing of magma mixing relative to eruption may be found in olivine phenocrysts. Type 3 olivines have pyroxene-magnetite symplectite rims as much as 500 microns thick. These crystals are strongly normally zoned, with Fo_{84} cores and Fo_{74} rims. The wide zoning pattern and thick rims suggest that these have been present and reacting in their current host for long periods of time, probably years to decades (Tilman, 2008). We suggest that these crystals were inherited by the HSA from a mafic magma not related to the 2006 eruption, much like Type 4 plagioclase (table 9). Type 3 olivines are also present in samples from the 1986 eruption and were noted by Johnston (1978) in samples from the 1976 eruption, indicating residence in the HSA mush for at least 30 years. Type 2 olivines have much narrower, pyroxene-only rims and range from Fo_{87} to Fo_{80}, with much narrower zonation in the olivine towards the rim, if present. Similar thin rims of orthopyroxene have been shown to form on olivine xenocrysts when they are introduced into a more silicic magma during magma mixing events (Coombs and Gardner, 2004). Rims on Type 2 olivine in the 2006 rocks range from 10 to 40 microns. The rim growth rate calibrated by Coombs and Gardner (2004) is parabolic, and thus by squaring the average rim width, a linear rate of rim growth with time for a similar melt composition and temperature yields 1.02 micron^2/hr. Applying this rate to the Augustine olivine rims indicates that the olivine crystals were introduced into a new host 4 to 64 days before eruptive quenching. A potentially important difference between their experiments and the Augustine magmas, however, is f_{O_2}. The Coombs and Gardner (2004) experiments were run at an oxygen fugacity of ~Ni-NiO, whereas the 2006 Augustine magmas had an oxygen fugacity of closer to Re-ReO_2 (RRO). Tilman (2008) ran a series of two experiments at this f_{O_2} and obtained a faster rim growth rate. While these results are preliminary, they suggest even shorter times between mixing and eruption, of approximately 12 days for a 40 micron rim. The short duration required to form the thin pyroxene rims from the experiments indicates that they could have formed either during mixing event 1, as olivine was transferred from basalt to andesite, or during mixing event 2, as olivine passed from low-silica andesite to intermediate or high-silica andesite.

Type 4 olivines, with hopper morphologies, are extremely rare in the HSA and uncommon in the mixed and mingled banded and dense intermediate andesite samples. They are similar to hopper olivines observed in the 1976 and 1986 deposits (Harris, 1994; Johnston, 1978). Because many of the hopper grains have a resorption surface that is surrounded by pyroxene growth, the hopper olivines probably grew before mixing event 2. The hopper shape reflects rapid cooling (Faure and others, 2003), and perhaps those olivines originated during mixing event 1 as a result of cooling of the replenishing basalt when it mixed with the cooler HSA (table 9). Following this, mixing event 2 resulted in resorption and pyroxene rim formation during introduction to the HSA.

Groundmass Evolution and Amphibole Reactions During Ascent, Heating, and Cooling

Because of the extreme variations in eruptive style and flux between the three phases of the 2006 eruption (Coombs and others, this volume), one might expect the eruptive products to reflect variations in ascent rate as well. Each discrete Vulcanian blast of the explosive phase was the result of sudden conduit depressurization, emptying the conduit catastrophically of roughly 2×10^6 m^3 of magma until equilibrium was reestablished (Coombs and others, this volume). The continuous phase saw steady ascent of magma from ~5 km depth to the surface. Magma that fed the lava flows of the effusive phase was presumably more degassed and ascended more slowly. Many recent studies have shown that the ascent history of magma will strongly affect the growth of microlites in the groundmass, because decompression drives water from the melt and stabilizes solid phases (for example, Cashman and Blundy, 2000; Geschwind and Rutherford, 1995; Hammer and others, 1999; Hammer and Rutherford, 2002). As microlites grow in the groundmass, the residual melt, and quenched glass, become more evolved. Thus, as a result of the changing ascent rates noted above for the 2006 eruption, we expect to see differences in microlite growth reflected in the groundmass glasses (fig. 11).

In addition to the speed and continuity of the ascent path, magma composition and temperature will affect microlite growth. For example, groundmass microlite content increased systematically with decreasing silica content in andesites and dacites from the 1953 to 1974 eruption of Trident Volcano, even in eruptive units with identical ascent paths (Coombs and others, 2000). Each phase of the 2006 Augustine eruption produced nearly the full range of magmatic compositions, though in widely varying proportions (Vallance and others, this volume). To test whether variations in microlite content and groundmass glass composition are functions of bulk composition, ascent rate, or both, we look at glass compositions and qualitatively at groundmass crystallinity in samples of all lithologies from all three phases.

Groundmass Glasses in the LSA

Low-silica andesite scoria contains microlite-rich groundmass and residual glass that varies widely in composition (fig. 11). This large range exists despite a relatively constant bulk-rock composition and phenocryst assemblage, indicating that the compositional variations reflect changes in microlite content. January 13 tephra follows a similar pattern, and thus these glasses probably evolved the same way. Could the compositional range of the LSAS and early tephra glasses reflect magma mixing instead of late-stage decompression crystallization? If this were the case, one would expect the evolved end of this trend to overlap with matrix glasses from the silicic endmember of the eruption, represented by HSA and the light colored regions in the banded clasts. Instead, the HSA and related samples have glasses that cluster at a lower

silica content than the most evolved LSAS and have K_2O contents that place them slightly below the LSAS trend. This suggests that the LSAS matrix-glass trend is not the result of mixing of melt phases between the two end members and that instead the groundmass glass trend is driven by decompression-induced crystallization.

The most evolved LSAS and tephra glasses range to 78.7 weight percent SiO_2, and some quartz was detected in the groundmass using semiquantitative EPMA. The highly evolved melt in the presence of quartz resulted from extensive groundmass crystallization and equilibration at very shallow depths (Cashman and Blundy, 2000). Plotting these evolved glass compositions on a projected quartz-albite-anorthoclase ternary diagram yields equilibration pressures of 25 MPa, equivalent to a depth of about 1 km. Interestingly, one-atmosphere experiments on natural Augustine pumice consistently yielded melt silica contents of 76±1 weight percent (Brugger and others, 2003). Those authors suggest that such magmas only reach more silicic groundmass melt compositions during high degrees of effective undercooling. This is likely the case at Augustine. The wide range in groundmass glass composition in LSAS samples could have resulted from magma parcels being evacuated from a variety of pressures/depths within the conduit during a single explosion (for example, Clarke and others, 2007).

Low-Silica Andesite Amphibole Reaction Rims

Very few amphibole phenocrysts were found in the LSAS, but those that were identified invariably have reaction rims, indicating breakdown of this hydrous phase at some pressure lower than its stability field, either during slow ascent or during a stalling-out period on its way to the surface (Rutherford and Hill, 1993). We suggest that LSAS amphibole reaction rims grew as this magma slowly broke its way to the surface before the eruption (see section A Magmatic Model for Augustine 2006, below). Applying rates of amphibole breakdown determined experimentally in dacites from Redoubt and Mount St Helens, we can estimate a time scale over which the rims likely formed in the Augustine magma, with a few caveats. The average bulk composition of the LSA is lower in silica content than either the Redoubt or St. Helens dacites, while the groundmass glasses range from similar (>76 weight percent) to lower in SiO_2 (~66 weight percent; Browne and Gardner, 2006; Rutherford and Hill, 1993). The temperatures of the LSA are generally hotter than those used in the Redoubt amphibole breakdown experiments (840ºC; Browne and Gardner, 2006), while those employed by Rutherford and Hill are more similar to the average temperatures of all LSA oxides analyzed (860 to 900ºC, fig. 17). Because temperature appears to have a great influence on amphibole reaction rates during decompression (Browne and Gardner, 2006), it is probably more appropriate here to apply the rates constrained by Rutherford and Hill (1993), despite the differences in bulk and groundmass glass compositions. Thus, the 40-to-100-micron thick rims observed in the LSA indicate that this magma spent ~20 to 57 days outside the amphibole stability field, at shallower depths than about 4 km. Given the first signs of phreatic explosions starting on December 10, and the first explosive phase of the eruption January 12, the range of thicknesses observed in the amphibole breakdown rims indicate initiation of ascent of the LSA magma sometime near mid-November 2005, which correlates very well with geodetic observations as described below.

Alternatively, rimmed amphibole crystals found in low-silica andesite may have derived from another magma, perhaps the high-silica andesite. If this was the case, reaction rims may have formed as the amphibole underwent heating (Browne and Gardner, 2006). Additional analyses of amphibole compositions would further constrain this possibility.

Groundmass Glass Compositions in the HSA

In contrast to the LSA, the high-silica andesite groundmass is nearly microlite-free and has very consistent groundmass glass compositions, for both the explosive and continuous phases. This is true even for HSA samples found in the same deposit as LSAS with microlite-choked groundmass. The HSA did not undergo extensive decompression-induced crystallization during ascent. Because HSA clasts erupted coevally with LSAS, these parcels of magma must have had the same ascent histories. The lack of microlite growth in the HSA is likely to the result of a combination of a more silicic starting composition, which would increase viscosity and inhibit crystal nucleation and growth, and the fact that HSA was likely heated immediately before eruption by mixing, slightly "superheating" the melt phase.

A Magmatic Model for Augustine 2006

Here we combine our petrologic data and conclusions with other geophysical and geologic evidence to construct a model of magma storage, mixing, and movement before and during the 2006 Augustine eruption. In addition to explaining the observations and events of 2006, any feasible model should also address the consistency in eruptive style and composition of the last several Augustine eruptions, which suggests a common, repeatable mechanism.

Several months before the beginning of the eruption, volatile-rich basalt rose through a hot, ductile mid-crustal pathway and intersected the crystal-rich HSA body, probably at a depth of 4–6 km bsl (fig. 20*A*). Evidence from melt inclusion analyses from 2006, 1986, and prehistoric samples (Webster and others, this volume) indicate maximum entrapment pressures of 160 to 200 MPa in rhyolitic inclusions in plagioclase, which indicates maximum depths of about 6 to 8 km for the HSA body, including the estimate from 1986 inclusions. Ascent of the basalt was not detected seismically, but small volcano-tectonic earthquakes began near sea level directly below Augustine's summit in late April 2005 (Jacobs

and McNutt, this volume; Power and Lalla, this volume), and a similarly located weak inflationary source was detected by continuous GPS starting in the summer of 2005 (Cervelli and others, this volume; Cervelli and others, 2006). This zone of geophysical unrest coincides with a region of low to medium seismic velocities interpreted to be dome material overlying sediments interlaced with dikes and sills; these sit atop zeolitized sedimentary strata below 0.9 km bsl (Kienle and others, 1979). We suggest that the shallow unrest resulted from pressurization of the volcanic edifice by gases exsolved from the basalt as it ascended, intersected the HSA, cooled, and crystallized. The total volume change for a modeled point source near sea level is roughly 2×10^5 m^3 (Cervelli and others, 2006), about 2.5 orders of magnitude less than the total erupted volume in 2006 (Coombs and others, this volume).

The introduction of wet basalt into the HSA body first partially reheated the HSA body, lowering its crystal content. The rate of heating of a silicic magma body by a newly introduced hotter body will depend on their size and geometry, but it can take hundreds of days to heat the silicic magma by tens of degrees (Snyder, 2000). Next, the basalt and a newly rejuvenated portion of the HSA body hybridized to form the erupted LSA. This process was likely aided by vesiculation of the basalt as it cooled and crystallized (Huppert and others, 1982; Thomas and others, 1993), causing density instability and convective overturn. The heating of the HSA and hybridization were probably coeval. The homogeneous composition of the LSA indicates that hybridization was thorough, and if it began at the onset of geophysical unrest, it was quick, taking 6 months or less.

A portion of the hybrid LSA then rose through the upper, crystal-rich portion of the HSA body. Whether it took the form of a dike or diapir is unknown and depends on the crystallinity (and thus rigidity) of the HSA body. The LSA then propagated as a dike into the dacite-porphyry crust above the HSA body and ascended toward the surface during the late precursory phase (fig. 20*B*). The LSA was apparently able to initiate dike formation because of its lower viscosity, whereas the crystal-rich HSA was not able to do so. This scenario of a newly arrived, less viscous magma creating a pathway for a resident, crystal-rich magma was proposed by Pallister and others (1996) for the eruption of Mount Pinatubo. Since then, this model has also been applied to the eruption of the Yunokuchi Pumice, Akagi, Japan (Umino and Horio, 1998) and the 1929 eruption of Komagatake volcano, Japan (Takeuchi and Nakamura, 2001). At Komagatake, it was shown that dike propagation of a less viscous mixed andesite magma could occur at a chamber overpressure of only 8 MPa, whereas unrealistically high overpressures would have been required to propagate a dike of the more viscous, crystal-rich silicic magma resident in the chamber.

The exact timing of LSA dike initiation is not known, but GPS data place some constraints on the dike's movement. Edifice-inflation rates increased on November 18, 2005, and GPS data are consistent with propagation of a small dike from 1.25 km depth to the surface between November 18 and January 11 (Cervelli and others, 2006; fig. 20*B*). The upward movement of such a dike at greater depths would not be detected by the Augustine GPS network (P. Cervelli, oral communication, 2008), so it is not known exactly when the dike started its ascent from the HSA body. Modeled dike ascent rates are not constant, and they slow from 100 m/hour around November 25. An offset occurred in the GPS time series on November 17, at a similar time as the appearance of new cracks at the summit of Augustine. This event could point towards the initiation of the rise of the dike just before the edifice inflation rate accelerated on November 18. If we also compare with the preliminary estimates of LSA ascent timescale from the amphibole reaction rims described above, rise of the LSA dike from a depth of ~4 km starting November 17 would indicate that the quickest rising magma would reach the surface around December 7, which is close to the time of the first of the observed phreatic explosions, and the slowest would reach the surface the week of January 12, marking the onset of the explosive phase of the eruption.

Phreatic explosions, increased SO_2 output, and heating of the edifice in December 2005 (McGee and others, this volume; Power and others, 2006; Wessels and others, this volume) all suggest that significant gas had accumulated at the tip of the LSA dike and that some made it to the surface ahead of the LSA magma. A strong swarm of VT earthquakes on January 10–11 likely recorded the final opening of the dike to the surface, but two explosions on January 11 contained little or no juvenile magma (Wallace and others, this volume), and deformation recorded by a summit GPS station continued unabated through these events, suggesting that not much magma was evacuated from the edifice (Cervelli and others, this volume).

LSA magma likely reached the surface on January 12 in the form of a small ephemeral lava dome, recorded by drumbeat earthquakes that signify lava effusion (Power and Lalla, this volume). Vulcanian blasts on January 13, 14, and 17 each drained the conduit to a depth of roughly 2 km below the surface (Coombs and others, this volume; fig. 20C), and produced dominantly LSA deposits, but including a small percentage of HSA as well (Vallance and others, this volume). In between explosions, the conduit refilled with LSA and minor amounts of HSA from the top of the rejuvenated magma body. Explosions were driven by overpressure in the conduit that developed below a degassed lava/magma cap, similar to those seen at Soufriere Hills Volcano, Montserrat (Druitt and others, 2002). The range in LSA groundmass glass compositions indicates that some LSA underwent extensive decompression-driven groundmass crystallization before eruption, likely during storage in the shallow portions of the conduit before explosive release. The continuation of the inflationary trend throughout January indicated that gas pressurization in the shallow subsurface continued throughout this period (Cervelli and others, this volume).

The presence of some HSA in explosive-phase deposits indicates that mixing occurred during the upward passage of the LSA through the HSA body, and/or some HSA was drawn into the dike during LSA ascent. Interestingly, the final, effusive phase of the 2006 eruption was also dominated by LSA,

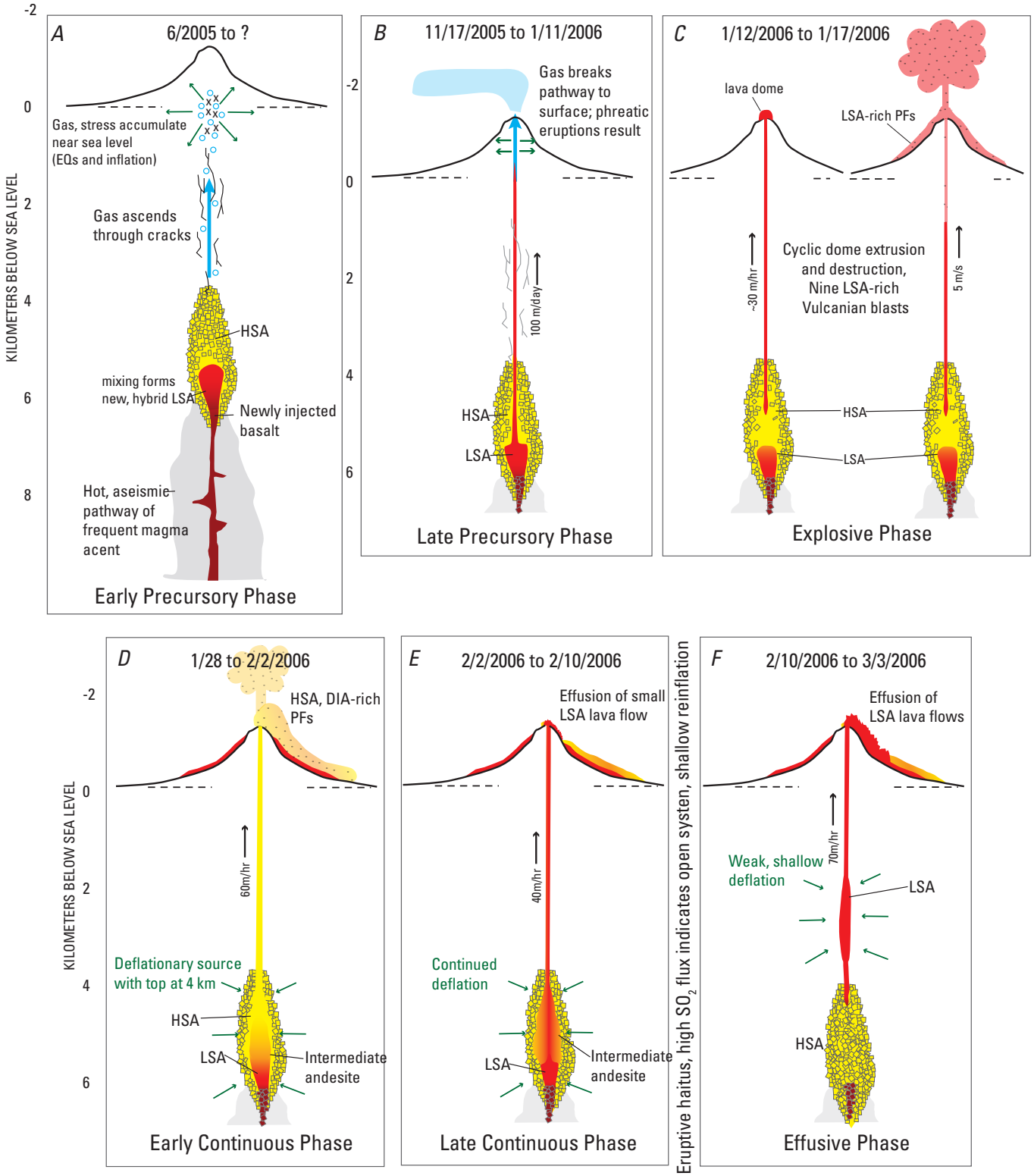

Figure 20. Schematic depiction of magma configuration and events for six time periods before and during the 2006 eruption. HSA is high-silica andesite, DIA is dense intermediate andesite, LSA is low-silica andesite, PF denotes pyroclastic flows.

indicating that in this case, not all of the hybrid andesite was erupted during the initial phase, but that instead some remained at the base of the HSA magma body. It is also clear that during the period between January 17 and 27, continued mixing between LSA and HSA created the more thoroughly mixed intermediate andesite that erupted during the continuous phase.

Slow effusion of a lava dome occurred from January 17 through 27. An explosion on January 27 destroyed this new dome and produced the largest single deposit of the 2006 eruption: about 20 million m^3 of predominantly HSA formed the Rocky Point pyroclastic flow (Coombs and others, this volume; Vallance and others, this volume). This event marked a distinct shift in the dominant composition of erupted material, likely coinciding with exhaustion of the LSA "slug" that made its way through the resident HSA and initially drove the eruption. Whereas earlier explosions were fed only from the conduit, the January 27 explosive event undoubtedly tapped the resident magma body. This is consistent with the fact that for the first time during the eruption, GPS signals record a deep deflation (>4 km depth) that begins around January 27 and continues through February 10 (Cervelli and others, this volume).

Following the explosive eruption of HSA on January 27, ascent and effusion of predominantly HSA occurred for the next several days (Coombs and others, this volume; fig. 20*D*). Little or no LSA was erupted during this interval, but HSA was accompanied by effusion of banded and DIA magmas (Vallance and others, this volume). We interpret this interval as the evacuation of the rejuvenated portion of the resident HSA body through an open conduit from ~5 km to the surface. Ascent rates were high enough for the groundmass to remain microlite-free, though this could also have resulted from the recent heating of the HSA by the LSA.

During the waning of the continuous phase, mass flux continued to be quite high as the north lava flow effused (fig. 20*E*). Eruptable HSA had been exhausted and mostly intermediate andesite was erupted. The deflationary trend overlaps this period, as well as the earlier continuous phase.

During the eruptive pause from February 10 to March 3, high SO_2 emission rates suggested that the system was open and that relatively shallow magma was degassing (McGee and others, this volume). Weak, shallow inflation during this period (Cervelli and others, this volume) is interpreted to have been caused by magma accumulation, somewhere between the HSA body and the surface. This relatively degassed, dense LSA must have been present at the base of the HSA magma body and ascended after the HSA was exhausted.

During the effusive phase, from March 3 through 16, degassed LSA ascended and erupted in the form of two lava flows and a new summit dome (fig. 20*F*). The DLSA brought with it numerous inclusions of fine-grained gabbro, chunks of crystallized portions of the plumbing system.

The 2006 Augustine Eruption in Context

The range in whole-rock compositions of deposits from the 2006 eruption matches that of the historical and most Holocene samples, essentially spanning the andesite range (fig. 7). Basalt and rhyolite erupted coevally in the late Pleistocene but have not erupted since (Waitt and Begét, 2009; J.E. Begét, oral communication). Those rocks fall along a lower K trend compared to historical lavas, including those from 2006. Prehistoric Holocene lavas span a limited SiO_2 range but fall along an intermediate K trend relative to Pleistocene and historical samples. Similarly, many trace-element arrays formed by 2006 and other historical magmas on variation diagrams are elevated in relation to those formed by the Pleistocene basalt and rhyolite. Similar temporal systematics (that is, progressive increase in highly incompatible elements at a given SiO_2 level) have been seen at nearby Redoubt volcano (Begét and Nye, 1994). The differences between the Pleistocene basalt and rhyolite and modern lavas mean that these exact compositions are not appropriate for modeling the modern Augustine magmatic system. However, they do suggest that similar magmas may exist in the modern Augustine system, even if they have not erupted during the Holocene.

Holocene Augustine lavas have high concentrations of compatible transition metals (Mg, Cr, Ni, Fe), and high molar Mg/(Mg+Fe) (Mg#) and dramatically low concentrations of all incompatible trace elements (including LIL, U, Th, Pb, REE, and HFSE) relative to other Aleutian lavas of similar SiO_2 content (fig. 21). Augustine magmas do not follow the liquid line of descent typical of most Aleutian volcanoes where basaltic parental magmas evolve to andesite and dacite accompanied by a steady increase in incompatible elements and decrease in compatible transition metals. Within the andesite range at Augustine the most highly incompatible elements only increase by about 50 percent, and MREE and HREE have constant concentrations (fig. 10). Over similar SiO_2 ranges at other Aleutian volcanoes all incompatible elements (including HREE) increase, with the most incompatible increasing by 200–300 percent (for example, Aniakchak; Dreher and others, 2005; C.J. Nye and others, unpublished data). There are several possible reasons for the low rate of increase of incompatible elements at Augustine, including (a) high crystal/liquid distribution coefficients associated with the high silica content of the groundmass; (b) high effective bulk partition coefficients during crystallization at high pressure, where the ratio of pyroxene ± amphibole to plagioclase is higher; (c) whole-rock concentrations of incompatible elements reflecting a large amount of crystal accumulation; or (d) these magmas being primitive high-Mg# andesites (Kelemen and others, 2003 and 2004), rather than highly evolved fractionates. Possibilities (c) and (d) are also at least qualitatively consistent with the high concentrations of compatible elements in these lavas.

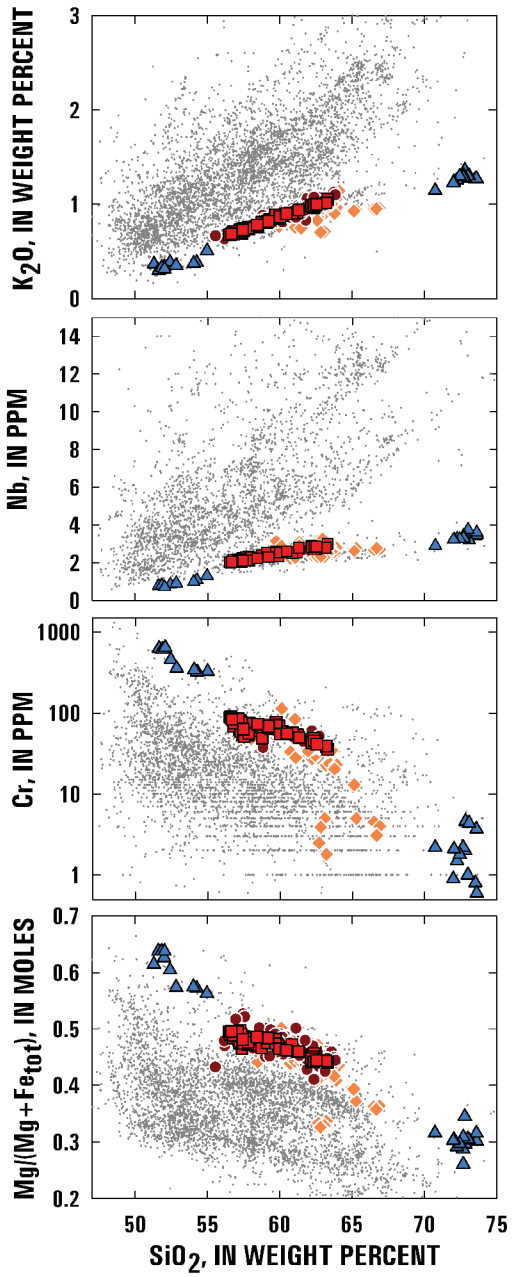

Figure 21. Comparison of Augustine magmas with other Aleutian arc magmas. Augustine magmas are different from the majority of Aleutian magmas in having relatively high Mg# (molar Mg/(Mg+Fe)) and compatible transition metals Cr (shown), as well as Ni and Mg (not shown), as well as low concentrations of incompatible elements, such as K and Nb (shown). The low concentrations of incompatible elements reflect relatively less enrichment with increasing silica in addition to lower-than-average initial concentrations of many incompatible elements. Colored symbols are Augustine lavas (red squares, 2006; dark red circles, pre-2006 historical; orange diamonds, prehistoric late Holocene; blue triangles, late Pleistocene). Gray dots are all other Aleutian analyses from the open literature and unpublished Alaska Volcano Observatory analyses.

It is beyond the scope of this paper to evaluate the above hypotheses. It is our intention instead to point out that Augustine magmas are quite distinct from typical Aleutian magmas, particularly those from the central arc. Trace element concentrations in minerals would be useful in constraining the mineral/melt distribution coefficients during crystallization, thus further constraining petrogenesis. Emphasis on phenocryst mineralogy and petrology in this study shows that especially the low-silica magmas, which erupted, are hybrids requiring the presence of an even lower-silica magma. Thus possibility (d), that these are simply primitive andesites, appears too simple an explanation.

Acknowledgments

It takes an observatory to document an eruption and our understanding of the 2006 eruption of Augustine would not be nearly as complete without the efforts of the entire staff of the Alaska Volcano Observatory. In addition, we thank Jim Webster, Charlie Mandeville, Peter Cervelli, John Power, and Jeff Freymueller for insightful discussion regarding the Augustine magmatic system. Charlie Bacon, Brandon Browne, and Jeff Freymueller provided critical reviews that helped to improve the manuscript. This work was funded by the U.S. Geological Survey's Volcano Hazards Program.

References Cited

Brugger, C.R., Johnston, D.A., and Cashman, K.V., 2003, Phase relations in silicic systems at one-atmosphere pressure: Contributions to Mineralogy and Petrology, v. 146, p. 356–369.

Cashman, K.V., and Blundy, J., 2000, Degassing and crystallization of ascending andesite and dacite: Philosophical Transactions of the Royal Society, v. 358, p. 1487–1513.

Cervelli, P.F., Fournier, T.J., Freymueller, J.T., Power, J.A., Lisowski, M., and Pauk, B.A., 2010, Geodetic constraints on magma movement and withdrawal during the 2006 eruption of Augustine Volcano, *in* Power, J.A., Coombs, M.L., and Freymueller, J.T., eds., The 2006 eruption of Augustine Volcano, Alaska: U.S. Geological Survey Professional Paper 1769 (this volume).

Cervelli, P.F., Fournier, T., Freymueller, J.T., and Power, J.A., 2006, Ground deformation associated with the precursory unrest and early phases of the January 2006 eruption of Augustine Volcano, Alaska: Geophysical Research Letters, doi: 10.1027/2006GL027219.

Clarke, A.B., Stephens, S., Teasdale, R., Sparks, R.S.J., and Diller, K., 2007, Petrologic constraints on the decompression history of magma prior to Vulcanian explosions at the Soufriere Hills Volcano, Montserrat: Journal of Volcanology and Geothermal Research, v. 161, p. 261–274.

Clynne, M.A., 1999, A complex magma mixing origin for rocks erupted in 1915, Lassen Peak, California: Journal of Petrology, v. 40, p. 105–132.

Coombs, M.L., and Gardner, J.E., 2004, Reaction rim growth on olivine in silicic melts—implications for magma mixing: American Mineralogist, v. 89, no. 5–6, p. 748–759.

Coombs, M.L., Eichelberger, J.C., and Rutherford, M.J., 2000, Magma storage and mixing conditions for the 1953-1974 eruptions of Southwest Trident volcano, Katmai National Park, Alaska: Contributions to Mineralogy and Petrology, v. 140, no. 1, p. 99–118.

Coombs, M.L., Bull, K.F., Vallance, J.W., Schneider, D.J., Thoms, E.E., Wessels, R.L., and McGimsey, R.G., 2010, Timing, distribution, and volume of proximal products of the 2006 eruption of Augustine Volcano, *in* Power, J.A., Coombs, M.L., and Freymueller, J.T., eds., The 2006 eruption of Augustine Volcano, Alaska: U.S. Geological Survey Professional Paper 1769 (this volume).

Costa, F., and Chakraborty, S., 2004, Decadal time gaps between mafic intrusion and silicic eruption obtained from chemical zoning patterns in olivine: Earth and Planetary Science Letters, v. 227, p. 517–530.

Daley, E.E., 1986, Petrology, geochemistry, and the evolution of magmas from Augustine Volcano, Alaska: University of Alaska Fairbanks, unpublished M.S. thesis, 103 p.

Detterman, R.L., and Reed, B.L., 1980, Stratigraphy, structure, and economic geology of the Iliamna Quadrangle, Alaska: U.S. Geological Survey Bulletin, 1368-B, 86 p.

Dreher, S.T., Eichelberger, J.C., and Larsen, J.F., 2005, The petrology and geochemistry of the Aniakchak caldera-forming ignimbrite, Aleutian Arc, Alaska: Journal of Petrology, v. 46, p. 1747–1768.

Druitt, T.H., Young, S.R., Baptie, B., Bonadonna, C., Calder, E.S., Clarke, A.B., Cole, P.D., Harford, C.L., Herd, R.A., Luckett, R., Ryan, G., and Voight, B., 2002, Episodes of cyclic Vulcanian explosive activity with fountain collapse at Soufriere Hills Volcano, Montserrat, *in* Druitt, T.H., and Kokelaar, B.P., eds., The eruption of Soufriere Hills Volcano, Montserrat, from 1995 to 1999: London, The Geological Society, p. 281–306.

Evans, B.W., Scaillet, B., and Kuehner, S.M., 2006, Experimental determination of coexisting iron-titanium oxides in the systems FeTiAlO, FeTiAlMgO, FeTiAlMnO, and FeTiAlMgMnO at 800 and 900°C, 1–4 kbar, and relatively high oxygen fugacity: Contributions to Mineralogy and Petrology, v. 152, p. 149–167.

Faure, F., Trolliard, G., Nicollet, C., and Montel, J.-M., 2003, A developmental model of olivine morphology as a function of the cooling rate and the degree of undercooling: Contributions to Mineralogy and Petrology, v. 145, p. 251–263.

Finney, B., Turner, S., Hawkesworth, C., Larsen, J.F., MNye, C., George, R., Bindeman, I., and Eichelberger, J.C., 2008, Magmatic differentiation at an island-arc caldera—Okmok Volcano, Aleutian Islands, Alaska: Journal of Petrology, v. 49, no. 857–884.

Geschwind, C.H., and Rutherford, M.J., 1995, Crystallization of microlites during magma ascent—The fluid mechanics of the 108086 eruptions at Mount St. Helens: Bulletin of Volcanology, v. 57, p. 356–370.

Ghiorso, M.S., and Evans, B.W., 2008, Thermodynamics of rhombohedral oxide solid solutions and a revision of the Fe-Ti two-oxide geothermometer and oxygen-barometer: American Journal of Science, v. 308, p. 957–1039.

Gill, J.B., 1981, Orogenic andesites and plate tectonics: Springer-Verlag, Berlin, 370 p.

Hammer, J.E., and Rutherford, M.J., 2002, An experimental study of the kinetics of decompression-induced crystallization in silicic melt: Journal of Geophysical Research, v. 107, p. 148–227.

Hammer, J.E., Cashman, K.V., Hoblitt, R.P., and Newman, S., 1999, Degassing and microlite crystallization during preclimactic events of the 1991 eruption of Mount Pinatubo, Philippines: Bulletin of Volcanology, v. 60, p. 335–380.

Harris, G.W., 1994, The petrology and petrography of lava from the 1986 eruption of Augustine volcano: University of Alaska Fairbanks unpublished M.S. thesis, Fairbanks, AK, 131 p.

Hildreth, E.W., 2007, Quaternary Magmatism in the Cascades—Geologic Perspectives: U.S. Geological Survey Professional Paper 1744, 136 p.

Huppert, H.E., Sparks, R.S.J., and Turner, J.S., 1982, Effects of volatiles on mixing in calc-alkaline magma systems: Nature, v. 297, p. 554–557.

Izbekov, P., Eichelberger, J.C., Patino, L.C., Vogel, T.A., and Ivanov, B.V., 2002, Calcic cores of plagioclase phenocrysts in andesite from Karymsky volcano—evidence for rapid introduction by basaltic replenishment: Geology, v. 30, p. 799–802.

Jacobs, K.M., and McNutt, S.R., 2010, Using seismic *b*-values to interpret seismicity rates and physical processes during the preeruptive earthquake swarm at Augustine Volcano 2005–2006, *in* Power, J.A., Coombs, M.L., and Freymueller, J.T., eds., The 2006 eruption of Augustine Volcano, Alaska: U.S. Geological Survey Professional Paper 1769 (this volume).

Jicha, B.R., and Singer, B.S., 2006, Volcanic history and magmatic evolution of Seguam Island, Aleutian Island arc, Alaska: Geological Soceity of America Bulletin, v. 118, p. 805–822.

Johnson, K.E., Strong, D.F., Harmon, R.S., Richardson, J. M., and Moorbath, S., 1996, Isotope and trace element geochemistry of Augustine volcano, Alaska—implications for magmatic evolution: Journal of Petrology, v. 37, p. 95–115.

Johnson, D.M., Hooper, P.R., and Conrey, R.M., 1999, XRF analysis of rocks and minerals for major and trace elements on a single low dilution Li-tetraborate fused bead: Advances in x-ray Analysis, v. 41, p. 843–867.

Johnston, D.A., 1978, Volatiles, magma mixing, and the mechanism of eruption at Augustine volcano, Alaska: University of Washington Ph.D. dissertation, 187 p., 20 plates.

Kelemen, P.B., Yogodzinski, G.M., and Scholl, D.W., 2003, Along strike variation in the Aleutian Island arc—genesis of high Mg# andesite and implications for continental crust, *in* Eiler, J., ed., Inside the Subduction Factory, American Geophysical Union Monograph 138, p. 1–54.

Kelemen, P.B., Hanghoj, K., and Greene, A.R., 2004, One view of the geochemistry of subduction-related magmatic arcs, with an emphasis on primitive andesite and the lower crust, *in* Rudnick, R.L., ed., The crust: Elsevier Ltd., p. 593–659.

Kienle, J., and Swanson, S.E., 1983, Volcanism in the eastern Aleutian Arc—late Quaternary and Holocene centers, tectonic setting and petrology: Journal of Volcanology and Geothermal Research, v. 17, no. 1-4, p. 393–432.

Kienle, J., Lalla, D.J., Pearson, C.F., and Barrett, S. A., 1979, Search for shallow magma accumulations at Augustine volcano: University of Alaska Fairbanks Geophysical Institute Final Report to U.S. Dept. of Energy, Washington D.C. 157 p.

Knaack, C., Cornelius, S.B., and Hooper, P.R., 1994, Trace element analyses of rocks and minerals by ICP-MS: Open File Report, Department of Geology, Washington State University [http://www.wsu.edu/~geolab/].

Kuritani, T., Yokoyama, T., Kobayashi, K., and Nakamura, E., 2003, Shift and rotation of composition trends by magma mixing—1983 eruption at Miyakejima Volcano, Japan: Journal of Petrology, v. 44, p. 1895–1916.

Larsen, J.F., 2005, Experimental study of plagioclase rim growth around anorthite seed crystals in rhyodacitic melt: American Mineralogist, v. 90, p. 417–427.

Lattard, D., Sauerzapf, U., and Kasemann, M., 2005, New calibration data for the Fe-Ti oxide thermo-oxybarometers from experiments in the Fe-Ti-O system at 1 bar, 1,000–1,300°C and a large range of oxygen fugacities: Contributions to Mineralogy and Petrology, v. 149, p. 735–754.

LeMaitre, R.W., 1991, A classification of igneous rocks and glossary of terms: Oxford, Blackwell Scientific Publications, 193 p.

McGee, K.A., Doukas, M.P., McGimsey, R.G., Neal, C.A., and Wessels, R.L., 2010, Emission of SO_2, CO_2, and H_2S from Augustine Volcano, 2002–2008, *in* Power, J.A., Coombs, M.L., and Freymueller, J.T., eds., The 2006 eruption of Augustine Volcano, Alaska: U.S. Geological Survey Professional Paper 1769 (this volume).

Murphy, M.D., Sparks, R.S.J., Barclay, J., Carroll, M.R., and Brewer, T.S., 2000, Remobilization of andesite magma by intrusion of mafic magma at the Soufriere Hills Volcano, Montserrat, West Indies: Journal of Petrology, v. 41, p. 21–42.

Nakamura, M., 1995, Continuous mixing of crystal mush and replenished magma in the ongoing Unzen eruption: Geology, v. 23, p. 807–810.

Nakamura, M., and Shimikata, S., 1998, Kinetic constraints on the mode of magma mixing and ascent in the 1991 Unzen eruption: Earth and Planetary Science Letters, v. 161, p. 119–133.

Nye, C., Coombs, M.L., Larsen, J.F., Izbekov, P., Tilman, M., and Cameron, C., 2008, Augustine Volcano—Mg-, Cr-, and Ni-rich; LILE, REE, and HFSE-poor: Geochimica et Cosmochimica Acta, v. 72, p. A692.

Pallister, J.S., Hoblitt, R.P., Meeker, G.P., Knight, R.J., and Siems, D.F., 1996, Magma mixing at Mount Pinatubo—petrographic and chemical evidence from the 1991 deposits, *in* Newhall, C.G., and Punonhbayan, R., eds., Fire and mud—eruptions and lahars of Mount Pinatubo: Seattle, University of Washington Press, p. 687–731.

Plank, T., Zimmer, M.M., Hauri, E.H., and Nye, C.J., 2006, The Augustine basalt: Eos (American Geophysical Union Transactions), Fall Meeting Supplement, v. 87, abs. V42B-06.

Power, J.A., 1988, Seismicity associated with the 1986 eruption of Augustine Volcano, Alaska: University of Alaska Fairbanks, unpublished M.S. thesis, 142 p.

Power, J.A., and Lalla, D.J., 2010, Seismic observations of Augustine Volcano, 1970–2007, *in* Power, J.A., Coombs, M.L., and Freymueller, J.T., eds., The 2006 eruption of Augustine Volcano, Alaska: U.S. Geological Survey Professional Paper 1769 (this volume).

Power, J.A., Nye, C.J., Coombs, M.L., Wessels, R.L., Cervelli, P.F., Dehn, J., Wallace, K.L., Freymueller, J.T., and Doukas, M.P., 2006, The reawakening of Alaska's Augustine Volcano: Eos (American Geophysical Union Transactions), v. 87, no. 37, p. 373, 377.

Pownceby, M.I., and O'Neill, H.St.C 1994, Thermodynamic data from redox reactions at high temperatures. IV. Calibration of the Re-ReO_2 oxygen buffer from EMF and NiO+Ni-Pd redox sensor measurements: Contributions to Mineralogy and Petrology, v. 118, p. 130–137.

Roman, D.C., Cashman, K.V., Gardner, C.A., Wallace, P., and Donovan, J., 2005, Storage and interaction of compositionally heterogeneous magmas from the 1986 eruption of Augustine Volcano, Alaska: Bulletin of Volcanology, v. 68, p. 240–254.

Rutherford, M.J., and Devine, J.D., 1996, Preeruption pressure-temperature conditions and volatiles in the 1991 dacitic magma of Mount Pinatubo, *in* Newhall, C.G., and Punongbayan, R.S., eds., Fire and Mud—eruptions and lahars of Mount Pinatubo, Philippines: Seattle, University of Washington Press, p. 751–766.

Rutherford, M.J., and Hill, P.M., 1993, Magma ascent rates from amphibole breakdown—an experimental study applied to the 1980-1986 Mount St. Helens eruptions: Journal of Geophysical Research, v. 98, p. 19667–19685.

Snyder, D., 2000, Thermal effects of the intrusion of basaltic magma into a more silicic magma chamber and implications for eruption triggering: Earth and Planetary Science Letters, v. 175, p. 257–273.

Stormer, J.C., 1983, The effects of recalculation on estimates of temperature and oxygen fugacity from analyses of multicomponent iron-titanium oxides: American Mineralogist, v. 68, p. 586–594.

Syracuse, E.M., and Abers, G.A., 2006, Global compilation of variations in slab depth beneath arc volcanoes and implications: Geochemistry, Geophysics, Geosystems, v. 7, no. 5, p. Q05017, doi:05010.01029/02005GC001045.

Takeuchi, S., and Nakamura, M., 2001, Role of precursory less-viscous mixed magma in the eruption of phenocryst-rich magma—evidence from the Hokkaido-Komagatake 1929 eruption: Bulletin of Volcanology, v. 63, p. 365–376.

Tappen, C.M., Webster, J.D., Mandeville, C.W., and Roderick, D., 2009, Petrology and geochemistry of prehistoric pumice fall eruptions (2100–1000 a.B.P.) at Mt. St. Augustine Volcano, Alaska: Journal of Volcanology and Geothermal Research, v. 183, p. 42–62.

Thomas, N., Tait, S., and Koyaguchi, T., 1993, Mixing of stratified liquids by the motion of gas bubbles—application to magma mixing: Earth and Planetary Science Letters, v. 115, p. 161–175.

Tilman, M.R., 2008, An investigation of symplectite-rimmed olivine and magmatic processes during the 2006 eruption of Augustine Volcano, Alaska: University of Alaska Fairbanks, unpublished M.S. thesis, 166 p.

Tsuchiyama, A., 1985, Dissolution kinetics of plagioclase in the melt of the system diopside-albite-anorthite and origin of dusty plagioclase in andesites: Contributions to Mineralogy and Petrology, v. 89, p. 1–16.

Umino, S., and Horio, A., 1998, Multistage magma mixing revealed in phenocryst zoning of the Yunokuchi Pumice, Akagi Volcano, Japan: Journal of Petrology, v. 39, p. 101–124.

Vallance, J.W., Bull, K.F., and Coombs, M.L., 2010, Pyroclastic flows, lahars, and mixed avalanches generated during the 2006 eruption of Augustine Volcano, *in* Power, J.A., Coombs, M.L., and Freymueller, J.T., eds., The 2006 eruption of Augustine Volcano, Alaska: U.S. Geological Survey Professional Paper 1769 (this volume).

Waitt, R.B., and Begét, J.E., 2009, Volcanic processes and geology of Augustine Volcano, Alaska: U.S. Geological Survey Professional Paper 1762, 78 p., 2 map plates [http://pubs.usgs.gov/pp/1762/].

Waitt, R.B., 2010, Ejecta and landslides from Augustine Volcano before 2006, *in* Power, J.A., Coombs, M.L., and Freymueller, J.T., eds., The 2006 eruption of Augustine Volcano, Alaska: U.S. Geological Survey Professional Paper 1769 (this volume).

Wallace, K.L., Neal, C.A., and McGimsey, R.G., 2010, Timing, distribution, and character of tephra fall from the 2005–2006 eruption of Augustine Volcano, *in* Power, J.A., Coombs, M.L., and Freymueller, J.T., eds., The 2006 eruption of Augustine Volcano, Alaska: U.S. Geological Survey Professional Paper 1769 (this volume).

Waythomas, C.F., and Waitt, R.B., 1998, Preliminary volcano-hazard assessment for Augustine Volcano, Alaska: U.S. Geological Survey Open-File Report 98-0106, 39 p., 1 plate, scale unknown.

Webster, J.D., Mandeville, C.W., Goldoff, B., Coombs, M.L., and Tappen, C., 2010, Augustine Volcano—The influence of volatile components in magmas erupted A.D. 2006 to 2,100 years before present, *in* Power, J.A., Coombs, M.L., and Freymueller, J.T., eds., The 2006 eruption of Augustine Volcano, Alaska: U.S. Geological Survey Professional Paper 1769 (this volume).

Wessels, R.L., Coombs, M.L., Schneider, D.J., Dehn, J., and Ramsey, M.S., 2010, High-resolution satellite and airborne thermal infrared imaging of the 2006 eruption of Augustine Volcano, *in* Power, J.A., Coombs, M.L., and Freymueller, J.T., eds., The 2006 eruption of Augustine Volcano, Alaska: U.S. Geological Survey Professional Paper 1769 (this volume).

Tables 2–8

Table 2. Summary of modal abundances for Augustine 2006 lithologies as determined by point counting.

[Each value is average of n samples within each lithology, in volume percent; one standard deviation is given in parentheses. All values, except for void space, are calculated on a void-free basis. At least, 1,000 points were counted for all samples. LSAS, low-silica andesite scoria; DLSA, dense low-silica andesite; DIA, dense intermediate andesite; FGGI, fine-grained gabbroic inclusions. n.p., not present]

	LSAS	DLSA	DIA	Banded	HSA	FGGI
Plagioclase	23.7 (3.1)	25.9 (3.4)	25.9 (7.0)	28.1 (6.2)	31.9 (5.2)	56.9 (10.6)
Clinopyroxene	5.8 (3.1)	6.1 (2.3)	4.8 (2.9)	5.2 (1.5)	6.4 (3.2)	4.3 (3.6)
Orthopyroxene	4.0 (1.4)	3.7 (1.0)	3.6 (1.8)	4.7 (1.3)	4.1 (1.5)	3.1 (0.2)
Opaques	1.8 (0.9)	2.4 (1.8)	2.6 (3.0)	1.6 (0.7)	1.8 (0.5)	3.8 (0.7)
Olivine	1.1 (0.9)	1.3 (0.4)	0.6 (0.5)	0.3 (0.3)	0.2 (0.2)	n.p.
Amphibole	n.p.	0.0 (0.1)	n.p.	0.0 (0.1)	0.1 (0.1)	6.1 (5.2)
Apatite	n.p.	n.p.	n.p.	0.0 (0.1)	0.0 (0.1)	n.p.
Anhydrite	0.0 (0.1)	n.p.	n.p.	0.0 (0.1)	n.p.	0.0 (0.1)
Total phenocrysts	36.7 (4.9)	39.5 (3.4)	37.7 (10.4)	40.0 (6.5)	44.8 (7.2)	73.6 (11.9)
Crystalline groundmass	63.1 (5.0)	60.2 (3.7)	51.5 (29.3)	21.6 (24.7)	1.2 (1.5)	0.1 (0.1)
Glass	0.1 (0.2)	0.0 (0.1)	10.7 (23.4)	38.3 (26.0)	53.9 (6.5)	26.3 (12.0)
Voids	33.4 (5.3)	19.8 (4.0)	22.1 (3.4)	38.7 (9.5)	37.4 (7.9)	29.8 (2.9)
n	12	7	5	8	7	2

Table 3. Representative whole-rock compositions of Augustine 2006 eruptive products.

[The prefix "06AU" has been truncated from all sample IDs. Total iron (FeO_t) as FeO]

Phase	Explosive				Continuous		Effusive		
Map unit	ExPfc	RPpf	ExPfc	RPpf	Cpf	Cpf	EfLf	Efba	EfLf
Lithology	DLSA	LSAS	DIA	HSA	DIA	HSA	DLSA	DIA	DIA
Sample ID	MRT037f	MRT009b	MRT037e	MC004c1	MRT017a	MRT017b	MLC057	KB002C	MLC028
Major elements measured by XRF in weight percent normalized to 100. LOI not determined. Total is original analytical total.									
SiO_2	57.07	57.20	58.39	62.52	59.97	62.27	57.07	59.11	62.23
TiO_2	0.732	0.711	0.682	0.558	0.625	0.555	0.729	0.668	0.569
Al_2O_3	17.59	17.79	17.37	16.48	17.00	16.92	17.46	17.05	16.77
FeO_t	6.70	6.71	6.38	5.39	5.98	5.19	6.60	6.27	5.26
MnO	0.144	0.148	0.144	0.129	0.137	0.126	0.143	0.139	0.128
MgO	4.87	4.57	4.49	3.43	4.09	3.28	5.04	4.40	3.37
CaO	8.59	8.52	8.11	6.58	7.60	6.71	8.74	7.94	6.73
Na_2O	3.45	3.50	3.53	3.78	3.59	3.81	3.38	3.48	3.82
K_2O	0.720	0.697	0.770	0.999	0.875	0.983	0.702	0.804	0.996
P_2O_5	0.125	0.141	0.134	0.137	0.133	0.139	0.127	0.134	0.134
Total	98.76	99.13	99.05	100.34	98.60	99.43	98.42	99.73	98.66
Trace elements measured by XRF, in ppm.									
Ni	28.6	24.3	26.0	19.9	26.5	18.7	35.9	32.2	20.6
Cr	62.0	52.7	56.5	45.3	51.8	41.7	82.0	67.0	45.7
Sc	26.4	23.2	23.0	17.7	21.3	17.3	26.6	23.0	17.5
V	204	194	186	134	164	131	203	179	139
Ba	306	303	340	457	386	443	301	356	435
Rb	12.5	12.6	13.8	19.4	16.0	19.6	12.6	14.5	19.7
Sr	324	342	328	321	320	329	319	318	323
Zr	86	86	91	114	102	107	85	96	107
Y	20.9	20.6	21.1	20.9	22.8	20.3	20.1	19.6	21.0
Nb	2.2	1.5	2.3	3.0	2.7	1.9	1.2	2.1	2.0
Ga	17.3	18.2	17.3	14.9	17.1	15.3	16.4	17.2	17.5
Cu	36.3	35.2	33.7	24.3	31.5	17.3	18.2	25.2	22.5
Zn	65.7	63.7	64.7	60.1	61.2	58.1	61.0	57.1	56.4
Trace elements measured by ICPMS, in ppm.									
La	7.81	7.90	8.60	9.92	9.68	10.56	7.83	9.12	10.51
Ce	17.40	17.57	18.94	21.22	21.11	22.66	17.40	20.07	22.50
Pr	2.474	2.503	2.653	2.860	2.893	3.024	2.485	2.802	3.021
Nd	11.10	11.41	11.68	12.26	12.61	13.19	11.14	12.34	12.85
Sm	2.900	3.034	3.106	3.042	3.205	3.198	2.945	3.211	3.184
Eu	1.003	1.019	1.012	0.903	1.006	1.001	1.001	1.020	0.965
Gd	3.306	3.349	3.309	3.072	3.505	3.366	3.301	3.439	3.285
Tb	0.576	0.580	0.579	0.539	0.614	0.573	0.575	0.590	0.576
Dy	3.614	3.697	3.691	3.438	4.016	3.653	3.737	3.794	3.621
Ho	0.766	0.776	0.770	0.718	0.852	0.765	0.767	0.799	0.763
Er	2.141	2.202	2.210	2.067	2.414	2.166	2.145	2.278	2.205
Tm	0.328	0.332	0.335	0.319	0.362	0.340	0.329	0.351	0.332
Yb	2.111	2.152	2.165	2.084	2.394	2.180	2.128	2.244	2.204
Lu	0.344	0.350	0.352	0.345	0.386	0.363	0.344	0.363	0.364

Table 3. Representative whole-rock compositions of Augustine 2006 eruptive products.—Continued

[The prefix "06AU" has been truncated from all sample IDs. Total iron (FeO_t) as FeO]

Phase	Explosive				Continuous		Effusive		
Map unit	ExPfc	RPpf	ExPfc	RPpf	Cpf	Cpf	EfLf	Efba	EfLf
Lithology	DLSA	LSAS	DIA	HSA	DIA	HSA	DLSA	DIA	DIA
Sample ID	MRT037f	MRT009b	MRT037e	MC004c1	MRT017a	MRT017b	MLC057	KB002C	MLC028
	Trace elements measured by ICPMS, in ppm.								
Ba	305	296	337	415	381	439	299	356	440
Th	1.446	1.376	1.615	2.082	1.930	2.144	1.454	1.757	2.143
Nb	2.088	2.028	2.286	2.576	2.526	2.702	2.056	2.387	2.693
Y	19.87	20.42	20.17	19.20	22.24	20.32	19.60	20.71	20.47
Hf	2.388	2.303	2.560	2.837	2.742	2.937	2.341	2.676	2.998
Ta	0.145	0.147	0.159	0.187	0.180	0.193	0.145	0.168	0.192
U	0.582	0.561	0.661	0.847	0.796	0.886	0.585	0.732	0.909
Pb	1.897	1.855	2.125	2.503	2.352	2.686	2.037	1.351	2.648
Rb	12.59	12.25	13.91	17.40	16.07	18.32	12.42	14.83	18.90
Cs	0.284	0.267	0.314	0.415	0.362	0.400	0.272	0.332	0.412
Sr	319	337	325	288	316	327	313	318	322
Sc	24.35	23.39	22.28	15.65	20.16	16.31	25.20	22.71	16.39
Zr	80.8	81.9	87.1	98.8	97.6	103.6	80.2	92.7	104.0

Table 4. Groundmass glass average compositions of Augustine 2006 eruptive products by lithology and sample.

[Sample lithology acronyms are as noted in text. FeO_t—All Fe analyzed as FeO. Analyses reported are normalized to 100% volatile-free. Original totals are reported. n denotes the total number of analyses averaged to give the reported glass compositions. Numbers in parentheses are the standard deviations from the averaged analyses (n total from each thin section)]

Sample-	06AUMC005c	06AUMRT037c	06AUMC007c	06AUMRT009b	06AUMRT037b	06AUMC008a
	LSAS	LSAS	LSAS	DLSA	DLSA	Banded
SiO_2	71.16 (1.57)	77.38 (0.52)	67.48 (1.02)	70.04 (2.07)	68.98 (2.70)	69.25
TiO_2	0.97 (0.29)	0.37 (0.05)	1.17 (0.19)	1.13 (0.12)	0.65 (0.28)	1.33
Al_2O_3	13.72 (0.92)	11.90 (0.28)	14.33 (0.37)	13.77 (0.72)	15.16 (1.30)	13.88
FeO_t	4.03 (0.46)	1.71 (0.19)	5.38 (0.66)	4.04 (0.31)	3.54 (0.69)	4.04
MnO	0.12 (0.07)	0.07 (0.08)	0.17 (0.10)	0.01 (0.00)	0.05 (0.03)	0.07
MgO	0.90 (0.11)	0.37 (0.05)	1.40 (0.21)	0.74 (0.12)	0.64 (0.19)	0.57
CaO	3.13 (0.49)	1.30 (0.18)	4.05 (0.25)	3.37 (0.89)	4.14 (1.07)	3.39
Na_2O	3.37 (0.42)	3.90 (0.12)	3.65 (0.23)	4.21 (0.57)	4.65 (0.59)	4.65
K_2O	2.06 (0.24)	2.90 (0.14)	1.76 (0.18)	1.93 (0.13)	1.80 (0.30)	2.08
P_2O_5	0.23 (0.08)	0.02 (0.04)	0.30 (0.05)	0.46 (0.36)	0.19 (0.08)	0.36
Cl	0.30 (0.08)	0.07 (0.02)	0.31 (0.03)	0.29 (0.03)	0.20 (0.07)	0.38
Totals	99.15	100.18	100.02	100.30	98.53	98.56
n	13	6	11	3	6	1

Table 4. Groundmass glass average compositions of Augustine 2006 eruptive products by lithology and sample.—Continued

[Sample lithology acronyms are as noted in text. FeO_t—All Fe analyzed as FeO. Analyses reported are normalized to 100% volatile-free. Original totals are reported. n denotes the total number of analyses averaged to give the reported glass compositions. Numbers in parentheses are the standard deviations from the averaged analyses (n total from each thin section)]

Sample	06AUMC005c	06AUMRT017a	06AUMRT037e	06AUKFB128	06AUMC004a	06AUMRT017b
	Banded	DIA	DIA	HSA	HSA	HSA
SiO_2	75.54 (0.61)	72.07 (3.65)	69.68	75.70 (0.42)	75.73 (0.68)	75.52 (0.51)
TiO_2	0.38 (0.13)	0.39 (0.12)	0.26	0.43 (0.19)	0.45 (0.18)	0.33 (0.13)
Al_2O_3	12.57 (0.29)	14.23 (1.78)	15.49	12.86 (0.16)	12.85 (0.39)	12.96 (0.34)
FeO_t	1.89 (0.16)	2.52 (0.72)	2.90	1.91 (0.11)	2.05 (0.18)	2.02 (0.16)
MnO	0.07 (0.07)	0.16 (0.08)	0.09	0.05 (0.04)	0.08 (0.08)	0.06 (0.03)
MgO	0.46 (0.13)	0.84 (0.49)	0.58	0.41 (0.04)	0.42 (0.06)	0.41 (0.04)
CaO	2.08 (0.24)	3.51 (1.18)	3.83	2.10 (0.13)	2.08 (0.06)	2.11 (0.17)
Na_2O	4.46 (0.33)	4.08 (0.95)	4.79	4.10 (0.19)	3.83 (0.38)	4.16 (0.16)
K_2O	2.10 (0.13)	1.83 (0.39)	1.78	2.12 (0.10)	2.16 (0.22)	2.07 (0.13)
P_2O_5	0.07 (0.04)	0.12 (0.07)	0.18	0.07 (0.05)	0.08 (0.03)	0.09 (0.03)
Cl	0.39 (0.07)	0.27 (0.07)	0.43	0.25 (0.07)	0.26 (0.06)	0.28 (0.07)
Totals	99.82	99.95	100.12	99.51	99.42	99.21
n	19	7	1	30	52	9

Sample	06AUKFB128	06AUMC004a	06AUMRT017b	06AUMC009p1
	HSA	HSA	HSA	HSA
SiO_2	75.70 (0.42)	75.73 (0.68)	75.52 (0.51)	75.34 (0.25)
TiO_2	0.43 (0.19)	0.45 (0.18)	0.33 (0.13)	0.28 (0.15)
Al_2O_3	12.86 (0.16)	12.85 (0.39)	12.96 (0.34)	12.80 (0.26)
FeO_t	1.91 (0.11)	2.05 (0.18)	2.02 (0.16)	1.83 (0.09)
MnO	0.05 (0.04)	0.08 (0.08)	0.06 (0.03)	0.09 (0.06)
MgO	0.41 (0.04)	0.42 (0.06)	0.41 (0.04)	0.36 (0.03)
CaO	2.10 (0.13)	2.08 (0.06)	2.11 (0.17)	2.03 (0.14)
Na_2O	4.10 (0.19)	3.83 (0.38)	4.16 (0.16)	4.69 (0.20)
K_2O	2.12 (0.10)	2.16 (0.22)	2.07 (0.13)	2.07 (0.06)
P_2O_5	0.07 (0.05)	0.08 (0.03)	0.09 (0.03)	0.09 (0.05)
Cl	0.25 (0.07)	0.26 (0.06)	0.28 (0.07)	0.42 (0.07)
Totals	99.51	99.42	99.21	99.50
n	30	52	9	5

Table 5. Representative pyroxene phenocryst compositions

[Acronyms of sample lithologies are as noted in the text. FeO_t – All Fe analyzed as FeO. Mole fractions of the wollastonite (Wo), enstatite (En), and ferrosilite (Fs) pyroxene quadrilateral components. Mg# is molar Mg /(Mg+Fe). n is the number of individual analyses averaged to provide representative data. Numbers in parentheses are standard deviations about the average representative analyses]

[Core compositions]

	LSAS Opx	LSAS Cpx	DLSA Opx	DLSA Cpx	DIA Opx	DIA Cpx
SiO_2	53.29 (0.72)	52.39 (0.57)	53.33 (0.10)	51.64 (0.26)	52.69 (0.36)	52.10 (0.18)
TiO_2	0.12 (0.03)	0.29 (0.14)	0.16 (0.03)	0.33 (0.13)	0.14 (0.03)	0.26 (0.08)
Al_2O_3	0.80 (0.16)	1.46 (0.45)	0.85 (0.03)	1.78 (0.22)	1.36 (0.70)	1.26 (0.16)
FeO_t	19.81 (0.15)	9.16 (0.64)	20.22 (0.45)	9.01 (0.10)	19.45 (2.43)	8.92 (0.28)
MnO	0.71 (0.05)	0.40 (0.16)	0.76 (0.04)	0.35 (0.09)	0.77 (0.36)	0.52 (0.03)
MgO	23.95 (0.36)	14.76 (0.27)	24.32 (0.23)	14.77 (0.13)	24.46 (1.61)	14.56 (0.20)
CaO	1.05 (0.11)	21.93 (0.27)	1.16 (0.25)	21.39 (1.36)	0.99 (0.34)	23.10 (0.15)
Na_2O	0.04 (0.01)	0.35 (0.06)	0.04 (0.05)	0.35 (0.06)	0.02 (0.03)	0.36 (0.02)
Totals	99.76	100.74	100.84	99.61	99.89	101.05
Wo	2	43	2	43	2	45
En	66	41	66	41	67	40
Fs	32	15	32	15	31	15
Mg #	0.68	0.74	0.68	0.75	0.69	0.75
n	5	3	3	2	3	2

	Banded Opx	Banded Cpx	HSA Opx	HSA Cpx
SiO_2	53.57 (0.39)	51.27 (2.74)	52.68 (0.83)	51.54
TiO_2	0.17 (0.02)	0.63 (0.63)	0.20 (0.04)	0.48
Al_2O_3	0.73 (0.13)	3.29 (3.17)	0.94 (0.15)	4.27
FeO_t	20.01 (0.49)	8.44 (0.72)	19.69 (1.34)	5
MnO	0.71 (0.04)	0.33 (0.13)	0.74 (0.18)	0.05
MgO	24.06 (0.24)	14.60 (0.85)	23.45 (0.79)	16.43
CaO	1.07 (0.09)	22.16 (0.30)	2.33 (2.38)	20.58
Na_2O	0.02 (0.02)	0.28 (0.04)	0.04 (0.06)	0.2
Totals	100.33	101.00	100.06	98.54
Wo	2	45	5	43.11
En	66	41	64	47.88
Fs	32	14	31	8.28
Mg #	0.68	0.76	0.68	0.85
n	4	4	3	1

Table 5. Representative pyroxene phenocryst compositions.—Continued

[Acronyms of sample lithologies are as noted in the text. FeO_t—All Fe analyzed as FeO. Mole fractions of the wollastonite (Wo), enstatite (En), and ferrosilite (Fs) pyroxene quadrilateral components. Mg# is molar Mg /(Mg+Fe). n is the number of individual analyses averaged to provide representative data. Numbers in parentheses are standard deviations about the average representative analyses]

[Rim compositions]

	LSAS Opx rim	LSAS Cpx rim 1	LSAS Cpx rim 2	DLSA Opx rim 1	DLSA Opx rim 2	DLSA Cpx rim	DIA Opx rim 1
SiO_2	53.75 (0.49)	50.44 (1.14)	53.96	53.04 (0.04)	49.06	51.48 (0.15)	53.21 (0.35)
TiO_2	0.15 (0.04)	0.75 (0.21)	0.18	0.16 (0.04)	0.75	0.30 (0.10)	0.16 (0.00)
Al_2O_3	0.84 (0.07)	4.41 (1.15)	1.49	0.80 (0.07)	5.11	1.62 (0.19)	0.79 (0.01)
FeO_t	19.49 (0.61)	8.52 (0.98)	19.07	19.31 (0.81)	7.03	9.15 (0.15)	20.32 (0.64)
MnO	0.65 (0.02)	0.12 (0.04)	0.61	0.67 (0.05)	0.17	0.37 (0.01)	0.78 (0.04)
MgO	24.18 (0.15)	15.06 (0.62)	23.95	24.40 (0.55)	15.28	14.97 (0.11)	24.37 (0.59)
CaO	1.06 (0.06)	20.40 (0.11)	1.26	1.10 (0.01)	20.52	21.94 (0.13)	1.07 (0.14)
Na_2O	0.01 (0.01)	0.24 (0.06)	0.23	0.03 (0.02)	0.27	0.35 (0.01)	0.01 (0.01)
Totals	100.13	99.92	100.75	99.48	98.2	100.15	100.70
Wo	2	42	3	2	42.87	43	2
En	67	43	66	67	44.42	41	66
Fs	31	14	31	31	11.67	15	32
Mg #	0.69	0.76	0.69	0.69	0.79	0.75	0.68
n	5	2	1	2	1	2	2

	DIA Opx rim 2	DIA Cpx rim	Banded Opx rim 1	Banded Opx rim 2	Banded Cpx rim	HSA Opx rim 1	HSA Opx rim 2	HSA Cpx rim
SiO_2	51.99	51.71 (0.74)	53.41 (0.74)	52.33	51.68 (1.70)	53.47 (0.23)	52.86	50.88
TiO_2	0.35	0.68 (0.01)	0.16 (0.03)	0.36	0.51 (0.34)	0.18 (0.02)	0.24	0.42
Al_2O_3	2.17	2.26 (0.39)	0.78 (0.19)	1.25	2.56 (1.44)	0.74 (0.06)	1.35	3.7
FeO_t	8.88	9.84 (0.74)	20.46 (0.35)	8.16	9.36 (0.57)	19.96 (0.22)	9.00	6.78
MnO	0.25	0.37 (0.13)	0.65 (0.05)	0.37	0.26 (0.06)	0.75 (0.15)	0.36	0.21
MgO	17.43	14.55 (0.07)	24.09 (0.45)	15.01	14.79 (0.40)	24.22 (0.11)	14.96	15.96
CaO	19.84	20.80 (0.37)	1.16 (0.11)	22.23	21.55 (1.22)	1.08 (0.10)	21.91	22.04
Na_2O	0.28	0.36 (0.03)	0.00 (0.00)	0.33	0.34 (0.05)	0.03 (0.04)	0.32	0.22
Totals	101.19	100.57	100.73	100.04	101.04	100.41	101.00	100.22
Wo	38	42	2	44.15	43	2	43.32	44.02
En	47	41	66	41.49	41	66	41.18	44.36
Fs	14	16	32	13.16	15	32	14.37	10.82
Mg #	0.78	0.73	0.68	0.77	0.74	0.69	0.75	0.81
n	1	2	3	1	4	2	1	1

Table 6. Representative Fe-Ti oxide pair analyses, temperatures, and oxygen fugacities from Augustine 2006 eruptive products.

[All analyses are averages of multiple points on individual grains; 1 standard deviation is in parentheses. Four select pairs from each lithology were chosen to represent the range of compositions, temperatures, and oxygen fugacities calculated from the oxide probe data. FeO_t is total Fe calculated to FeO. n is the number of analyses per grain. Temperature and oxygen fugacity (f_{O_2}) calculated using QUILF (Andersen and others, 1993) and then decreased by 30 degrees °C because the QUILF algorithm overestimates temperatures by 30 °C in magma with oxygen fugacity RRO (Rutherford and Devine, 1996)]

[HSA lithology]

	06AUMC010p1		06AUMC010p1		06AUMC010p1		06AUMC010p1		06AUMC005cp1		06AUMC005cp1		06AUMC005cp1		06AUMC005cp1	
	HSA		HSA		HSA		HSA		Banded		Banded		Banded		Banded	
Ti-magnetite																
	Pair 2a		Pair 3		Pair 5		Pair 8		Pair 1a		Pair 2		Pair 4		Pair 5	
TiO_2	8.05	(0.30)	7.12	(0.49)	7.54	(0.47)	7.68	(0.67)	7.28	(0.53)	7.34	(0.45)	7.37	(0.22)	7.28	(0.53)
Al_2O_3	2.36	(0.14)	2.19	(0.09)	2.07	(0.06)	2.00	(0.10)	2.00	(0.09)	2.04	(0.07)	1.99	(0.08)	2.00	(0.09)
FeO_t	81.17	(0.97)	82.08	(0.92)	80.12	(0.75)	82.87	(1.62)	82.17	(2.15)	81.26	(1.30)	82.57	(0.45)	82.17	(2.15)
MnO	0.42	(0.11)	0.47	(0.07)	0.41	(0.08)	0.45	(0.10)	0.43	(0.11)	0.42	(0.11)	0.40	(0.11)	0.43	(0.11)
MgO	1.95	(0.09)	1.80	(1.80)	1.72	(0.06)	1.70	(0.05)	1.59	(0.04)	1.61	(0.04)	1.55	(0.05)	1.59	(0.04)
Cr_2O_3	0.24	(0.05)	0.28	(0.07)	0.28	(0.04)	0.24	(0.06)	0.27	(0.03)	0.29	(0.04)	0.27	(0.05)	0.27	(0.03)
SiO_2	0.07	(0.01)	0.11	(0.11)	0.11	(0.04)	0.08	(0.02)	0.08	(0.04)	0.05	(0.03)	0.04	(0.05)	0.08	(0.04)
Total	94.26		94.05		92.31		95.02		98.32		93.01		94.19		92.47	
n	4		7		9		11		15		9		9		11	
Ilmenite																
TiO_2	35.15	(1.95)	33.58	(3.44)	33.19	(2.15)	31.14	(1.74)	34.03	(1.65)	33.22	(2.48)	32.75	(1.97)	34.03	(1.65)
Al_2O_3	0.43	(0.02)	0.40	(0.121)	0.39	(0.39)	0.40	(0.04)	0.36	(0.04)	0.37	(0.03)	0.37	(0.04)	0.36	(0.04)
FeO_t	59.23	(1.12)	59.18	(1.41)	58.35	(0.52	60.69	(1.28)	58.66	(1.47)	60.86	(0.94)	60.02	(0.36)	58.66	(1.47)
MnO	0.26	(0.06)	0.33	(0.05)	0.27	(0.03)	0.28	(0.05)	0.27	(0.08)	0.29	(0.11)	0.27	(0.10)	0.27	(0.08)
MgO	2.03	(0.03)	1.92	(0.11)	1.79	(0.04)	1.60	(0.05)	1.77	(0.07)	1.58	(0.08)	1.63	(0.04)	1.77	(0.07)
Cr_2O_3	0.12	(0.06)	0.10	(0.05)	0.09	(0.03)	0.11	(0.07)	0.08	(0.07)	0.12	(0.05)	0.10	(0.04)	0.08	(0.07)
SiO_2	0.01	(0.02)	0.03	(0.04)	0.01	(0.01)	0.07	(0.07)	0.04	(0.04)	0.04	(0.09)	0.01	(0.02)	0.04	(0.04)
Total	97.23		95.54		94.09		94.28		95.21		96.48		95.14		94.13	
n	3		7		6		8		5		11		13		5	
T (°C)	840		823		839		855		826		837		838		840	
$\log f_{O_2}$	-10.57		-10.72		-10.53		-10.16		-10.75		-10.51		-10.50		-10.40	

Table 6. Representative Fe-Ti oxide pair analyses, temperatures, and oxygen fugacities from Augustine 2006 eruptive products.—Continued

[All analyses are averages of multiple points on individual grains; 1 standard deviation is in parentheses. Four select pairs from each lithology were chosen to represent the range of compositions, temperatures, and oxygen fugacities calculated from the oxide probe data. FeO_t is total Fe calculated to FeO. n is the number of analyses per grain. Temperature and oxygen fugacity (f_{O_2}) calculated using QUILF (Andersen and others, 1993) and then decreased by 30 degrees °C because the QUILF algorithm overestimates temperatures by 30 °C in magma with oxygen fugacity RRO (Rutherford and Devine, 1996)]

[DIA and DLA lithologies]

	06AUMRT006		06AUMRT006		06AUJFL001b		06AUMRT009b		06AUMC008bp1		06AUMC008bp1		06AUMC008bp1		06AUMC005cp5	
	DIA		DIA		DIA		DLSA		LSAS		LSAS		LSAS		LSAS	
Ti-magnetite	DIA Pair 1		Pair 3		Pair 1		Pair 1		Pair 1		Pair 3		Pair 6		Pair 4	
TiO_2	8.31	(1.00)	7.54	(0.75)	7.22	(0.43)	10.19	(0.93)	7.73	(0.35)	8.01	(1.06)	11.33	(1.57)	10.40	(1.15)
Al_2O_3	2.18	(0.08)	1.88	(0.21)	2.06	(0.08)	2.11	(0.06)	1.92	(0.10)	2.25	(0.06)	3.20	(0.27)	3.33	(0.13)
FeO_t	81.39	(1.20)	81.22	(0.63)	82.52	(0.79)	80.05	(1.27)	81.72	(1.23)	81.55	(0.95)	76.54	(0.65)	78.72	(0.65)
MnO	0.42	(0.13)	0.43	(0.08)	0.43	(0.07)	0.43	(0.07)	0.40	(0.40)	0.43	(0.09)	0.41	(0.07)	0.36	(0.07)
MgO	2.09	(0.09)	1.94	(0.14)	1.73	(0.04)	2.55	(0.09)	2.00	(0.05)	2.09	(0.08)	2.77	(0.25)	3.05	(0.13)
Cr_2O_3	0.27	(0.04)	0.22	(0.02)	0.30	(0.06)	0.30	(0.04)	0.29	(0.05)	0.31	(0.07)	0.12	(0.02)	0.18	(0.07)
SiO_2	0.29	(0.06)	0.50	(0.36)	0.51	(0.19)	0.27	(0.07)	0.05	(0.02)	0.04	(0.04)	0.11	(0.03)	0.13	(0.20)
Total	94.96		93.72		94.77		95.90		94.10		94.69		94.48		96.16	
n	15		6		14		14		11		5		5		6	
Ilmenite																
TiO_2	34.11	(1.95)	34.88	(2.01)	32.29	(2.06)	35.36	(1.54)	36.38	(2.68)	36.34	(1.25)	36.01	(0.73)	30.82	(5.10)
Al_2O_3	0.44	(0.04)	0.36	(0.04)	0.38	(0.05)	0.52	(0.08)	0.49	(0.21)	0.41	(0.04)	0.63	(0.03)	0.91	(0.51)
FeO_t	59.86	(0.97)	59.37	(0.91)	60.45	(1.20)	58.37	(1.13)	57.60	(2.23)	57.46	(0.66)	59.34	(0.48)	60.62	(3.68)
MnO	0.26	(0.08)	0.28	(0.07)	0.24	(0.10)	0.25	(0.04)	0.26	(0.10)	0.32	(0.06)	0.18	(0.07)	0.23	(0.12)
MgO	2.05	(0.08)	1.96	(0.06)	1.77	(0.14)	2.37	(0.16)	2.41	(0.14)	2.20	(0.09)	2.56	(0.05)	2.95	(0.33)
Cr_2O_3	0.11	(0.04)	0.10	(0.06)	0.11	(0.04)	0.12	(0.03)	0.06	(0.05)	0.11	(0.06)	0.12	(0.02)	0.12	(0.04)
SiO_2	0.12	(0.16)	0.18	(0.11)	0.46	(0.24)	0.17	(0.05)	0.05	(0.08)	0.02	(0.02)	0.01	(0.01)	0.03	(0.02)
Total	96.95		97.12		95.70		97.17		97.24		96.86		98.85		95.68	
n	13		13		16		7		9		6		4		4	
T (°C)	853		829		836		890		825		827		925		968	
$\log f_{O_2}$	-10.31		-10.70		-10.48		-9.91		-10.87		-10.84		-9.45		-8.51	

Table 7. Representative olivine analyses from Augustine 2006 eruptive products.

[Each analysis is representative of one point from core or rim of olivine crystal. Relative error is less than 1 % on each analysis. Texture refers to symplectite rimmed (Symplectite), euhedral unrimmed (Euhedral), pyroxene rimmed (Px rimmed), and hopper (Hopper) olivine respectively. FeO_t is total Fe calculated as Fe^{2+}. Fo is mole percent forsterite content. Mg# is mols Mg divided by total mols of Mg, Fe^{2+}, and Fe^{3+}]

	HSA		Banded		Banded		DIA		DIA	
Sample ID	06AUMRT017b		06AUMRT037a		06AUMC008a		06AUJFL001b		06AUJFL001b	
Texture	Symplectite		Symplectite		Euhedral		Symplectite		Px rimmed	
	Core	Rim	Core	Rim	Core	Rim	Core	Rim	Core	Rim
SiO_2	39.22	38.25	38.42	37.75	39.24	39.40	39.64	38.06	40.42	40.26
TiO_2	0.03	0.01	0.02	0.00	0.04	0.04	0.02	0.05	0.01	0.01
Cr_2O_3	0.01	0.02	0.00	0.00	0.03	0.11	0.01	0.00	0.00	0.05
FeOt	17.33	22.01	20.74	21.18	15.09	14.80	20.20	23.05	13.70	13.71
MnO	0.37	0.36	0.36	0.46	0.20	0.22	0.44	0.50	0.27	0.05
MgO	44.54	40.58	39.68	40.12	43.70	43.36	40.14	38.78	46.97	46.28
CaO	0.13	0.05	0.06	0.09	0.15	0.11	0.07	0.06	0.16	0.18
Total	101.78	101.48	99.44	99.76	98.45	98.05	100.54	100.68	101.76	100.62
Fo	81.77	76.38	77.02	76.76	83.58	83.73	77.60	74.58	85.70	85.71
Mg#	0.82	0.77	0.77	0.77	0.84	0.84	0.78	0.75	0.86	0.86

	DLSA		DLSA		DLSA		LSAS		LSAS	
Sample ID	06AUMRT032a		06AUMRT032a		06AUMC008bp3		06AUJFL001e		06AUMC008bp1	
Texture	Euhedral		Hopper		Symplectite		Px rimmed		Euhedral	
	Core	Rim	Core	Rim	Core	Rim	Core	Rim	Core	Rim
SiO_2	40.31	41.00	39.13	38.73	40.21	39.42	39.24	38.45	39.81	38.91
TiO_2	0.00	0.00	0.03	0.00	0.00	0.02	0.02	0.00	0.10	0.02
Cr_2O_3	0.03	0.03	0.03	0.04	0.00	0.03	0.01	0.03	0.04	0.05
FeOt	13.06	13.22	16.02	19.17	21.45	20.41	14.42	15.16	15.76	18.74
MnO	0.12	0.23	0.27	0.39	0.45	0.30	0.28	0.18	0.20	0.37
MgO	46.89	46.04	45.73	43.14	37.97	38.30	46.47	45.30	43.20	40.49
CaO	0.18	0.18	0.17	0.15	0.05	0.06	0.16	0.16	0.17	0.19
Total	100.89	100.98	101.60	101.87	100.14	98.54	100.82	99.49	99.29	98.77
Fo	86.38	85.92	83.34	79.72	75.54	76.72	84.92	84.03	82.82	79.07
Mg#	0.86	0.86	0.84	0.80	0.76	0.77	0.85	0.84	0.83	0.79

Table 8. Representative amphibole phenocryst compositions from Augustine 2006 eruptive products.

[Sample lithology acronyms are as noted in the text. One standard deviation is in parentheses. FeO_t is total Fe calculated as Fe^{2+}. Compositions are averages of n points on a single phenocryst]

	06AUMC004cp1	06aujfl001b	06aumrt032b	06aumrt037e	06aumrt037c	06aumc013a
	HSA	DIA	DIA	DIA	LSAS	FGGI
SiO_2	45.52 (0.61)	42.74 (0.42)	45.84 (0.22)	45.90	44.28 (0.17)	45.00 (0.80)
TiO_2	2.03 (0.48)	2.10 (0.63)	1.48 (0.33)	1.81	1.44 (0.12)	1.52 (0.62)
Al_2O_3	8.15 (0.17)	12.09 (0.19)	8.63 (0.11)	9.21	9.31 (0.21)	9.26 (0.52)
FeO_t	11.63 (0.28)	10.97 (0.36)	12.64 (0.38)	12.70	13.00 (0.33)	12.08 (0.41)
MnO	0.25 (0.04)	0.18 (0.06)	0.37 (0.14)	0.37	0.44 (0.09)	0.38 (0.11)
MgO	15.68 (0.15)	14.89 (0.07)	14.91 (0.18)	14.91	14.77 (0.29)	15.14 (0.29)
CaO	11.83 (0.63)	12.17 (0.56)	12.86 (0.38)	12.29	11.15 (0.85)	12.75 (0.10)
K_2O	0.15 (0.02)	0.24 (0.01)	0.12 (0.02)	0.22	0.17 (0.03)	0.11 (0.04)
Na_2O	1.77 (0.21)	2.30 (0.19)	1.64 (0.05)	1.74	1.78 (0.07)	1.79 (0.15)
Cl	0.06 (0.04)	0.05 (0.04)	0.07 (0.4)	0.06	0.06 (0.01)	0.08 (0.02)
Total	97.08 (1.09)	97.73 (0.72)	98.56 (0.82)	99.22	96.38 (1.61)	98.10 (0.69)
n	4	5	4	1	3	4

Appendixes 1–5. Additional Descriptions and Compositional Data for Samples Used in This Study

Appendix 1. Samples of Augustine Volcano 2006 eruptive products used in this study, sorted by eruptive unit and lithologic type.

[This appendix appears only in the digital version of this work—in the DVD-ROM that accompanies the printed volume and as a separate file accompanying this chapter on the Web at http://pubs.usgs.gov/pp/1769]

This table lists samples of Augustine Volcano 2006 eruptive products used in this study. The samples are sorted by eruptive unit and lithologic type.

Appendix 2. Modal Mineralogy and Point Count Data for the Augustine Eruptive Lithologies.

[This appendix appears only in the digital version of this work—in the DVD-ROM that accompanies the printed volume and as a separate file accompanying this chapter on the Web at http://pubs.usgs.gov/pp/1769]

This table presents the modal mineralogy data, determined from 1,000 point counts from thin sections of each lithology. These data form the basis for the average modal mineralogy data presented in table 2 and figure 4.

Appendix 3. Augustine Whole-Rock Geochemical Analyses.

[This appendix appears only in the digital version of this work—in the DVD-ROM that accompanies the printed volume and as a separate file accompanying this chapter on the Web at http://pubs.usgs.gov/pp/1769]

This appendix includes data collected by the Washington State University Geoanalytical Laboratory for the Alaska Volcano Observatory. The data include analyses from 2006 Augustine eruptive products, as well as pre-2006 historical, and early Holocene and Pleistocene samples.

Appendix 4. Groundmass Glass Electron Microprobe Analyses from Augustine 2006 Samples used in this Study.

[This appendix appears only in the digital version of this work—in the DVD-ROM that accompanies the printed volume and as a separate file accompanying this chapter on the Web at http://pubs.usgs.gov/pp/1769]

This appendix includes glass compositional analyses from several major lithologies form the 2006 eruptive products. It also includes glass data from tephra samples from December 24, 2005 and January 13, 14, and 17,2006. Tephra analyses from 1986 samples are also included for comparison. The data included in this appendix is also plotted in figure 11 in the text.

Appendix 5. Representative Electron Microprobe Analyses of Plagioclase Phenocrysts in Augustine 2006 Samples used in this Study.

[This appendix appears only in the digital version of this work—in the DVD-ROM that accompanies the printed volume and as a separate file accompanying this chapter on the Web at http://pubs.usgs.gov/pp/1769]

The electron microprobe analyses presented here represent the core to rim transects shown in figure 12 of the text.

The 2006 Eruption of Augustine Volcano, Alaska
Power, J.A., Coombs, M.L., and Freymueller, J.T., editors
U.S. Geological Survey Professional Paper 1769

Chapter 16

Augustine Volcano—The Influence of Volatile Components in Magmas Erupted A.D. 2006 to 2,100 Years Before Present

By James D. Webster[1], Charles W. Mandeville[1], Beth Goldoff[1], Michelle L. Coombs[2], and Christine Tappen[3]

Abstract

The petrology and geochemistry of 2006 eruptive products of Augustine Volcano, Alaska, have been investigated through analyses of whole-rock samples, phenocrysts, silicate melt inclusions, and matrix glasses to constrain processes of magma evolution, eruption, and degassing. Particular attention was directed toward the concentrations and geochemical relationships involving the magmatic volatile components H_2O, CO_2, S, and Cl. The analytical results for 2006 samples have been integrated with data for samples of Pleistocene basalt, prehistoric andesites, and 1986 andesites from Augustine to provide a broad view of volatile behavior in Augustine magmas. The observation of generally similar geochemical features for this range of eruptions indicates that magmatic and volatile degassing processes have been relatively consistent during the past 2,100 years.

Augustine andesites range from low-silica to high-silica compositions and contain phenocrysts of plagioclase, orthopyroxene, and clinopyroxene, with lesser olivine, amphiboles, iron-titanium oxides, and apatite. The groundmass varies from strongly crystallized and/or oxidized to comparatively clear, microlite-poor vesicular glass. Coexisting iron-titanium oxides of 2006 rock samples, which are generally consistent with those of prior eruptive materials, indicate f_{O_2} values of approximately NNO+1.5 to NNO+2.5 and oxide crystallization temperatures of 835 to 1,052°C.

The compositions of matrix and melt-inclusion glasses range from rhyodacite to rhyolite and show relationships that reflect magma evolution involving fractional crystallization and multiple stages of mingling and/or mixing. In particular, melt inclusions of low-silica andesites express mixing of magmas with more widely varying compositions, than do melt inclusions of high-silica andesites and dacites. The melt inclusions of 2006, 1986, and prehistoric andesites contain moderate to high concentrations of H_2O and Cl and lesser CO_2 and SO_2. Comparing the abundances of H_2O, CO_2, and Cl in these melt inclusions with experimentally established volatile solubilities for felsic melts indicates that the 2006 and prehistoric samples are most consistent with the ascent of fluid-saturated magmas containing 1 weight percent of H_2O-enriched vapor under closed-system conditions and that pressures of volatile phase exsolution range from 150 to less than 20 MPa. This closed-system behavior was maintained to quite shallow depths prior to eruption, and this pressure range is consistent with constraints derived from 2006 geodetic measurements indicating magma storage and crystallization at 4 to 6 km and upwards to near-surface depths. The magmatic fluids were relatively oxidizing and included H_2O-enriched and HCl-, H_2S-, S_2-, and $SO_2 \pm CO_2$-bearing vapors; hydrosaline aqueous liquids largely enriched in Cl^-, SO_4^{2-}, alkalis, and H_2O; and moderately saline, H_2O-poor liquids containing Cl^-, SO_4^{2-}, and alkali elements.

Introduction

The diverse 2006 eruptive activities of Augustine Volcano, Alaska, included pyroclastic flows; explosive injection of glassy juvenile ash, rock fragments, and gases into the troposphere and lower stratosphere; and lahars, lava flows, dome-forming extrusions, associated block-and-ash flows, and small phreatic explosions (Power and others, 2006; Vallance and others, this volume; McGee and others, this volume; and other contributions to this volume). The estimated total volume of 2006 eruptive materials is approximately 73 million

[1]Department of Earth and Planetary Sciences, American Museum of Natural History, Central Park West at 79th St., New York, NY 10024-5192.

[2]Alaska Volcano Observatory, U.S. Geological Survey, 4200 University Drive, Anchorage, AK 99508.

[3]251 Pleasant Street, New London, NH 03257.

m^3 (dense-rock equivalent, or DRE; Coombs and others, this volume). The compositions of the erupted magmas, based on whole-rock data, range from basaltic andesite to dacite, though high- through low-silica andesitic magmas were dominant (Larsen and others, this volume; Vallance and others, this volume). Analyses of groundmass glasses establish the maximum in the range in silica content of the most chemically evolved melts as >79 weight percent (Izbekov and others, 2006; Larsen and others, this volume).

Knowledge of the silica content of the eruptive products is important, because the concentration of SiO_2 controls the physical properties of magma, through melt polymerization, which exerts a strong control on eruptive behavior of volcanoes. In this regard, the 2006 Augustine magma compositions changed from (1) dominantly low-SiO_2 andesitic scoria during the January explosive phase, to (2) dominantly high-SiO_2 andesite during a continuous phase of rapid lava effusion in late January and early February, to (3) dense low- and intermediate-SiO_2 andesites during the final, effusive phase in March (Coombs and others, this volume; Vallance and others, this volume; Larsen and others, this volume). Concurrently, the phases of eruptive activities ranged from (1) a series of Vulcanian explosions that produced ash plumes and pyroclastic flows, lahars, and mixed snow and rock avalanches during the explosive phase, to (2) continuous eruption of ash plumes and pyroclastic flows, to (3) an intervening eruptive pause, to (4) late-stage, dome growth and emission of lava flows during the effusive phase.

Magmatic volatile components also control eruptive activities and magmatic processes because they influence: melt viscosity and magma rheology, rates of component diffusion through melts, the thermal stability of aluminosilicate melts and minerals, and the exsolution of fluids. The manner of fluid exsolution exerts a strong control on styles of volcanic eruption and on the compositions and textures of eruptive materials. Thus, it is important to establish the compositions of melt and coexisting magmatic fluids during magma evolution, pre- and syn-eruptive fluid exsolution, and subsequent post-eruptive degassing at Augustine Volcano.

During volcanic activity preceding 2006, Augustine erupted magmas that were variably enriched in the magmatic volatile components H_2O, CO_2, S, and Cl. This observation is well demonstrated from extensive investigations of the 1976 and 1986 eruptions. Johnston's (1978, 1979) analyses of materials erupted in 1976, for example, measured elevated Cl concentrations (0.3 to 0.6 weight percent) in silicate melt inclusions and estimated preeruptive H_2O concentrations to have averaged 6.5 ± 1.5 weight percent. The former study also concluded that some melts erupted in 1976 were saturated in a Cl- and H_2O-rich fluid. Roman and others (2006) studied 1986 eruptive materials, and measured the abundances of H_2O, CO_2, Cl, and SO_3 in melt inclusions. This study also determined that magma mixing processes continued during magma ascent, based on relationships involving H_2O, K_2O, and SiO_2 in the melt-inclusion data. Recent research on materials erupted in prehistoric time has determined highly variable enrichments of magmatic H_2O and Cl (Tappen and others, 2009) and evidence of preeruptive volatile phase saturation of some fractions of these ancient magmas (Webster and others, 2006).

The objectives of this investigation are to determine the petrologic characteristics, major-element compositions, and abundance of volatile components of silicate melt inclusions and matrix glasses representing magmas erupted in A.D. 2006 and those erupted in prehistoric time (for example, 2,100, 1,700, 1,400, and 1,000 years before present) and more recently (A.D. 1986). The petrology and geochemistry of 2006 eruptive products are addressed in more detail by Larsen and others (this volume). We have integrated compositional data for 238 melt inclusions and 42 analyses of matrix glasses to illuminate relationships between the volatile components and processes of magma evolution, magmatic volatile phase exsolution, and ensuing processes of volcanic eruption at Augustine Volcano.

We refer to fluids and/or volatile phases, in this chapter, to include all noncrystalline, polycomponent phases, but this terminology does not bear on silicate melts that also are fluids by this definition. Relatively low-density, volatile component-enriched phases are denoted vapor, and higher density phases are referred to as liquid. The low-density phases are commonly dominated by H_2O and/or CO_2, and higher-density liquids are most commonly enriched in H_2O and electrolytes and may also involve molten sulfides. We refer to electrolyte-enriched fluids as saline, and the relatively dense fluids that are dominated by aluminosilicate constituents are addressed as melts.

Samples Investigated

This investigation reports petrologic and petrographic descriptions and compositional data for nine rock samples collected from 2006 tephra, dome, pyroclastic-flow, and lahar units (collected in February and August of 2006); a pumice sample from a 1986 pyroclastic-flow deposit; and a sample of Pleistocene basalt (table 1; appendix I). The 2006 samples include high- and low-silica andesites representing magma erupted during the three phases of the 2006 eruption: the explosive, continuous, and concluding effusive phase.

Our 1986 sample (AVO 208) was collected from a broad pyroclastic-flow deposit on the north flank of the volcano during the summer of 2003 (table 1). The porphyritic olivine basalt (RBW91A137) was found as a juvenile clast in the mid-section of a 10-m thick hyaloclastite outcrop on the volcano's south flank, and was collected there in 1991 by Dr. Richard B. Waitt (U.S. Geological Survey). This singular basalt outcrop contains ≤18 cm-wide, rounded to subangular, porphyritic olivine basalt clasts in a palagonite matrix and is presumably Pleistocene in age (Waitt and Begét, 2009).

The data resulting from the investigation of these samples are compared with results from Tappen and others (2009) of similar research on five samples of prehistoric fall deposits (tephra units C1 (AVO 201), C2 (AVO 202), H (AVO 204),

Table 1. Descriptions and collection localities for rock samples from Augustine Volcano, Alaska.

Rock Sample	Unit	Age of Eruption	Sample Type	Sample Location
RBW91A137	Juvenile clast-bearing hyaloclastite	Pleistocene[1]	Porphyritic olivine basalt	South flank of volcano
AVO 201	Lower C1 tephra	≈ 1,000 yr B.P.	Light-gray pumiceous tephra	Near South Point
AVO 202	Lower C2 tephra	≈ 1,000 yr B.P.	Light-gray pumiceous tephra	Near South Point
AVO 203	Tephra I	≈ 1,700 yr B.P.	Light-gray pumiceous tephra	Yellow Cliffs
AVO 204	Tephra H	≈ 1,400 yr B.P.	Light-gray pumiceous tephra	Between SE Point and East Point
AVO 205	Tephra G	≈ 2,100 yr B.P.	Light-gray pumiceous tephra	Near NE Point
AVO 208	Pyroclastic flow	A.D. 1986	Pumiceous tephra	North slope of volcano
06AUMC010.p1	Pyroclastic flow	A.D. 2006	High-silica andesite	NNE of crater
06AUMC008B.p1A	Lahar	A.D. 2006	Low-silica andesite scoria; banded	SSE coast of island
06AUMC005c.p5A	Lahar	A.D. 2006	Low-silica andesite scoria	SSW coast of island
06AUCWM007	Pyroclastic flow	A.D. 2006	Low-silica andesite scoria	N slope near crater rim
06AUCWM012	Block and ash flow	A.D. 2006	High-silica andesite	N slope near crater rim
06AUCWM014	Block and ash flow	A.D. 2006	Dense low-silica andesite	N slope near crater rim
06AUJW001	Dome extrusion	A.D. 2006	Oxidized, dense low-silica andesite	Crater rim
06AUJW004	Pyroclastic flow	A.D. 2006	Dense low-silica andesite	N slope near crater rim
06AUJW010	Block and ash flow	A.D. 2006	Dense low-silica andesite	N slope near crater rim

[1]Basalt estimated to have formed during Pleistocene eruption (Waitt and Begét, 2009).

I (AVO 203), G (AVO 205), using the nomenclature of Waitt and Begét, 2009), and with samples from the 1986 eruption studied by Roman and others (2006). Details on sample localities, petrology, and geochemistry for the prehistoric tephra samples are included therein.

Methods

Sample Preparation

Phenocrysts, silicate melt inclusions, and matrix glasses were analyzed in polished thin sections and in grain mounts prepared by gently crushing the rocks, picking individual phases, and mounting these phases on glass slides with epoxy. Three to five polished thin sections were prepared from each of the 2006 samples and studied petrographically.

The great majority of silicate melt inclusions in these samples are, as described below, vitreous and free of daughter crystals, but most melt inclusions hosted by clinopyroxene of the basalt sample (RBW91A137) are partially crystallized so they were re-fused to glass by heating mineral separates of melt inclusion-bearing, clinopyroxene phenocrysts at 1,100 to 1,150°C for 4 to 6 hours in open crucibles at one atmosphere.

Electron Microprobe Analysis

Electron microprobe analyses (EPMA) of glass and minerals were conducted with a Cameca SX-100 at the American Museum of Natural History (AMNH). Pyroxene, amphibole, and plagioclase phenocrysts, as well as glass in melt inclusions and in groundmass were analyzed for SiO_2, Al_2O_3, Na_2O, K_2O, CaO, FeO, MnO, TiO_2, MgO, F, P_2O_5, Cl, and S using wavelength-dispersive techniques at 15 KeV. We used a 2-nA beam current to analyze Na_2O, K_2O, FeO, SiO_2, and F, and a 10-nA beam current to analyze all other elements. The peak counting times for Na_2O, K_2O, SiO_2, and F were 20 seconds; for FeO were 20 to 30 seconds; for Al_2O_3, CaO, MnO, TiO_2, and MgO were 30 seconds; and for P_2O_5, Cl, and S were 40 to 60 seconds. Standards for S, Cl, and F were $BaSO_4$, scapolite, and synthetic MgF_2, respectively. The major- and trace-element concentrations of internal "standard" glasses (a felsic peralkaline obsidian and a natural topaz rhyolite reference glass that

are generally similar in composition to that of the glasses of this study) were also determined to monitor analytical accuracy and instrumental drift. The 1-σ analytical precision for the glass analyses has been estimated from 26 analyses of the obsidian (conducted during five analytical sessions spanning a one-year period and given here in relative percent): 0.7 for SiO_2, 1 for Al_2O_3, 3 for K_2O, 4 for Cl, 5 for Na_2O, 8 for CaO, 10 for FeO, 30 for F and TiO_2, and 60 for MnO. The abundances of MgO, S, and P_2O_5 are <0.005 weight percent in this obsidian and hence unrepresentative of the melt-inclusion compositions, so their 1-σ precisions were estimated from melt-inclusion data from individual samples to be ≤8, 25, and 25 relative percent, respectively.

To minimize Na and K migration during glass analyses, these constituents were analyzed with a 2-nA beam current during the first pass and the melt inclusions and areas of matrix glass were moved constantly under a defocused beam. We also used a subcounting (time zero intercept) routine for some Na analyses in melt inclusions from low-silica andesite. The stability of the Na and K signals for glass analyses reported in this study was confirmed by conducting 3 successive analyses on the same area of glass of randomly selected samples. Most melt-inclusion and matrix-glass analyses utilized an 8-µm electron-beam diameter, but a 4-µm beam diameter was required for some analyses of matrix glasses to avoid vesicles and microlites. Additionally, the small size and paucity of crystal-free melt inclusions in sample 06AUJW001 demanded the use of a 2-µm beam diameter for analysis on a stationary point on the melt inclusion, but the glass was moved under the beam during analysis.

Pairs of adjoining titanomagnetite and ilmenite grains were analyzed for Al_2O_3, FeO, MnO, TiO_2, and MgO with the electron beam set at 40 nA, 15-Kev, and with a 1-µm beam diameter. All elements were counted for 30 seconds at the peak position. Major- and trace-element concentrations of minerals were verified on magnetite and ilmenite standards.

Infrared Spectroscopic Analyses of Glasses

Dissolved H_2O and CO_2 concentrations in the glass of melt inclusions were measured by Fourier Transform Infrared (FTIR) spectroscopy utilizing techniques described by Newman and others (1986) and Mandeville and others (2002) that are summarized here. Room-temperature infrared (IR) spectroscopic measurements on melt inclusions of prehistoric and 1986 samples were conducted in transmittance mode using a Nicolet 20SXB FTIR spectrometer attached to a Spectra Tech IR Plan microscope at the AMNH. IR spectra were collected over the mid-IR to near-IR regions using a KBr beam splitter, MCT/A detector, globar source, and 1,000 scans with a spectral resolution of 4 cm^{-1}. More recent transmission FTIR analyses of melt inclusions in 2006 samples were performed with a Thermo Electron Nexus 670 spectrometer interfaced with a Continuum IR microscope at the AMNH utilizing a KBr beam splitter, MCT/A detector, globar source, and 200 to 400 scans with 4 cm^{-1} spectral resolution. For all analyses, the IR objective and spectrometer were purged with dry nitrogen at a rate of 15 liters/minute.

The melt inclusion and matrix glasses were analyzed 3 to 4 times each, and the total dissolved H_2O and CO_2 concentrations in these glasses were determined from the intensity of IR bands at 4,500 cm^{-1} (hydroxyl OH^-) and 5,200 cm^{-1} (molecular H_2O) and 2,350 cm^{-1} (CO_2). The reported H_2O concentrations refer to total H_2O. The thicknesses of the doubly polished, melt inclusion-bearing phenocryst wafers were measured 8 to 10 times using a Mitutoyo digimatic indicator which has a precision of ±2 µm. The 1-σ precision for H_2O and CO_2 analyses of these glasses is estimated as 0.1 and 0.02 weight percent, respectively.

Results

Description of the Rock Samples

All of the prehistoric tephra, 1986, and 2006 rock samples are porphyritic and contain phenocrysts of plagioclase, orthopyroxene, and clinopyroxene with plagioclase dominant; the abundance of orthopyroxene is subequal to or exceeds that of clinopyroxene. Most samples also contain minor to trace phenocrystic olivine and amphibole, and the accessory phases include apatite and Fe-Ti oxides. Larsen and others (this volume) report that all 2006 rocks that they examined contain 36 to 44 volume percent phenocrysts, and Tappen and others (2009) observed 30 to 40 volume percent phenocrysts in the prehistoric tephra. The groundmass materials are vesicular and vitreous to strongly devitrified. All rocks contain trace to abundant microlites. The Pleistocene olivine basalt (RBW91A137) is porphyritic and contains 0.2 to 11 volume percent plagioclase (An_{74-91}), 12.2 to 14.2 volume percent clinopyroxene ($Wo_{35-42}En_{48-53}Fs_{5-11}$) 3.5 to 6.5 volume percent olivine ($Fa_{13-22}Fo_{77-88}$), 1.7 volume percent amphibole (Mg numbers of 63-73), and trace amounts of orthopyroxene ($Wo_2En_{66}Fs_{32}$) (Daley, 1986; C. Tappen, unpublished data). Additional petrographic details for all samples are provided in the appendix and by Tappen and others (2009).

The whole-rock compositions for three of these samples were determined and are reported in table 2. The other six samples were not analyzed, but given their textural and mineral-chemical characteristics that are described below, we determine that most are low- to high-silica andesites on the basis of comparisons with sample descriptions and analyses from Larsen and others (this volume).

Phenocrysts

Plagioclase

Plagioclase occurs as phenocrysts and microphenocrysts, and individual crystals appear twinned, broken, rounded,

Table 2. Bulk compositions of whole-rock samples, Augustine Volcano, Alaska

[Major to trace elements (including Ni-Zn) measured by X-ray fluorescence and all other trace elements by inductively coupled plasma mass spectroscopy at Washington State University]

Rock Sample	06AUMC005c.p5	06AUMC008b.p1	06AUMC010.p1
(wt percent)			
SiO_2	57.42	57.35	62.61
Al_2O_3	17.67	17.52	16.81
TiO_2	0.72	0.72	0.56
MgO	4.61	4.75	3.36
CaO	8.51	8.46	6.64
MnO	0.14	0.14	0.13
FeO[1]	6.58	6.73	5.36
Na_2O	3.48	3.46	3.81
K_2O	0.74	0.74	0.98
P_2O_5	0.13	0.13	0.14
TOTAL	99.61	99.11	98.87
(ppm)			
Ni	28	28	24
Cr	56	60	43
V	195	195	130
Ga	17	17	17
Cu	36	36	20
Zn	61	63	57
La	8.21	8.21	10.36
Ce	17.22	17.28	20.98
Pr	2.28	2.31	2.66
Nd	10.55	10.76	11.77
Sm	3.05	3.08	3.13
Eu	1.02	1.00	0.97
Gd	3.32	3.30	3.24
Tb	0.57	0.58	0.56
Dy	3.61	6.71	3.51
Ho	0.78	0.79	0.76
Er	2.15	2.25	2.19
Tm	0.33	0.33	0.33
Yb	2.11	2.16	2.19
Lu	0.34	0.35	0.36
Ba	314	313	427
Th	1.46	1.49	2.12
Nb	2.26	2.21	2.83
Y	20.84	21.38	21.39
Hf	2.43	2.51	2.98
Ta	0.16	0.16	0.20
U	0.55	0.58	0.81
Pb	2.15	1.94	2.50
Rb	13.0	13.0	18.2
Cs	0.30	0.29	0.40
Sr	319	320	312
Sc	24.9	26.1	20.3
Zr	83	83	104

[1]All iron reported as FeO.

or euhedral. Plagioclase is also a dominant component of glomeroporphyritic aggregates containing orthopyroxene and clinopyroxene ± Fe-Ti oxides. These multiphase clots have been observed previously in the products of other eruptions by Johnson (1986) and Tappen and others (2009) and may represent breakdown of amphibole and pyroxene or remobilized phenocrysts from earlier magmas. Most plagioclase crystals range from 0.05 to 3.5 mm in length, but a few rare phenocrysts are as large as 4.8 mm in length. Plagioclase phenocrysts exhibit a variety of internal textural features including: simple normal and reverse zoning, simple oscillatory zoning, oscillatory zoning with complex internal resorption-growth boundaries and/or as rims, and other oscillatory zoned phenocrysts contain coarse sieve textures in cores. Although most are characterized by simple oscillatory zoning; more rarely, plagioclase phenocrysts are composed of coarsely sieved cores surrounded by growth boundaries that are both oscillatory in composition and appear complexly resorbed. Melt inclusions, inclusions of orthopyroxene microlites, and oxide inclusions occur within these compositional resorption-growth boundaries. Other growth zones contain dusty material that is texturally reminiscent of crystallized groundmass.

Plagioclase phenocrysts and microphenocrysts from seven 2006 samples range from andesine to bytownite (An_{36-82}; table 3). Larsen and others (this volume) provide a detailed analysis of plagioclase petrography, geochemistry, and crystallization history for 2006 samples.

Pyroxenes

Orthopyroxene is more abundant than clinopyroxene in most samples. Pyroxenes typically have subhedral to euhedral crystal morphologies, but some grains are distinctly rounded. Most pyroxene phenocrysts are not zoned.

Orthopyroxene phenocrysts are typically larger than clinopyroxene phenocrysts. The former exhibit lengths as large as 1.8 mm while most are <1.2 mm in length. Orthopyroxene phenocrysts in three 2006 samples are hypersthene with $Wo_{1-3}En_{64-76}Fs_{21-33}$ and Mg numbers of 66-78 (table 4). Clinopyroxene occurs as subhedral to euhedral crystals with most phenocrysts ranging from 0.05 to 1 mm in length. A few rare phenocrysts are up to 2 mm in length. Clinopyroxene phenocrysts in three 2006 samples are augitic with $Wo_{44-45}En_{41-47}Fs_{7-14}$ and Mg numbers of 74 to 87. Most phenocrysts contain ≤2 weight percent Al_2O_3, but some contain nearly 5 weight percent Al_2O_3.

Iron-titanium oxides

Ilmenite and titanomagnetite occur as phenocrysts, microphenocrysts, and microlites in the groundmass, and as inclusions in other phenocrysts of these samples. The oxides are subhedral to anhedral, and some are as large as 0.5 mm in length although most are ≤0.3 mm long. All but two of the samples contain both oxides in physical contact with one another, and most exhibit little to no visible evidence of exsolution.

The composition of ilmenite in four 2006 samples ranges from X_{ilm} 0.50 to 0.72 and the corresponding titanomagnetite compositions range from X_{usp} 0.21 to 0.48 (calculated with QUILF of Andersen and others, 1993, and evaluated by Bacon and Hirshmann, 1988). Estimated equilibration temperatures and oxygen fugacities (f_{O_2}), based on the compositions of coexisting oxide minerals, are reported in table 5. We note that because of the elevated f_{O_2} of these magmas, which are outside of the acceptable calibration range for the QUILF algorithm (Evans and others, 2006; Lattard and others, 2005), we reduced the temperatures determined with QUILF and reported in the figures and tables by 30°C (Rutherford and Devine, 1996). This approach is consistent with that of Larsen and others (this volume).

Amphibole

Approximately one-half of the 2006 samples studied contain rare amphibole, and sample 06AUJW001 contains several volume percent amphibole. Most of the rare amphibole phenocrysts are subhedral and rounded, and some crystals are embayed. Of the amphiboles observed in these samples, roughly half of the crystals show either reaction rims or rim alteration, and the other half are devoid of evidence of mineral replacement of amphibole rims. Some amphibole occurs as inclusions in other silicate minerals.

Analyzed amphiboles contain from 45.4 to 49.4 weight percent SiO_2, 6.2 to 9.4 weight percent Al_2O_3, 14.8 to 15.9 weight percent MgO, and 11.4 to 13.0 weight percent FeO (table 6). The TiO_2 content ranges from 1.0 to 2.4 weight percent, and total alkalis vary from 1.3 to 2.3 weight percent. Na_2O and K_2O exhibit negative correlations with the SiO_2 contents of amphibole (table 6). All 2006 amphiboles analyzed in this study are identified as magnesio-hornblende based on the classification of Leake (1997) and Hawthorne and Oberti (2007). Chlorine concentrations range from 0.06 to 0.09 weight percent with the highest value occurring in the core of an iron-rich crystal that is zoned with respect to Mg, Ti, Ca, F and Cl (table 6). Fluorine concentrations in 2006 amphiboles vary widely from below detection (<0.02 weight percent) to 0.47 weight percent in the rim of this zoned crystal (table 6). One amphibole from a dense, intermediate-silica andesite scoria clast (06AUJFL001b; Larsen and others, this volume, their table 8) erupted during the continuous phase (January 28 to February 10, 2006) contains 42.8 weight percent SiO_2, 14.9 weight percent MgO, 10.96 weight percent FeO, 2.3 weight percent Na_2O, 9.9 weight percent CaO, and 0.05 weight percent Cl as well as elevated Al_2O_3 (for example, 11.4 weight percent) slightly extending the range of compositions determined for 2006 samples.

Olivine

Olivine is a very minor phase in most of the 2006 rocks studied. It typically occurs as small rounded, subhedral, embayed, and altered grains generally <0.6 mm in diameter. The typical form of alteration involves oxidation along rims

Table 3. Compositions of plagioclase in 2006 rock samples of Augustine Volcano, Alaska.

[Electron microprobe analyses (wt percent) of representative plagioclase phenocrysts from seven rock samples]

Rock Sample	06AU JW004	06AU JW004	06AU JW010	06AU JW010	06AU CWM007	06AU CWM007	06AU CWM012	06AU CWM012	06AU MC005	06AU MC005	06AU MC008	06AU MC008	06AU MC010	06AU MC010
Composition	Anorthitic	Albitic	Anorthitic	Albitic	Anorthitic	Albitic	Anorthitic	Subequal An-Ab	Anorthitic	Subequal An-Ab	Anorthitic	Albitic	Anorthitic	Albitic
SiO_2	48.20	55.02	51.16	57.50	51.55	58.36	47.64	54.26	52.48	56.69	48.84	60.86	54.12	56.60
Al_2O_3	33.28	29.50	31.74	26.95	30.59	26.89	33.63	28.52	30.62	27.80	31.49	23.88	29.91	27.28
TiO_2	0.01	0.00	0.00	0.01	0.03	0.07	0.04	0.03	0.00	0.05	0.00	0.03	0.02	0.00
MgO	0.04	0.02	0.03	0.08	0.04	0.03	0.02	0.04	0.01	0.00	0.06	0.04	0.02	0.03
CaO	16.38	9.77	14.30	8.99	13.48	9.00	16.80	10.93	13.21	10.33	16.24	7.20	12.70	9.62
MnO	0.02	0.00	0.03	0.00	0.00	0.00	0.04	0.00	0.07	0.00	0.03	0.00	0.05	0.00
FeO	0.47	0.23	0.40	0.38	0.52	0.29	0.41	0.49	0.38	0.05	0.79	0.87	0.33	0.29
Na_2O	2.33	7.07	3.50	5.57	3.54	5.86	1.99	5.99	3.90	5.68	2.42	6.93	4.04	6.20
K_2O	0.02	0.12	0.05	0.18	0.10	0.15	0.07	0.11	0.08	0.14	0.06	0.42	0.07	0.19
TOTAL	100.75	101.73	101.21	99.66	99.85	100.64	100.63	100.37	100.74	100.74	99.93	100.23	101.26	100.21
Chemical Formula														
Si	2.20	2.45	2.30	2.58	2.35	2.59	2.18	2.45	2.37	2.52	2.25	2.71	2.42	2.54
Al	1.79	1.55	1.69	1.43	1.64	1.41	1.81	1.52	1.63	1.46	1.71	1.25	1.57	1.44
Ti	0.00	0.00	0.00	0.00	0.00	0.00	0.00	0.00	0.00	0.00	0.00	0.00	0.00	0.00
Mg	0.00	0.00	0.00	0.01	0.00	0.00	0.00	0.00	0.00	0.00	0.00	0.00	0.00	0.00
Ca	0.08	0.47	0.69	0.43	0.66	0.43	0.82	0.53	0.64	0.49	0.80	0.34	0.61	0.46
Mn	0.00	0.00	0.00	0.00	0.00	0.00	0.00	0.00	0.00	0.00	0.00	0.00	0.00	0.00
Fe	0.02	0.01	0.02	0.01	0.02	0.01	0.02	0.02	0.01	0.02	0.03	0.03	0.01	0.01
Na	0.21	0.61	0.31	0.48	0.31	0.50	0.18	0.52	0.34	0.49	0.22	0.60	0.35	0.54
K	0.00	0.01	0.00	0.01	0.01	0.01	0.00	0.01	0.00	0.01	0.00	0.02	0.00	0.01
End Members														
An	79.44	43.03	69.11	46.62	67.39	45.50	82.02	49.91	64.88	49.73	78.49	35.58	63.21	45.67
Ab	20.45	56.34	30.60	52.26	32.02	53.60	17.58	49.49	34.65	49.47	21.16	61.95	36.38	53.26
Or	0.12	0.63	0.29	1.11	0.60	0.90	0.41	0.60	0.47	0.80	0.35	2.47	0.41	1.07

[1]FeO represents all iron.

Table 4. Compositions of pyroxenes in 2006 rock samples of Augustine Volcano, Alaska.

[Electron microprobe analyses (wt. percent) of representative orthopyroxene (opx) and clinopyroxene (cpx) phenocrysts from three rock samples. Original iron analysis was determined as FeO and is reported herein separately as Fe_2O_3 and FeO. Chemical formula and end members computed with PRBDATNT (Harlow and others, 2006)]

Rock Sample	06AUM C008b.p1a	06AUM C008b. p1a	06AUM-C008b.p1a	06AUM-C008b.p1a	06AUJ W001	06AUJ W001	06AUJ W001	06AUJ W001	06AUC WM012	06AUC-WM012	06AUC-WM012	06AUC WM012
Mineral	Opx	Opx	Cpx	Cpx	Opx	Opx	Cpx	Cpx	Opx	Cpx	Cpx	Cpx
SiO_2	52.75	53.66	50.02	51.08	53.21	53.57	52.31	52.83	53.23	53.00	52.84	52.37
TiO_2	0.24	0.32	0.08	0.43	0.20	0.17	0.24	0.32	0.05	0.34	0.31	0.25
Al_2O_3	0.83	1.44	4.85	2.16	1.14	0.82	1.29	1.49	0.62	1.59	1.54	1.28
Fe_2O_3	0.81	4.54	2.31	2.32	0.17	0.00	1.86	0.95	0.00	2.23	0.33	0.70
FeO	20.15	12.38	4.14	7.25	18.73	20.71	6.93	8.62	19.65	6.80	8.60	7.36
MnO	0.75	0.49	0.18	0.39	0.57	0.74	0.34	0.33	1.08	0.35	0.30	0.31
MgO	22.63	25.66	15.80	14.10	24.16	23.13	14.58	14.36	23.02	14.46	14.43	14.91
CaO	1.70	1.39	20.95	21.16	1.13	1.10	21.51	21.19	0.89	21.17	21.22	21.26
Na_2O	0.01	0.07	0.26	0.34	0.00	0.03	0.42	0.36	0.07	0.78	0.35	0.29
K_2O	0.00	0.04	0.01	0.00	0.00	0.00	0.02	0.04	0.01	0.00	0.02	0.00
TOTAL	99.87	99.99	98.60	99.23	99.31	100.27	99.50	100.49	98.62	100.72	99.94	98.73
Chemical Formula												
Si	1.96	1.94	1.85	1.92	1.97	1.98	1.95	1.96	1.99	1.95	1.97	1.97
Al_{IV}[1]	0.04	0.06	0.15	0.08	0.03	0.02	0.05	0.04	0.01	0.05	0.03	0.03
Al	0.00		0.06	0.02	0.02	0.01	0.01	0.02	0.02	0.02	0.03	0.02
Ti	0.01	0.01	0.02	0.01	0.01	0.01	0.01	0.01	0.00	0.01	0.01	0.01
Fe^{3+}	0.02	0.12	0.06	0.07	0.01	0.00	0.05	0.03	0.00	0.06	0.01	0.02
Fe^{2+}	0.63	0.37	0.13	0.23	0.58	0.64	0.22	0.27	0.62	0.21	0.27	0.23
Mn	0.02	0.02	0.01	0.01	0.02	0.02	0.01	0.01	0.03	0.01	0.01	0.01
Mg	1.26	1.38	0.87	0.79	1.33	1.27	0.81	0.79	1.28	0.79	0.80	0.83
Ca	0.07	0.05	0.83	0.85	0.05	0.04	0.86	0.84	0.04	0.84	0.85	0.86
Na	0.00	0.01	0.02	0.03	0.00	0.00	0.03	0.03	0.01	0.06	0.03	0.02
K	0.00	0.002	0.00	0.00	0.00	0.00	0.00	0.00	0.00	0.00	0.00	0.00
Mg numbers[2]	66	78	87	77	69	66	78	74	66	78	74	78
End Members												
En	64.39	76.35	47.62	42.25	68.08	65.06	43.01	41.72	66.36	43.15	41.80	43.44
Fs	32.12	20.66	7.00	12.19	29.62	32.69	11.44	14.03	31.78	11.41	14.00	12.03
Wo	3.49	2.98	45.38	45.56	2.30	2.25	45.55	44.25	1.86	45.43	44.20	44.53

[1] Tetrahedrally coordinated aluminum.
[2] Mg numbers = 100x(cations Mg/(cations Mg + cations Fe^{2+})). Data are based on analyses of 4 orthopyroxene and 5 clinopyroxene phenocrysts from sample 06AUMC008b.p1a, 4 orthopyroxene and 4 clinopyroxene phenocrysts from sample 06AUJW001, and 6 orthopyroxene and 5 clinopyroxene phenocrysts from sample 06AUCWM012.

Table 5. Compositions of iron-titanium oxide minerals in 2006 samples of Augustine Volcano, Alaska.

[Electron microprobe analyses (wt percent) of representative ilmenite (ilm) and titanomagnetite (usp = ulvospinel) grains. FeO represents all iron]

Rock Sample	06AUM C008	06AUM C008	06AUC WM007	06AUC-WM007	06AUC WM012	06AUC-WM012	06AU JW004	06AUJ W004
Mineral	Ilm	Usp	Ilm	Usp	Ilm	Usp	Ilm	Usp
Oxide (wt percent)								
TiO_2	33.28	12.00	33.69	12.84	35.41	7.99	36.12	9.29
Al_2O_3	0.61	2.92	0.37	1.67	0.41	2.01	0.44	1.98
FeO	58.99	76.74	57.03	78.03	61.86	85.24	61.26	83.69
MnO	0.17	0.35	0.26	0.44	0.32	0.47	0.29	0.44
MgO	2.64	3.23	1.96	2.14	1.88	1.74	1.95	1.94
TOTAL	95.79	95.58	93.45	95.46	100.03	97.83	100.18	97.70
X_{usp}[1]	-	0.376	-	0.374	-	0.221	-	0.258
X_{ilm}[1]	0.642	-	0.619	-	0.627	-	0.627	-
Av. T (°C)[2]	960±55		977±39		845±7		875±29	
Log fo_2[3]	-9.01±0.8		-8.75±0.6		-10.47±0.1		-10.05±.04	
DFMQ[4]	2.0±0.1		2.0±0.3		2.5±0.1		2.3±0.1	
No. of pairs analyzed	10		8		7		8	

[1] Cation assignment based on Stormer (1983). Ulvospinel = usp.

[2] Av. T (°C) = average temperature in °C calculated with QUILF from Andersen and others (1993); data also evaluated using methods of Bacon and Hirshmann (1988), and corrected by reducing temperatures by 30°C given that the range in fo_2 exceeds that of the useful range for QUILF; see text for discussion.

[3] Log fo_2 calculated with QUILF from Andersen and others (1993).

[4] DFMQ = number of log units from the fayalite-magnetite-quartz buffer based on Chou (1978).

and along internal cracks. Representative compositions of olivine phenocrysts in 2006 rocks are reported in table 7 of Larsen and others (this volume).

Groundmass

The groundmass of these samples varies from strongly crystallized and/or oxidized to comparatively clear, microlite-poor vesicular glass. Typically, the high-silica rocks contain trace microlites in the groundmass. For example, samples 06AUJW001, 06AUMC008, 06AUCWM007, and 06AUCWM014 contain relatively fresh matrix glass. Conversely, the low-silica rock samples contain a felty, microlite-rich groundmass. The matrix glasses of these samples are dacitic to rhyolitic in bulk composition. The matrix glasses from these samples also contain a range of volatile component abundances; H_2O varies from 0.09 to 0.12 weight percent, and CO_2 is not observed at the 30-ppm limit of detection. The compositions of the matrix glasses are generally consistent with those of the corresponding melt inclusions except that the former generally contain less H_2O, Cl, and S (table 7).

Description of the Melt Inclusions of the 2006, 1986, and Pleistocene Basalt Samples

Silicate Melt Inclusions in the 2006 Samples

Melt inclusions occur in plagioclase, orthopyroxene, clinopyroxene, amphibole, and apatite. Most of these inclusions contain one or more vapor and/or glass-contraction bubbles and are partially crystallized to completely vitreous; the glass appears colorless to light pink or brown in color. The melt inclusions range from <1 to >100 microns in diameter, but most are <50 microns in size.

We focused our investigation on melt inclusions in plagioclase and pyroxene phenocrysts. The 131 melt inclusions in 2006 samples analyzed for this study were unheated

Table 6. Compositions of amphiboles in 2006 rock samples of Augustine Volcano, Alaska.

[Electron microprobe analyses (wt percent) of representative amphibole phenocrysts in two rock samples. Amphiboles not zoned chemically]

Rock Sample	06AUMC008	06AUMC008	06AUMC008	06AUMC008	06AUMC008	06AUMC008	06AUJW001	06AUJW001	06AUJW001	06AUJW001
SiO_2	45.36	47.23	46.84	46.97	47.55	48.08	48.44	47.84	47.09	49.44
TiO_2	2.43	1.63	1.53	1.51	1.62	1.49	1.53	1.30	0.97	1.36
Al_2O_3	9.45	7.69	7.12	7.07	7.12	7.11	6.86	7.31	8.41	6.22
FeO[1]	12.08	11.37	12.21	11.97	11.67	12.08	11.49	12.66	12.99	11.95
MnO	0.22	0.32	0.35	0.35	0.37	0.32	0.37	0.54	0.59	0.39
MgO	15.08	15.38	15.65	15.50	15.55	15.65	15.75	15.25	14.77	15.93
CaO	11.38	11.09	11.19	11.20	11.17	11.15	11.19	10.87	10.01	11.18
Na_2O	2.10	1.49	1.50	1.39	1.50	1.48	1.31	1.22	1.41	1.29
K_2O	0.23	0.13	0.10	0.11	0.16	0.11	0.09	0.08	0.11	0.11
S	b.d.	0.01	0.01	0.01	0.01	b.d.[2]	0.01	b.d.	b.d.	b.d.
F	0.07	0.17	b.d.	b.d.	0.23	b.d.	0.04	0.47	0.07	0.17
Cl	0.07	0.06	0.06	0.07	0.07	0.08	0.06	0.06	0.09	0.08
O=F,Cl	0.05	0.09	0.02	0.02	0.12	0.02	0.03	0.23	0.05	0.10
TOTAL	98.49	96.60	96.56	96.17	97.05	97.58	97.16	97.59	96.55	98.13
Chemical Formula										
T-Site Si^{+4}	6.58	6.93	6.84	6.89	6.97	6.98	7.05	6.96	6.94	7.14
T-Site $^{V}Al^{+3}$	1.42	1.07	1.16	1.11	1.03	1.02	0.95	1.05	1.06	0.86
C-Site $^{I}Al^{+3}$	0.20	0.26	0.06	0.11	0.20	0.20	0.22	0.21	0.40	0.20
C-Site Ti^{+4}	0.27	0.18	0.17	0.17	0.18	0.16	0.17	0.14	0.11	0.15
C-Site Fe^{+3}	0.09	0.02	0.47	0.37	0.03	0.09	0.02	0.29	0.03	0.01
C-Site Fe^{+2}	1.38	1.37	1.02	1.10	1.41	1.38	1.38	1.25	1.57	1.43
C-Site Mn^{+2}	0.03	0.04	0.04	0.04	0.05	0.04	0.05	0.07	0.07	0.05
C-Site Mg^{+2}	3.26	3.37	3.41	3.39	3.40	3.39	3.42	3.31	3.24	3.43
B-Site Ca^{+2}	1.77	1.74	1.75	1.76	1.75	1.73	1.75	1.69	1.58	1.73
B-Site Na^{+}	0.01	0.01	0.08	0.06	0.00	0.02	0.00	0.05	0.00	0.01
A-Site Na^{+}	0.58	0.41	0.35	0.33	0.43	0.40	0.37	0.30	0.40	0.35
A-Site K^{+}	0.04	0.03	0.02	0.02	0.03	0.02	0.02	0.01	0.02	0.02
TOTAL	15.62	15.44	15.37	15.36	15.46	15.42	15.38	15.31	15.42	15.37
Mineral	mghb[3]	mghb	mghb	mghb	mghb	mghb	mghb	mghb	mghb	mghb

and naturally vitreous. We strove to locate and analyze melt inclusions in the periphery of plagioclase and pyroxene phenocrysts, as they are more likely to represent newer (that is, 2006) magma, but we also studied randomly located melt inclusions in these phenocrysts. Melt inclusions are most abundant in plagioclase, and some of the plagioclase-hosted inclusions occur in compositionally zoned boundary layers that are aligned parallel to the crystallographic growth planes of the host mineral; these boundary layers appear mottled when viewed petrographically with crossed nichols in transmitted light. Prior research has suggested that such patchy or sieve-textured zones form during heating and resorption events (Bacon and others, 1992; Lowenstern, 1995; Browne and others, 2006; Blundy and Cashman, 2001, 2005; Tappen and others, 2009). A small number of the melt inclusions analyzed were located in these resorption-growth boundary

Table 6. Compositions of amphiboles in 2006 rock samples of Augustine Volcano, Alaska. —Continued

[Electron microprobe analyses (wt percent) of representative amphibole phenocrysts in two rock samples. Amphiboles not zoned chemically]

Rock Sample	06AUJW001	06AUJW001	06AUJW001	06AUJW001	06AUJW001	06AUJW001	06AUJW001	06AUJW001	06AUJW001
SiO_2	49.35	48.50	48.51	46.94	46.18	47.22	48.78	48.44	49.11
TiO_2	1.35	1.35	1.23	1.01	1.07	1.15	1.14	1.23	1.36
Al_2O_3	7.28	7.20	7.16	8.52	8.90	8.55	7.00	7.13	6.18
FeO[1]	13.12	12.77	12.52	13.51	13.58	13.05	12.78	12.88	11.88
MnO	0.47	0.52	0.51	0.55	0.52	0.58	0.54	0.52	0.43
MgO	14.92	15.13	15.16	14.71	14.57	14.63	15.41	15.18	15.75
CaO	10.49	10.74	10.65	10.19	9.89	10.20	10.62	10.60	11.02
Na_2O	1.48	1.25	1.14	1.47	1.40	1.32	1.31	1.35	1.12
K_2O	0.11	0.11	0.13	0.12	0.12	0.10	0.09	0.18	0.11
S	0.01	b.d.	b.d.	b.d.	0.01	b.d.	b.d.	0.01	0.01
F	0.23	0.40	0.26	b.d.	0.20	0.06	0.26	0.11	0.15
Cl	0.06	0.07	0.07	0.05	0.07	0.07	0.07	0.07	0.06
O=F,Cl	0.12	0.20	0.14	0.01	0.11	0.04	0.14	0.07	0.08
TOTAL	98.89	98.06	97.36	97.07	96.50	96.95	98.04	97.73	97.18
				Chemical Formula					
T-Site Si^{+4}	7.09	7.05	7.08	6.86	6.80	6.92	7.08	7.05	7.15
T-Site $^{V}Al^{+3}$	0.91	0.95	0.92	1.14	1.20	1.08	0.92	0.95	0.85
C-Site $^{I}Al^{+3}$	0.33	0.28	0.31	0.33	0.34	0.40	0.27	0.28	0.21
C-Site Ti^{+4}	0.15	0.15	0.14	0.11	0.12	0.13	0.12	0.14	0.15
C-Site Fe^{+3}	0.01	0.01	0.01	0.22	0.03	0.06	0.02	0.01	0.02
C-Site Fe^{+2}	1.57	1.55	1.52	1.44	1.37	1.55	1.54	1.56	1.43
C-Site Mn^{+2}	0.06	0.06	0.06	0.07	0.07	0.07	0.07	0.07	0.05
C-Site Mg^{+2}	3.20	3.28	3.30	3.21	3.20	3.20	3.33	3.30	3.42
B-Site Ca^{+2}	1.62	1.67	1.67	1.60	1.56	1.60	1.65	1.65	1.72
B-Site Na^{+}	0.08	0.00	0.01	0.04	0.05	0.01	0.00	0.01	0.01
A-Site Na^{+}	0.34	0.35	0.32	0.38	0.35	0.37	0.37	0.37	0.31
A-Site K^{+}	0.02	0.02	0.03	0.02	0.02	0.02	0.02	0.03	0.02
TOTAL	15.35	15.37	15.34	15.40	15.37	15.39	15.39	15.40	15.33
Mineral	mghb	mghb	mghb	mghb	mghb	mghb	mghb	mghb	mghb

[1]FeO represents all iron. [2]Below detection limit = b.d. [3]Mghb=magnesiohornblende.

layers, but the compositions of these inclusions show no systematic differences with those trapped in other portions of plagioclase. We avoided analysis of melt inclusions located in the patchy-mottled sieve-textured cores of plagioclase phenocrysts. Melt inclusions in pyroxene do not typically occur within compositional boundaries, because most pyroxene phenocrysts are more homogeneous than the corresponding plagioclase phenocrysts for individual samples. We also avoided melt inclusions that contain crystals, lay along cracks, or those that contain multiple or excessively large vapor and/or glass-contraction bubbles that are indicative of leakage after entrapment.

The silicate melt inclusions of these samples are dacitic to rhyolitic in bulk composition (table 7). Melt inclusions from 2006 samples contain 0.4 to 6 weight percent CaO, 0.8 to 5 weight percent FeO, and 0.2 to 2.0 weight percent MgO.

Table 7. Average compositions of silicate melt inclusions and matrix glass of rock samples from Augustine Volcano, Alaska.

[Major to trace elements in matrix glass (mat gl) and representative melt inclusions (MI) hosted by plagioclase (plag), clinopyroxene (cpx), or orthopyroxene (opx) determined by electron microprobe; H_2O and CO_2 measured by fourier-transform infrared spectroscopy]

Rock Sample	06AUMC 005c.p5 plag MI	06AUM-C008b. p1 plag MI	06AUM-C008b. p1 mat gl	06AUM C010. p1 plag MI	06AUJ W001 mat gl	06AU JW004 plag MI	06AUJ W004 mat gl	06AUC-WM007 plag MI	06AUC-WM007 mat gl	06AUJ W010 plag MI	06AUC-WM012 plag MI	06AUC-WM014 mat gl	AVO208 (1986) plag MI[1]	1986 plag and cpx MI[2]	Prehistoric MI[3]	Prehistoric mat gl[3]	RB-W91A137 cpx MI
(wt. percent)																	
SiO_2	70.17± 2.23	69.90± 2.56	71.19± 3.18	72.17± 1.91	73.76± 1.04	72.56± 1.52	74.30± 2.04	73.44± 1.89	75.86± 2.69	75.69± 0.86	73.26± 1.25	65.34± 3.43	71.86± 1.45	72.96± 1.25	72.63± 1.56	75.39± 2.20	54.92± 1.54
Al_2O_3	13.54± 1.21	13.69± 1.52	13.26± 2.67	12.13± 0.70	12.61± 0.23	12.26± 0.46	12.14± 0.72	12.04± 0.55	13.10± 3.44	11.77± 0.67	11.50± 0.57	15.68± 1.38	12.19± 0.19	12.57± 0.42	12.38± 0.61	12.93± 0.48	14.61± 0.73
TiO_2	0.39± 0.28	0.40± 0.24	0.59± 0.42	0.26± 0.10	0.36± 0.04	0.29± 0.16	0.39± 0.14	0.30± 0.20	0.43± 0.17	0.27± 0.15	0.37± 0.09	0.96± 0.10	0.35± 0.11	0.26± 0.08	0.19± 0.08	0.33± 0.07	0.62± 0.11
MgO	0.54± 0.34	0.72± 0.35	0.51± 0.26	0.35± 0.15	0.36± 0.05	0.52± 0.16	0.24± 0.13	0.41± 0.24	0.25± 0.20	0.44± 0.09	0.60± 0.11	0.46± 0.12	0.47± 0.08	0.17± 0.05	0.36± 0.12	0.49± 0.14	5.89± 0.91
CaO	2.81± 0.84	3.21± 0.95	2.99± 1.46	1.79± 0.45	1.93± 0.14	1.87± 0.24	1.69± 0.99	1.81± 0.32	1.71± 1.40	1.78± 0.20	1.70± 0.30	1.85± 0.55	1.92± 0.12	2.11± 0.14	2.04± 0.25	2.38± 0.44	10.33± 1.59
MnO	0.09± 0.04	0.08± 0.05	0.09± 0.09	0.11± 0.09	0.05± 0.02	0.08± 0.06	0.04± 0.02	0.04± 0.06	0.05± 0.07	0.09± 0.06	0.06± 0.06	0.06± 0.02	0.06± 0.03	n.a.[5]	0.06± 0.03	0.06± 0.03	0.16± 0.03
FeO[4]	2.85± 1.43	2.97± 1.02	3.95± 2.11	1.59± 0.27	1.68± 0.26	2.07± 0.61	1.92± 0.64	1.84± 0.87	1.52± 0.40	1.85± 0.50	2.47± 0.30	4.77± 0.93	2.00± 0.33	1.84± 0.32	1.59± 0.52	1.82± 0.29	6.86± 1.13
Na_2O	4.56± 0.51	4.55± 0.83	4.09± 2.05	3.86± 0.42	4.39± 0.11	4.85± 0.93	4.24± 0.24	5.50± 0.87	4.28± 0.91	5.21± 0.45	3.91± 0.59	04.43± 0.18	3.80± 0.31	3.82± 0.28	4.10± 0.33	4.23± 0.27	2.04± 0.50
K_2O	1.72± 0.16	1.82± 0.27	2.26± 0.38	2.14± 0.56	2.19± 0.08	2.23± 0.20	2.62± 0.37	2.20± 0.30	2.72± 0.62	2.52± 0.28	2.27± 0.25	1.48± 0.18	2.03± 0.06	1.80± 0.21	1.61± 0.27	1.84± 0.21	0.61± 0.12
P_2O_5	0.11± 0.11	0.10± 0.08	0.14± 0.15	0.05± 0.02	0.05± 0.01	0.05± 0.03	0.07± 0.01	0.08± 0.06	0.07± 0.02	0.06± 0.04	0.07± 0.03	0.30± 0.06	0.07± 0.03	n.a.	0.05± 0.02	0.06± 0.03	0.15± 0.03
S	0.02± 0.01	0.02± 0.02	0.01± 0.01	0.02± 0.01	0.01± 0.01	0.02± 0.03	0.00± 0.01	0.02± 0.01	0.01± 0.01	0.01± 0.01	0.02± 0.01	b.d.[6]	0.02± 0.01	0.02± 0.01	0.02± 0.01	0.01± 0.01	0.23± 0.11
Cl	0.36± 0.03	0.38± 0.12	0.33± 0.24	0.44± 0.13	0.23± 0.02	0.45± 0.14	0.26± 0.08	0.41± 0.12	0.20± 0.05	0.43± 0.06	0.56± 0.15	0.35± 0.02	0.44± 0.07	0.29± 0.06	0.31± 0.06	0.32± 0.03	0.30± 0.04
F	0.02± 0.02	0.03± 0.03	0.03± 0.04	0.03± 0.06	0.03± 0.04	0.03± 0.06	0.03± 0.03	0.06± 0.09	0.15± 0.02	0.03± 0.03	0.06± 0.08	0.02± 0.02	0.03± 0.04	n.a.	0.02± 0.03	0.03± 0.05	0.03± 0.04
TOTAL	97.18	97.88	100.63	94.76	98.68	97.00	97.94	97.96	101.00	100.15	96.91	95.76	95.30	96.02	95.38	99.88	97.26
Number of analyses	13	54	6	23	9	14	6	8	6	6	13	3	14	8	79	18	6
CO_2	<0.003	n.a.	n.a.	<0.003	<0.003	<0.003	n.a.	n.a.	n.a.	n.a.	<0.003	n.a.	n.a.	0.011± 0.007	0.009± 0.033	n.a.	n.a.
H_2O	4.1 ± 0.01	n.a.	n.a.	3.08 ± 1.30	0.01	1.70 ± 0.56	n.a.	n.a.	n.a.	n.a.	3.16 ± 0.14	n.a.	2.58 ± 0.98	3.46 ± 1.92	4.19 ± 1.82	n.a.	n.a.

[1]Data of this study. [2]Data of Roman and others (2006). [3]Data of Tappen and others (2009) for melt inclusions hosted by plagioclase, pyroxene, and amphibole. [4]All iron reported as FeO. [5]Constituent not analyzed. [6]Constituent below detection limit; matrix glass analyses for 06AUCWM014 may have included iron-titanium oxides in groundmass glass.

Silicate Melt Inclusions in the 1986 Sample

The silicate melt inclusions from sample AVO 208 are rhyolitic in composition and are somewhat more chemically evolved than some melt inclusions of the 2006 samples. The melt inclusions contain less cafemic constituents than those in 2006 rocks; the concentrations of CaO, FeO, and MgO in the former range from 1.8 to 2.1, 1.5 to 2.4, and 0.3 to 0.6 weight percent, respectively. Water was measured in several of these melt inclusions, and the average concentration is 2.6 weight percent. Sulfur varies from 0.02 to 0.04 weight percent and Cl from 0.38 to 0.51 weight percent, respectively.

Silicate Melt Inclusions in the Basalt

The clinopyroxene-hosted silicate melt inclusions in the basalt sample (RBW91A137) are basaltic-andesite to andesitic in composition. Water was not measured directly in these melt inclusions, but the apparent H_2O concentration of most of these reheated melt inclusions varies from 2 to 4 weight percent using the volatile-by-difference method. These estimated H_2O concentrations could be lower than those in the melt at the time of entrapment due to diffusive loss of H_2 and H_2O out the melt inclusions during reheating and refusion. Sulfur varies from 0.08 to 0.36 and Cl from 0.27 to 0.37 weight percent, respectively.

What do the Melt Inclusion Compositions Represent?

Some silicate melt inclusions are influenced by syn- and post-entrapment processes that modify their compositions and render them nonrepresentative of the bulk melt at the time of entrapment (Lowenstern, 1995; Danyushevsky and others, 2000; Anderson, 2003, Bodnar and Student, 2006). Melt-inclusion compositions may be modified, for example, by host crystallization after entrapment, because post-entrapment crystallization of plagioclase on melt inclusion-host wall contacts increases the SiO_2, FeO, MgO, and K_2O contents and simultaneously reduces the abundances of Al_2O_3, CaO, and Na_2O in the residual melt of the inclusion. Neither the plagioclase- or pyroxene-hosted melt inclusions of this study exhibit trends indicative of this process.

Melt-inclusion glass may also be modified by leakage or post-entrapment diffusive re-equilibration. Consequently, we analyzed no melt inclusions on cracks and the felsic melt inclusions did not require re-fusion to glass prior to analysis, so we consider the abundances of volatile components to represent those of the local melt at the time or entrapment. It is conceivable that H_2O was partially exchanged between bulk magma and entrapped melt after entrapment, through the diffusion of H_2 through the host phenocrysts (Roedder, 1984; Massare and others, 2002), but we cannot constrain the potential consequences of this process. As noted previously, however, the pyroxene-hosted basaltic-andesite melt inclusions were refused and quenched to glass prior to analysis, and their compositions are likely to reflect some diffusive loss of H_2O.

The average compositions of the felsic melt inclusions of 2006 high-silica andesites are equivalent, at the 1-σ level of confidence, with their corresponding areas of matrix glass except for differences in the volatile-components H_2O, S, and Cl. This observation is important as it indicates that the compositions of the late-stage aliquots of melt that quenched to form matrix glass and melt entrapped in growing plagioclase and pyroxene were alike, and, thus, the melt inclusions are compositionally representative of the late-stage melts of 2006 magmas.

Compositional Relationships Involving Melt Inclusions in the Basalt, 1986, and 2006 Samples

The integration of these melt inclusion data sets provides important insights into the evolution of 2006 and earlier Augustine magmas. The differentiation of relatively primitive to residual rhyolitic melts caused the alkalis to increase in abundance and to exhibit increased dispersion in the highly felsic melts. For example, the melt inclusions in 2006 eruptive materials that were analyzed contain higher alkali contents than the melt inclusions from prehistoric tephra. The whole-rock data detail the overall trend.

Before proceeding, we note that detailed analysis and interpretation of the Pleistocene basalts (Larsen and others, this volume) show them to be geochemically distinct from all younger, historic eruptive materials of Augustine Volcano; the geochemical trends characterizing Pleistocene basalts are inconsistent with those of younger volcanic rocks. The former rocks exhibit trends that are lower in K_2O and related large-ion lithophile trace elements; rare-earth elements (REE); and the high-field strength elements Zr, Hf, Nb, and Ta than those of rocks representing historic eruptions. Therefore, in the figures (fig. 1) and discussion that follow, we include data from whole-rock samples and melt inclusions of the Pleistocene basalts in order to provide some constraints on the geochemistry of relatively primitive Augustine magmas, even though the compositions of these older basaltic magmas may be geochemically distinct from the younger basaltic magmas that are not yet well constrained.

The compositions of melt inclusions and matrix glasses exhibit geochemical trends that reflect processes of magma evolution. Magmatic differentiation, for example, is accompanied by decreasing concentrations of alkaline earth elements and increasing abundances of alkali elements in residual fractions of melt. Plots of CaO and MgO versus Na_2O and K_2O in the integrated data sets for Augustine rocks show two distinct relationships (fig. 2). One correlation (that is, mixing trend 1) involves the melt inclusions, groundmass glasses, and some whole-rock data of predominantly low-silica rock samples that is best fit with a linear trend expressing the consequences of magma evolution dominated by hybridization. Although the melt inclusions of the Pleistocene basalt (RBW91A137) may be geochemically distinct from

younger basaltic magmas of Augustine Volcano, we interpret the mixing line to be directed toward their compositions because (1) this trend is consistent with the abundances of nonvolatile components in whole-rock samples, and (2) we have no other constraints at this time.

The second correlation (that is, mixing trend 2, fig. 2) is also best fit with a linear curve, but in this case the trend involves either small reductions in alkaline earth concentrations with increasing alkali abundances or no statistically significant change in CaO and MgO (figs. 2*A*, 2*B*, 2*C*). Many of the melt inclusions that contain less K_2O and Na_2O, represented by the second trend, also contain lower FeO and TiO_2 concentrations. This second trend characterizes the geochemistry of melt-inclusion and matrix glasses from dacitic and high-silica andesitic rock samples of prehistoric, 1986, and 2006 eruptions, and it includes glasses from some 2006 low-silica andesites. Given its linear nature, we interpret it to reflect magma evolution also dominated by magma mixing and/or mingling, but of two relatively silicic end members.

The chemical evolution of magmas can be expressed with the Larsen Index ([(SiO_2x0.333)+(K_2O)]-(CaO+FeO+Mg)) on a weight percent basis; Carmichael and others, 1974). We have applied this index to the Augustine melt-inclusion data in order to interpret the behavior of P, S, and Cl. Phosphorus, for example, shows significant dispersion in the integrated data sets (fig. 3*A*). The highest P values occur in dacitic to rhyodacitic melt inclusions. In addition, the P concentrations of all of these relatively felsic melt inclusions decrease from values as high as 0.35 weight percent to values near zero as their compositions vary from dacite to rhyolite. Relative to P, the S concentrations of all dacitic to rhyolitic melt inclusions show somewhat less dispersion and range from 100 to 700 ppm (fig. 3*B*), and this range is similar to that determined for felsic melt inclusions in 1976 magmas (100 to 500 ppm S; Johnston, 1978). Chlorine also exhibits significant dispersion in the dacitic to rhyodacitic melt inclusions, as it varies from 0.1 to nearly 0.8 weight percent (fig. 3C). This range is consistent with the 0.3 to 0.6 weight percent Cl determined in melt inclusions of 1976 rocks by Johnston (1978) and the 0.22 to 0.37 weight percent Cl in 1986 melt inclusions studied by Roman and others (2006).

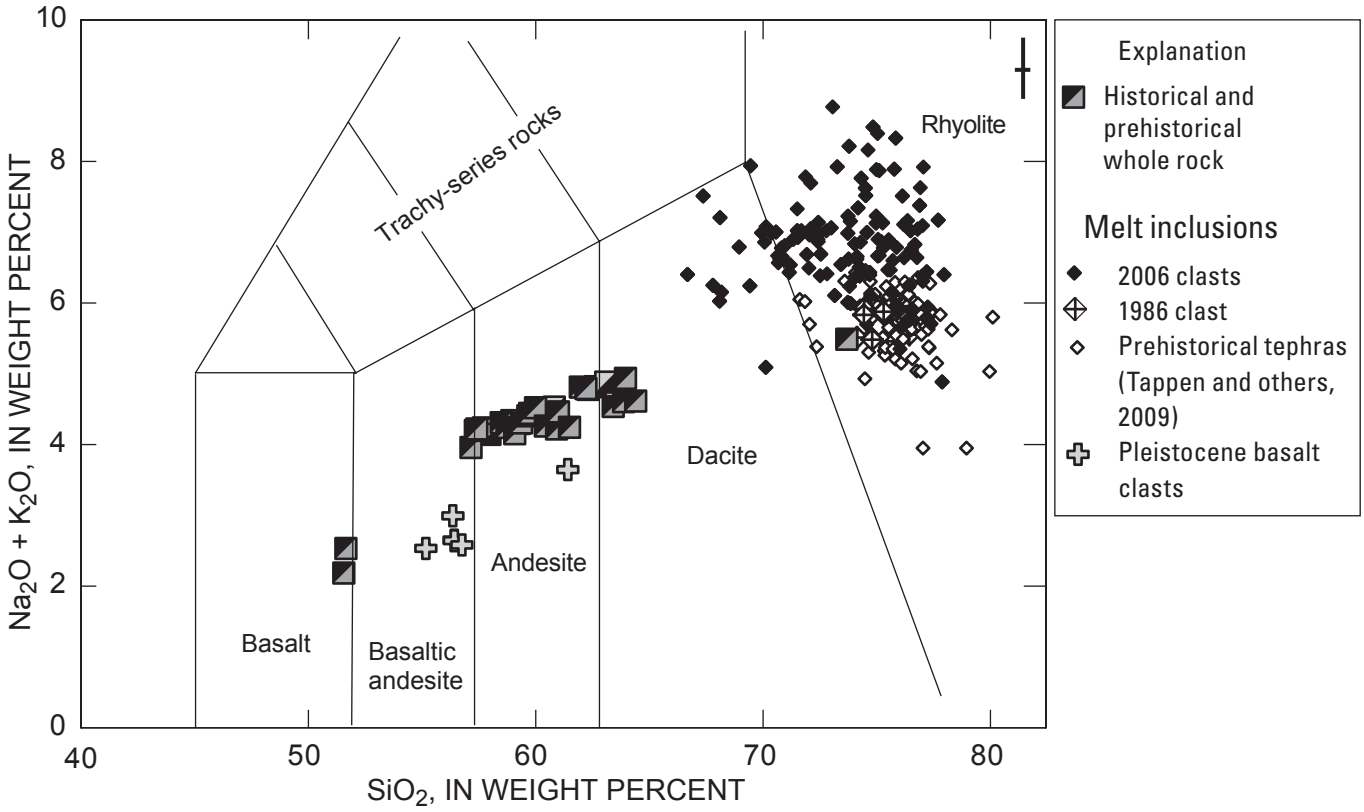

Figure 1. Plot of the relation between concentrations of total alkali elements and silica in Augustine Volcano whole-rock samples (Keinle and Forbes, 1976; Daley, 1986; Larsen and others, this volume) (black and gray squares) and silicate melt inclusions from 2006 rock samples (see text and appendix for descriptions) (black diamonds), prehistoric tephra (open diamonds), 1986 tephra (gridded diamonds), and reheated andesitic melt inclusions from Pleistocene basalt (filled crosses). Data reflect magma evolution and are reported on an anhydrous basis with analytical totals normalized to 100 weight percent. Representative and relative 1-σ precision for melt-inclusion analyses shown in upper right corner. Rock fields after Le Bas and others (1986).

It is noteworthy that the S contents of all felsic melt inclusions are distinctly less than those of the basaltic-andesite melt inclusions of the Pleistocene basalt. Moreover, the presence of 0.08 to 0.36 weight percent S and 0.27 to 0.37 weight percent Cl in these basaltic-andesite melt inclusions (from sample RBW91A137) is consistent with those of basaltic melt inclusions hosted by Fo_{80-85} olivine phenocrysts of Augustine basalt (Johnston, 1978; Zimmer and others, 2004). The latter inclusions contain 0.24 to 0.45 weight percent S and 0.3 to 0.6 weight percent Cl, as well as H_2O concentrations approaching 5 weight percent. Interestingly, these abundances of volatile components in mafic to intermediate-silica content melt inclusions are also consistent with observations made from other mafic, subduction-related magmas. Wade and others (2006), for example, determined that high-Al basaltic liquids from Arenal Volcano contained up to 4 weight percent H_2O, >0.2 weight percent S, and approximately 0.15 weight percent Cl. Straub and Layne (2003) measured 0.7 to 0.9 weight percent Cl and also estimated up to 10 weight percent H_2O in andesitic melt inclusions of volcanic rocks from the Izu arc. Gurenko and others (2005) found 0.04 to 0.29 weight percent S in basaltic-andesite melt inclusions from Chikurachki volcano, Russia. Moreover, Anderson (1982) reports that up to 0.33 weight percent S occurs in rehomogenized melt inclusions of such magmas on a world-wide basis; just as Wallace (2005) notes that these volatile abundances are consistent with those recorded for other subduction-related volcanic systems.

The integrated 2006-, 1986-, and prehistoric-sample melt-inclusion data exhibit no distinct relationships involving CO_2 and magma differentiation, because the CO_2 abundances of most melt inclusions are below the limit of detection. The inclusions do, however, contain widely ranging abundances of H_2O (fig. 4). The H_2O concentrations of the melt inclusions from 2006 samples range from 1.2 to 4.7 weight percent, range from approximately 2 to 6 weight percent for the 1986 samples (that is, ours and those of Roman and others, 2006), and range from approximately 2 to 8 weight percent for melt inclusions of prehistoric samples. These data have been plotted, for comparison, relative to the computed H_2O and CO_2 concentrations of vapor-saturated rhyolitic melt at pressures of 20 to 400 MPa (200 to 4,000 bars) and temperatures of 900 to 1,000°C. Plots like these provide key constraints on pressures of melt and magmatic fluid equilibration as addressed below.

Discussion

Magma Evolution at Augustine During the Past 2,100 Years

Outcrops at Augustine are dominated by andesite and dacite (Waitt and Begét, 2009); basaltic and basaltic-andesite rocks are rare at the surface. This skewed compositional distribution of volcanic rocks indicates that the more primitive mafic magmas feeding this volcano differentiate significantly before eruption. Prior research concluded that magma mixing/mingling is crucial to the evolution of Augustine magmas and that the geochemical features of this process are overprinted by crystal fractionation, assimilation, and fluid exsolution. Johnston (1978) was one of the first to articulate this after systematic analysis of 1976 eruptive products. He surmised that fluid-saturated, residual dacitic melt mixed with fluid-undersaturated basaltic melt, and that extensive crystallization occurred afterward within the resulting mixed products. In a recent study of the compositionally heterogeneous materials of the 1986 eruption, Roman and others (2006) determined that some batches of erupted magma reflect mixing in the shallow crust of newly arrived, comparatively mafic magma with compositionally evolved magma that was residual from the 1976 eruption. They also concluded that some 1986 material represents juvenile magma that evolved without mixing. More complex mixing processes for 1986 magmas were called upon by Harris (1994) and Johnson and others (1996). In this three-component scenario, relatively new magma mixed with magma residual from the 1976 eruption and with partially crystallized residual "rind" material that was low in K_2O and very low in related incompatible elements (Larsen and others, this volume).

Other research has interpreted evidence of a stronger role of fractional crystallization. Daley (1986) argued from analyses of prehistoric, 1935, 1963–64, and 1976 eruptive materials, that andesitic magmas formed by crystal fractionation of parental basaltic magmas at comparatively high pressures, and this process was followed by subsequent fractionation of andesitic liquid to dacitic compositions by low-pressure crystallization. To Daley (1986), magma mixing had only minor effects on magma evolution. Moreover, Johnson and others (1996) concluded that closed-system crystal fractionation was the dominant evolutionary process for some 1976 magmas, even though their interpretation of oxygen isotopic characteristics of whole-rock data was consistent with magma mixing. More recent research (Tappen and others, 2009) on tephra from 4 prehistoric eruptions reveals that crystal fractionation was dominant even though the phenocrysts also provide ample evidence of mixed and/or mingled magmas. Given the extent of prior research on processes of magma differentiation in 1986 and older magmas, we focus herein on processes reflected in 2006 rocks in the following discussion, but we also compare these results with those bearing on prior eruptions to provide a broad context for processes of magma evolution at Augustine Volcano (fig. 5).

Mixing and/or Mingling in 2006 Magmas

The 2006 eruptive materials afford ample evidence of magma hybridization. During our field work and that of others in the summer of 2006 (Vallance and others, this volume; Larsen and others, this volume; Tilman, 2008), a large variety of banded rocks, that are definitive evidence of incomplete mixing of magmas of differing compositions, was observed (fig. 6). In addition, hand sample 06AUMC008B.p1A exhibits light- and intermediate-gray banding on a smaller scale. The

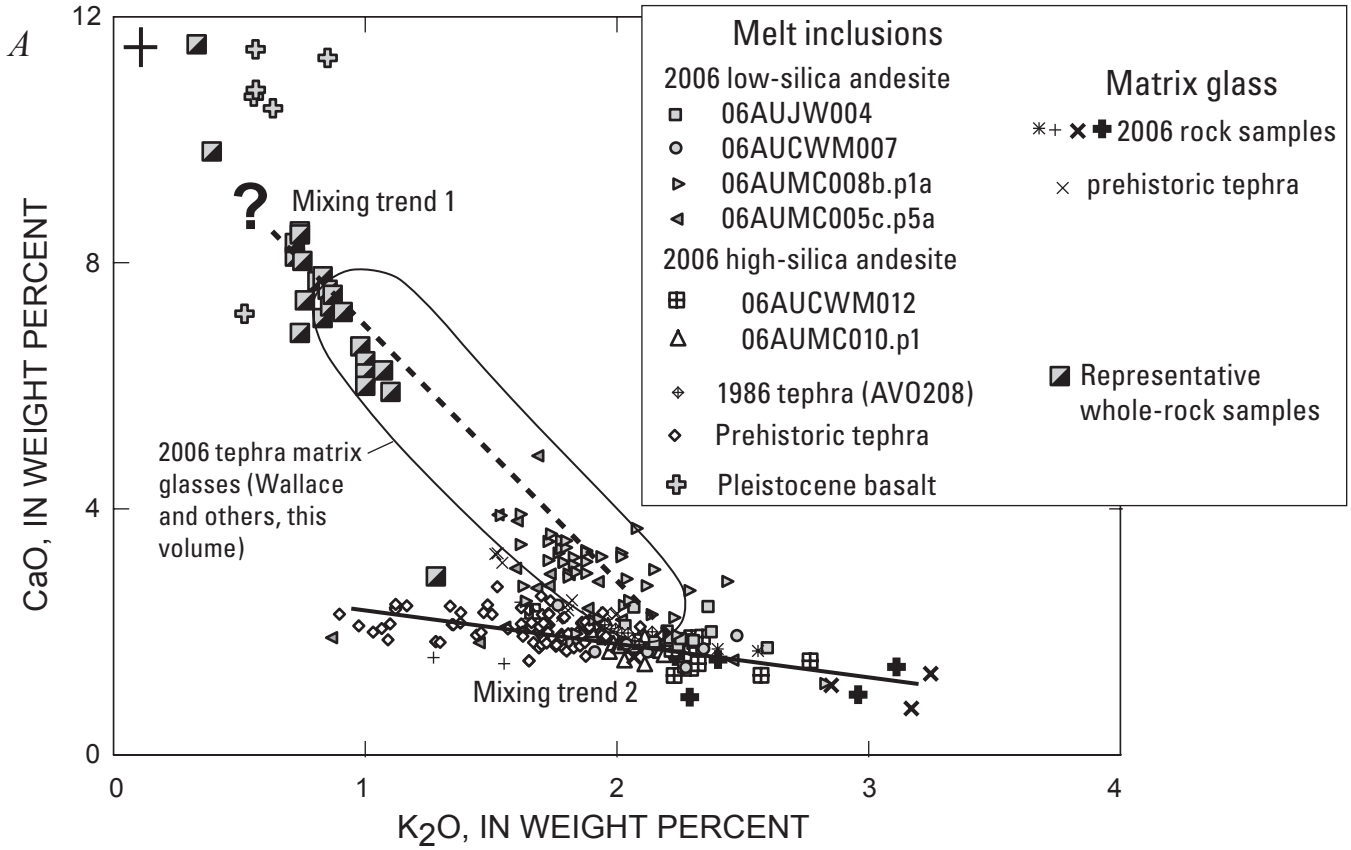
A
Melt inclusions
2006 low-silica andesite
06AUJW004
06AUCWM007
06AUMC008b.p1a
06AUMC005c.p5a
2006 high-silica andesite
06AUCWM012
06AUMC010.p1
1986 tephra (AVO208)
Prehistoric tephra
Pleistocene basalt
Matrix glass
2006 rock samples
prehistoric tephra
Representative whole-rock samples
Mixing trend 1
Mixing trend 2
2006 tephra matrix glasses (Wallace and others, this volume)
CaO, IN WEIGHT PERCENT
K2O, IN WEIGHT PERCENT
0
4
8
12
0
1
2
3
4

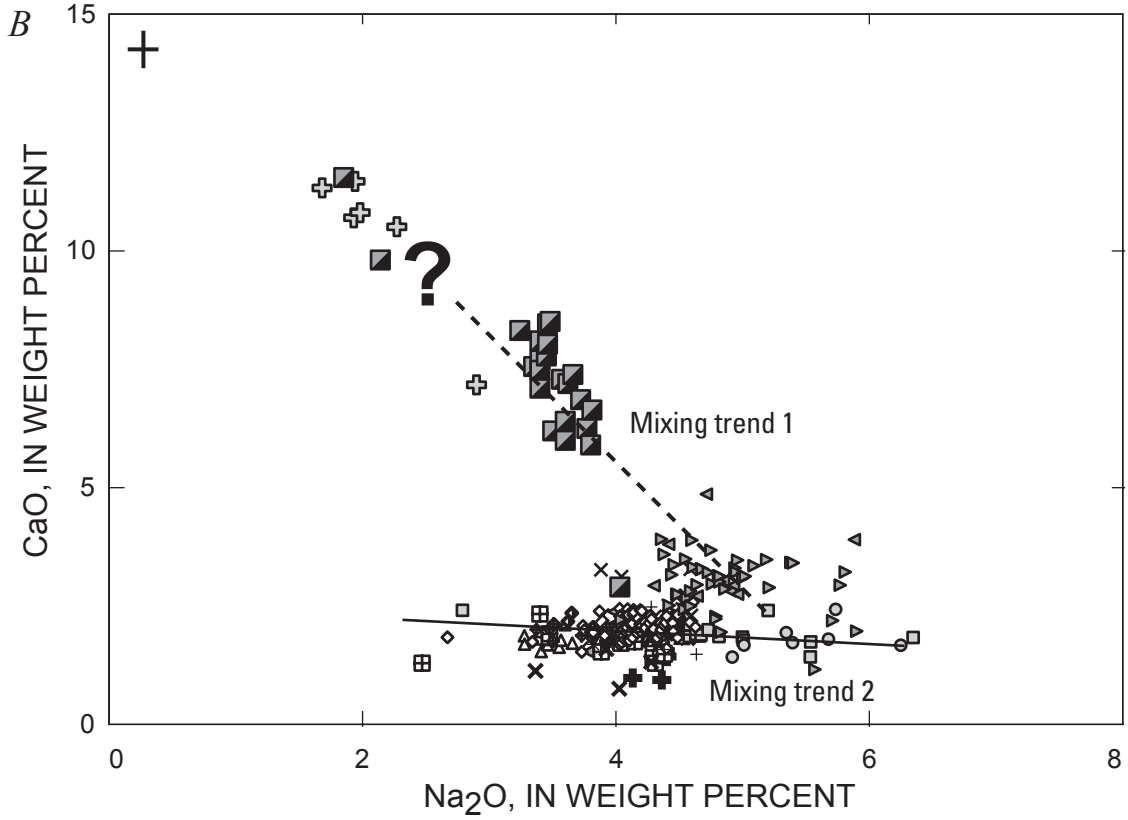
B
Mixing trend 1
Mixing trend 2
CaO, IN WEIGHT PERCENT
Na2O, IN WEIGHT PERCENT
0
5
10
15
0
2
4
6
8

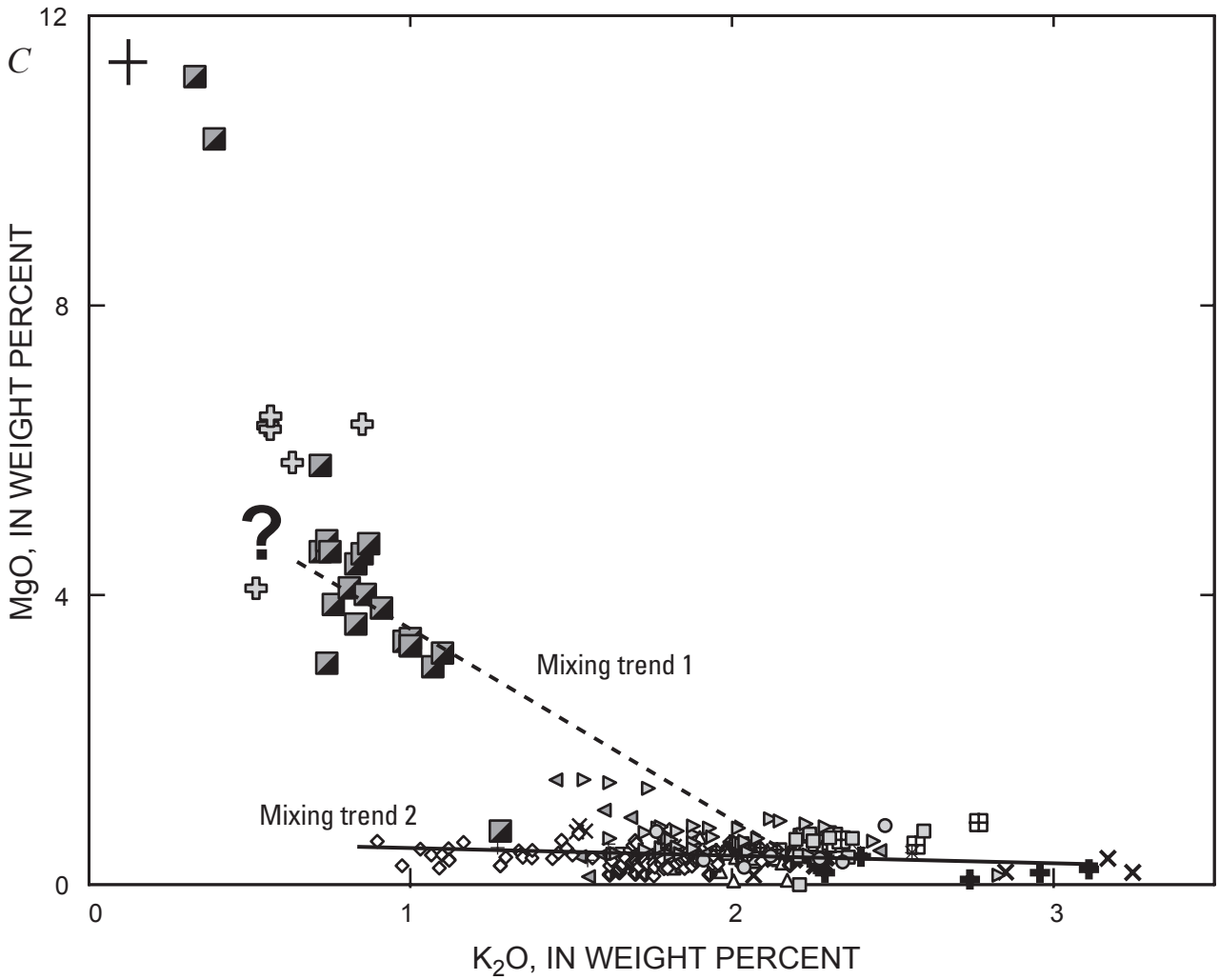

Figure 2. Plots of the relations between the concentrations of CaO and K_2O (*A*), CaO and Na_2O (*B*), and MgO and K_2O (*C*) for Augustine Volcano melt inclusions, matrix glasses, and whole-rock samples; the curves are schematic. Felsic melt inclusions from low-silica andesitic 2006 rock samples are shown with small gray-filled symbols and include 06AUJW004 (squares), 06AUCWM007 (circles), 06AUMC008b.p1A (right-pointing triangles), and 06AUMC005c.p5A (left-pointing triangles). Reheated melt inclusions from Pleistocene basalt sample (RBW91A137) represented by large filled crosses. Felsic melt inclusions from high-silica andesitic 2006 rock samples are shown with small clear-filled symbols and include 06AUCWM012 (gridded squares) and 06AUMC010.p1 (upward-pointing triangles). Other felsic melt inclusions from high-silica andesitic to dacitic rock samples are shown with small clear-filled symbols and include prehistoric tephra (open diamonds) (Tappen and others, 2009), our 1986 ignimbrite sample AVO 208 (gridded diamonds), other 1986 tephra (diamonds clear on one side and filled on right-hand side; sample 86E-63-2 of Roman and others, 2006). Our matrix glass analyses include samples 06AUCWM007 (bold X's), 06AUCMW014 (faint crosses), 06AUJW004 (bold crosses), 06AUJW001 (bold asterisks), 06AUMC008b.p1A (faint asterisks), and prehistoric tephra (faint X's). Elliptical field represents approximate range in CaO and K_2O for hundreds of matrix glass analyses from 2006 tephra (Wallace and others, this volume). Representative whole-rock samples shown as large, variably filled squares (Tappen and others, 2009; Keinle and Forbes, 1976; Daley, 1986; Harris, 1994). The data acquired from low-silica rock samples are consistent with upper curve (dashed line of mixing trend 1) and reflect consequences of magma mixing/mingling and other processes. Large question mark reflects unknown compositional characteristics of the basaltic mixing end member. Data from dominantly high-silica rock samples are consistent with the lower curve (solid line of mixing trend 2). This trend also reflects melt evolution dominated by magma mixing/mingling that apparently involved two high-silica magmas with varying K_2O and Na_2O concentrations and marginally varying CaO and SiO_2 concentrations. The silica content of nearly all of the latter melt inclusions, normalized to an H_2O-free basis, ranges from 71 to 78 weight percent. Representative and relative 1-σ precision for glass analyses is shown as cross in upper left corner. See text for discussion.

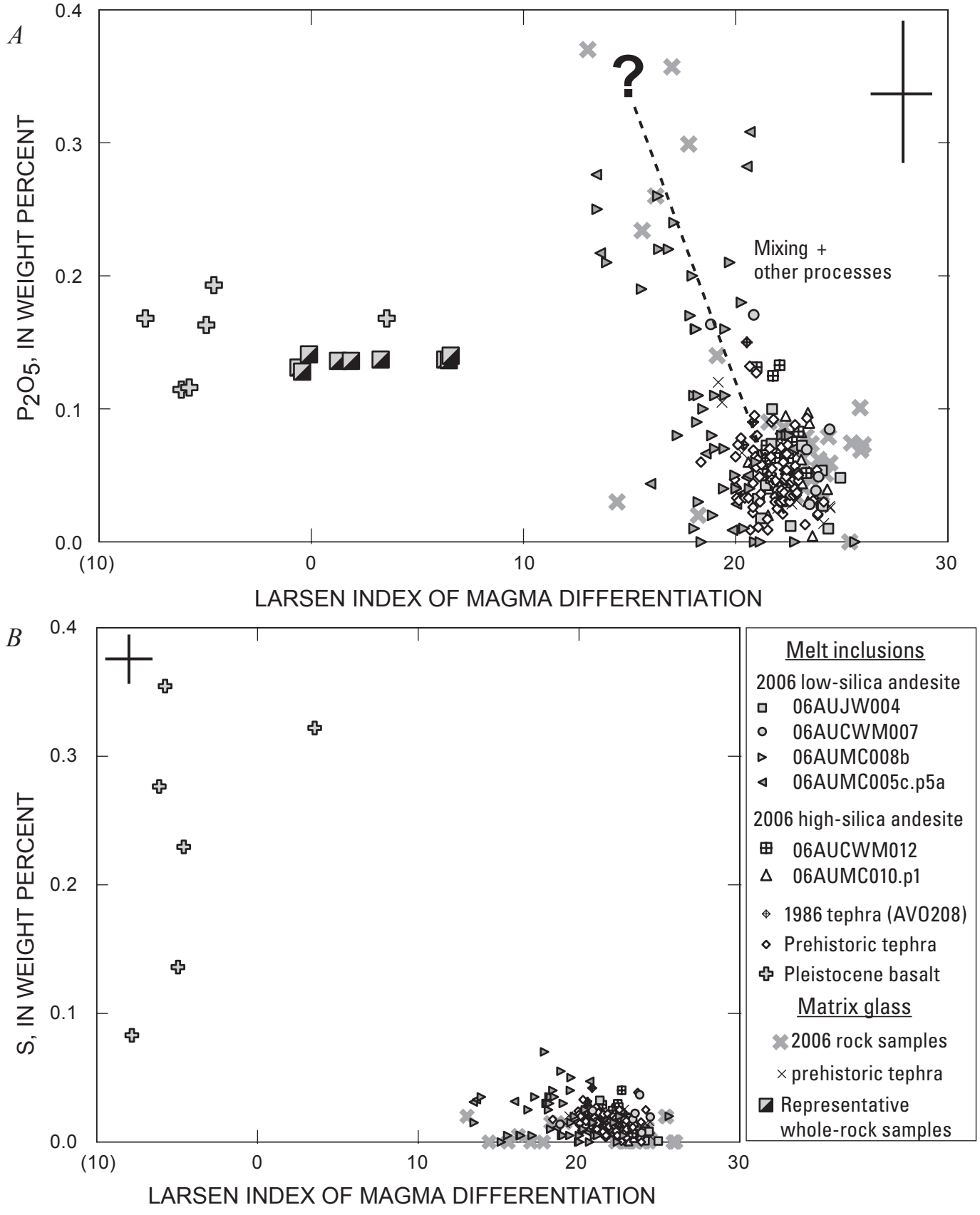
A
0.4
0.3
0.2
0.1
0.0
P2O5, IN WEIGHT PERCENT
?
Mixing +
other processes
(10)
0
10
20
30
LARSEN INDEX OF MAGMA DIFFERENTIATION
B
0.4
0.3
0.2
0.1
0.0
S, IN WEIGHT PERCENT
(10)
0
10
20
30
LARSEN INDEX OF MAGMA DIFFERENTIATION
Melt inclusions
2006 low-silica andesite
06AUJW004
06AUCWM007
06AUMC008b
06AUMC005c.p5a
2006 high-silica andesite
06AUCWM012
06AUMC010.p1
1986 tephra (AVO208)
Prehistoric tephra
Pleistocene basalt
Matrix glass
2006 rock samples
prehistoric tephra
Representative
whole-rock samples

mixing-based origin of these macroscopic features is further supported by microscopic-scale textural features in 2006 samples. These observations include the presence of numerous reversely zoned plagioclase phenocrysts, resorption-growth features in plagioclase, and partially resorbed and orthopyroxene-rimmed olivine phenocrysts. Moreover, the temperatures recorded by coexisting iron-titanium oxide minerals contained in the groundmass of 2006 rock samples (for example, 835 to 1,052°C) vary significantly (fig. 7), and they are consistent with the temperature ranges estimated for 2006 magmas by Larsen and others (this volume) and for temperature estimates of older Augustine magmas (Johnston, 1978; Johnson, 1986; Roman and others, 2006, Tappen and others, 2009). This observed dispersion in temperature for oxides within individual samples is a consequence of mixing processes (fig. 7). In fact, many of the plagioclase-hosted inclusions that occur within distinct resorption-growth zones are a result of and an indication of the interaction of extant plagioclase phenocrysts with younger aliquots of magma that were hotter and more H_2O enriched, and, therefore, they reflect the interaction of younger magma with phenocrysts of an older magma. The apparent method of entrapment of these inclusions (that is, heating through magma mixing) is consistent with their geochemical characteristics further supporting the occurrence of magma mingling and/or mixing.

The variety of mixing processes involving materials erupted in 2006 is complex; Larsen and others (this volume), for example, call for two stages of hybridization. In their model, the initial two-component mixing event involved a juvenile batch of hot, relatively volatile-rich, mafic magma that combined with cooler, crystal-rich, high-silica andesitic magma (that was likely residual from 1986 or older eruptive

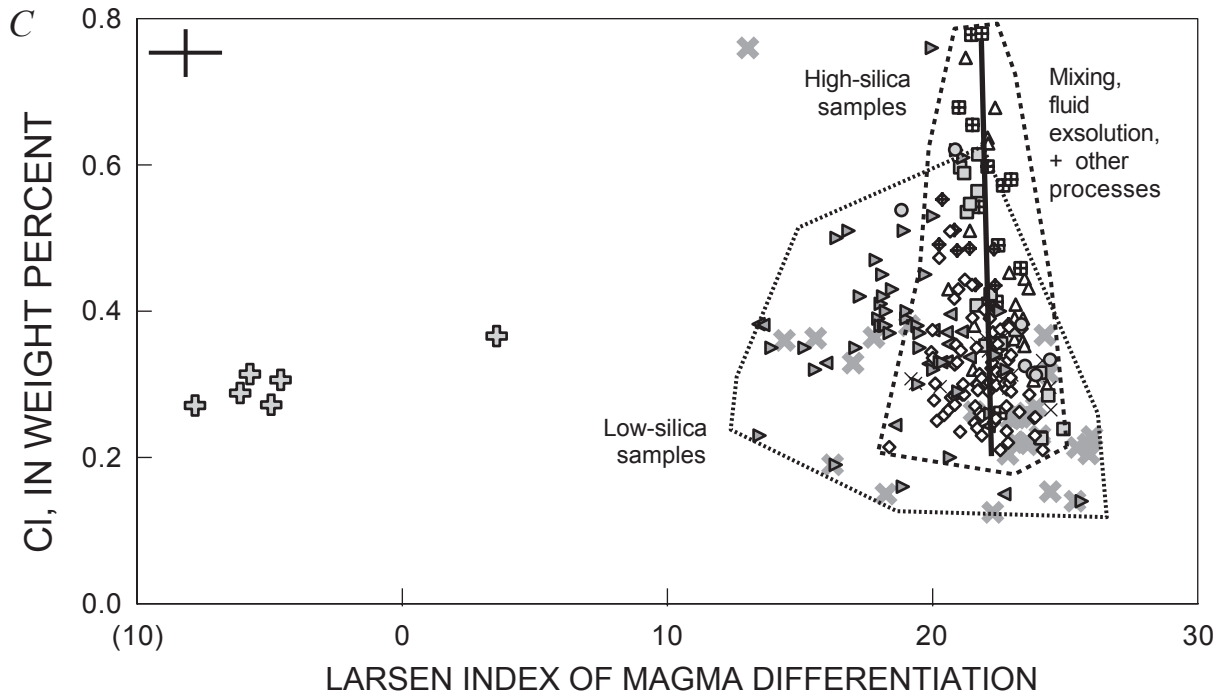

Figure 3. Plots of the relation between the concentrations of P_2O_5 (*A*), S (*B*), and Cl (*C*) and the Larsen differentiation index (for example, [[SiO_2x0.333] + K_2O] versus [CaO + MgO + FeO]] on a wt. percent basis) for melt inclusions and matrix glasses of Augustine Volcano rock samples; samples and symbols same as in figure 2, except all 2006 matrix glasses are shown as gray X's and those of prehistoric tephra shown as faint X's. Data express the changes in volatile- and fluxing-component concentrations in residual melt with progressive magma evolution assuming that basaltic-andesite melt inclusions (filled crosses) are geochemically representative of magmas parental to prehistoric, 1986, and 2006 magmas. *A*, Phosphorus concentrations generally decrease from Pleistocene andesitic melt inclusions and all whole rocks to that of the felsic melt inclusions from 2006, 1986, and prehistoric high-silica andesitic and dacitic rock samples and for most of the felsic melt inclusions of low-silica andesites of same eruptive units. However, the P_2O_5 contents of some felsic melt inclusions of low-silica andesites evolved to higher abundances with magma evolution. *B*, Sulfur concentrations of felsic melt inclusions of all Augustine rock samples are very low and reflect sulfide crystallization and/or exsolution of magmatic fluid(s). *C*, Chlorine concentrations of melt inclusions are highly variable; fields for low-SiO_2 andesitic rocks (dotted envelope) and high-SiO_2 andesitic rocks (dashed envelope) shown for comparison. Chlorine data reflect magma mixing, fractional crystallization, and fluid(s) exsolution as described in text. Representative and relative 1-σ precision for glass analyses is shown as cross in upper corners.

activities) to form the 2006 low-silica andesitic magma. The second mixing event that they observe involved syneruptive hybridization of low-silica and high-silica andesitic magma to form intermediate-silica andesitic rocks.

Our mixing trend 1 (fig. 2) is consistent with the first two-component mixing process of Larsen and others (this volume) that involved the combination of an unidentified mafic magma with older crystal-rich, high-silica andesitic residual magma. Interestingly, our analyses of glass compositions (figs. 2 and 3) allow us to provide some constraints on the composition of the melt in the high-silica andesitic magma that was involved in the mixing. Based on the curves shown in these figures, this melt contained ≤2 weight percent CaO, ≤1 weight percent MgO, ≥2.2 weight percent K_2O, ≥5 weight percent Na_2O, ≤0.05 weight percent P_2O_5, and ≤0.2 weight percent Cl. Close inspection of the most alkali-enriched melt inclusions of figures 2*A* and 2*B* also shows several data points representing more highly evolved glasses from the low-silica andesite samples, and it is important to note that these glass compositions are not compatible with the mixing trend 1 line because they imply a break-in-slope of the trend. These highly evolved samples of glass contain 3 or more weight percent K_2O and nearly 6 weight percent Na_2O, and we interpret them to reflect the consequences of fractional crystallization

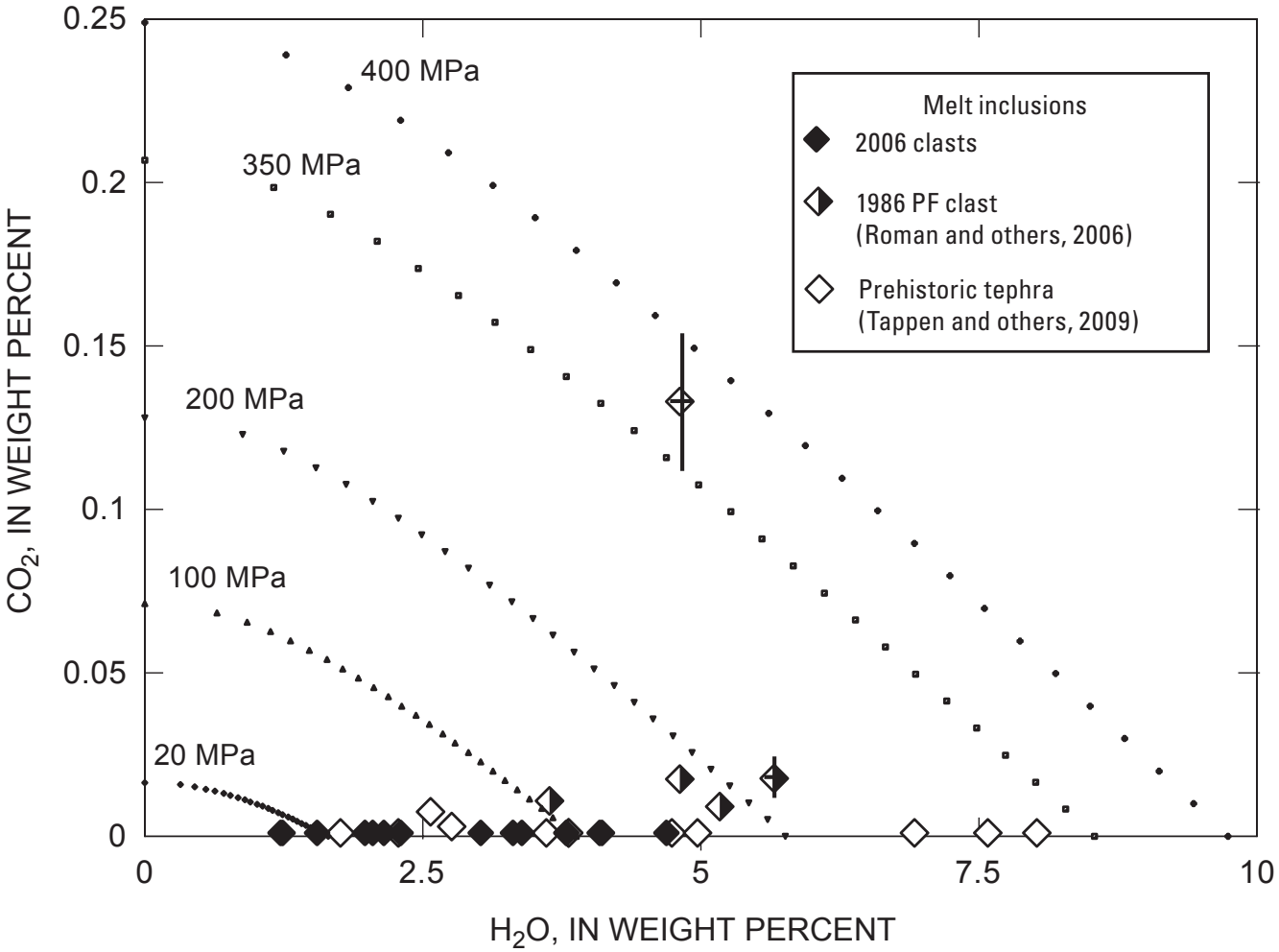

Figure 4. Plots of the relation between CO_2 and H_2O in 28 silicate melt inclusions from Augustine Volcano rock samples including prehistoric rocks (open diamonds; Tappen and others, 2009), 1986 tephra (diamonds filled on right side; sample 86E-63-2 of Roman and others, 2006), and our 2006 samples (filled diamonds). Data are plotted in reference to isobaric curves for rhyolitic melt saturated in CO_2- and H_2O-dominated fluid(s) using model of Newman and Lowenstern (2002). Melt inclusions in this plot reflect either minimum trapping pressure (given independent evidence that a melt inclusion represents fluid-saturated melt) or pressures at which a fluid-phase would have exsolved (if no such evidence is available). Prehistoric melt inclusions represent trapping or fluid-exsolution pressures ranging from 20 to >350 MPa, melt inclusions from 1986 samples represent trapping or fluid-exsolution pressures of about 10 to 220 MPa, and melt inclusions from 2006 samples reflect trapping or fluid-exsolution pressures of about 20 to 160 MPa. Estimated values for 1-σ precision for CO_2 and H_2O in glasses are shown as vertical and horizontal lines for two representative high- and low-CO_2 melt inclusions. See text for discussion.

of low-silica andesitic magma that occurred subsequent to mixing. Relatively late-stage fractionation, like this, is consistent with the presence of microlite-enriched groundmass in the low-silica andesitic rocks (Larsen and others, this volume).

Our mixing trend 2 is based on glass compositions, and it is inconsistent with the second hybridization process recognized by Larsen and others (this volume). Through their analysis of whole-rock data, Larsen and others described mixing of low- and high-silica andesitic magmas to generate hybrid andesitic magmas with intermediate silica contents. Compared with this second mixing trend of Larsen and others (this volume), our mixing trend 2 involves highly variable K_2O abundances that are not compatible with the bulk geochemistry of most of the andesites studied by Larsen and others (this volume). The origin of the felsic, low K_2O-end member is discussed in more detail below.

Fractional Crystallization in Magmas Erupted from Augustine in 2006

The 2006 rock samples contain normally zoned plagioclase and pyroxene phenocrysts, as well as highly evolved rhyolitic matrix glasses and silicate melt inclusions contained within andesitic to dacitic whole rocks. These features are normal products of fractional crystallization. The effects of fractional crystallization are also seen in the presence of fine-grained gabbroic inclusions, erupted in 2006, that are low in incompatible elements. These geochemical characteristics led Larsen and others (this volume) to interpret the gabbro to represent accumulated residual crystals. It is also noteworthy that the groundmass of the 2006 low-silica andesitic rocks contains abundant microlites and exhibits a felty texture; whereas, the matrix of high-silica andesitic rocks are microlite-poor and

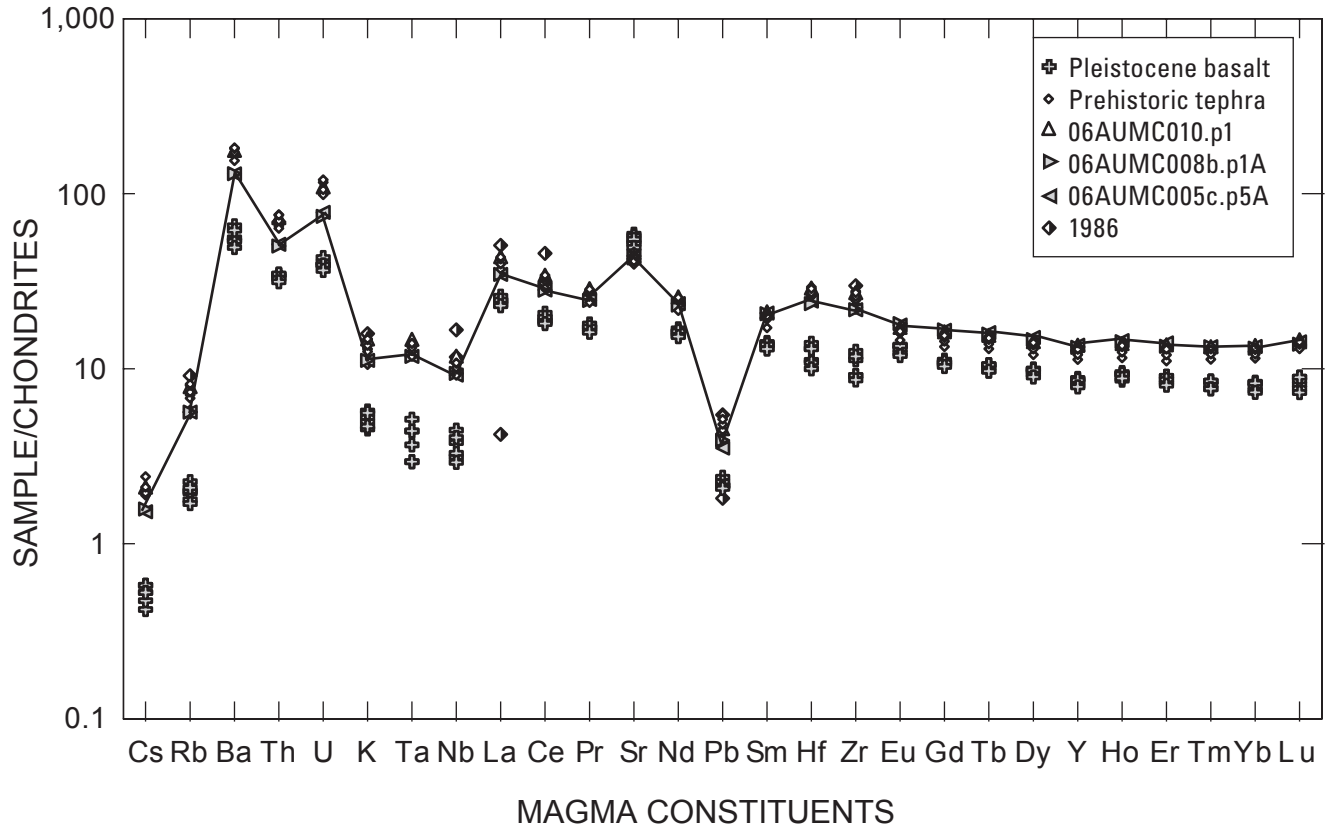

Figure 5. Plot of potassium and trace-element concentrations of Augustine Volcano whole-rock samples normalized to chondritic values (Sun and McDonough, 1995) for five prehistoric tephra (diamonds; from Tappen and others, 2009), six Pleistocene basalts (open crosses; Larsen and others, this volume), 06AUMC010.p1 (open upward-pointing triangles), 06AUMC008b.p1A (gray-filled right-pointing triangles), and 06AUMC005c.p5A (gray-filled left-pointing triangles), and 1986 tephra. Drawn line fitted to normalized data of sample 06AUMC005c.p5A as an example of 2006 eruptive materials relative to older eruptive materials. See text for discussion.

Figure 6. Photograph of large banded boulder within 2006 Augustine pyroclastic-flow deposit showing textural evidence of magma mingling. Bolder located on north slope of Augustine Volcano. One-half meter long rock hammer shown for scale.

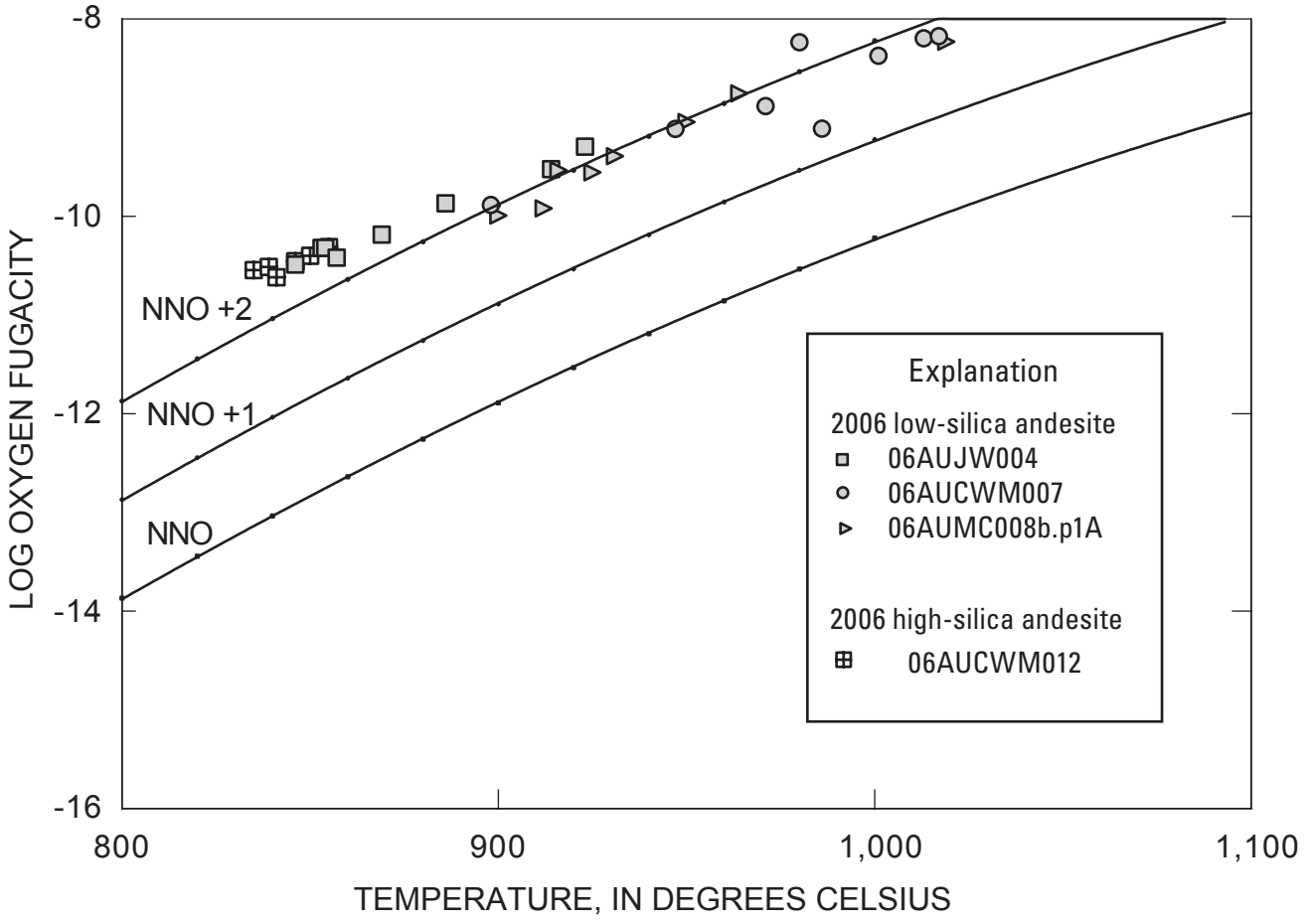

Figure 7. Plot of calculated equilibration temperature (°C) and log of oxygen fugacity (relative to nickel-nickel oxygen buffer = NNO) for coexisting (and "touching") pairs of ilmenite and titanomagnetite. Iron-titanium oxide minerals in 2006 rock samples: 06AUJW004 (gray-filled squares), 06AUCWM007 (gray-filled circles), 06AUCWM012 (gridded squares), and 06AUMC008b.p1A (gray-filled triangles). Data calculated using techniques of Andersen and others (1993) and evaluated using the method of Bacon and Hirshmann (1988), and corrected by reducing temperatures 30°C because these algorithms are not directly applicable to these oxide minerals at such elevated oxygen fugacities. See text for discussion of these methods.

contain glass suitable for microbeam analysis. This indicates that post-mixing, late-stage crystallization of magma forming the low-silica andesites influenced the composition of their near-final and final melts. As explained below and by Larsen and others (this volume), this stage of crystallization may have been facilitated by shallow magma ascent and decompression- and degassing-related processes.

A detailed trace-element analysis of whole-rock samples by Larsen and others (this volume), however, indicates that the high-silica andesites are not fractional crystallization-derived differentiates of the low-silica andesitic magmas that formed by magma mixing. In particular, the abundances of Cr and Ni of the high-silica andesites are too enriched and the concentrations of large-ion lithophile and some high-field strength elements are not sufficiently enriched to reflect an origin based solely on fractional crystallization.

The Behavior of Volatile Components in Evolving Augustine Magmas During the Previous 2,100 Years

Prior research indicates that some fractions of 1976, 1986, and 2006 magmas were fluid saturated during ascent (Johnston, 1978; Roman and others, 2006; Webster and others, 2006), so it is pertinent to consider the evidence and consequences of fluid exsolution on magma differentiation at Augustine. The analysis of volatile-component and fluid behavior in the most recently erupted Augustine magmas is challenging, however, due to the complex histories involving magma mixing, mingling, and fractional crystallization.

In discussion that follows, the compositions of silicate melt inclusions from our prehistoric, 1986, and 2006 eruptive materials are shown to provide distinct geochemical evidence of preeruptive fluids in some fractions of the corresponding magmas. Interpretation of the melt-inclusion data further suggests that initial volatile phase exsolution occurred prior to the entrapment of many of the melt inclusions. Specifically, the melt-inclusion data are compared with experimentally determined solubilities of volatile components in coexisting melt and fluid(s), but this approach can be problematic. Augustine magmas exsolve volatile phases that are variably enriched in the four principal volatile components H_2O, CO_2, S, and Cl (Symonds and others, 1990; McGee and others, this volume), and the sum of their partial pressures ($p_{H_2O} + p_{CO_2} + p_{S_{species}} + p_{Cl_{species}}$) must equal the total pressure of a fluid-saturated magma. It follows that all four components must be considered simultaneously in data treatments like this. For example, the presence of elevated S and/or Cl in a fluid phase will dilute the H_2O and CO_2 concentrations and alter the activity-composition mixing relationships (Botcharnikov and others, 2004; Webster and others, 2005) and, hence, change the larger behavior of H_2O and CO_2 in such fluids. Unfortunately, most experimental data are limited at present to pseudo-ternary systems including silicate melt-H_2O-CO_2, melt-H_2O-Cl, or melt-H_2O±S so we are forced to address the melt-inclusion data with individual pseudo-ternary systems in the discussion that follows.

H_2O in Augustine Magmas

The abundances of the components H_2O and K_2O, which are relatively incompatible in the phenocrysts and microlites in magmas like these, serve as a useful gauge of the extent of residual melt evolution (Anderson, 1976; Johnston, 1978; Roman and others, 2006). In particular, prior studies have interpreted negative correlations between K_2O and H_2O in silicate melt inclusions to represent the consequences of polybaric, decompression crystallization of fluid-saturated magma during ascent (Roman and others, 2006; Atlas and others, 2006). Therefore, we have plotted the concentrations of H_2O versus K_2O for a set of melt inclusions that were analyzed by FTIR and largely represent prehistoric, 1986, and 2006 high-silica andesitic and dacitic rock samples (fig. 8). Figure 8*A* includes 4 modeled trends that express the influence of (A) fluid-absent crystallization of 20 weight percent plagioclase, pyroxene, Fe-Ti oxides, and apatite (in modal abundances that are compatible with 2006 Augustine rocks), (B) complete degassing of an open magmatic system with no concurrent crystallization, (C) polybaric crystallization of 25 weight percent phenocrysts from this same mineral suite in a magma that also contains 4 weight percent exsolved aqueous fluid, and (D) mixing of magmas that may or may not be fluid saturated. The lengths of the arrows designating these trends are quantitative representations of the influence of these processes.

Trend A (fig. 8*A*) is consistent with the positive correlation involving the three most H_2O-enriched, prehistoric melt inclusions, and hence, may reflect the geochemical evolution of these and potentially other fractions of Augustine melts via fluid-absent fractional crystallization. Trend B is inconsistent with the negative correlation of H_2O versus. K_2O that is exhibited by most of the data. The slope of trend C is consistent with the general orientation of the melt-inclusion data field, but this trend requires 25 weight percent crystallization to generate the requisite increase in K_2O content and this degree of crystallization is problematic. It is too extensive for such felsic melts, because it would reduce the FeO, MgO, and CaO contents of the final residual melt to values near zero. Thus, we interpret these melt inclusions to reflect magma evolution dominated by magma mixing and/or mingling (symbolized by trend D) with associated fractional crystallization of fluid-saturated magmas because they are part of the clustered data of figure 2 best interpreted by linear mixing curves.

It should be noted that other processes influence magmatic systems like these. In a study of plagioclase-hosted, felsic melt inclusions in rocks produced during the April 10, 1980 to March 19, 1982, eruptions of Mount St. Helens, Blundy and Cashman (2005) noted a similar negative correlation involving H_2O and K_2O (fig. 8*B*). They computed temperatures of plagioclase-melt equilibrium and estimated the range in crystallization of the magmas involved. Their

results showed distinct and robust correlations between magmatic temperature, water fugacity, crystallinity, and the compositions of residual fractions of melt in the Mount St. Helens magmas. Blundy and Cashman (2001, 2005) and Blundy and others (2006) concluded that the batches of magma represented by their melt inclusions underwent contemporaneous: (1) decompression crystallization, (2) loss of volatile components to magmatic vapor, and (3) associated release of latent heat within the magma due to phenocryst growth. They also concluded that the latent-heat effects may have increased temperatures in Mount St. Helens magmas locally by as much as 100°C, and that, in general, such latent-heat temperature increases are likely in any magma that decompresses slowly enough to undergo crystallization.

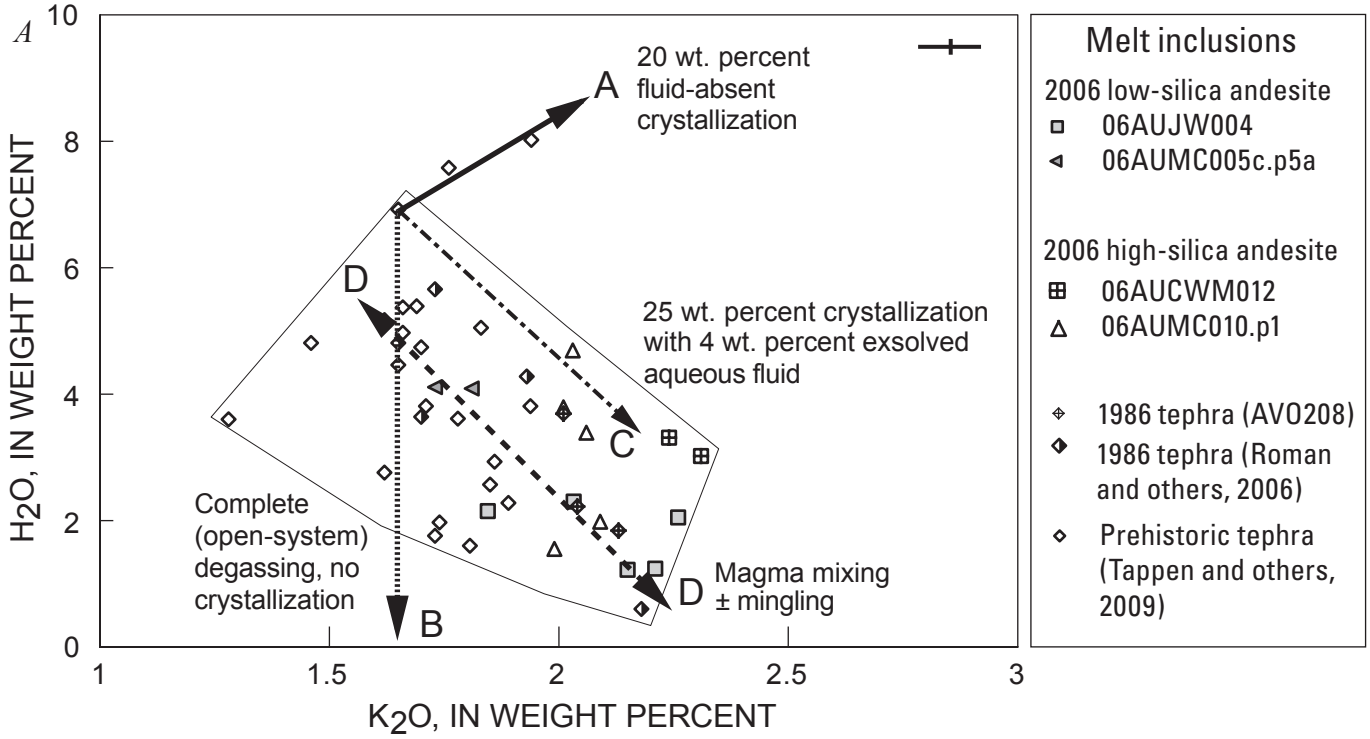

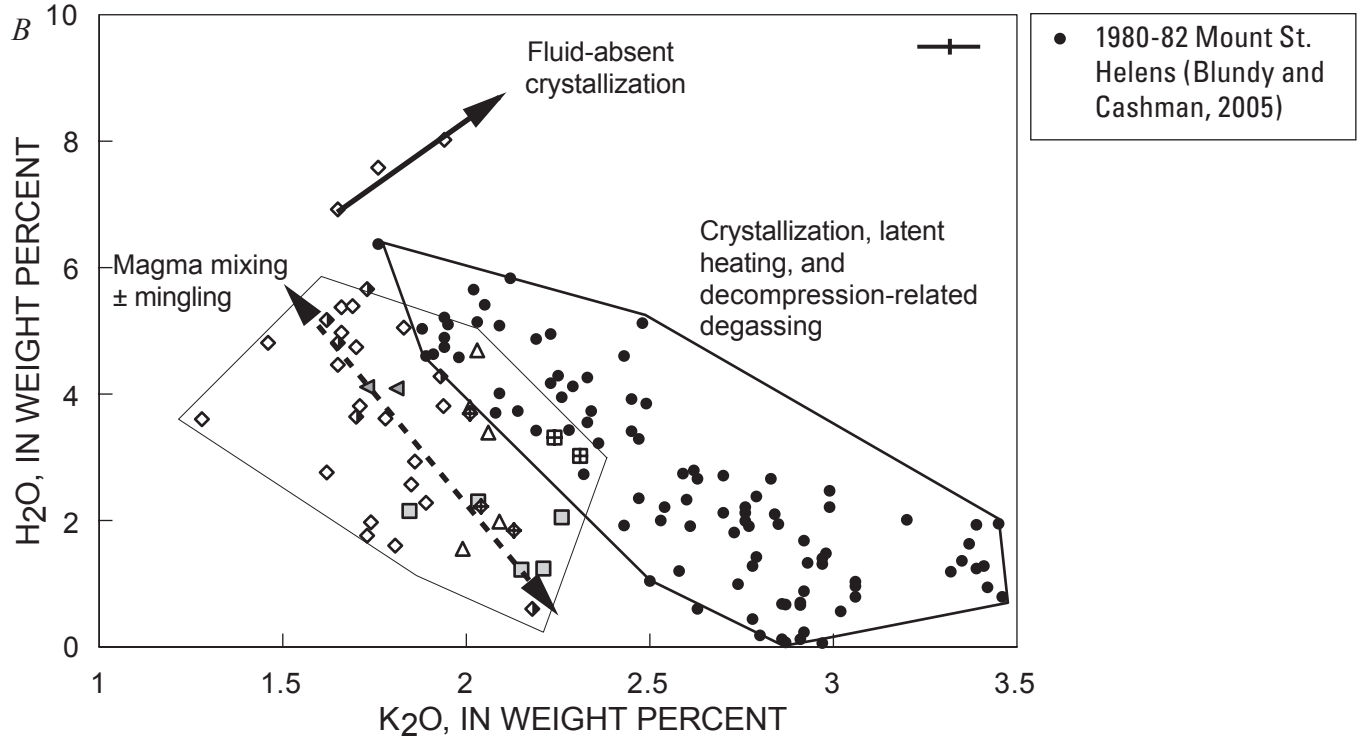

These Mount St. Helens magmas show little textural evidence of magma mixing or mingling which led the authors to note that these processes can account for some common textural features that would otherwise be attributed to preeruptive magma mixing. We conclude that reheating of Augustine magmas, by latent heat release, must also have occurred, but the effects of this process were likely subordinate to reheating caused by magma mixing and/or mingling, given the ample evidence of the latter process.

Sulfur and Chlorine in Augustine Magmas

The S concentrations of most of the rhyodacitic and rhyolitic Augustine melt inclusions are distinctly lower than those of the rehomogenized basaltic-andesite melt inclusions (fig. 3*B*) and the basaltic melt inclusions analyzed by Johnston (1978) and Zimmer and others (2004). These felsic melt inclusions also contain less S than the 0.2 to >0.3 weight percent reported for other subduction-related, calc-alkaline magmas (Anderson, 1982; Wade and others, 2006; Gurenko and others, 2005). The latter concentrations greatly exceed the measured average of 0.02 ± 0.01 weight percent S in all felsic melt inclusions of this study, and these differences indicate that some process of reducing S in the felsic melts occurs in Augustine magmas as they differentiate.

The behavior of S in magmatic systems varies with its oxidation state, and therefore the range in valence states of S in these magmas must be constrained. The 2006 magmas crystallized at f_{O_2} values of approximately NNO+1.5 to NNO+2.5 (fig. 7, table 5; Larsen and others, this volume). This range is similar to the range of circa NNO to NNO+2 reported for prehistoric (Tappen and others, 2009) and 1986 magmas (Roman and others, 2006). At these elevated values of f_{O_2}, the majority of sulfur present would be oxidized to S^{6+} (Carroll and Rutherford, 1988; Mandeville and others, 1998), so the magmatic fluids would contain a mixture of SO_4^{2-}, SO_2, H_2S, and S_2 at shallow crustal pressures (Luhr, 1990; Gerlach and others, 1996; Scaillet and Pichavant, 2003; Jugo and others, 2005; Burgisser and Scaillet, 2007). These theoretical constraints on magmatic $SO_4^{2-}$and SO_2 are compatible with the observation of significant SO_2 concentrations in volcanic vapor of the 2006 eruptive activities (McGee and others, this volume).

Sulfide and sulfate minerals have only rarely been observed at Augustine. For example, Johnston (1978) reported minor sulfides in 1976 rocks, Tappen and others (2009) observed very rare sulfide mineral inclusions in silicate phenocrysts of primitive prehistoric andesites, and anhydrite makes up less than 0.6 volume percent of some 2006 lithologies (Larsen and others, this volume). The presence of these crystalline phases during the early stages of evolution of the relatively primitive magmas, as evidenced by the depletion of S in the less-evolved melt inclusions (fig. 3*B*), would tend to deplete the S abundances of subsequent, residual melts. In fact, if pyrrhotite is included in the fluid-absent crystallization modeling, it would require 1 weight percent sulfide crystallization to generate a rhyolitic melt with only 200 ppm S (that is, a value that is similar to

◀ **Figure 8.** Plots of the relation between H_2O and K_2O in 45 silicate melt inclusions from 2006, 1986, and prehistoric rock samples from Augustine Volcano, Alaska. *A*, The enveloped area (fine, solid polygon) suggests that the K_2O concentrations correlate with H_2O for the data set, but melt inclusions from individual samples may variably reflect a variety of processes. (Trend A) The bold arrow quantitatively defines the influence of polybaric, 20 weight percent crystallization of Augustine felsic melt containing 6.9 and 1.65 wt. percent H_2O and K_2O, respectively, and is consistent with the three most H_2O-enriched melt inclusions that are also inconsistent with the other inclusions. (Trend B) The dotted arrow reflects the consequences of complete, open-system degassing of H_2O with no crystallization. (Trend C) The length of this dot-dash arrow quantitatively reflects the effect of 25 wt. percent crystallization of magma containing 4 wt. percent exsolved aqueous fluid during magma ascent and polybaric decompression. (Trend D) These melt inclusions also reflect consequences of mixing and/or mingling of multiple magmas, and the dashed arrow represents the differentiation of residual rhyolitic melts by mixing of relatively hydrous and Na_2O-, K_2O-, and Cl-deficient magma with relatively anhydrous magma. Mixing apparently occurred during contemporaneous crystallization and fluid exsolution. *B*, The H_2O and K_2O concentrations of silicate melt inclusions (filled circles) from Mount St. Helens eruptions of April, 10, 1980 to March 19, 1982, (Blundy and Cashman, 2005) are included with the Augustine melt inclusion data. Blundy and Cashman (2005) interpret this negative correlation, by the use of associated constraints on melt-plagioclase equilibration temperatures and modeling, to represent the consequences of decompression crystallization of fluid-saturated felsic magmas and the concurrent release of latent heat of crystallization. These Mount St. Helens magmas show little textural evidence of magma mixing or mingling, but they may have undergone loss of H_2O and other volatile components to magmatic vapor as they ascended and decompressed. The extent of crystallization increased, even though these magmas may have been heated by as much as 100°C by latent heating effects, because of the reduction in the fugacities of volatile components as they were sequestered by vapor. Blundy and others (2006) note that these processes can generate textural characteristics similar to those of magma mixing. Given the very similar nature of this relationship to that exhibited by the Augustine melt inclusions, this process may have also played a minor role in the evolution of Augustine magmas. Representative and relative 1-σ precision for glass analyses is shown in upper right corners. See text for discussion.

those of most of the felsic melt inclusions) from the basaltic-andesite melt inclusion compositions which is inconsistent with the lack of sulfide mineral inclusions in other phenocrysts of these rocks.

Mixing of magmas does not appear to be solely responsible for the trends involving S in most of the felsic melt inclusions. The apparent mixing trends expressed by the major constituents CaO, K_2O, and Na_2O (fig. 2) and some minor constituents P_2O_5 and Cl (fig. 3) in these inclusions exhibit strong variability in the abundances of these components as a result of varying degrees of mixing (that is, they show widely varying concentrations along the mixing lines). In contrast, the concentrations of S of the felsic melt inclusions are much more highly focused (that is, much less dispersed) at the average value of 0.01 weight percent, and, hence, they are inconsistent with this process. Mixing must have generated some variability in the mixed products, but other processes were apparently involved as well.

As sulfides are rare and only present in Augustine rocks at abundance levels well below that required to remove significant S from the residual melts and because magma mixing is not solely responsible for the strong reduction in S concentrations with melt evolution, the involvement of a fluid or fluid phases in S sequestration is required. The partition coefficient for S, D_S (weight percent S in fluid/weight percent S in melt) has been determined experimentally to range from approximately 10 to 80, 100 to 300, and 100 to 900 for basaltic (Scaillet and Pichavant, 2003), andesitic (Scaillet and Pichavant, 2003), and rhyodacitic (Botcharnikov and others, 2004) melts, respectively, at pressures of 100 to 300 MPa and temperatures and oxygen fugacities relevant to Augustine magmas (≤1,050°C and f_{O_2} of NNO to NNO+2) (fig. 7; Roman and others, 2006; Tappen and others, 2009). Thus, exsolved aqueous magmatic fluids would be highly efficient in stripping S from melts of the 2006, 1986, and prehistoric Augustine magmas. Importantly, values of D_S increase with reduced pressure (Scaillet and Pichavant, 2003), so the efficiency of this process would increase with the reduction in pressure that accompanies magma ascent. The differentiation of the residual fractions of melt to more felsic compositions would also enhance the efficiency of S sequestration given that D_S is greater for felsic as compared to mafic melts. Moreover, hydrothermal fluids are also capable of dissolving sulfide minerals not trapped as inclusions in other phenocrysts (Reed, 1997); so it is conceivable that any sulfide minerals that may have crystallized relatively early in these magmas were dissolved by fluids during later stages of fluid-saturated magma evolution.

The Cl concentrations of most felsic melt inclusions from the high-silica andesitic to dacitic rocks are variable, and yet, the Cl contents of many of them either equal or exceed those of the more primitive basaltic-andesite melt inclusions (fig. 3*C*). The Cl contents of melt inclusions from low-silica andesites studied are also variable, but in this case most of them are more equivalent to those of the basaltic-andesite melt inclusions (fig. 3*C*). In addition, the Cl concentrations of matrix glasses that we analyzed and those of Wallace and others (this volume) are quite similar to those of the melt inclusions from low-silica andesites. These comparisons indicate that the Cl concentration of some of the felsic melts represented by the melt inclusions from high-silica andesites increased to a limited extent during differentiation, and the trends apparently reflect the varied consequences of magma mixing, fluid(s) exsolution, and fractional crystallization as described below.

The Cl concentrations in the set of melt inclusions that were analyzed by FTIR (and largely represent prehistoric, 1986, and 2006 high-silica andesitic and dacitic rock samples; fig. 9*A*) correlate negatively with H_2O in general, but this is not true for the various subsets of data (distinguished by individual rock samples and stages of eruption) comprising this larger data set. This lack of correlation for melt inclusions from individual samples is the likely result of a variety of magmatic processes, and hence, the larger trend in this figure has been interpreted relative to a series of modeled trends expressing various processes of magma differentiation. For example, some subsets of these data may be consistent with the trend (A) that expresses fluid-absent, isobaric crystallization of 20 weight percent of a rhyolitic melt under closed-system conditions. Alternatively, some of these melt-inclusion data may be consistent with any of several polybaric, closed-system degassing trends that are shown and involve a reduction in pressure of 200 to 50 MPa. These degassing trends include: (B) 20 weight percent crystallization of a rhyolitic melt that is in equilibrium with a fluid containing 2 weight percent Cl (with an average value of D_{Cl} [concentration of Cl in fluid(s)/concentration of Cl in silicate melt] of 10 averaged for changing pressure) or (C) 20 weight percent crystallization of a rhyolitic melt that is in equilibrium with a fluid containing 1 weight percent Cl (with an average value of D_{Cl} of 5 averaged for changing pressure). These values of D_{Cl} are appropriate for this range of felsic melt compositions and this range in pressure (Webster and others, 1999). As magmatic processes do not necessarily occur at equilibrium, figure 9*A* includes a modeled trend (D) for the crystallization and degassing of magma that exsolves a Cl-free aqueous fluid under open-system conditions. Experimental research summarized by Baker and others (2005) demonstrates that H_2O diffuses more quickly than Cl through silicate melts, so (D) addresses magmatic degassing processes in which there is insufficient time for Cl to achieve an equilibrium distribution between melt and fluid(s). Trend D also involves preferential loss of H_2O with no loss of Cl to the fluid, such that the degassing magma has, in effect, a D_{Cl} value of 0, and some of these data appear consistent with this trend. Trend (E) appears more consistent with the larger, integrated data set, and it reflects the consequences of mixing two magmas that contain different H_2O and Cl contents. In summary, given the strong evidence for magma mixing as a dominant process of evolution

of magmas erupted in 2006 and because of the relationships in figures 3C and 8, we suggest that the progressive evolution of late-stage, felsic Augustine melts of the high-silica andesitic magmas involved the mixing and/or mingling of relatively hydrous and K_2O-, Na_2O-, and Cl-deficient rhyolitic melt with relatively anhydrous, K_2O-, Na_2O-, and Cl-enriched rhyolitic melt.

To interpret these processes more fully, it is useful to apply empirically derived and modeled Cl and H_2O solubilities for geologically relevant melt compositions to the melt-inclusion data. Such comparisons provide key constraints on pressures of fluid phase exsolution and on the type of fluid phase(s) that exsolve. The curves in figure 9*B* express the solubilities of H_2O and Cl in rhyolitic melt for 3 pressure conditions, and they represent the exsolution of either a H_2O- ($\pm$ CO_2) bearing vapor phase, a saline liquid, or vapor plus saline liquid as the (Cl/H_2O) ratio of the silicate melt progressively increases. In addition, the 20- and 200-MPa volatile component solubility curves for H_2O-deficient conditions involve a range in Cl concentrations. This range reflects the computed range in maximum Cl solubility for the corresponding range in glass compositions of the melt inclusions (Webster and De Vivo, 2002). It is crucial to account for the range in melt composition because Cl solubility in silicate melts varies strongly with bulk composition (Webster and De Vivo, 2002). These solubility curves also account for the influences of S and pressure on Cl solubility in silicate melts. Specifically, the solubility of Cl in melts that are saturated in S-bearing fluid(s) decreases dramatically with increasing S in the system (Botcharnikov and others, 2004; Webster and others, 2005). Chlorine solubility also decreases with decreasing pressure for silicate melts that are saturated in a saline liquid (Webster and others, 1999).

The compositions of the three, H_2O-enriched prehistoric melt inclusions that contain <0.33 weight percent Cl plot above but near the 200-MPa curve for vapor plus coexisting silicate melt, and hence, they imply pressures of volatile saturation that exceed 200 MPa and that the fluid would have been an aqueous (or potentially aqueous-carbonic) vapor when fluid saturation occurred. Unlike these three, most other melt inclusions are consistent with saturation of Augustine magmas in fluid(s) at lower pressures ranging from 20 to 200 MPa under closed-system conditions, and the latter data are inconsistent with magma storage and evolution at a single pressure (such as within a magma chamber). Interestingly, the compositions of melt inclusions from 2006 samples contain generally lower H_2O concentrations and exhibit larger (Cl/H_2O) ratios than melt inclusions from prehistoric or 1986 tephra. These relationships indicate that (1) the fluid(s) would have exsolved at generally lower pressures than those in the other, older magmas and (2) the compositions of the magmatic fluid phase(s) represented by the melt inclusions from 2006 samples would have been more highly saline. In fact, some aliquots of the fluids at the lower pressures included anhydrous saline liquids.

H_2O and CO_2 in Augustine Magmas

One can derive additional constraints on pressures of melt entrapment, the concentrations of CO_2 and H_2O in magmatic volatile phases, and applicable pressure-composition paths of magma ascent and degassing by comparing the concentrations of H_2O and CO_2 in felsic melt inclusions with experimentally determined and modeled solubilities of H_2O and CO_2 in rhyolite melt (Newman and Lowenstern, 2002; Moore, 2008). However, this procedure does not account for Cl or S species in the fluids. In the following discussion on fluid geochemistry and degassing processes, it must be recognized that the results of comparing the H_2O and CO_2 abundances of melt inclusions with theoretical H_2O and CO_2 solubilities in silicate melts can be interpreted in two ways. One interpretation is that the locations of the melt inclusion data, relative to the isobaric volatile-component solubility curves, determine pressures at which the corresponding aliquots of magma should have saturated in a H_2O- and CO_2-dominated fluid (vapor) phase as magma ascended toward the surface. Alternatively, if independent evidence—that the melt inclusions represent fluid-saturated magma at the time of melt entrapment—is available, then the locations of the melt-inclusion data relative to the isobaric volatile-component solubility curves constrain the pressure of melt inclusion entrapment. Note that the latter approach does not necessarily establish the initial pressures of or the corresponding maximum depths of magmatic volatile-phase exsolution, because the melt represented by a given melt inclusion could have exsolved a volatile phase at depths and pressures greater than those indicated and the melt inclusion simply represents fluid-saturated melt that was trapped in a growing phenocryst at some time well after the stage of initial magmatic fluid exsolution.

To this end, the H_2O and CO_2 abundances of melt inclusions from the 2006 rocks are plotted along with those collected from prehistoric tephra C (AVO 201), G (AVO 205), H (AVO 204), and I (AVO 203) and from several 1986 pumice samples (ours and those of Roman and others, 2006), and the concentrations of these volatile components are compared with the theoretical (Newman and Lowenstern, 2002) isobaric vapor-saturation curves for CO_2- and H_2O-bearing rhyolite melt (figs. 10*A* and 10*B*). This assessment indicates that the aliquots of rhyolite melt represented by most of these melt inclusions would saturate in H_2O- $\pm$ CO_2-bearing fluid(s) at pressures of 20 to 200 MPa. This observation is consistent with that detected previously in plots of H_2O versus Cl in that the Cl, CO_2, and H_2O data are inconsistent with magma storage and evolution at a single pressure (that is, within a magma chamber). It is noteworthy, however, that the compositions of 5 of these melt inclusions imply pressures of fluid phase saturation that exceed 200 MPa and that 1 inclusion indicates pressures that exceed 350 MPa. This is similar to that observed with H_2O versus Cl, and given that the bulk of the melt inclusions from these eruptions of Augustine Volcano provide roughly similar pressure estimates based on plots

A

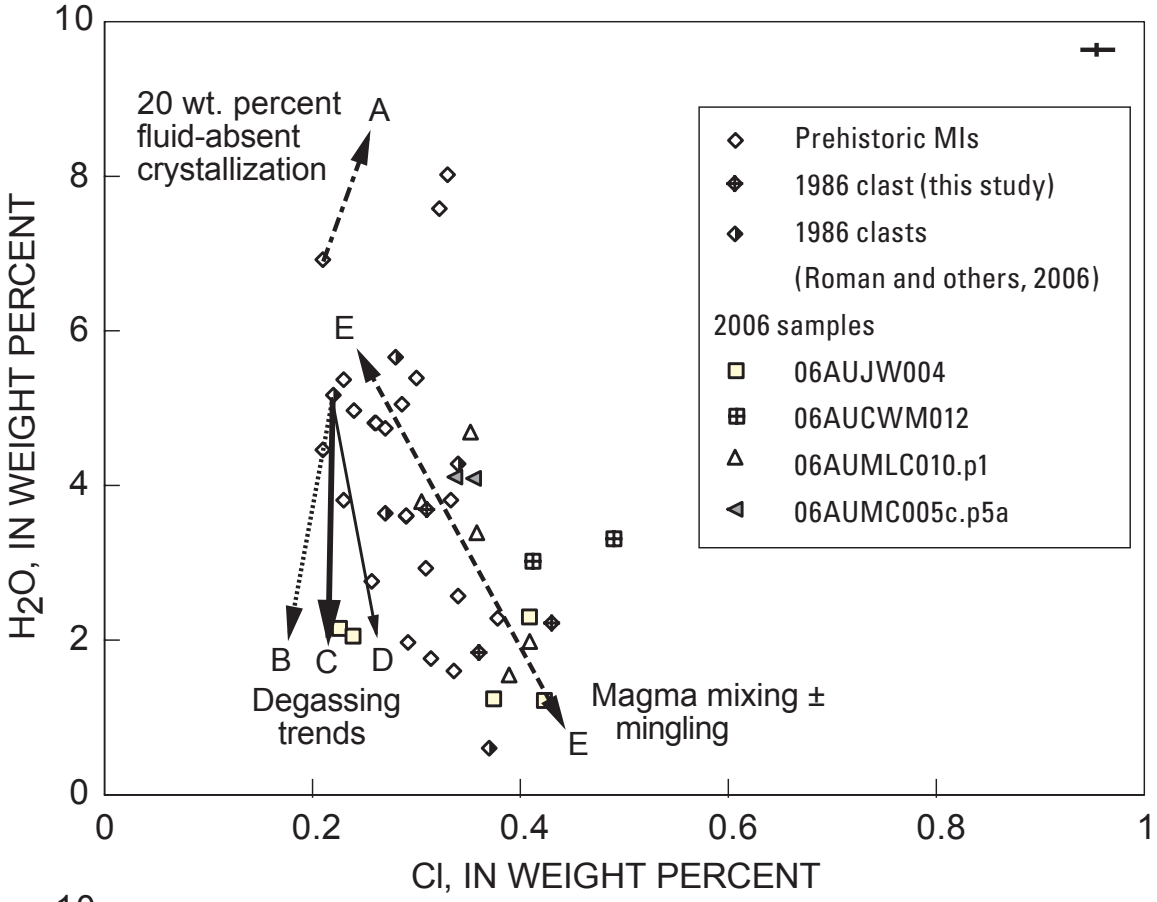
20 wt. percent
fluid-absent
crystallization
A
E
B
C
D
Degassing
trends
Magma mixing ±
mingling
E
Prehistoric MIs
1986 clast (this study)
1986 clasts
(Roman and others, 2006)
2006 samples
06AUJW004
06AUCWM012
06AUMLC010.p1
06AUMC005c.p5a
H2O, IN WEIGHT PERCENT
Cl, IN WEIGHT PERCENT
0
2
4
6
8
10
0
0.2
0.4
0.6
0.8
1

B

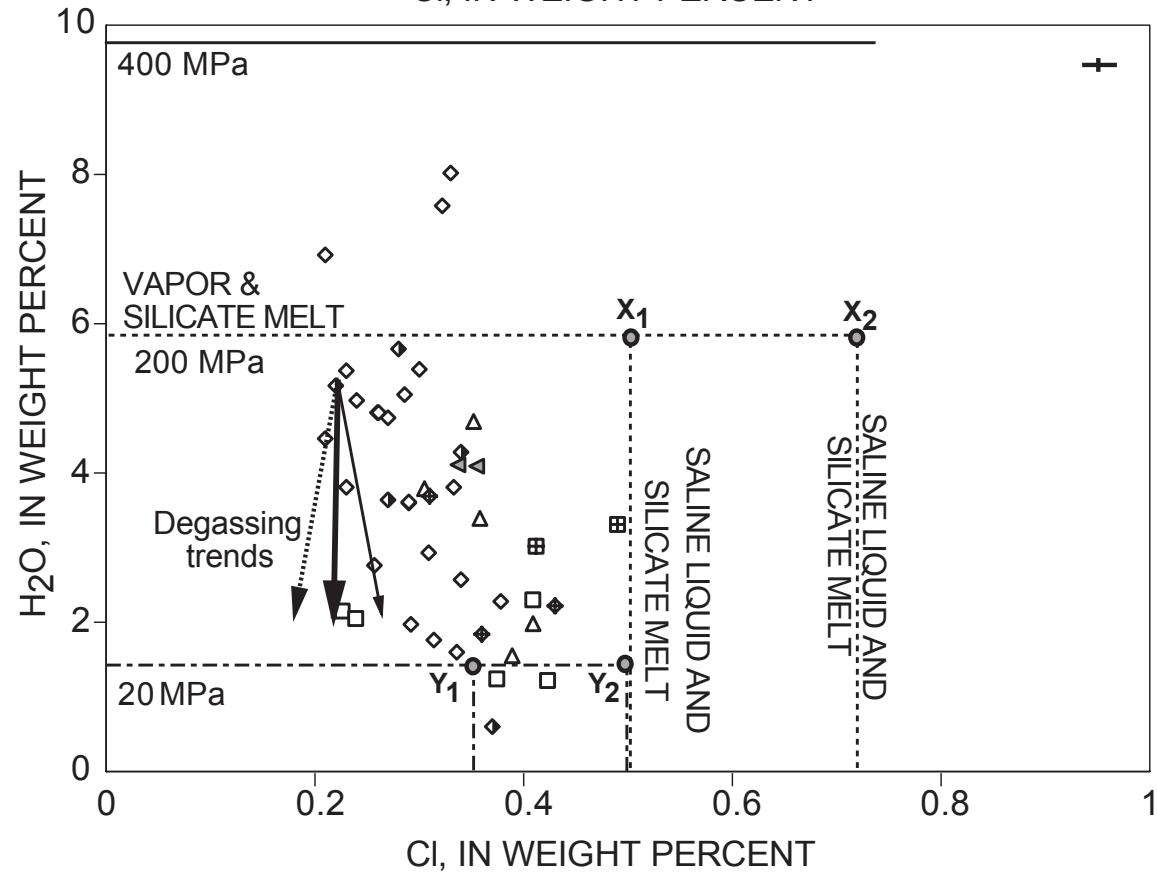
400 MPa
VAPOR &
SILICATE MELT
200 MPa
20 MPa
X1
X2
Y1
Y2
Degassing
trends
SALINE LIQUID AND
SILICATE MELT
SALINE LIQUID AND
SILICATE MELT
H2O, IN WEIGHT PERCENT
Cl, IN WEIGHT PERCENT
0
2
4
6
8
10
0
0.2
0.4
0.6
0.8
1

involving two pseudo-ternary systems, we interpret this agreement to indicate that most of these melt inclusions represent magma that was fluid saturated at the time of entrapment and, therefore, that pre-eruptive saturation of Augustine magmas in fluid(s) was a common process.

The comparison of the melt-inclusion compositions with the volatile solubility curves indicates that many felsic fractions of Augustine magma would have coexisted with volatile phases comparatively enriched in H_2O over CO_2 (fig. 10*A*). In fact, the H_2O content of the fluid(s), not accounting for the influence of Cl and S, was ≥95 mole percent for most aliquots of 2006 and prehistoric magmas and ≥ 85 mole percent for most fractions of 1986 magma.

To establish potential pressure-composition paths of magma ascent and degassing for the recent Augustine magmas, we relate the melt-inclusion data to a series of theoretical curves that express the reduction in H_2O and CO_2 concentrations of residual rhyolitic melt in evolving magmas as they ascend from depths equivalent to pressures of ≥ 350 MPa (fig. 10*B*). The 2006 and prehistoric data are most consistent with the rise of magmas containing 1 weight percent of H_2O-enriched vapor under closed-system conditions. This modeled curve is based on initial conditions involving a fluid-saturated magma at 950°C and approximately 400 MPa; the rhyolitic melt in this magma contains 9.5 weight percent H_2O and 100 ppm CO_2 at the initiation of fluid-saturated ascent and crystallization. Of particular importance is that the pressures estimated from H_2O and CO_2 in melt inclusions in 2006 samples range from 150 to 20 MPa only. This pressure range is consistent with crystallization of 2006 magma from the depths indicated by geodetic measurements (that is, for magma storage at 4 to 6 km) up to depths near the surface (Cervelli and others, this volume). The melt inclusions from 1986 tephra are more compatible with the rise of a fluid-saturated magma that contains 3 weight percent of H_2O-enriched vapor under closed-system conditions; the rhyolitic melt contains 7 weight percent H_2O and 500 ppm CO_2 as it passes through the depth equivalent to 350 MPa. In both cases, the vapor-saturated magmas are assumed to be crystallizing at 950°C while at a depth of 14 km (about 350 MPa).

These magmatic fluids were stable in the presence of melt at pressures ranging from 350 MPa to values <20 MPa. This range of pressure corresponds to depths of magmatic degassing that extend over the range of 14 km to 800 m, and, clearly, degassing must have continued at more shallow conditions (that is, as magma ascended and breached the volcanic edifice). Moreover, the modeling based on relationships involving H_2O and CO_2 is consistent with closed-system magma ascent as polybaric crystallization and degassing progressed, and the computed initial mass of fluids, which ranges from 1 to 3 weight percent and represents minimum fluid quantities, is consistent with prior work on other calc-alkaline, subduction-related magmatic systems (Wallace and Anderson, 2000; Scaillet and Pichavant, 2003; Wallace, 2005).

◀ **Figure 9.** Plots of the relation between H_2O and Cl in 45 silicate melt inclusions from Augustine Volcano samples including prehistoric rocks (open diamonds; Tappen and others, 2009), 1986 tephra sample 86E-63-2 of Roman and others (2006) (diamonds filled on right side), our 1986 tephra (gridded diamonds), low-silica andesitic sample 06AUJW004 (open squares), and high-silica andesitic samples 06AUCWM012 (gridded squares) and 06AUMC010.p1 (upward-pointing triangles). *A,* Melt-inclusion compositions are compared with trends describing: (A, dot-dash arrow) the result of 20 weight percent isobaric crystallization of fluid-absent rhyolitic melt on H_2O and Cl concentrations of residual melt; (B) polybaric, 20 wt. percent crystallization and exsolution of 4 weight percent aqueous fluid (with an average fluid/melt D_{Cl} = 10); (C) polybaric, 20 weight percent crystallization and exsolution of 4 weight percent Cl-bearing aqueous fluid (with average D_{Cl} = 5); (D) 20 weight percent polybaric crystallization and exsolution of 4 weight percent H_2O and no loss of Cl to fluid (i.e., with D_{Cl} = 0); and (trend E) mixing and/or mingling of H_2O-enriched and Na_2O-, K_2O-, and Cl-deficient magma with H_2O-deficient magma. *B,* Melt inclusion data are plotted relative to modeled solubilities of H_2O in H_2O-rich vapor-saturated rhyolite melt at 400 (solid curve), 200 (dashed curve), and 20 (dot-dash curve) MPa and 900°C (after Newman and Lowenstern, 2002), and Cl solubility in rhyolitic melts saturated in Cl-rich, H_2O-poor saline liquid (after Webster and De Vivo, 2002; Webster and others, 1999; 2005). At X_1 and X_2 (200 MPa), and at Y_1 and Y_2 (20 MPa), silicate melt coexists with vapor plus saline liquid. The 20- and 200-MPa volatile component solubility curves for H_2O-deficient conditions involve a range in Cl concentrations. The differences in Cl concentration between X_2-X_1 and Y_2-Y_1 reflect the computed ranges in maximum Cl solubility for the corresponding range in composition for this set of melt inclusions for two pressure conditions (Webster and De Vivo, 2002). The curves also account for the influences of sulfur (Webster and others, 2005; Botcharnikov and others, 2004) and pressure (Webster and others, 1999) on Cl solubility in silicate melts. These data, in conjunction with observations of figure 3B, indicate that at relatively higher pressures >200 MPa the dominant fluid phase coexisting with residual fractions of silicate melt was H_2O- and (potentially CO_2-) enriched vapor; whereas with magma ascent to lower pressures (approaching 20 MPa) the dominant magmatic fluid phase coexisting with evolving silicate melt was saline Cl- (and presumably S-) enriched liquid. Representative and relative 1-σ precision for glass analyses is shown in upper right corners. See text for discussion.

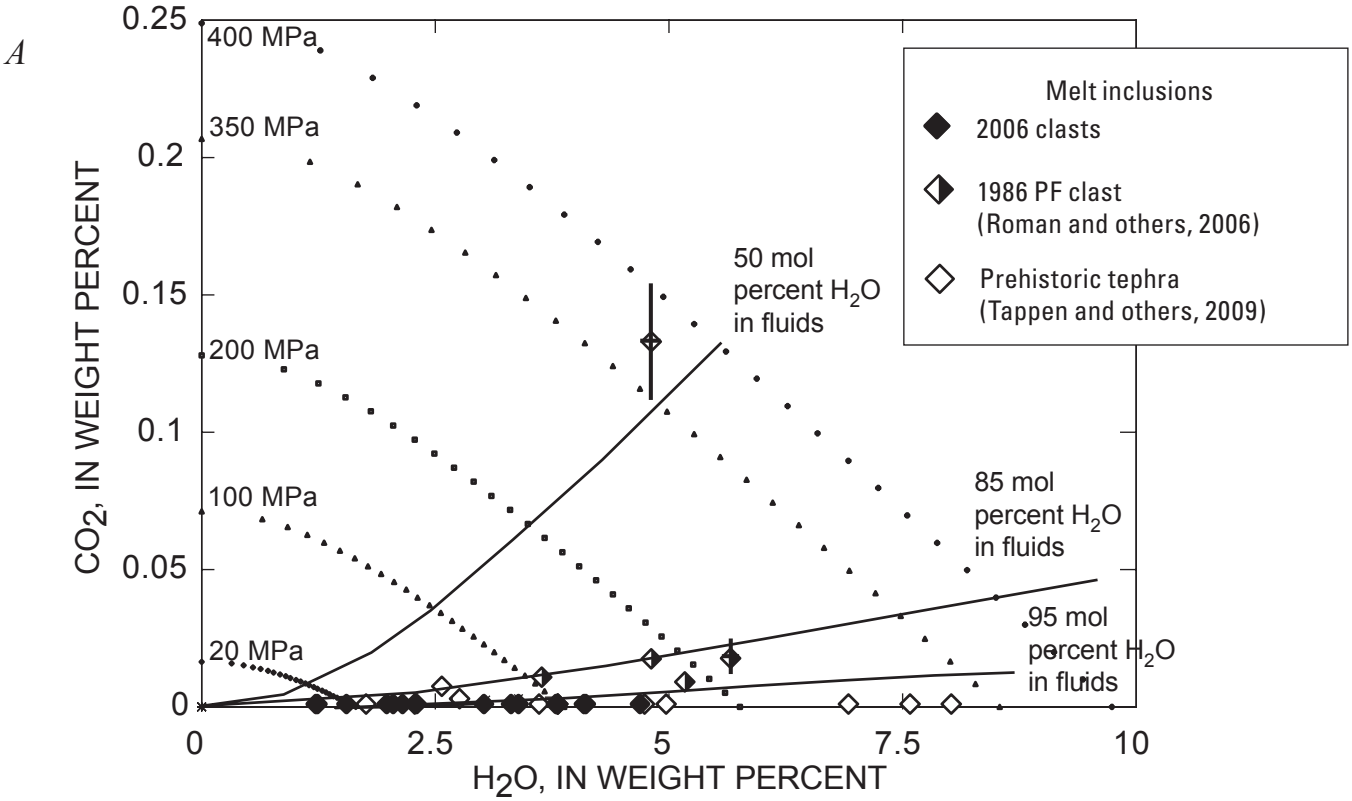
A
0.25
0.2
0.15
0.1
0.05
0
400 MPa
350 MPa
200 MPa
100 MPa
20 MPa
50 mol percent H_2O in fluids
85 mol percent H_2O in fluids
95 mol percent H_2O in fluids
Melt inclusions
2006 clasts
1986 PF clast (Roman and others, 2006)
Prehistoric tephra (Tappen and others, 2009)
CO_2, IN WEIGHT PERCENT
0
2.5
5
7.5
10
H_2O, IN WEIGHT PERCENT

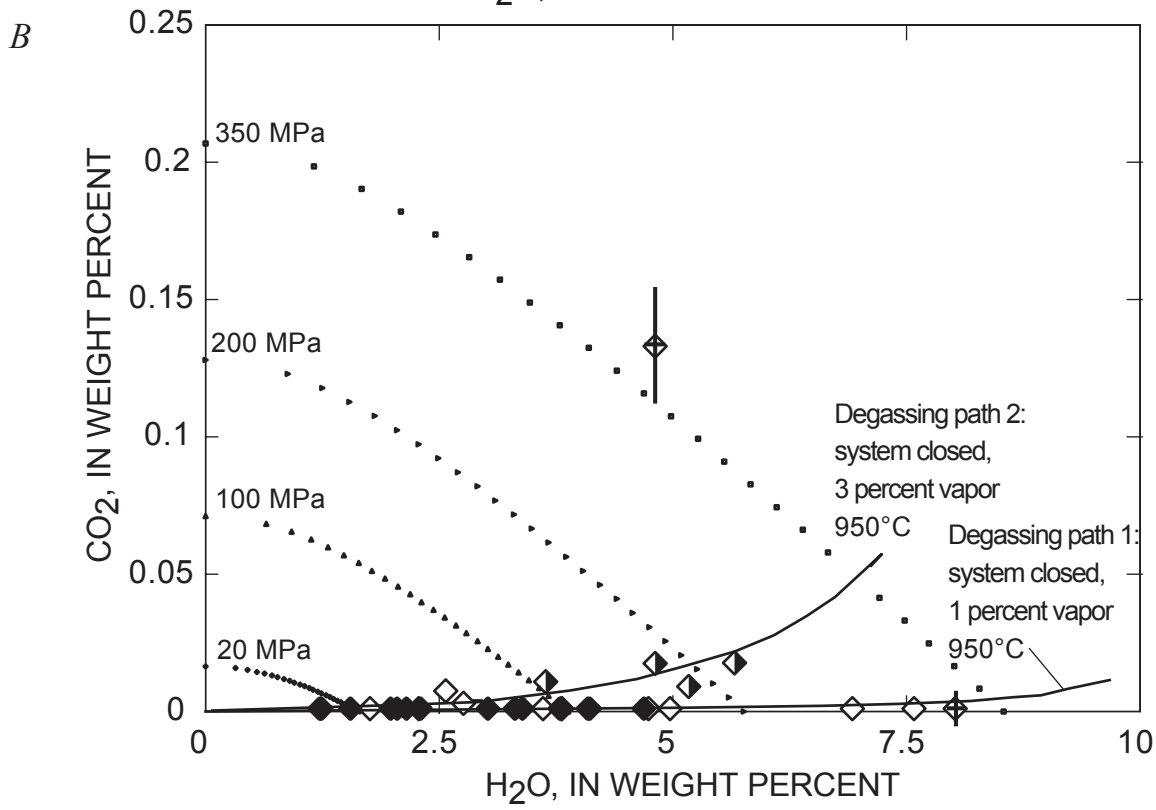
B
0.25
0.2
0.15
0.1
0.05
0
350 MPa
200 MPa
100 MPa
20 MPa
Degassing path 2: system closed, 3 percent vapor 950°C
Degassing path 1: system closed, 1 percent vapor 950°C
CO_2, IN WEIGHT PERCENT
0
2.5
5
7.5
10
H_2O, IN WEIGHT PERCENT

Developing a Model for the Behavior of Fluid Phase(s) During Magma Ascent and Differentiation

The relationships involving H_2O, CO_2, Cl, and S in the integrated melt-inclusion data reveal that the 2006, 1986, and prehistoric magmas contained one or more fluid phases before eruption, which is consistent with the results of prior research on 1976 (Johnston, 1978) and 1986 (Roman and others, 2006) magmas. These data also indicate that volatile components were sequestered by magmatic fluids as magma mixing ± mingling and fractional crystallization occurred, and that the fluids were stable through an extended pressure range and depth of magma ascent. In this developing model, we focus primarily on shallow-crustal processes influencing magmas after the ascent of hot, volatile-enriched basaltic magma into the crust and after this mafic magma mixed (our mixing event 1) with other more-evolved magma that was residing in the Augustine conduit and reservoir system. This involvement of relatively hot basaltic magma likely represents a potential eruption-triggering mechanism, because of the input of additional thermal energy and volatile components by the basaltic magma (Larsen and others, this volume). Thus, we focus on the potential role of fluids that were present (1) after mixing event 1 (fig. 2) and (2) during and subsequent to mixing event 2 (fig. 2). This treatment is relevant to the 2006 and older eruptions.

The integration of phenocryst and melt-inclusion compositional data demonstrates that these magmas behaved as quasi-closed systems, with regard to volatile component escape, until the magmas reached very shallow crustal depths (that is, ≤800 m). The compositions and rim textures of amphiboles, for example, provide relevant constraints on depths of crystallization and rates of magma ascent, respectively. Comparison of the compositions of 2006 Augustine amphiboles with those grown during hydrothermal experiments on similar bulk compositions at pressure, temperature and f_{O_2} conditions pertinent to Augustine magmas allows us to constrain the more narrow range of magmatic conditions that bear on amphibole crystallization in these magmas. Experimental work on amphibole stability in Mount St. Helens dacite at 850 to 940°C and 70 to 260 MPa (Rutherford and Devine, 2008) indicates that amphiboles contain ≤11 weight percent Al_2O_3 if crystallized below 200 MPa (fig. 11). This is a result of the fact that the Al content of amphiboles is largely dependent on the pressure-sensitive Al-Tschermak [^{M}(Mg,Fe)+ ^{T}Si = ^{M}Al + ^{T}Al], temperature-dependent edenite [^{T}Si +^{A}vacancy = ^{T}Al + ^{A}(Na,K)], and Ti-Tschermak [2^{T}Ti + ^{M}Mn =2^{T}Al +^{M}Ti] substitution mechanisms. In related work, Moore and Carmichael (1998) conducted hydrothermal experiments involving calc-alkaline andesites and basaltic andesites from western Mexico that are strikingly similar in bulk composition and intrinsic f_{O_2} to the 2006 Augustine low-silica and high-silica andesites. Amphiboles generated in experiments on the calc-alkaline andesite at 101 to 285 MPa, 900 to 975°C, and log f_{O_2} of NNO +2 contain ≥10 weight percent Al_2O_3 and ≥15.6 weight percent MgO (fig. 11). In contrast, most Augustine 2006 amphiboles with similar MgO contents contain ≤9.5 weight percent Al_2O_3. In addition, amphibole was not stable in Moore and Carmichael's (1998) calc-alkaline andesite experiments at temperatures >970°C. Amphiboles in Moore and Carmichael's (1998) experiments on the basaltic andesite contain ≥11.9 weight percent Al_2O_3 and >16.0 weight percent MgO at 950° to 1,000°C and 222 to 303 MPa. Interestingly however, most Augustine 2006 amphiboles contain <16 weight percent MgO (as well as Al_2O_3 contents ≤9.5 weight percent; fig. 11), so it is likely that Augustine amphiboles crystallized at pressures <170 MPa, and the rarity of amphiboles also indicates that these magmas passed through the low-pressure portion of the amphibole stability field (~130 to 170 MPa) rapidly. In addition, the lack of decompression-driven reaction rims on many of these amphiboles may indicate rapid magma ascent from depths of 4 to 5 km (Rutherford and Hill, 1993) and/or lack of favorable reaction kinetics for amphibole breakdown (Browne and Gardner, 2006). Interestingly, one of the 2006 amphiboles analyzed (table 6) exhibits an ~ 7-fold increase in F content from core to rim, and Rutherford and Devine (2008) observed similar variations of F concentration in amphiboles from the 2004-2006 dacite of Mount St. Helens. The latter study

◀ **Figure 10.** Plots of the relation between CO_2 and H_2O in 35 silicate melt inclusions from 2006, 1986, and prehistoric Augustine Volcano rock samples; symbols same as in figure 4. *A*, Data are plotted relative to isopleths for compositions of fluids in equilibrium with rhyolitic melts (calculated using model of Newman and Lowenstern, 2002), with fluids ranging from 95 mole percent H_2O (and 5 mole percent CO_2) to 50 mole percent H_2O (and 50 mole percent CO_2). Most melt inclusions are consistent with fluids in 1986 magma(s) containing ≤15 mole percent CO_2 and 85 mole percent H_2O, and many melt inclusions from the 2006 and prehistoric samples indicate that those batches of magma represented by these samples contained only trace CO_2 and so the fluids were CO_2-deficient. *B,* Data are plotted relative to a calculated closed-system degassing paths (using Newman and Lowenstern, 2002). Degassing path 1 applies to rhyolite melt initially saturated with 1 wt. percent vapor containing ≥95 mole percent H_2O at 950°C; this path (and these conditions) are consistent with evolution of fluid-saturated 2006 magmas. Path 2 applies to rhyolite melt initially saturated with 3 weight percent vapor containing approximately 85 mole percent H_2O at 950°C. Estimated values for 1-σ precision for CO_2 and H_2O in glasses are shown as vertical and horizontal lines for two representative high- and low-CO_2 melt inclusions. See text for discussion.

demonstrated that these changes in F content near the rim preceded the formation of reaction rim products, and it attributed this feature to amphiboles that were not within the amphibole stability field during magma ascent.

As part of our working model, we suggest that some of the 2006 and 1986 melt inclusions from high-silica andesites (that is, those of mixing trend 2, fig. 2) represent aliquots of younger felsic magma that interacted with older felsic magma while passing through the volcanic conduit at shallow crustal levels. Indeed, it is clear that some of these melt inclusions reflect shallow pressures of entrapment (due to their low volatile component abundances) while also showing other geochemical differences that reflect varying stages of evolution resulting from mixing and fractional crystallization. Thus, some of these mixing/mingling processes occurred within the conduit system. This interpretation is consistent with the conclusion of Roman and others (2006) that some 1986 magma formed via differentiation within the dike network that comprises the volcanic conduit and not within a magma chamber. It is also compatible with the bulk geochemistry of the two felsic end-member type magmas that are consistent with mixing trend 2 (fig. 2).

Given these constraints on magma composition, what can one establish about the compositions of the dominant fluids involved? It has been demonstrated that some fractions of the 2006, 1986, 1976, and prehistoric magmas contained a Cl-bearing aqueous vapor and other fractions contained Cl-rich saline liquid. In this regard, the results of prior experimental and theoretical research indicate that Cl-bearing magmas, and Cl-enriched magmas in particular, may also contain two fluids (Cl-bearing aqueous or aqueous-carbonic vapor plus saline liquid) at the shallow crustal pressures and magmatic temperatures characterizing volcanic conduits (Shinohara, 1994; Webster and Mandeville, 2007). In such systems, HCl is the dominant chloride species in volcanic vapors at surface or near-surface pressures (Giggenbach, 1996; 1997; Edmonds and others, 2002), which is consistent with prior study of Augustine's volcanic emanations indicating that it releases H_2O-dominated vapors containing significant HCl (Symonds and others, 1990). Conversely, alkali chlorides and alkaline earth chlorides are the dominant Cl-bearing species in coexisting magmatic saline liquids (Giggenbach, 1995). It follows that magmatic vapor and saline liquid should tend to separate from one another because of their strongly differing densities. The vapor will tend to

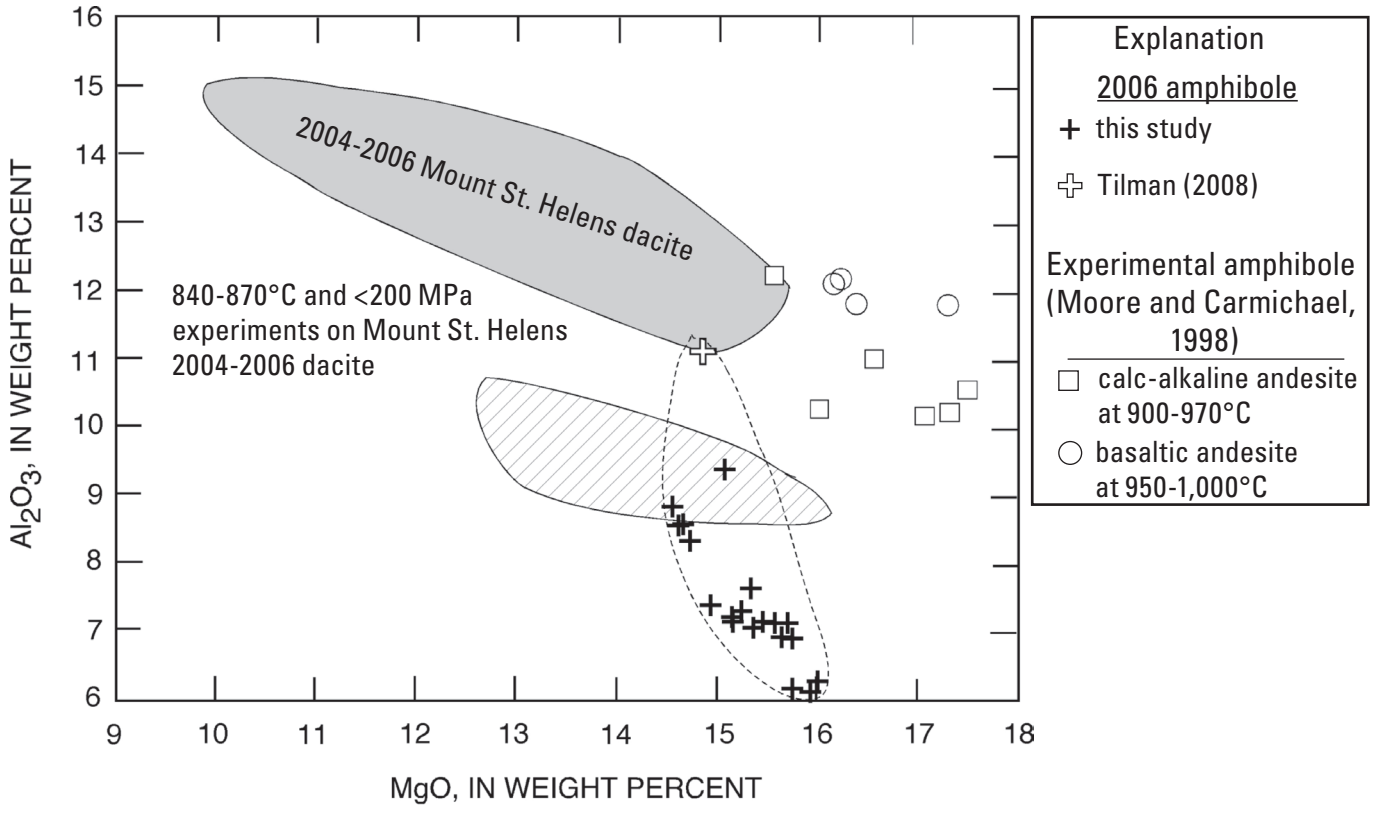

Figure 11. Plot of the relation between the concentrations of Al_2O_3 and MgO in amphiboles of Augustine Volcano rock samples compared to other natural and experimental amphibole compositions. Natural and experimental amphibole compositions from Mount St. Helens 2004–6 dacite from Rutherford and Devine (2008). Data from relatively rare Augustine 2006 amphiboles indicate they crystallized in the lower-pressure region of the amphibole stability field (~130 to 170 MPa).

ascend more rapidly through magma, and the saline liquid may either collect within a stratified "dryout" zone or horizon (Henley and McNabb, 1978) in the conduit (Hardee, 1982; Shmulovich and Churakov, 1998) or it may slowly ascend through the magma because its density is roughly half that of the encompassing silicate melt. In this regard, molten salt was observed flowing from fissures in the Vesuvius crater in the first decade following the 1944 eruption (Chiodini and others, 2001). Moreover, recent experimental studies have determined high solubilities of SO_4^{2-} in alkali chloride-enriched hydrothermal fluids at the pressures relevant to volcanism (Newton and Manning, 2005; Webster and others, 2007). Thus, the relatively oxidizing magmatic fluids at Augustine likely included H_2O-enriched and HCl-, H_2S-, S_2-, and SO_2- ± CO_2-bearing vapors; hydrosaline aqueous liquids largely enriched in Cl^-, SO_4^{2-}, alkalis, and H_2O; to moderately saline, H_2O-poor liquids containing Cl^-, SO_4^{2-}, and alkali elements.

The fluids at Augustine may also have played a significant role in the differentiation of evolved magma passing through shallowly located dikes. For example, one mechanism of forming a partially degassed and relatively anhydrous end-member melt composition that retains relatively high Cl contents during differentiation, that is, one similar to that involved in mixing/mingling at Augustine, involves the exsolution and loss of a saline liquid from felsic magma at low pressures. This is supported by close inspection of the volatile-component solubility relationships for H_2O and Cl that demonstrate that some fractions of felsic Augustine melt, represented by the most Cl-rich and H_2O-deficient melt inclusions, could exsolve a highly saline liquid (with or without coexisting vapor) and still contain moderate concentrations of H_2O at 20 MPa (at or near Y_1 and Y_2 in fig. 9*B*). This observation is a consequence of the strong deviations from ideal mixing behavior that occur in NaCl- and H_2O-bearing systems containing a saline liquid with or without vapor (Webster, 1992; Shinohara, 1994; Botcharnikov and others, 2004), and it is consistent with the modeled results of degassing trends B and C (fig. 9*A*). Even though the saline liquid is enriched in Cl, the exsolution of this phase does not reduce the Cl content of the melt significantly, because the activities of H_2O and chloride species are buffered at constant values in all phases present at equilibrium in a closed system (Shinohara, 1994; Webster and Mandeville, 2007). Thus, the subsequent separation and escape of a saline liquid from melt reduces the H_2O concentrations of the residual silicate melt, while maintaining elevated Cl levels in the melt.

Determining the origin of the low-K_2O end-member melt composition involved in mixing trend 2 is more of a challenge. It is difficult to envision how fractional crystallization could generate felsic melt compositions with such low K_2O concentrations like these without crystallizing alkali feldspar, which these rocks do not contain. This K_2O-enriched phase would have to have fractionated in significant quantities to generate the low K_2O values. Larsen and others (this volume) suggest that the low-K_2O matrix glasses may have formed by melting of low-K_2O, fine-grained gabbroic cumulate material, which follows the interpretation of Harris (1994) that mafic magma of the 1986 eruption mixed with magma residual from the 1976 eruption and also with low-K_2O, partially crystallized chamber residua. We suggest that the comparatively low concentrations of K, Na, Fe, S, and Cl in the melt inclusions representing this end-member composition are consistent with their mobilization in a fluid phase. Moreover, the elevated H_2O concentrations of this second "type" melt require that this style of fluid exsolution must have occurred at pressures greater than those bearing on the formation of the other end-member melt (for example, 100 to 200 MPa) because of the strong, positive relationship between pressure and water solubility in silicate melts. Experiments have demonstrated that the interaction of silicate melt with an HCl-bearing aqueous vapor tends to strip alkalis and Cl from the melt; in fact, some experiments have generated peraluminous melt compositions through the interaction of HCl-enriched vapors with melts that were initially subaluminous to metaluminous (Webster and Holloway, 1988; Williams and others, 1997; Frank and others, 2003). As discussed, the components in the vapor exsolved from Augustine magmas included HCl. Thus, it is plausible that the interaction of rhyolitic melt with HCl-bearing aqueous vapor at pressures of 100 to 200 MPa could have generated the observed geochemical characteristics of this second magma-mixing end member.

Relationships Involving Volatile Components, Fluids, and Eruptive Processes

Magma differentiation strongly influences volcanic activity, because the rate and style of eruptions vary directly with magma rheology, melt viscosity, and the concentrations of volatile components in late-stage magma as well as with temperature and pressure. Most melt inclusions chosen for this study represent silica-enriched residual melts with widely varying H_2O and Cl concentrations, and these parameters variably influence the viscosity of differentiated and fluid-saturated residual melts. We suggest that as the aliquots of younger and more hydrous felsic magma, which were variably depleted in Cl, Na_2O, K_2O, and FeO, ascended through the conduit system, they interacted at shallow depths with older and less hydrous felsic magma that had previously lost H_2O via degassing. The latter magma contained elevated concentrations of Cl, Na_2O, K_2O, and FeO that are more typical of evolved rhyolitic melts. The interaction of these magmas involved the exchange of heat as well as volatile components which played a critical role in subsequent eruptive processes.

Relationships involving H_2O, Cl, and CO_2 in some felsic melt inclusions, interpreted through experimental data from the corresponding melt-H_2O-CO_2 and melt-H_2O-Cl pseudoternaries provide independent indications (1) that the exsolution of fluid(s) from residual melt occurred at depths ≤14 km (that is, equivalent to approximately 350 MPa), (2) of the entrapment of fluid(s)-saturated melt at pressures as low as 20 MPa, and hence (3) that Augustine's magmatic volatile phase(s) remained in equilibrium with the rhyolitic melts to depths of ≤800 m (that is, that closed-system behavior was

maintained to quite shallow depths). Combination of these constraints with the observed lack of rimming or alteration of some amphibole phenocrysts (that crystallized in the 170 to 130 MPa range) suggests that the final ascent of amphibole-bearing magmas was also rapid.

It is noteworthy that before the 2006 eruption, precursory unrest in the form of increased seismicity, inflation, and pressurization at sea level began in mid-2005 (Cervelli and others, 2006; Power and Lalla, this volume). Similarly, seismic hypocenters preceding the 1986 eruption began to ascend from depths of 600 m to the crater just nine months before that eruptive phase began (Power, 1988; Roman, 2001; Power and Lalla, this volume), and similar seismic behavior was also observed before the 1976 eruption (Kienle, 1987). These seismic activities have been interpreted to signal hydraulic fracturing of overlying rock as magma (that is, fluid) pressure increased (Roman, 2001). This interpretation is consistent with observations from a similar study in which magmatic gas movement at Redoubt Volcano was called on as the source of some of its shallow seismic activity (Wolf and Eichelberger, 1997). We suggest these signals may also indicate that the fluid overpressures in Augustine magmas (with apparent fluid abundances of 1 to 3 weight percent) exceeded the confining rock strength and that they are indications of the separation of fluid(s) from magma at depths of 800 m or less. Augustine's crater rim is approximately 1.2 km in elevation, which means that some fluid-melt separation took place above sea level and well within the edifice. Interestingly, related modeling of the 2006 events by Coombs and others (this volume), based on average volumes of erupted material per explosion and the estimated conduit dimensions, determines that each Vulcanian explosion involved evacuation of the conduit to a depth of 1.9 km below the summit. In addition, they estimate an average evacuation depth, during eruptions, of 1 km. Thus, it is well supported that the separation and ascent of magmatic fluid at these quite shallow depths may have generated some of the recorded seismic behavior, while opening pathways for subsequent magma ascent.

Acknowledgments

We sincerely thank the staff of the Alaska Volcano Observatory for their considerable support and assistance during fieldwork on Augustine Island, and for subsequent collaborative assistance. We thank Dr. Richard B. Waitt of the USGS for providing the basalt sample (RBW-91A-137) and Dr. Chris Nye of the Alaska Division of Geological and Geophysical Surveys for sharing trace-element data for 6 Augustine basalt samples. Dr. George Harlow kindly shared his mineral recalculation program PRBDATNT. We thank Professor Jessica Larsen and Mariah Tilman of the University of Alaska at Fairbanks for providing data on amphiboles of 2006 rock samples. John Pallister, John Power, and Bruno Scaillet kindly provided detailed and thoughtful reviews of the manuscript. This research was supported by National Science Foundation award EAR-0308866 to J.D. Webster.

References Cited

Anderson, A.T., Jr., 1976, Magma mixing—petrological process and volcanological tool: Journal of Volcanology and Geothermal Research, v. 1, p. 3–33.

Anderson, A.T., Jr., 1982, Parental basalts in subduction zones—implications for continental evolution: Journal of Volcanology and Geothermal Research, v. 87, p. 7047–7060.

Anderson, A.T., Jr., 2003, An introduction to melt (glass ± crystals) inclusions, chap. 14 *in* Samson, I., Anderson, A., and Marshall, D., eds., Fluid inclusions—analysis and interpretation: Mineralogical Association of Canada, v. 32, p. 353–364.

Andersen, D.J., Lindsley, D.H., and Davidson, P.M., 1993, QUILF—A program to assess equilibria among Fe-Mg-Ti oxides, pyroxenes, olivine, and quartz: Computers and Geosciences, v. 19, p. 1333–1350.

Atlas, Z.D., Dixon, J.E., Sen, G., Finny, M., Pozzo, A.L.M.-D., 2006, Melt inclusions from Volcán Popocatépetl and Volcán de Colima, Mexico—Melt evolution due to vapor-saturated crystallization during ascent: Journal of Volcanology and Geothermal Research, v. 153, p. 221–240.

Bacon, C.R., and Hirshmann, M.M., 1988, Mg/Mn partitioning as a test for equilibrium between coexisting Fe-Ti oxides: American Mineralogist, v. 73, p. 57–61.

Bacon, C.R., Newman, S., and Stolper, D., 1992, Water, CO_2, Cl, and F in melt inclusions in phenocrysts from three Holocene explosive eruptions, Crater Lake, Oregon: American Mineralogist, v. 77, p. 1021–1030.

Baker, D.R., Freda, C., Brooker, R.A., and Scarlato, P., 2005, Volatile diffusion in silicate melts and its effects on melt inclusions: Annals of Geophysics, v. 48, p. 699–717.

Blundy, J., and Cashman, K., 2001, Ascent-driven crystallization of dacite magmas at Mount St. Helens, 1980-1986: Contributions to Mineralogy and Petrology, v. 140, p. 631–650.

Blundy, J., and Cashman, K., 2005, Rapid decompression-driven crystallization recorded by melt inclusions from Mount St. Helens volcano: Geology, v. 33, p. 793–796.

Blundy, J., Cashman, K., and Humphreys, M., 2006, Magma heating by decompression-driven crystallization beneath andesitic volcanoes: Nature, v. 443, p. 76–809.

Bodnar, R.J., and Student, J.J., 2006, Melt inclusions in plutonic rocks: petrography and microthermometry. chap. 1 *in* Webster, J., ed., Melt inclusions in plutonic rocks: Mineralogical Association of Canada v. 36, p. 165–188.

Botcharnikov, R.E., Behrens, H., Holtz, F., Koepke, J., and Sato, H., 2004, Sulfur and chlorine solubility in Mt. Unzen rhyodacitic melt at 850°C and 200 MPa: Chemical Geology, v. 213, p. 207–225.

Browne, B.L., and Gardner, J.E., 2006, The influence of magma ascent path on the texture, mineralogy, and formation of hornblende reaction rims: Earth and Planetary Science Letters, v. 246, p. 161–176.

Browne, B.L., Eichelberger, J.C., Patino, L.C., Vogel, T.A., Uto, K., and Hoshizumi, H., 2006, Magma mingling as indicated by texture and Sr/Ba ratios of plagioclase phenocrysts from Unzen volcano, SW Japan: Journal of Volcanology and Geothermal Research, v. 154, p. 103–116.

Burgisser, A., and Scaillet, B., 2007, Redox evolution of a degassing magma rising to the surface: Nature, v. 445, p. 194–197.

Carmichael, I.S., Turner, I., and Verhoogen, J., 1974. Igneous Petrology: McGraw-Hill, 739 p.

Carroll, M.R., and Rutherford, M.J., 1988, Sulfur speciation in hydrous experimental glasses of varying oxygen state—results from measured wavelength shifts of sulfur X-rays. American Mineralogist, v. 73, p. 845–849.

Cervelli, P.F., Fournier, T.J., Freymueller, J., and Power, J.A., 2006, Ground deformation associated with the precursory unrest and early phases of the January 2006 eruption of Augustine Volcano, Alaska: Geophysical Research Letters, v. 33, 5 p., doi: 10.1029/2006GL027219.

Cervelli, P.F., Fournier, T.J., Freymueller, J.T., Power, J.A., Lisowski, M., and Pauk, B.A., 2010, Geodetic constraints on magma movement and withdrawal during the 2006 eruption of Augustine Volcano, *in* Power, J.A., Coombs, M.L., and Freymueller, J.T., eds., The 2006 eruption of Augustine Volcano, Alaska: U.S. Geological Survey Professional Paper 1769 (this volume).

Chiodini, G., Marini, L., and Russo, M., 2001, Geochemical evidences of high-temperature hydrothermal brines at Vesuvio Volcano (Italy): Geochimica et Cosmochimica Acta, v. 65, p. 2129–2147.

Chou, I.-M., 1978, Calibration of oxygen buffers at elevated P and T using the hydrogen fugacity sensor: American Mineralogist, v. 63, p. 690–703.

Coombs, M.L., Bull, K.F., Vallance, J.W., Schneider, D.J., Thoms, E.E., Wessels, R.L., and McGimsey, R.G., 2010, Timing, distribution, and volume of proximal products of the 2006 eruption of Augustine Volcano, *in* Power, J.A., Coombs, M.L., and Freymueller, J.T., eds., The 2006 eruption of Augustine Volcano, Alaska: U.S. Geological Survey Professional Paper 1769 (this volume).

Daley, E.E., 1986. Petrology, geochemistry, and the evolution of magmas from Mt. St. Augustine volcano, Alaska: unpublished M.S. thesis, University of Alaska, Fairbanks, 106 p.

Danyushevsky, L.V., Della-Pasqua, F.N., and Sokolov, S., 2000, Re-equilibration of melt inclusions trapped by magnesian olivine phenocrysts from subduction-related magmas—petrological implications: Contributions to Mineralogy and Petrology, v. 138, p. 68–83.

Edmonds, M., Pyle, D., and Oppenheimer, C., 2002, HCl emissions at Soufriére Hills Volcano, Montserrat, West Indies, during a second phase of dome building: November 1999 to October 2000: Bulletin of Volcanology, v. 64, p. 21–30.

Evans, B.W., Scaillet, B., and Kuehner, S.M., 2006, Experimental determination of coexisting iron–titanium oxides in the systems FeTiAlO, FeTiAlMgO, FeTiAlMnO, and FeTiAlMgMnO at 800 and 900° C, 1–4 kbar, and relatively high oxygen fugacity: Contributions to Mineralogy and Petrology, v. 152, p. 149–167.

Frank, M.R., Candela, P.A., and Piccoli, P.M., 2003, Alkali exchange equilibria between a silicate melt and coexisting magmatic volatile phase—an experimental study at 800ºC and 100 MPa. Geochimica et Cosmochimica Acta, v. 67, p. 1415–1427.

Gerlach, T.M., Westrich, H.R., and Symonds, R.B., 1996, Preeruption vapor in magma of the climactic Mount Pinatubo eruption—source of the giant stratospheric sulfur dioxide cloud, *in* Newhall, C.G., and Punongbayan, R.S., eds., Fire and mud—eruptions and lahars of Mount Pinatubo, Philippines: PHIVOLCS and University of Washington Press, p. 415–433.

Giggenbach, W.R., 1997, The origin and evolution of fluids in magmatic-hydrothermal systems, chap. 15 *in* Barnes, H.L., ed., Geochemistry of hydrothermal ore deposits 3rd ed.: John Wiley and Sons Inc. New York, p. 737–796.

Giggenbach, W.R., 1996, Chemical composition of volcanic gases, *in* Scarpa, R., and Tilling, R., eds., Monitoring and mitigation of volcano hazards: Springer Berlin, p. 221–256

Giggenbach, W.R., 1995, Composition of magmatic components in hydrothermal fluids, chap. 11 *in* Thompson, J.F.H., ed., Magmas, fluids, and ore deposits, vol. 23: Mineralogical Association of Canada, p. 247–261.

Gurenko, A.A., Belousov, A.B., Trumbull, R.B., Sobolev, A.V., 2005, Explosive basaltic volcanism of the Chikurachki volcano (Kurile arc, Russia)—insights on pre-eruptive magmatic conditions and volatile budget revealed from phenocryst-hosted melt inclusions and groundmass glasses: Journal of Volcanology and Geothermal Research, v. 147, p. 203–232.

Hardee, H.C., 1982, Permeable convection above magma bodies: Tectonophysics, v. 84, p. 179–195.

Harlow, G.E., Murphy, A.R., Hozjan, D.J., de Mille, C.N., and Levinson, A.A., 2006, Pre-Columbian jadeite axes from Antigua, West Indies—description and possible sources: Canadian Mineralogist, v. 44, p. 305–321.

Harris, G., 1994. The petrology and petrography of lava from the 1986 eruption of Augustine volcano: University of Alaska, Fairbanks, unpub. M.S. thesis, 131 p.

Hawthorne, F.C., and Oberti, R., 2007, Classification of amphiboles: Reviews in Mineralogy and Geochemistry, v. 67, p. 55–88.

Henley, R.W., and McNabb, A., 1978, Magmatic vapor plumes and ground-water interaction in porphyry copper emplacement: Economic Geology, v. 73, p. 1–20.

Huebner, J.S., and Sato, M., 1970, The oxygen fugacity-temperature relationships of manganese oxide and nickel oxide buffers: American Mineralogist, v. 55, p. 934–952.

Izbekov, P., Wallace, K., Larsen, J., Nye, C., and Eichelberger, J., 2006, Variations of glass composition at the start of the 2006 eruption, Augustine Volcano, Alaska [abs.]: Geological Society of America Abstracts with Programs, v. 38, no. 5, p. 76–77.

Johnson, K.E., 1986, Isotope geochemistry of Augustine volcano, Alaska: Southern Methodist University, unpub. M.S. thesis, 144 p.

Johnson, K.E., Harmon, R.S., Richardson, J.M., Moorbath, S., and Strong, D.F., 1996, Isotope and trace-element geochemistry of Mt. St. Augustine volcano, Alaska—implications for magmatic evolution: Journal of Petrology, v. 37, p. 95–115.

Johnson, M.C., and Rutherford, M.J., 1989, Experimental calibration of the aluminum-in-magnesio-hornblende geobarometer with application to Long Valley caldera (California) volcanic rocks: Geology, v. 17, p. 837–841.

Johnston, D.A., 1978, Volatiles, magma mixing, and the mechanism of eruption of Mt. St. Augustine Volcano, Alaska: Seattle, Washington, University of Washington, unpub. Ph.D. dissertation, 177 p.

Johnston, D.A., 1979, Onset of volcanism at Mt. St. Augustine Volcano, Lower Cook Inlet: U.S. Geological Survey Circular 804-B, 78–80.

Jugo, P.J., Luth, R.W., and Richards, J.P., 2005, An experimental study of the sulfur content in basaltic melts saturated with immiscible sulfide or sulfate liquids at 1300°C and 1.0 GPa: Journal of Petrology, v. 46, p.783–798.

Kienle, J., 1987, Mt. St. Augustine works, but how?: Proceedings, Hawaii Symposium on How Volcanoes Work, p. 139.

Kienle, J., and Forbes, R.B., 1976, Augustine—evolution of a volcano: Geophysics Institute, University of Alaska Fairbanks, Annual Report 1975/76, p. 26–48.

Kienle, J., and Swanson, S.E., 1980, Volcanic hazards from future eruptions of Mt. St. Augustine volcano, Alaska: Geophysics Institute, University of Alaska, Fairbanks, Report UAG R-275, 122 p.

Larsen, J.F., Nye, C.J., Coombs, M.L., Tilman, M., Izbekov, P., and Cameron, C., 2010, Petrology and geochemistry of the 2006 eruption of Augustine Volcano, *in* Power, J.A., Coombs, M.L., and Freymueller, J.T., eds., The 2006 eruption of Augustine Volcano, Alaska: U.S. Geological Survey Professional Paper 1769 (this volume).

Lattard, D., Sauerzapf, U., and Kasemann, M., 2005, New calibration data for the Fe-Ti oxide thermo-oxybarometers from experiments in the Fe-Ti-O system at 1 bar, 1,000–1,300ºC and a large range of oxygen fugacities: Contributions to Mineralogy and Petrology, v. 149, p. 735–754.

Leake, B.E., 1997, Nomenclature of amphiboles; Report of the Subcommittee on Amphiboles of the International Mineralogical Association Commission on New Minerals and Mineral Names: American Mineralogist, v. 82, p. 1019–1037.

Le Bas, M.J., Le Maitre, R.W., Streckeisen, A., and Zanettin, B., 1986, A chemical classification of volcanic rocks based on the total alkali-silica diagram: Journal of Petrology, v. 27, p. 745–750.

Lowenstern, J.B., 1995, Applications of silicate-melt inclusions to the study of magmatic volatiles. chap. 4 *in* Thompson, J.F.H., ed., Magmas, fluids, and ore deposits: Mineralogical Association of Canada, v. 23, p. 71–99.

Luhr, J.F., 1990, Experimental phase relations of water-and sulfur-saturated arc magmas and the 1982 eruptions of El Chichon Volcano: Journal of Petrology, v. 31, p. 1071–1114.

Mandeville, C.W., A. Sasaki, G. Saito, K. Faure, R. King and E. Hauri, 1998, Open-system degassing of sulfur from Krakatau 1883 magma: Earth and Planetary Science Letter*s*, v. 160, no. 3/4, p. 709–722.

Mandeville, C.W., Webster, J.D., Rutherford, M.J., Taylor, B.E., Timbal, A., and Faure, K., 2002, Determination of molar absorptivities for infrared absorption bands of H_2O in andesitic glasses: American Mineralogist, v. 87, p. 813–821.

Massare, D., Métrich, N., Clocchiatti, R., 2002, High-temperature experiments on silicate melt inclusions in olivine at 1 atm—inference on temperatures of homogenization and H_2O concentrations: Chemical Geology, v. 183, p. 87–98.

McGee, K.A., Doukas, M.P., McGimsey, R.G., Neal, C.A., and Wessels, R.L., 2010, Emission of SO_2, CO_2, and H_2S from Augustine Volcano, 2002–2008, *in* Power, J.A., Coombs, M.L., and Freymueller, J.T., eds., The 2006 eruption of Augustine Volcano, Alaska: U.S. Geological Survey Professional Paper 1769 (this volume).

Moore, G., 2008, Interpreting H_2O and CO_2 contents in melt inclusions—constraints from solubility experiments and modeling, chap. 9 *in* Putirka, K.D, and Tepley III, F.J., eds., Minerals, inclusions,, and volcanic processes: Reviews in Mineralogy and Geochemistry, v. 69, p. 333–361.

Moore, G., and Carmichael, I.S.E., 1998, The hydrous phase equilibria (to 3 kbar) of an andesite and basaltic andesite from western Mexico—constraints on water content and conditions of phenocryst growth: Contributions to Mineralogy and Petrology, v. 130, p. 304–319.

Newman, S., and Lowenstern, J.B., 2002, VOLATILECALC—a silicate melt-H_2O-CO_2 solution model written in

Visual Basic for excel: Computers and Geosciences, v. 28, p. 597–604.

Newman, S., Bacon, C.R., and Stolper, E., 1986, Measurement of water in rhyolitic glass—calibration of an infrared spectroscopic technique: American Mineralogist, v. 71, p. 1527–1541.

Newton, R.C., and Manning, C.E., 2005, Solubility of anhydrite, $CaSO_4$, in NaCl-H_2O solutions at high pressures and temperatures: Journal of Petrology, v. 46, p. 701–716.

Nye, C.J., 2006, The 2006 eruption of Augustine Volcano—overview [abs.]: Geological Society of America Abstracts with Programs, v.38, no. 5, p. 28.

Power, J.A., 1988, Seismicity associated with the 1986 eruption of Augustine Volcano, Alaska: University of Alaska, Fairbanks, unpub. Ph.D. dissertation, 142 p.

Power, J.A., Nye, C.J., Coombs, M.L., Wessels, R.L., Cervelli, P.F., Dehn, J., Wallace, K.L., Freymueller, J.T., and Doukas, M.P., 2006, The reawakening of Alaska's Augustine Volcano: Eos (American Geophysical Union Transactions), v. 87, no. 37, p. 373–377.

Power, J.A., and Lalla, D.J., 2010, Seismic observations of Augustine Volcano, 1970–2007, *in* Power, J.A., Coombs, M.L., and Freymueller, J.T., eds., The 2006 eruption of Augustine Volcano, Alaska: U.S. Geological Survey Professional Paper 1769 (this volume).

Reed, M.H., 1997, Hydrothermal alteration and its relationship to ore fluid composition. chap. 7 *in* Barnes, H.L., ed., Geochemistry of hydrothermal ore deposits, 3rd ed: John Wiley and Sons, p. 303–365.

Roedder, E., 1984, Fluid inclusions: Reviews in Mineralogy and Geochemistry, v. 12, 644 p.

Roman, D.C., 2001, The 1986 eruption of Mt. St. Augustine Volcano, Alaska—magma storage and ascent. The University of Oregon unpub. Ph.D. dissertation, 129 p.

Roman, D.C., Cashman, K.V., Gardner, C.A., Wallace, P.J., and Donovan, J.J., 2006, Storage and interaction of compositionally heterogeneous magmas from the 1986 eruption of Mt. St. Augustine Volcano, Alaska: Bulletin of Volcanology, v. 68, p. 240–254.

Rutherford, M.J., and Devine, J.D., III, 1996, Preeruption pressure-temperature conditions and volatiles in the 1991 dacitic magma of Mount Pinatubo, *in* Newhall, C.G., and Punongbayan, R.S., eds., Fire and Mud—Eruptions and lahars of Mount Pinatubo, Philippines: Seattle, University of Washington Press, p. 751–766.

Rutherford, M.J., and Devine, J.D., III, 2008, Magmatic conditions and processes in the storage zone of the 2004-2006 Mount St. Helens dacite, chap. 31 *in* Sherrod, D.R., Scott, W.E., and Stauffer, P.H., eds., A volcano rekindled—the renewed eruption of Mount St. Helens, 2004–2006: U.S. Geological Survey Professional Paper 1750.

Rutherford, M.J., and Hill, P.M., 1993, Magma ascent rates from amphibole breakdown—an experimental study applied to the 1980–1986 Mt. St. Helens eruptions: Journal of Geophysical Research, v. 93, p. 19,667–19,685.

Scaillet, B., and Pichavant, M., 2003, Experimental constraints on volatile abundances in arc magmas and their implications for degassing processes, chap. 2, *in* Oppenheimer, C., Pyle, D.M., and Barclay, J., eds., Volcanic degassing: Geological Society of London Special Publication, v. 213, p. 23–52.

Shinohara, H., 1994, Exsolution of immiscible vapor and liquid phases from a crystallizing silicate melt—implications for chlorine and metal transport: Geochimica et Cosmochimica Acta, v. 58, p. 5215–5221.

Shmulovich, K.I., and Churakov, S.V., 1998, Natural fluid phases at high temperatures and low pressures: Journal of Geochemical Exploration, v. 62, p. 183–191.

Stormer, J.C., 1983, The effects of recalculation on estimates of temperature and oxygen fugacity from analyses of multicomponent iron-titanium oxides: American Mineralogist, v. 68, p. 586–594.

Straub, S.M., and Layne, G.D., 2003, The systematics of chlorine, fluorine, and water in Izu arc front volcanic rocks—implications for volatile recycling in subduction zones: Geochimica et Cosmochimica Acta, v. 67, no. 21, p. 4179–4203.

Sun, S.-S., and McDonough, W.F., 1995, The composition of the Earth: Chemical Geology, v. 120, p. 223–253.

Symonds, R.B., Rose, W.I., Gerlach, T.M., Briggs, P.H., and Harmon, R.S., 1990, Evaluation of gases, condensates, and SO_2 emissions from Augustine volcano, Alaska—the degassing of a Cl-rich volcanic system: Bulletin of Volcanology, v. 52, p. 355–374.

Tappen, C., Webster, J.D., Mandeville, C.W., and Roderick, D., 2009, Petrology and geochemistry of ca. 2100–1000 a.B.P. magmas of Augustine Volcano, Alaska, based on analysis of prehistoric pumiceous tephra: Journal of Volcanology and Geothermal Research, v. 183, p. 42–62.

Tilman, M.R., 2008, An investigation of symplectite-rimmed olivine and magmatic processes during the 2006 eruption of Augustine Volcano, Alaska: University of Alaska, Fairbanks, unpub. M.S. thesis, 166 p.

Vallance, J.W., Bull, K.F., and Coombs, M.L., 2010, Pyroclastic flows, lahars, and mixed avalanches generated during the 2006 eruption of Augustine Volcano, *in* Power, J.A., Coombs, M.L., and Freymueller, J.T., eds., The 2006 eruption of Augustine Volcano, Alaska: U.S. Geological Survey Professional Paper 1769 (this volume).

Wade, J.A., Boudon, G., Nougrigat, S., Poteaux, S., and Michel, A., 2006, The volatile content of magmas from Arenal volcano, Costa Rica: Journal of Volcanology and Geothermal Research, v. 157, p. 94–120.

Waitt, R.B., and Begét, J.E., 2009, Volcanic processes and geology of Augustine Volcano, Alaska. USGS Professional Paper 1762, 78 p., 2 map plates [http://pubs.usgs.gov/pp/1762/].

Wallace, K.L., Neal, C.A., and McGimsey, R.G., 2010, Timing, distribution, and character of tephra fall from the 2005–2006 eruption of Augustine Volcano, *in* Power, J.A., Coombs, M.L., and Freymueller, J.T., eds., The 2006 eruption of Augustine Volcano, Alaska: U.S. Geological Survey Professional Paper 1769 (this volume).

Wallace, P.J., 2005, Volatiles in subduction zone magmas—concentrations and fluxes based on melt inclusion and volcanic gas data: Journal of Volcanology and Geothermal Research, v. 140, p. 217–240.

Wallace, P.J., and Anderson, A.T., Jr., 2000, Volatiles in magma, *in* Sigurdsson, H., ed., Encyclopedia of volcanoes: Academic Press, San Diego, p. 149–170.

Waythomas, C.F., and Waitt, R.B., 1998, Preliminary volcano-hazard assessment for Augustine volcano, Alaska: U.S. Geological Survey Open-File Report 98-106, 39 p.

Webster, J.D., 1992, Fluid-melt interactions involving Cl-rich granites—experimental study from 2 to 8 kbar: Geochimica et Cosmochimica Acta, v. 56, p. 679–687.

Webster, J.D., and DeVivo, B., 2002, Experimental and modeled solubilities of chlorine in aluminosilicate melts, consequences of magma evolution, and implications for exsolution of hydrous chloride melt at Mt. Somma-Vesuvius: American Mineralogist, v. 87, p. 1046–1061.

Webster, J.D., and Holloway, J.R., 1988, Experimental constraints on the partitioning of Cl between topaz rhyolite melt and H_2O and $H_2O + CO_2$ fluids—new implications for granitic differentiation and ore deposition: Geochimica et Cosmochimica Acta, v. 52, p. 2091–2105.

Webster, J.D., and Mandeville, C.W., 2007, Fluid immiscibility in volcanic environments, chap. 10 *in* Leibscher, A., Heinrich, C., eds., Fluid-fluid equilibria in the crust: Reviews in Mineralogy and Geochemistry, v. 65, p. 313–362.

Webster, J.D., Kinzler, R.J., and Mathez, E.A., 1999, Chloride and water solubility in basalt and andesite liquids and implications for magmatic degassing: Geochimica et Cosmochimica Acta, v. 63, p. 729–738.

Webster, J.D., Sintoni, M.F., and De Vivo, B., 2005, The role of sulfur in promoting magmatic degassing and volcanic eruption at Mt. Somma-Vesuvius, *in* De Vivo, B., ed., Volcanism in the Campania Plain—Vesuvius, Campi Flegrei and Ignimbrites: Elsevier, Developments in Volcanology, v. 9, p. 221–236.

Webster, J.D., Sintoni, M.F., De Vivo, B., Lima, A., 2007, Volatile solubilities in Mt. Somma-Vesuvius phonolite melt and new insights on degassing of sulfur, chlorine, and water [abs.]: Eos (American Geophysical Union Transactions), v. 88, V42B-03.

Webster, J.D., Mandeville, C.W., Gerard, T., Goldoff, B., and Coombs, M.L., 2006. Volatile abundances and magma geochemistry of recent (2006) through ancient eruptions (< 2100 a BP) of Augustine Volcano, Alaska [abs.]: Eos (American Geophysical Union Transactions), v. 87, V42B-05.

Williams, T.J., Candela, P.A., and Piccoli, P.M., 1997, Hydrogen-alkali exchange between silicate melts and two-phase aqueous mixtures—an experimental investigation: Contributions to Mineralogy and Petrology, v. 128, p. 114–126.

Wolf, K.J., and Eichelberger, J.C., 1997, Syneruptive mixing, degassing and crystallization at Redoubt Volcano, eruption of December, 1989 to May 1990: Journal of Volcanology and Geothermal Research, v. 75, p. 19–37.

Zimmer, M.M., Plank, T., Hauri, E.H., Faust Larsen, J., and Kelemen, P.B., 2004, Volatile contents in mafic magmas from two Aleutian volcanoes—Mts. St. Augustine and Makushin [abs.]: Eos (American Geophysical Union Transactions), v. 85 no. 46, V34A-01.

Appendix 1. Sample Descriptions

2006 Samples

06AUMC005C.p5a Low-silica andesite scoria. Petrographic description: the sample is a vesicular, porphyritic andesite with brownish felty matrix contains areas of trace glass and many microlites. Plagioclase shows remelting/reequilibration growth zones containing orthopyroxene needles and melt inclusions. Melt inclusions are pink to dark brown in color. Plagioclase phenocrysts show complex and variable growth zoning; some contain growth zones with dusty dark groundmass material entrained. Orthopyroxene and clinopyroxene phenocrysts are subequal in abundance. Pyroxenes do not appear, in general, to be as zoned as the plagioclase phenocrysts do but pyroxenes do show more incipient oxidation/alteration. Some glomerocrystic clots contain plagioclase, pyroxenes, and iron-titanium oxides. Minor embayed and altered olivine phenocrysts. Coexisting oxides (ilmenite and magnetite) occur in matrix and phenocrysts; ilmenite is typically rimmed by magnetite with no visible exsolution textures; 0.025 to 0.6 mm diameter for coexisting oxides. No amphibole or quartz observed. No anhydrite observed.

06AUMC008b.p1A Low-silica andesite scoria. Petrographic description: the sample is a porphyritic andesite with a plagioclase- and oxide-microlite-rich, brownish, felty groundmass. Plagioclase is dominant phenocryst; some show oscillatory zoning. Others have sieve-textured cores and others show dusty groundmass material in growth zones. Melt inclusions occur in some plagioclase remelting/reequilibration/growth zones; melt inclusions somewhat less abundant than in other 2006 samples. Plagioclase phenocrysts are as much as 2. 5 mm in length. Clinopyroxene phenocrysts more abundant than orthopyroxene phenocrysts. Orthopyroxene phenocrysts up to 1.2 mm in length. Some orthopyroxene rimmed by clinopyroxene. Some complex glomeroporphyritic clots have oxides, plagioclase, and pyroxenes. Several volume percent euhedral, some unaltered olivine phenocrysts (up to 2 mm in diameter). Olivine also present as microlites in groundmass. Minor amphibole; some unaltered but others show alteration. Coexisting oxides (ilmenite and magnetite) occur in matrix and phenocrysts; ilmenite is typically rimmed by magnetite with no visible exsolution textures; 0.025 to 0.6 mm diameter for coexisting oxides. No quartz observed.

06AUMC010p1 High-silica andesite. Petrographic description: the sample is a porphyritic andesite that contains plagioclase as dominant phenocryst. Many plagioclase phenocrysts appear skeletal with other mineral inclusions partially entrained in the skeletal plagioclase. Smaller plagioclase laths and glass shards appear aligned. Plagioclase phenocrysts show complex zoning and growth history; oscillatory zoning, remelting/re-equilibration/growth zones with melt inclusions. Other plagioclase phenocrysts appear quite clean of inclusions. Plagioclase phenocrysts up to 4.5 mm in length. Melt inclusions in plagioclase are relatively abundant and pink to brown in color. Orthopyroxene phenocrysts less abundant than clinopyroxene phenocrysts; some orthopyroxene appears replaced by clinopyroxene. Pyroxenes show less zoning than plagioclase, but some pyroxenes show oxidation. Orthopyroxene and clinopyroxene phenocrysts up to 1 mm in length. Minor olivine phenocrysts present. Coexisting oxides (ilmenite and magnetite) occur in matrix and phenocrysts; ilmenite is typically rimmed by magnetite with no visible exsolution textures; 0.025 to 0.15 mm diameter for coexisting oxides. We observed no amphibole. No quartz observed.

06AUCWM007 Low-silica andesite scoria. Petrographic description: porphyritic andesite with phenocryst abundances listed in order of decreasing modal abundance. Plagioclase is subhedral to euhedral and occurs as crystals 0.2 to 1.7 mm in diameter and also as glomeroporphyritic crystal clots in association with orthopyroxene, clinopyroxene, and Fe-Ti oxides. Some plagioclase phenocrysts contain melt inclusions in remelting/reequilibration growth zones and many other plagioclase phenocrysts contain dusty matrix-enriched growth zones. Orthopyroxene occurs as subhedral to euhedral phenocrysts from 0.1 to 0.6 mm in diameter and as part of glomeroporphyritic crystal clots in association with plagioclase, clinopyroxene, and Fe-Ti oxides. Orthopyroxene is more abundant than clinopyroxene phenocrysts by an approximate ratio of 2:1, and is also present in the groundmass glass as fine needles. Clinopyroxene occurs as phenocrysts from 0.1 to 0.3 mm in diam. and also as glomerocrysts in glomeroporphyritic crystal clots in association with plagioclase, orthopyroxene, and Fe-Ti oxides. Some orthopyroxene undergoing replacement by clinopyroxene. Titanomagnetite and ilmenite occur as phenocrysts ranging from 0.03 to 0.2 mm and present also in glomeroporphyritic crystal clots. There are touching oxide pairs in contact with matrix glass that exhibit no exsolution lamellae and these should be good for preeruptive temperature- f_{O_2} estimates. One very rare pyroxene-rimmed olivine grain was observed.

Groundmass glass is clear in color with abundant microlites of clinopyroxene, orthopyroxene, plagioclase, and oxides. Rough volumetric proportion of vesicularity 45 to 50 percent based on blue epoxy. Note no amphibole observed in thin section, however, 1 amphibole was handpicked from crushed rock crystal concentrate. No visible quartz.

06AUCWM012 High-silica andesite. Petrographic description: Porphyritic andesite with phenocrysts in order of decreasing abundance: plagioclase occurs as large subhedral to euhedral crystals from 0.2 to 2.0 mm. Plagioclase also present as glomerocrysts. Many contain good glassy melt inclusions in plagioclase. Some plagioclase phenocrysts contain melt inclusions in remelting/ reequilibration growth zones and many other plagioclase phenocrysts contain dusty matrix-enriched growth zones. Orthopyroxene occurs as subhedral to euhedral crystals up to 1.0 mm and as part of glomeroporphyritic crystal clots. Orthopyroxene is more abundant than clinopyroxene by less than 2:1 (maybe 60/40). Orthopyroxene also contains good melt inclusions. Clinopyroxene occurs as subhedral to euhedral crystals from 0.2 to 0.7 mm and also in glomeroporphyritic clots associated with orthopyroxene, plagioclase, and Fe-Ti oxides. Pyroxenes show less zoning than plagioclase. Titanomagnetite and ilmenite occur as phenocrysts from 0.05 to 0.2 mm in diameter. Many touching oxide pairs in contact with glass with no exsolution lamellae that are good for temperature and oxygen fugacity estimation. Three amphibole grains were found in two thin sections and have the following occurrences: one small subhedral-embayed grain that has no reaction rim and is clean up to contact with matrix glass; one large 0.7 mm grain rimmed by pyroxene; one small amphibole inclusion in plagioclase. Groundmass glass is clear (rhyolitic) and in many areas is microlite-free and forms either thin stringers and wisps to more massive-texured glass near phenocryst clots. Despite high phenocryst abundance, matrix glass is highly vesiculated. No visible quartz.

06AUCWM014 Dense low-silica andesite. Petrographic description: Porphyritic andesite with phenocrysts in order of decreasing abundance: plagioclase occurs as large subhedral to euhedral crystals from 0.2 to 1.8 mm, some with partly resorbed/ spongy cores and as part of glomeroporphyritic crystal clots in association with orthopyroxene, clinopyroxene, Fe-Ti oxides. Some plagioclase phenocrysts contain melt inclusions in remelting/reequilibration growth zones and many other plagioclase phenocrysts contain dusty matrix-enriched growth zones. Orthopyroxene occurs as large subhedral to euhedral crystals from 0.2 to 1.2 mm in diameter and is also present as part of glomeroporphyritic crystal clots associated with plagioclase, clinopyroxene, and oxides. Abundance of orthopyroxene is equivalent to that of clinopyroxene. Clinopyroxene occurs as subhedral to euhedral crystals ranging from 0.1 to 1.0 mm in diameter, and in glomeroporphyritic crystal clots. Some clinopyroxene replaces orthopyroxene. Olivine is common and occurs as isolated phenocrysts as much as 0.6 mm in diameter but it is always completely rimmed by orthopyroxene± clinopyroxene. All olivine phenocrysts contain small brown spinel inclusions. Groundmass glass is brown in color and has a felty texture as it is enriched in clinopyroxene, orthopyroxene, plagioclase, and Fe-Ti oxide microlites. Titanomagnetite and ilmenite occur as rare phenocrysts up to 0.2 mm in size, with most crystals < 0.05 mm. Titanomagnetite and ilmenite exhibit extensive exsolution lamellae, so won't be good for temperature and oxygen fugacity estimation. Groundmass vesicularity ~ 35 to 40 percent. No amphibole crystals or amphibole pseudomorphs were observed. No visible quartz.

06AUJW001 Oxidized dense low-silica andesite. Petrographic description: Sample is a vesicular and somewhat inflated rx; matrix contains large areas of apparently good glass undergoing spherulitic devitrification with numerous oxides and some (minor) microlites. Porphyritic andesite with phenocrysts in order of decreasing abundance: plagioclase-dominated rock with some in plagioclase as part of glomeroporphyritic crystal clots in association with orthopyroxene, clinopyroxene, and Fe-Ti oxides Some plagioclase contains melt inclusions in remelting/re-equilibration growth zones and other plagioclase phenos contain dusty matrix growth zones; also the plagioclase-hosted melt inclusions tend to be more crystallized than those in other samples. Plagioclase phenocrysts are 0.05 to 3.5 mm in length; some larger plagioclase phenocrysts show complex and variable growth histories in their patterns of zonation. Orthopyroxene phenocrysts 0.05 to 1 mm, and clinopyroxene phenocrysts are 0.1 to 2 mm in length; some orthopyroxene undergoing replacement by clinopyroxene. The pyroxenes do not appear, in general, to be as zoned as the plagioclase phenocrysts. Sample contains significant but small amphibole phenocrysts with strong red-brown color; their margins do not show typical reaction rims but some show embayment and/or filling or replacement by plagioclase. Minor altered/embayed olivine phenocrysts are as much as 0.6 mm in diameter. Coexisting oxides (ilmenite and magnetite) occur in matrix and phenocrysts; ilmenite is typically rimmed by magnetite; significant exsolution features present; 0.03 to 0.3 mm diameter for coexisting oxides. There are far fewer melt inclusions in this sample than in other samples, and many of the largest plagioclase phenocrysts and as part of glomerocrysts contain few to no melt inclusions. No visible quartz.

06AUJW004 Dense low-silica andesite. Petrographic description: porous, porphyritic andesite containing brownish microlite-rich felty groundmass that still contains minor glass. Phenocrysts in order of decreasing abundance, plagioclase is 0.05 to 3.4 mm

in length. Most plagioclase phenocrysts are relatively clean of matrix or oxides, but many very large plagioclase phenocrysts or in glomerocrystic clots show extensive and complex zoning. Some plagioclase contains melt inclusions in remelting/reequilibration growth zones and sieve textured cores. The plagioclase phenocrysts tend to contain clear to generally brownish melt inclusions, but many of the largest unbroken plagiocase phenocrysts and glomerocrysts contain few to no melt inclusions. Pyroxenes are subequal in abundance with orthopyroxene phenocryst 0.05 to 1.8 mm in length, and clinopyroxene phenocrysts are 0.05 to 1 mm in length. Some evidence of plagioclase replacing pyroxene. Rare embayed and altered olivine phenocrysts are as much as 0.5 mm in diameter. Also contains amphibole phenocrysts which are rare and some appear to be undergoing replacement by pyroxene. Coexisting oxides (ilmenite and magnetite) occur in matrix and phenocrysts; ilmenite is typically rimmed by magnetite. Most oxides show no exsolution features; 0.025 to 0.5 mm diameter for coexisting oxides. No visible quartz.

06AUJW010 Dense low-silica andesite. Petrographic description: porphyritic rock containing brownish microlite-rich felty groundmass enriched in plagioclase and iron-titanium oxides. Plagioclase is the dominant phenocryst, phenocrysts are 0.05 to 4.8 mm in length; and it occurs as part of glomerocrystic clots containing pyroxenes and oxides. Approximately 20 to 25 percent of plagioclase phenocrysts contain sieve-textured cores, contain pyroxene inclusions, exhibit reheated growth zones that contain melt inclusions, and/or dusty growth zones that appear to have incorporated devitrified groundmass during late-stage plagioclase growth. Plagioclase phenocrysts contain clear to generally brownish melt inclusions, but the number of melt inclusions is not large. Zoning patterns in plagioclase show evidence of complex and variable growth histories. Orthopyroxene is more abundant than clinopyroxene. Orthopyroxene phenocrysts are 0.05 to 1.8 mm, and clinopyroxene phenocrysts are 0.05 to 0.8 mm in length; pyroxene phenocrysts show little optical evidence of zoning. Some pyroxene replaced by plagioclase. Minor altered (oxidized) and embayed olivine phenocrysts are as much as 0.4 mm in diameter. Coexisting oxides (ilmenite and magnetite) occur in matrix and phenocrysts; ilmenite is typically rimmed by magnetite. Significant exsolution features present; 0.025 to 0.4 mm diameter for coexisting oxides. No amphibole phenocrysts observed. No visible quartz.

Other samples

RBW-91A-137A Vesicular porphyritic olivine basalt. Petrographic description: porphyritic rock containing (in decreasing modal abundance) clinopyroxene, plagioclase, olivine, amphibole, and trace orthopyroxene. Clinopyroxene phenocrysts are oscillatory zoned and are as much as 3.5 mm in length; some show sieve-textured cores. Clinopyroxene phenocrysts are either euhedral or rounded (appearing partially resorbed); some clinopyroxene makes up most of glomeroporphyritic clots. Plagioclase phenocrysts are euhedral and are as much as 2.5 mm in length. Olivine phenocrysts are rounded, partially embayed, and bordered and apparently replaced by pyroxene. Olivine phenocrysts are as much as 1.5 mm in diameter. Groundmass is highly vesicular and holocrystalline, and contains pyroxene and tabular plagioclase microlites. Melt inclusions occur in olivine, pyroxene, and plagioclase; most inclusions are partially to fully crystallized but minor glassy inclusions are present.

AVO 208 Porphyritic pumiceous andesite. Petrographic description: porphyritic rock containing clear, highly vesicular, glassy groundmass containing few microlites of plagioclase, pyroxene, and iron-titanium oxides. Plagioclase is the dominant phenocryst and is as much as 2.5 mm in length. Plagioclase occurs as part of glomerocrystic clots containing pyroxenes and oxides. Some plagioclase phenocrysts contain clear to pinkish melt inclusions in remelting/re-equilibration growth zones, but unlike other samples few plagioclase phenocrysts contain dusty groundmass-bearing growth zones. Many oscillatory zoned plagioclase phenocrysts present. Orthopyroxene phenocrysts and clinopyroxene phenocrysts are subequal and far less abundant than plagioclase; pyroxene phenocrysts <1 mm in diameter. Pyroxene phenocrysts are not as strongly zoned as plagioclase. Trace olivine phenocrysts (<0.5 mm in diameter) appear resorbed, embayed, and replaced by pyroxene. Trace of amphibole observed. Melt inclusions are pink to clear to heavily crystallized and dark. Coexisting oxides (ilmenite and magnetite) occur in matrix and phenocrysts; ilmenite is typically rimmed by magnetite, with 0.025 to 0.4 mm diameter for coexisting oxides. No quartz observed.